

# Particle Acceleration in the Corona: Simulation and Observation

**Jingnan Guo**

Supervisor:

Prof. Wei-qun Gan(a)

Prof. Jörg Büchner(b)

Dr. Lyndsay Fletcher(c)

Prof. Eckart Marsch(b)

(a)Purple Mountain Observatory, Chinese Academy of Sciences, China

(b)Max-Planck-Institut für Sonnensystemforschung, Germany

(c)Department of Physics and Astronomy, University of Glasgow, U.K.

May, 2011

*Submitted in total fulfilment of the requirements for the degree of Ph.D.  
in Solar Physics*

# Contents

<b>Abstract</b>	<b>5</b>
<b>1 Introduction</b>	<b>9</b>
1.1 General Properties of the Sun . . . . .	9
1.1.1 The Solar Interior . . . . .	11
1.1.2 The Photosphere . . . . .	11
1.1.3 The Chromosphere and Transition Region . . . . .	12
1.1.4 The Corona and Solar Wind . . . . .	13
1.2 Solar Flare Observations . . . . .	14
1.2.1 A Classic Flare Scenario . . . . .	14
1.2.2 Radio, Microwave and EUV Emissions . . . . .	15
1.2.3 Soft and Hard X-ray Emissions . . . . .	16
1.2.3.1 Thermal and Nonthermal Components . . . . .	18
1.2.3.2 Temporal Characteristics of Hard X-ray . . . . .	21
1.2.4 Gamma-ray Emissions . . . . .	21
1.2.5 RHESSI . . . . .	22
1.3 Magnetic Reconnection and Solar Flare Models . . . . .	23
1.3.1 Theories of Magnetic Reconnection . . . . .	25
1.3.1.1 Sweet-Parker 2-D Reconnection Model . . . . .	25
1.3.1.2 Petschek 2-D Reconnection Model . . . . .	26
1.3.1.3 Turbulent 2-D Reconnection Model . . . . .	26
1.3.1.4 3-D Magnetic Reconnection and Magnetic Null Points . . . . .	26
1.3.2 Observations and Flare Models . . . . .	28
1.3.2.1 HXR Footpoints . . . . .	30
1.3.2.2 SXR Loops & Chromospheric Evaporation . . . . .	31
1.3.2.3 Coronal X-ray Sources & Reconnection Evidences . . . . .	31
1.3.2.4 Flares & CMEs Relations . . . . .	33
1.4 Particle Acceleration in Flares . . . . .	34
1.4.1 Direct Acceleration by Electric Field . . . . .	35
1.4.1.1 Parallel Electric Field Acceleration . . . . .	36
1.4.1.2 Perpendicular Electric Field Acceleration . . . . .	38
1.4.2 Stochastic Acceleration . . . . .	40
1.4.3 Shock Acceleration . . . . .	42

<b>2</b>	<b>3-D MHD Simulation and an X-type Magnetic Null Point</b>	<b>43</b>
2.1	Basic Equations of the 3-D MHD Simulation . . . . .	43
2.2	Initial and Boundary Conditions of the MHD Simulation . . . . .	44
2.2.1	Initial Conditions . . . . .	44
2.2.2	Boundary Conditions . . . . .	46
2.3	A 3-D Numerical X-type Magnetic Null Point . . . . .	46
2.4	Resistive Electric Fields . . . . .	50
2.4.1	Electric currents . . . . .	50
2.4.2	Resistivity $\eta$ . . . . .	52
2.5	Summary of MHD simulations . . . . .	52
<b>3</b>	<b>Test Particle Simulations in Convective Electric Fields at an X-Null</b>	<b>55</b>
3.1	An Overview of Test Particle Simulations . . . . .	55
3.2	How can a Perpendicular Convective Electric Field Accelerate Particles? .	58
3.3	Simulation of Particle Accelerations near the 3-D X-null . . . . .	61
3.3.1	Particle Acceleration under Different Plasma Flow Conditions . .	62
3.3.2	Single Proton Orbit Study for Case 3 . . . . .	63
3.3.3	Single Proton Orbit Study for Case 4 . . . . .	67
3.3.4	Single Electron Orbit Study for Case 3 . . . . .	69
3.3.5	Single Electron orbit Study for Case 4 . . . . .	70
3.3.6	Influence of the Initial Energy . . . . .	71
3.4	Discussions and Conclusions . . . . .	73
<b>4</b>	<b>Particle Acceleration at a Slow-reconnecting Null Point</b>	<b>77</b>
4.1	3-D MHD Simulation of a Slow-reconnecting Null point . . . . .	77
4.2	The Structure of the Magnetic Fields near the Null & Particle Drift Velocities	81
4.3	Simulation of Particle Accelerations near the New X-null . . . . .	82
4.3.1	Particle Acceleration under Different Plasma Flow Conditions . .	83
4.3.2	Compare the Acceleration Efficiencies of the New and the Old X-null . . . . .	86
4.3.3	Energy Gain of Electrons . . . . .	88
4.4	Summaries and Discussions . . . . .	89
<b>5</b>	<b>Relationship between Hard and Soft X-ray Emission Components</b>	<b>91</b>
5.1	Introduction . . . . .	92
5.2	Thermal and Non-thermal X-ray Emission Components of Solar Flares . .	94
5.3	Observations . . . . .	95
5.3.1	Light curves, Images, and Spectra . . . . .	95
5.3.2	Semi-calibrated light curves and their rate of change . . . . .	99
5.3.3	Spectral fit and the rate of change of photon flux and model pa- rameters . . . . .	101
5.3.4	Transition and Pivot energy . . . . .	102
5.4	Discussion . . . . .	104
5.5	Conclusions . . . . .	107
<b>6</b>	<b>Summary and Outlook</b>	<b>117</b>

<b>A</b>	<b>Normalization of the MHD Equations</b>	<b>121</b>
<b>B</b>	<b>Magnetic Field Extrapolation</b>	<b>125</b>
<b>C</b>	<b>Leapfrog and Lax Wendroff Schemes</b>	<b>131</b>
<b>D</b>	<b>Test Particle Calculations</b>	<b>133</b>
<b>E</b>	<b>Regularized Time Derivatives of Photon Fluxes</b>	<b>135</b>
	<b>Bibliography</b>	<b>137</b>
	<b>Publications</b>	<b>149</b>
	<b>Acknowledgements</b>	<b>151</b>
	<b>Curriculum Vitae</b>	<b>153</b>



# Abstract

*Me: "I am not happy with the result cause the electrons rarely get accelerated."*

*A friend: "Come on. Leave the electrons alone. They are always so negative."*

## *Simulation of Particle Acceleration:*

Particle acceleration at numerical magnetic X-null points in the solar corona has been studied. We first calculated the electromagnetic fields by 3-D magnetohydrodynamic (MHD) simulations (Chapter 2) and then we exposed charged particles to these fields within a full-orbit relativistic test-particle approach (Chapter 3). The 3-D magnetic configuration is chosen so that the resulting coronal magnetic field contains a null. Driven by photospheric plasma motion, the MHD simulation reveals the coronal plasma motion and the self-consistent electric and magnetic fields. In a subsequent test particle experiment the particle energies and orbits (determined by the forces exerted by the convective electric field and the magnetic field around the null) are calculated in time. Test particle calculations show that protons can be accelerated up to 30 keV near the null if the local plasma flow velocity is of the order of 1000 km/s (in solar active regions). The final parallel velocity is much higher than the perpendicular velocity so that accelerated particles escape from the null along the magnetic field lines. Higher electric fields result in higher final average energies, more efficient acceleration, and larger deviations of final energies. Stronger convective electric fields during big flare explosions can accelerate protons up to 2 MeV and electrons to 3 keV.

## *Observation of Solar Flares:*

A prominent  $\sim 50$  second hard X-ray (HXR) pulse of a simple GOES class C7.5 flare on 20 February 2002 is used to study the association between high energy, non-thermal and impulsive evolution, and low energy, thermal and gradual evolution. We use regularized methods to obtain time derivatives of photon fluxes to quantify the time evolution

as a function of photon energy, obtaining a break energy between impulsive and gradual behaviour. These break energies are consistent with a constant value of  $\sim 11$  keV in agreement with those found spectroscopically between thermal and non-thermal components, but the relative errors of the former are greater than 15% and much greater than a few percent errors found from the spectral fitting. These errors only weakly depend on assuming an underlying spectral model for the photons, pointing to the current data being inadequate to reduce the uncertainties rather than the result of a problem associated with an assumed model. The time derivative method is used to test for the presence of a ‘pivot energy’ in this flare. Although these pivot energies are marginally consistent with a constant value of  $\sim 9$  keV, its values in the HXR rise phase appear to be lower than those in the decay phase. Assuming that electrons producing the high-energy component have a power law distribution and are accelerated from relatively hot regions of a background plasma responsible for the observed thermal component, a low limit is obtained for the low-energy cutoff. This limit is always lower than the break and pivot energies and locates in the tail of the Maxwellian distribution of the thermal component.

### 中文摘要

太阳日冕中的粒子加速机制和产生硬X射线的过程是太阳高能物理中最具挑战性也有最有意义的问题之一。粒子加速的机制以及高能的非热粒子和加热的热粒子之间的关系是我博士学习的主要课题。

磁零点通常被认为是加速粒子的一个重要区域。在磁零点附近，原本做拉莫运动带电粒子可以弱磁化甚至达到非绝热状态，电场（即使是垂直于磁场的对流电场）便可以在这一过程中有效的加速带电粒子。然而，磁零点附近的电磁场结构却很难从观测中直接得到，而解析解又不够接近太阳日冕的真实情况。通过利用三维MHD程序构建日冕磁零点附近的电场和磁场的结构，并且把带电粒子（质子和电子）投入到这个电磁场中，我们第一次在数值上研究了三维磁零点附近的粒子加速过程。

平行电场的有效的加速过程已经被大量的学者研究过，其加速原理也非常容易理解：不管是磁化的还是非磁化的带电粒子都可以在沿着电场的方向（同时也是磁场的方向）被自由的加速。在磁零点附近，弱磁化的粒子可以直接被电场加速到很高的能量，而这一能量依赖于电场的强度和空间范围。磁化的粒子虽然在垂直于电磁场方向的平面做拉莫回旋运动，但是在平行于电磁场的方向上却可以被自由的加速。并且，平行于电场的磁场可以有助于稳定粒子的轨道，使其保持在电磁场的方向运动。然而，平行电场的大小在理想磁流体中小到可以忽略不计，只有磁重联过程中的有效电阻和电流片才能生成可靠稳定的平行电场。不管是观测还是MHD模拟都面临着量化有效电阻和定位电流片的难题。另一方面，垂直电场却广泛存在于太阳日冕中，并且可以达到上百V/m的量级，也通常被认为是MHD方程组中的对流电场分量（ $-VXB$ ）。因此利用MHD模拟得到的磁零点结构以及其附近生成的对流电场，我们研究了带电粒子的被加速的可能性以及其轨迹和能量变化。在均匀稳定的电磁场中，如果电场和磁场相互垂直，那么带电粒子很难被加速，因为拉莫运动会抵消掉增加和减少的能量。然而我们的模拟表明，在非均匀的磁场中，尤其当磁场非常弱时，粒子可以经历有效磁场曲率漂移和梯度漂移。当这一漂移沿着电场的方向时，粒子的动能就会改变。在磁零点附近，带电粒子甚至可以脱磁—拉莫运动的半径非常大以至于粒子感觉不到磁场的作用而只受到电场加速的作用。因而，当湍流速度在1000km/s时，质子可以被加

速到30keV的能量，并且最终平行于磁场方向的能量远大于垂直于磁场方向的能量。然而，由于其较小的回旋半径，电子却很难被弱磁化，也就很难在对流电场中得到有效的加速。

从观测上看，耀斑过程中加速的电子产生的光子谱通常有热分量和非热的幂率谱分量。而光变曲线上又可以看出明显的低能缓变项（随时间）和高能快变项。虽然这个缓变的分量通常被认为是热的部分，而快变的分量通常被认为非热的。然而，进一步的定量的分析还没有被研究过。我们将力图通过求解光变对时间的导数以及这一导数对光子能量的关系来定量的分析热和非热，缓变和快变之间的关系。利用RHESSI的数据，我们选取了一个简单的硬X射线耀斑。按GOES的等级，这个发生在2002年2月20号的耀斑只有C7.5级，且有明显和干净的脉冲和缓变两个分量。通过计算耀斑光变曲线对时间的导数，我们可以得到任意时间点光变导数和能量的关系。这一关系给出了脉冲分量和缓变分量的明确过度。另一方面，从耀斑能谱的拟合上，我们可以得到热和非热幂律谱之间的过度。通过比较这两个过度能量之间的关系，我们可以了解更多关于热和非热，脉冲和缓变分量之间的关系。结果表明，当脉冲相发生时，耀斑的热温度变化可以忽略不计的情况下，这两个过度能量都在11 keV左右。虽然数据的误差很难避免，但两者有很强的可比性。同时我们用这个新的光变求导的方法测试了支点能量(pivot energy)存在与否的假设。我们发现，即使这个支点能量是合理的定义，在耀斑上升相，其数值比在耀斑下降相时要小一些。



# 1 Introduction

*Every act of seeing leads to consideration, consideration to reflection, reflection to combination, and thus it may be said that in every attentive look on nature we already theorise.*

*Johann Wolfgang von Goethe*

Within our galaxy, the Sun is regarded as a small and relatively insignificant G2V star. Not brighter than 85% of all other resident stars, for the last 4.5 billion years the Sun has nevertheless supplied the necessary energy to allow life to evolve and populate most of the Earth's surface, while shaping its benign climate and driving its dynamic weather system. The Sun's close proximity to our planet allows the detailed study of the physical processes shaping its atmosphere and outer layers, knowledge that can then be applied to the understanding of other comparable stars.

Current topics of scientific inquiry include the Sun's regular cycle of sunspot activity, the physics and origin of flares and prominence(s), the magnetic interaction between the chromosphere and the corona, and the origin of the solar wind.

This thesis aims at investigating how the energetic particles are accelerated through reconnection processes during solar activities, especially solar flares. Two distinct albeit complementary approaches are here employed: test particle calculations in numerical electromagnetic fields obtained from Magnetohydrodynamics(MHD) simulations and observational analysis using the Reuven Ramaty High Energy Solar Spectroscopic Imager (RHESSI, see Section 1.2.5) (Lin et al. 2002).

The introduction chapter first offers a succinct overview of the Sun, then a review of the multiwavelength observations of solar flares. This is followed by a summary of the flare models indicated and constrained by these observations, including a review of the main topics concerning magnetic reconnection process and particle acceleration mechanisms.

## 1.1 General Properties of the Sun

Our Sun, which is halfway through its life expectancy ( 9 Gyr), represents only one of the billions of stars filling our universe, and it accounts for about 99.8% of the Solar System's mass. The Sun, by mass, is composed of about 70% hydrogen, 28% helium, and 2% of other heavy elements, including iron, nickel, oxygen, silicon, sulfur, magnesium, carbon, neon, calcium, and chromium. It is a moderately active star of radius  $6.96 \times 10^8$ m, with a

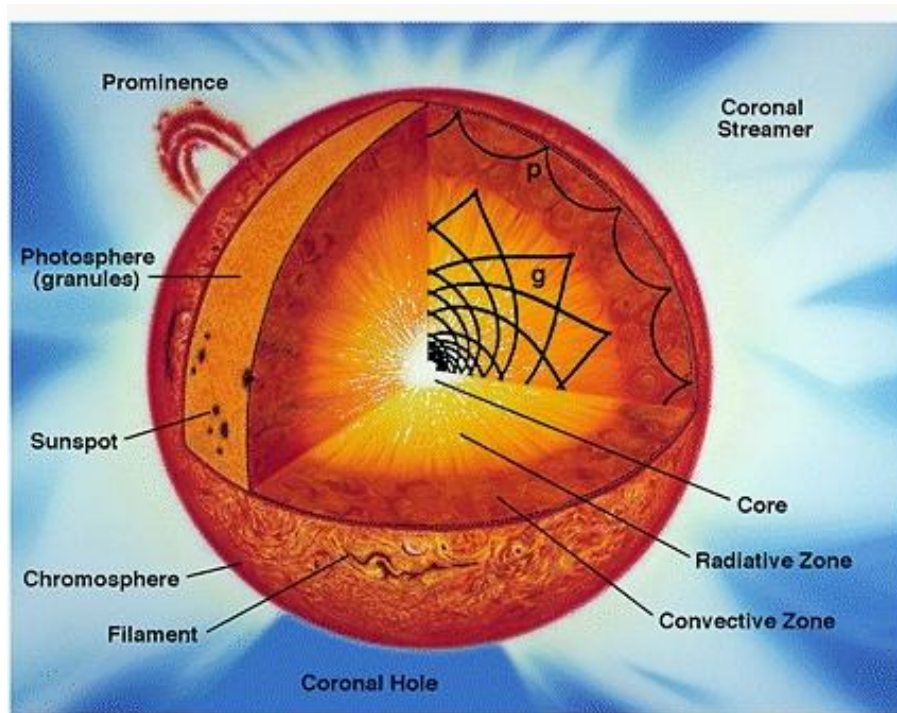


Figure 1.1: The structure of the Sun from interior to atmosphere (from <http://sohowww.nascom.nasa.gov/gallery>)

distance  $1.49 \times 10^{11}$  m (defined to be 1 AU) from the Earth, which is about 200 times its own radius. Watching from the Earth's elliptical orbit, the solar surface has a distance of about 722 km per arcsec. The Sun has a mass of  $1.99 \times 10^{30}$  kg and an average density of  $1.4 \text{ g cm}^{-3}$ . It has a total luminosity of  $3.84 \times 10^{26}$  W and an effective surface temperature of approximately 5777 K and a much higher core temperature of about 15 MK. At the solar surface, the gravitational acceleration is  $274 \text{ m s}^{-2}$  and the rotation period is 27 days at equator.

Under a first order approximation, the physical properties of the quiet Sun are just a function of its radius. Solar activities, which are closely related to the intense solar magnetic field, are overlapped to the quiet Sun. Indeed, even the quiet Sun features complicated structures everywhere and continuous dynamical processes, from small-scale phenomena such as network heating events, nanoflares, bright points, and soft X-ray jets, to large-scale structures, such as transequatorial loops or coronal arches.

Scientists focus most of their research on active regions due to their violent characteristics and their potentially hazardous effects on Earth. Active regions, although present only on a small fraction of the whole solar surface, harbor most of the solar activities. They tend to be located in areas of strong magnetic field concentrations, visible as sunspot groups in optical wavelengths or magnetograms. Due to permanent magnetic activity in terms of magnetic flux emergence, flux cancellation, magnetic reconfiguration, and magnetic reconnection, variant dynamic processes such as plasma heating, flares, and Coronal Mass Ejections (CMEs) occur in active regions.

To get a clear overall idea of the workings of the Sun, this section will describe the general properties of the Sun starting from the inside solar core to the outside solar surface

(see Figure 1.1), with an emphasis on the active regions in the solar atmosphere.

### 1.1.1 The Solar Interior

The description of solar interior encompasses everything below the Sun's optical surface, divided into hydrogen-burning core, radiative region and convective zone, as shown in Figure 1.1.

The interior core of the Sun, with a density of up to  $1.5 \times 10^5 \text{kgm}^{-3}$ , containing half of the Sun's mass and extending to nearly a quarter of the solar radius, is effectively the power source of the star. As a main sequence star, the Sun generates its energy by burning  $7 \times 10^{11} \text{kgs}^{-1}$  of hydrogen into helium. The rest of the star is heated by energy that is transferred outward from the core through many successive layers to the solar photosphere. The energy is then radiatively transported through a radiative zone from about 0.2 to 0.7 solar radius, and thereafter convectively transported through convective region up to the atmosphere. The time scale for a random walk of the photons through the radiative zone is about  $10^6$  years, while the convective transport time is just of a few months.

The interface layer between the radiative and convective zone is called tachocline, and it represents the location where the Sun's magnetic fields are generated. The interplay between the rigid-body rotation of the radiative zone and the fluid differential rotation of the convective zone causes weak poloidal field and stronger toroidal field. This magnetic field is further enhanced by the perturbing effect of convecting flows above the tachocline, twisting the field lines into rope-like structures; these can potentially be so twisted to have kinks and even rise up under buoyant force, observed as emerging magnetic flux on the solar surface, especially in active regions (Parker 1993).

### 1.1.2 The Photosphere

The solar atmosphere is generally described as being composed of multiple layers, with the lowest layer being the photosphere, followed by the chromosphere, the transition region and the corona on the top (see Figure 1.1).

The solar photosphere represents the effective surface of the Sun, and it is a relatively thin layer 500 km thick. The bottom of the photosphere, where the optical depth at 500 nm is 1, is thought to be the layer between the optically opaque interior and the transparent solar atmosphere. The photosphere has a temperature range from 6000 K at the bottom to 4000K at the top and a density of about  $10^{23} \text{m}^{-3}$ . Most of the energy radiated by the Sun is emitted in the photosphere at visible, UV and infrared wavelengths. The main structures on the photosphere are granules, sunspots and faculae.

Observations of the photosphere show that it is covered by convection cells called granules, each approximately thousands of kilometers in diameter with hot rising gas in the bright centers and cooler gas falling back down along the narrow dark edges between them. A typical granule has a lifespan from about 8 minutes to 20 minutes, resulting in a continually shifting "boiling" pattern. Super granular cells up to 30,000 km across, with longer lifetime up to 24 hours are also detectable using Doppler measurements.

Also seen on the photosphere are localized enhancements in the magnetic field in both bright small faculae and dark sunspots. Faculae are concentrations of magnetic field lines

and they are often found in the canyons between granules. A sunspot is a region with an intense magnetic field inhibiting hot plasmas convecting upwards and resulting in a lower temperature (about 4000K) than its surroundings (about 6000K). These spots often appear on both sides of the equator in two latitude bands which are thought to be regions with the strongest field shearing. The total number of spots fluctuates over an approximately 11 year-long cycle, which is consistent with the solar magnetic activity cycle. Frequently, in magnetic active regions, spots are visible in groups that have two opposite magnetic polarities (bipolar group), typically with a strongly concentrated leading magnetic polarity surrounded by a more fragmented trailing group with opposite polarity.

### 1.1.3 The Chromosphere and Transition Region

The regions of the Sun above the photosphere can be observed with telescopes operating across the electromagnetic spectrum, from radio through visible light to gamma-rays. Above the photosphere we find the 2500 km thick chromosphere, with a density of around  $10^{18}\text{m}^{-3}$  and temperatures ranging from about 4000 K at the lower interface to around 25,000 K at the top. The energy transport in the chromosphere is mainly through radiation and waves. There is little absorption here and most of the radiation originates from spectral emission at UV and optical wavelengths such as the first Balmer line,  $H_{\alpha}$ , the near-IR line from He I, and the UV line produced by calcium II.

The chromosphere exhibits a very wide variety of structures, including sunspots, plage, spicules, prominence, filaments, flares and eruptions. The cold sunspots in the photosphere could extend up to the chromosphere and be heated up. Enhancement in the local magnetic field seen as faculae in the photosphere also appears in the chromosphere as patches of bright emission called plage. Spicules are vertical dynamic jets growing upwards from the photosphere with velocities up to  $20\text{-}30\text{ km s}^{-1}$ . Spicules often rise to the top of the chromosphere and then sink back down again over the course of about 10 minutes. They are associated with regions of enhanced vertical magnetic fields which are the edges of the supergranular cells. Filaments or prominence, which are cool and dense clouds of material suspended by helix magnetic fields, can be seen in  $H_{\alpha}$  emissions.

Above the chromosphere there is the very thin (about only 100 km) transition region where the temperature rises rapidly and the density drops from  $10^{17}\text{m}^{-3}$  to  $10^{16}\text{m}^{-3}$ . A lower transition region (about 0.5 MK) shows structure very similar to chromosphere, with networks and plages, but in upper transition region (about MK), structures are more similar to corona. The temperature range and height of the transition region is still not well restrained. In fact, it can be observed with different temperatures and variant heights when using different emission lines at UV and EUV wavelengths, for instance, C IV at 100,000 K or S VI at 200,000 K. The transition region is very dynamic and it has typical brightening shown as blinkers. In the quiet Sun area, brightness variability in the transition region is larger than in any other layer of solar atmosphere.

The sharp increase of temperature above the photosphere is known as the coronal heating problem and its mechanism is not well understood. Many coronal heating theories have been proposed, and those receiving the most attention are magnetic reconnection and wave heating.

### 1.1.4 The Corona and Solar Wind

If we observe the Sun in other wavelengths than visible, for instance in X-rays or radio wavelengths, the brightest emission comes from the corona, while the photosphere becomes almost invisible, just opposite to optical wavelengths. Lying above the transition layer, and extending to several solar radius above the photosphere, the corona is very tenuous, with a number density of about  $10^{15} \text{ m}^{-3}$ , and very hot at 1-3 MK. Due to this high temperature, the corona has strong EUV lines (produced by highly ionized iron) and X-rays (a combination of thermal continuum and spectral lines) often in the configuration of hot loops of plasma indicating closed field lines in active regions. Apart from these active regions, coronal structures also include quiet Sun, X-ray bright points, and coronal holes. The coronal shape and level of activity varies in phase with the solar magnetic cycle, i.e. over 11 years. At solar maximum the corona is irregularly shaped at the equator and many active regions can be observed. At solar minimum the corona is regularly shaped with less active regions.

In MHD descriptions for solar atmosphere, plasma  $\beta$  are defined as the ratio of plasma pressure to magnetic pressure. In the solar corona where the density is very small,  $\beta \ll 1$ , the magnetic field dictates the dynamics of the gas: magnetic field for instance rather than plasma motions dominates the evolution of the system. Also, particles are mostly ionized in high temperature coronal environment. The charged particles cannot easily cross the strong magnetic fields due to the gyration motion, e.g., plasma and magnetic field are frozen into each other in this ideal MHD condition. However, dynamic corona environment may over-stress the magnetic field and cause topological changes by adjusting the large-scale magnetic field. The magnetic reconnection processes can be switched on and the frozen-in condition breaks down. Meantime, a large amount of nonpotential energy is liberated and converted into heating of plasma, acceleration of particles, and kinematic motion of coronal plasma.

Solar winds are streams of energetic particles, mostly electrons and protons, leaving the corona into interplanetary space. The total flux of particles carried away from the Sun by the solar wind is about  $1.3 \times 10^{31}$  per second. The total mass loss per year is about  $(2 - 3) \times 10^{-14}$  solar mass. Only about 0.01% of the Sun's total mass has been lost through the solar wind since its formation. Although this mass loss comparing to the whole Sun is really small, larger solar wind events may have a negative impact on modern human activities including geomagnetic storms that can knock out power grids on Earth, and burning out orbiting satellite navigation systems; other physical effects, but of no detrimental to us include the production of auroras, such as the Northern Lights, and the production of the plasma tails of comets, which naturally, always point away from the Sun.

The solar wind can be separated into slow and fast components. The slow solar wind has a velocity of less than 400 km/s, a number density of about  $8 \text{ rmc m}^{-3}$ , a temperature of 1.4-1.6 MK, and a composition that is a close match to that of the corona. In contrast, the fast solar wind has a typical velocity larger than 400 km/s, a lower temperature of 0.8 MK and it nearly matches the composition of the Sun's photosphere. The slow component tends to originate from the equatorial regions where the hot plasma is able to escape at the edges of the bright wedge-shaped regions known as the "helmet streamers". The fast component comes from the corona holes, i.e. funnel-like regions of open field lines.

The outer edges of the Sun's corona can be transported away due to the open magnetic flux acting as an efficient conduit for flushing heated plasma from the corona into the solar wind when chromospheric upflows at their footpoints are present. The northern and southern polar zones, rather than the equatorial zones, are the locations of coronal holes. Due to this efficient transport mechanism, coronal holes contain less plasma than quiet Sun where heated plasma remains trapped in the closed field lines and thus appear darker. Also related to the open field lines are polar plumes, where bright thin vertical strips of emission are seen, thought to represent plasma escaping from the corona holes.

## 1.2 Solar Flare Observations

Solar flares, the local brightening of emissions in active solar regions, were first observed in the white light continuum by Carrington and Hodgson (Hodgson 1859). In the typical flares with spatial extent of around 10-100 Mm,  $10^{29}$  to  $10^{33}$  ergs of total energy can be released in a few minutes to a few tens of minutes and radiation emitted virtually across the entire electromagnetic spectrum: gamma-rays, X-rays, ultraviolet, white light,  $H_\alpha$  line, infrared, microwave, and radio. Space missions such as Skylab, SMM, Yohkoh, SoHO, TRACE, and RHESSI, have considerably boosted our observational base. For overviews on solar flares, see Tandberg-Hanssen and Emslie (1988); Zirin (1988) and Aschwanden (2005).

In general, a flare can be described as a catastrophic event that is triggered by an instability of the dynamic magnetic fields; a flare then evolves into a more stable state by reconstructing the magnetic topology and liberating free nonpotential magnetic energies in the form of currents that spawn primary plasma heating and particle acceleration. Different flare models including magnetic reconnection processes and particle acceleration and plasma heating mechanisms have been developed and compared with observations. Numerical simulations, such as MHD simulations, PIC (particle-in-cell) simulations and test particle simulations, have also been employed to further investigate the mechanism of flare explosions and the process of energy releases. In this section we introduce some basic observational facts relating to solar flares with an emphasis on the RHESSI (Section 1.2.5) observations.

### 1.2.1 A Classic Flare Scenario

Flares always occur in active regions on the Sun where sunspots and complicated magnetic fields are under development. Due to the association with active regions, flares follow the eleven-year solar cycle. Classification of flares is normally based on their extent and brightness in certain wavelengths. According to the maximum soft X-ray (1-8 Å) emission measured with GOES satellites, flares are classified as (from weak to strong): A, B, C, M, and X.

A typical solar flare has three distinct phases: preflare, impulsive, and decay. In the preflare phase the coronal plasma in the flare region slowly heats up and there is an intensifying of soft X-rays emissions and brightening in UV/EUV. In the impulsive phase, a large number of energetic particles, including electrons and ions, are accelerated by the energy released in the corona. As they are transported downward to the footpoints of the

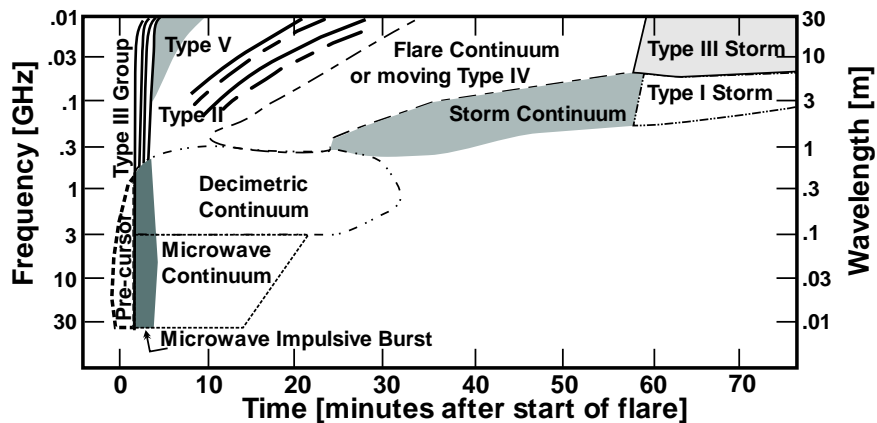


Figure 1.2: A schematic of the radio spectrum of a flare (from Hannah). In reality the radio emission of a flare can vary considerably from this simplified example.

magnetic tube, the particles lose most of their energy in Coulomb collisions with dense, ambient plasma and they produce hard X-ray emission, known as thick-target nonthermal bremsstrahlung (Brown 1971). Therefore, the appearance of hard X-ray footpoint sources at chromospheric altitude is a characteristic of the impulsive phase. The thermal soft X-ray and  $H_{\alpha}$  emissions also reach their maxima (often later than the impulsive peak) when energy is more gently released, manifested in decimetric pulsations. Sometimes, the rapid increase in  $H_{\alpha}$  intensity and pulsations of decimetric emission are separated from impulsive phase, known as a flash phase. Finally, during the decay phase most of the coronal plasma returns to its original state, except in the high corona (higher than 0.2 solar radius) where magnetic reconfiguration, plasma ejections and shock waves continue to accelerate the particles causing meter-wave radio bursts and interplanetary particle events.

### 1.2.2 Radio, Microwave and EUV Emissions

Radio emission is often observed as bursts at metric wavelengths and provides direct information on the radiation from particle beams, plasma and shock waves emanating from the flare region. Roughly, according to observation, radio emission can be split into 5 different types, see Figure 1.2. For a more comprehensive discussion, one could see Dulk (1985).

Type I bursts are long lasting (hours to days) noise storms that occur above active regions. They might represent plasma oscillations excited by electrons energized by continuous magnetic reconnection above the active region. Type II bursts are associated with large flares and are interpreted as plasma emission due to a shock wave that propagates outwards from the flare. Type III bursts are common features of the radio spectrum, occurring over short time periods but extend over a wide range of frequencies. Type III are most closely correlated to the impulsive phase of flares and hard X-ray bursts. They are produced by beams of mildly relativistic electrons propagating from the low corona out into interplanetary space along open magnetic field lines that excite plasma emission (most likely Langmuir waves). The frequency of this emission is directly proportional to the density of the emitting plasma. So the highest frequency type III bursts are caused

by oscillations in the low corona while the lowest frequency bursts are due to oscillations in interplanetary space near 1 AU. Type IV bursts are broadband continuum emissions, caused by either a gyrosynchrotron emission, a plasma emission from a plasmoid, or high filled coronal loops of nonthermal particles. When originating from a CME or expanding loop, we are looking at a moving type IV emission. Type V bursts are continuum emissions that are sometimes observed after Type III bursts. They are thought to arise from both forward and counter-streaming Langmuir waves that might have been generated by the passage of the Type III burst electrons.

At much higher frequencies, up to hundreds of GHz, microwave emissions, produced by gyrosynchrotron emission from extremely hot thermal or relativistic nonthermal electrons, are observed to be coincident with soft X-ray loops.

When electron beams evaporate chromospheric plasma into the coronal loops, the heated thermal plasmas are often seen as postflare Extreme Ultraviolet EUV loops. EUV observations always show the complexity and dynamics of the coronal structures because they highlight some of the coronal magnetic field structures along which the hot plasma is flowing.

The Extreme-Ultraviolet Imaging Telescope (EIT) onboard the Solar and Heliospheric Observatory (SOHO) produces full disk images of the Sun in He II (304 Å), Fe IX (171 Å), Fe XII (195 Å), and Fe XV (284 Å) showing plasma at temperatures of around 0.06 to 0.08 MK, 1 MK, 1.5 MK, and 2 MK respectively. The Transition Region And Coronal Explorer (TRACE) also produces EUV images (Fe IX / X, 171 Å; Fe XII / XXIV, 195 Å; and Fe XV, 284 Å;) with higher resolution (0.5" pixel size as opposed to 2.6" EIT pixel size) but non-full-disk image ( $8.5 \times 8.5$  arc minutes).

### 1.2.3 Soft and Hard X-ray Emissions

The main mechanisms generating X-rays are: (1) Free-free continuum radiation: this describes the *bremsstrahlung* emission from an electron deflected by another charged particle without being captured. The emission is more efficient if the collision occurs with a heavy particle, such as a proton or a heavier atomic nucleus. (2) Free-bound radiation: this is the emission caused by an electron when captured by an ion (*recombination*). Since the capture probability depends on the charge and mass of the ion, the strength of free-bound radiation is very sensitive to the abundance of heavy and ionized metals such as Fe and Ni. This process produces a continuum with additional sharp steps corresponding to the atomic energy levels of the final bound state of the electron. (3) Bound-bound radiation: this is the emission from excited electrons falling back into a lower energetic state in an ion, a process that produces line emissions.

In flare cases, there are generally three types of *bremsstrahlung*. When the colliding electrons have the same temperature or same thermal energy as the ambient plasma, thermal *bremsstrahlung* dominates and contributes to the soft part of the X-ray spectrum. When nonthermal electrons are accelerated in the corona and transferred downward to the denser and colder plasma in the chromosphere, they are collisionally slowed down to local thermal speeds, namely thick-target *bremsstrahlung*. And thin-target *bremsstrahlung* occurs when electrons continuously propagate without being braked and the X-ray spectrum is nearly unchanged from the injection spectrum. Figure 1.3 shows the high energy spectrum of a typical solar flare during its impulsive phase.

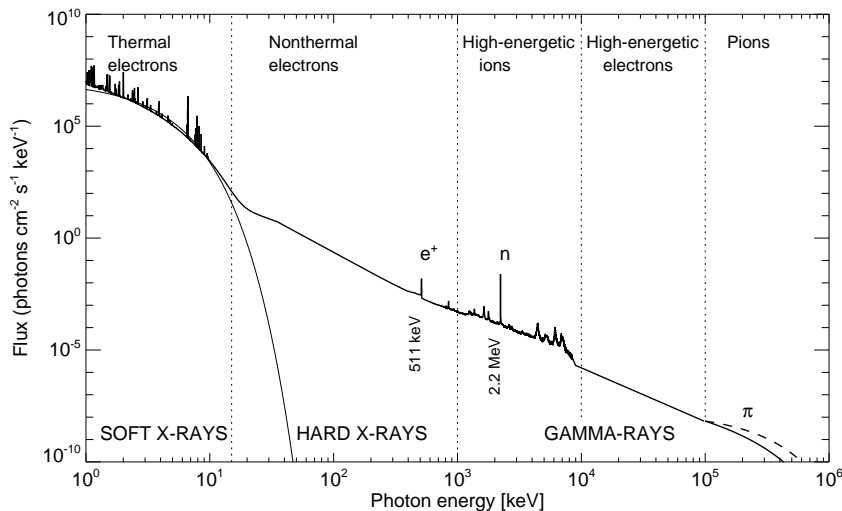


Figure 1.3: The high energy spectrum from the impulsive stage of a large flare (Aschwanden 2005). The photon energy extends from soft X-rays ( $\approx 1$ -10 keV), hard X-rays ( $\approx 10$  keV-1 MeV), to gamma-rays ( $\approx 1$  MeV-100 GeV). The energy spectrum is dominated by different process: thermal electrons (in soft X-rays), bremsstrahlung from nonthermal electrons (in hard X-rays), nuclear de-excitation lines (in 0.5-8 MeV gamma-rays), bremsstrahlung from high-energetic electrons (in 10-100 MeV gamma-rays), and pion-decay (in  $>100$  MeV gamma-rays), as well as spectral emission line, electron-positron annihilation, and neutron capture lines

Frequently, when electrons follow field lines until they reach a density high enough for thick-target bremsstrahlung collisions, the emitted hard X-ray sources are often observed as footpoints. For some flares, besides the footpoint hard X-ray sources, a third coronal X-ray source above the soft X-ray loop (Masuda et al. 1994) is observed. This looptop hard X-ray emission contains a thermal part, dominating low energies, and a weak nonthermal part consistent with thin-target bremsstrahlung. In the flare loop, the accelerated electrons lose only a small fraction of energy and continue to propagate towards the chromosphere where they produce thick-target photon spectrum which is flatter (harder) than the thin-target spectrum it may have transversed before.

However, recent RHESSI observations have found a new class of events in which the hard X-ray emission is predominantly from the coronal flare loop with little or no emission from the footpoints (Veronig and Brown 2004). The high column densities in the loops (attributed to chromospheric evaporation driven by energetic downward electrons) implies that the corona itself functions as a thick target to the injected electron beam, or more probably, as an intermediate thin-thick target (ITTT). The ITTT model let the coronal region act as a thick target on particles with energies lower than a critical energy and as thin target on electrons with energies larger than this critical energy. This results in a characteristic hard X-ray spectrum showing a broken power-law (double power-law) as well as soft X-ray emission due to collisional heating, thus altering the spectrum of the electron beam that reaches the footpoints and causing thick target emission in the process. Battaglia and Benz (2007) have tested the ITTT model in a series of flares using RHESSI data. The results, however, indicate that such a simple model cannot account for all of

the observed relations between the nonthermal spectra of coronal and footpoints sources. Most inconsistencies can be solved by the inclusion of non-collisional energy loss of the electron in the flare loop due to electric field.

### 1.2.3.1 Thermal and Nonthermal Components

X-ray emissions during solar flares are generated mainly by heated up or highly accelerated electrons. X-ray spectral observations (Figure 1.3) are normally split into two components: (a) Soft X-rays from energies lower than a certain energy threshold (between 5 keV and 20 keV) and often thought to be thermal in origin and (b) Hard X-rays above this energy level generated by nonthermal electrons. The determination of this transition energy between photon thermal and nonthermal emissions is very important and different spectral fitting models often produce different results. In this thesis, we have developed and applied a different method to study the transition energy. The rate of change of photon fluxes at different energies during an HXR pulse is calculated with a regularization method (Kontar and MacKinnon 2005) and two temporal components are identified. The low-energy component has an energy-independent rate of change of the fluxes. The rate of change of the high-energy component fluxes is proportional to the logarithm of the photon energy, suggesting a power-law photon spectrum. The transition energy of these components are found to be in agreement with the transition energy of the isothermal and power-law components identified through spectral fits.

The observed thermal and nonthermal X-ray emissions are often a reflection of thermal and nonthermal electrons that are generated in solar flares. The nonthermal electrons are energetic electrons normally impinging downward onto either a thin or thick target and emitting the Hard X-ray Bremsstrahlung. The acceleration region is generally believed to be located in the solar corona where magnetic reconnection takes place and collisionless particles can be easily accelerated. For a review of acceleration process see Aschwanden (2005), Aschwanden (2002) and Tandberg-Hanssen and Emslie (1988). Recent observations also show that the site of acceleration does not have to be localized at the coronal source (e.g. Fletcher and Hudson 2008).

### Thermal Component

The thermal plasma is often observed as a Soft X-ray source shaping the heated up flare loop where the electron temperature is in the range of 10 - 30 MK (Pallavicini et al. 1977, Metcalf and Fisher 1996, Aschwanden 2005). For a thermal bremsstrahlung source observed at Earth's distance, Brown (1974) obtained the standard expression for the continuum photon energy flux as a function of the photon energy  $\epsilon = h\nu$  as :

$$F_{th}(\epsilon) = 8.1 \times 10^{-39} \int_V \frac{\exp(-\epsilon/k_B T)}{T^{1/2}} n_{th}^2 dV [\text{keVs}^{-1} \text{cm}^{-2} \text{keV}^{-1}], \quad (1.1)$$

where  $k_B$  is the Boltzmann constant and  $n_{th}(\mathbf{r})$ ,  $T(\mathbf{r})$  are the electron density ( $\text{cm}^{-3}$ ) and temperature (Kelvin) at position  $\mathbf{r}$  in the thermal source whose total volume is  $V$  ( $\text{cm}^3$ ). The corresponding photon spectrum is  $f_{th}(\epsilon) = F_{th}(\epsilon)/\epsilon$ . Assuming a uniform number density and temperature throughout the source volume, one can obtain the thermal photon

spectrum to be (Aschwanden 2005):

$$f_{th}(\epsilon) = 2.6 \times 10^7 \left( \frac{EM_{49}}{T_7^{1/2}} \right) \frac{1}{\epsilon} \exp\left(-\frac{\epsilon}{0.86T_7}\right) \text{ [photons cm}^{-2}\text{s}^{-1}\text{keV}^{-1}\text{]}, \quad (1.2)$$

where,  $EM_{49}$  ( $=n_{th}^2V$ ) is the thermal emission measure in the units of  $10^{49}\text{cm}^{-3}$ ; temperature  $T_7$  here is in the units of  $10^7\text{K}$ ;  $\epsilon$  is in keV. The convenience in employing these units is that they are close to the typical values of thermal emission and temperature observed during flares. For instance, if a thermal source have thermal emission measured to be  $EM_{49} = 0.1$  and the temperature to be  $T_7 = 2$ , the thermal photon fluxes at 5 keV and 10 keV are  $2 \times 10^4$  and  $549 \text{ photons cm}^{-2}\text{s}^{-1}\text{keV}^{-1}$  respectively.

The total plasma thermal energy has the form:

$$W_{th} = 3n_{th}k_BTV = 8.0 \times 10^{27} T_7 \sqrt{EM_{49}V_{arc}} = 4.1 \times 10^{29} EM_{49}T_7/n_{11} \text{ [erg]}, \quad (1.3)$$

where  $V_{arc}$  (the source volume) and  $n_{11}$  (thermal electron density) are in the units of  $\text{arcsec}^3$  and  $10^{11}\text{cm}^{-3}$  respectively.

### Nonthermal Component

The spectrum of Nonthermal electrons is often in the form of a power-law with a low-energy cutoff  $E_c$ . The existence of  $E_c$  is decisive for converging the total injected nonthermal electron power  $P(E > E_c)$  given as:

$$P = \int_{E_c}^{\infty} E \cdot F_{nth}(E) dE, \quad (1.4)$$

where  $E$  is electron energy and  $F_{nth}(E)$  is the corresponding electron spectrum. In the simplest approach, it is assumed that the electron spectrum has the shape of a power-law which can be written as:

$$F_{nth}(E) = A_E(E/\text{keV})^{-\delta}, \quad (1.5)$$

with the unit of electrons  $\text{s}^{-1}\text{keV}^{-1}$  (Brown 1971).  $\delta$  is the electron spectra index and  $A_E$  is the normalization parameter, i.e., the electron energy flux at 1 keV. The resulted photon spectrum also has a power-law distribution:

$$f_{nth}(\epsilon) = A_\epsilon(\epsilon/\text{keV})^{-\gamma}, \quad (1.6)$$

with the unit of photons  $\text{s}^{-1}\text{cm}^{-2}\text{keV}^{-1}$ .  $\gamma$  is the photon spectra index and the normalization parameter is  $A_\epsilon$ .

In the thick target model, electron power-law index has the relation with photon power-law index as:  $\delta = \gamma + 1$  and normalization parameter  $A_E$  can be obtained from  $A_\epsilon$  as (Brown 1971, Saint-Hilaire and Benz 2005):

$$A_E = 6.44 \times 10^{33} \frac{\gamma(\gamma - 1)}{B(\gamma - 1, 1/2)} A_\epsilon, \quad (1.7)$$

where  $B$  is the beta-function. The injected nonthermal power (Eq. 1.4) is then given as (Saint-Hilaire and Benz 2005, Fletcher et al. 2007):

$$P_c = \frac{A_E}{\delta - 2} E_c^{-(\delta-2)} \text{ [keVs}^{-1}\text{]}. \quad (1.8)$$

The total energy in nonthermal electrons above the low-energy cutoff is then:

$$W_{nth}(E > E_c) = \int_{\tau_s}^{\tau_e} P_c(\tau) d\tau, \quad (1.9)$$

where  $\tau_s$  and  $\tau_e$  are the starting and ending time of the flare nonthermal component.

The number of nonthermal electrons in the injected beam per second is then:

$$N_{nth} = \int_{E_c}^{\infty} F_{nth}(E) dE = \frac{A_E}{\delta - 1} E_c^{-(\delta-1)} \text{ [electrons s}^{-1}\text{]}. \quad (1.10)$$

### Low-energy Cutoff

Note that to make sure nonthermal energy power  $P_c$  and number flux  $F_{nth}$  converge as an finite positive value,  $\delta$  should be larger than 2 and  $E_c$  larger than 1. Normally,  $\delta$  is typically in the range of 3 to 8 (Dennis 1985). Assuming  $\delta$  is 5, nonthermal power  $P_c \propto E_c^{-3}$  with a cutoff energy at 10 keV can be 27 ( $= (1/3)^{-(5-2)}$ ) times larger than that with the cutoff energy at 30 keV. Similarly the nonthermal number flux with a cutoff energy at 10 keV is 81 ( $= (1/3)^{-(5-1)}$ ) times larger than that with the cutoff energy at 30 keV. The determination of a precise value for the low-energy cutoff is therefore very important to evaluate the beam power and electron number of the nonthermal component in solar flares.

However, the low-energy cutoff in the electron distribution has been very difficult to determine because of the high minimum photon energy detectable by the HXR spectrometers (typically larger than 20 keV before RHESSI) and the presence of strong thermal bremsstrahlung at low energies. Aschwanden (2005) estimated the low-energy cutoff by assuming the energy equivalence between thermal and nonthermal energies (i.e.,  $W_{th} = W_{nth}(E > E_c)$  in Eqs. 1.3 and 1.9). The cutoff energy is represented by the intersection of the thermal with the nonthermal photon spectrum (however, in this thesis this intersection point is taken as a transition energy instead). The evaluated cutoff energy is in the range of  $E_c \approx 5 - 20$  keV. Benka and Holman (1994) obtained  $E_c$  to be 20 - 40 keV with a hybrid thermal/nonthermal model. Gan et al. (2002) have found that many of the double-power law spectra obtained from BATSE on the Compton Gamma Ray Observatory (CGRO) were consistent with the flattening that results from a low-energy cutoff ranging from 45 - 97 keV. A cutoff energy as high as 73 keV has also been found for the 2003 July 23  $\gamma$ -ray flare (Holman 2003). The existence of nonthermal spectra down to energy ranges of  $\approx 8 - 15$  keV in microflares (Krucker et al. 2002) suggests that the value of the low-energy cutoff is strongly dependent on the flare size. Although it is not difficult to fit the power-law spectrum with a certain low-energy cutoff, it is often the case that the cutoff energy is not uniquely determined. Cutoff energies below a limit point can sometime fit the spectrum equally well because at low energies the fluxes contributed from the nonthermal bremsstrahlung are usually much less than those from the thermal bremsstrahlung (Sui et al. 2002). Recent work carried out by Emslie (2003) also suggests that there is no need to impose an arbitrary low-energy cutoff since electrons with energies  $\leq kT$  (where T is the temperature of the target which the injected electrons interact

with) essentially lose no energy in the warm target, while those with energies in the range from  $\sim kT$  to  $\sim 5kT$  suffer with a significantly smaller energy-loss rate than they would in a cold-target model.

In this thesis we evaluate the low limit of cutoff energy by assuming that the fraction of the thermal electrons accelerated into a non-thermal distribution  $\alpha$  should be less than 1 in the stochastic acceleration model where non-thermal electrons are accelerated from a thermal background (Benz 1977, Petrosian and Liu 2004, Grigis and Benz 2006). At the peak of the flare we studied, the minimum possible  $E_c$  is around 5.2 keV, and throughout the event it is always smaller than the transition energy  $\epsilon_r$ , which is around 10 keV.

### 1.2.3.2 Temporal Characteristics of Hard X-ray

We propose that each of the spiky structure of the hard X-ray burst on timescales of a few seconds represents an *elementary flare burst* by de Jager and de Jonge (1978). Observations of X-rays at tens of keV with the BATSE detector (on board of the Compton Gamma Ray Observatory) show pulses with widths of only hundreds of milliseconds to a second or two (Aschwanden et al. 1995). The RHESSI (Section 1.2.5), however, has not been able to detect these short pulses (Fletcher et al. 2010). HXR quasi-periodic pulsations with periods from tens of seconds to a few minutes have been observed by both *Yohkon/HXT* and RHESSI (Foullon et al. 2005, Ofman and Sui 2006, Li and Gan 2008, Inglis and Nakariakov 2009). These are oscillations of the X-ray intensity (in the range from a few to tens of keV) with a modulation depth of up to 90%. These pulsations could be caused by magnetic fields variations leading to a change of trapped particle precipitation rates (Inglis and Nakariakov 2009), or perturbations to the accelerator itself (Ofman and Sui 2006).

Often the hard X-ray spectrum of flares initially shows a steep spectral slope(soft), which flattens at the peak of the flare(hard), and then becomes steeper again(soft) in the decay phase of the flare (Parks and Winckler 1969, Kane and Anderson 1970, Van Beek et al. 1974, Fletcher and Hudson 2002, Battaglia and Benz 2006). This soft-hard-soft spectral evolution of the HXR pulses is one of the most important characteristics of high-energy emissions and may constrain the nature of particle acceleration (Grigis and Benz 2005). Some flares that are particularly well associated with solar energetic particle events continue to harden after the peak (Frost and Dennis 1971), i.e. following a soft-hard-harder spectral pattern. This may reflect the presence of long-lived high energy coronal sources (Krucker et al. 2008b).

## 1.2.4 Gamma-ray Emissions

Gamma-rays occupy the high-energy end of the wavelength spectrum from MeV to GeV in large solar flares, see Figure 1.3. Gamma-ray emission is produced mostly by interactions of highly energetic particles with an ambient plasma. Coulomb collisions between electrons and ions produce continuum gamma-ray emissions by bremsstrahlung. Collisions between accelerated ions and thermal ions produce nuclear de-excitation lines in the continuum background. Collisions between protons produce neutrons, pions and positrons and the neutron capture line at 2.223MeV; pion-decay radiation and positron annihilation radiation at 511keV are also detectable. Gamma-rays, through both the con-

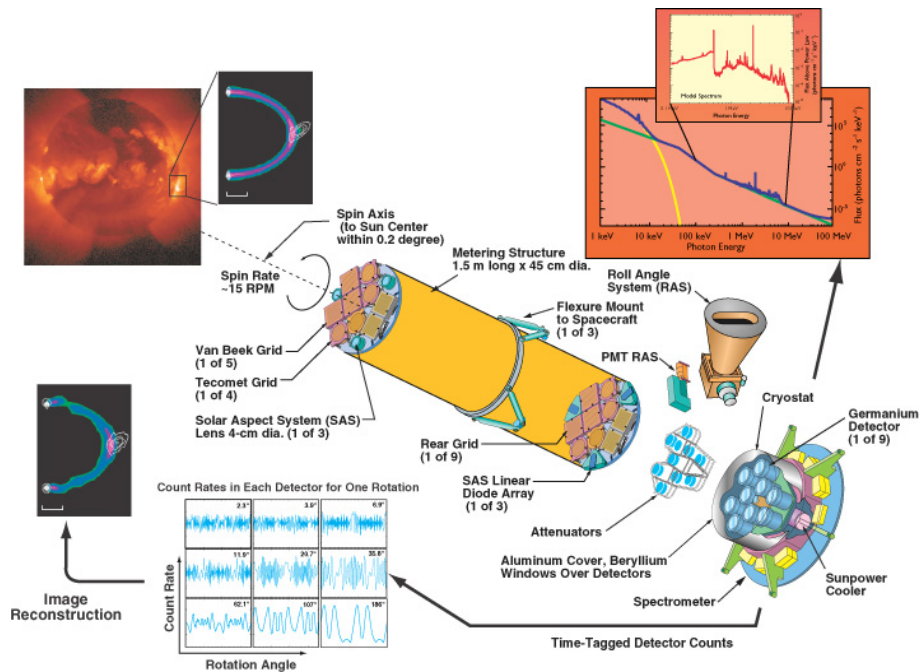


Figure 1.4: Schematic of the RHESSI instrument illustrating the imaging spectroscopy (from Lin et al. (2002)). *Upper-left images* shows X-rays and gamma-rays from a solar flare passing through the slits of the front and rear grids to reach the germanium detector. *Lower-left images* give an example of the modulated detector count rate (which can be analyzed to reconstruct the image) generated by the rotating spacecraft. The germanium detectors are cryogenically cooled to provide high spectral resolution capable of resolving narrow gamma-ray lines and steep solar continuum spectra (*upper right*). The attenuators (*lower right*) are inserted automatically when the count rate approaches saturation. The SAS, RAS and PMTRAS provide solar pointing and roll aspect information.

tinuum and line spectrum supply information on electrons as well as on ions. Through gamma-ray observations, we will study the properties of the acceleration mechanisms (maximum energy, electron/ion ratios, electron/ion acceleration efficiencies, and pitch angle distributions) and the properties of the ambient plasma (chromospheric ion abundances, coronal trapping times) (Aschwanden 2005).

RHESSI (Section 1.2.5) observations produced the first gamma-ray images of a flare (Hurford et al. 2003) and found that the centroid of the 2.223 MeV image is displaced from that of the 0.3-0.5 MeV image, implying a difference in acceleration and/or propagation between the accelerated electron and ion populations. However, there are only four flares ever reported to show single or double (in one case) gamma-ray sources (Hurford et al. 2003, Hurford et al. 2006).

## 1.2.5 RHESSI

Launched on February 2002, the Reuven Ramaty High Energy Solar Spectroscopic Imager (RHESSI), (Lin et al. 2002), shown in Figure 1.4, is designed to investigate particle acceleration and energy release processes in solar flares, through imaging and spectroscopy of hard X-ray/gamma-ray continua emitted by energetic electrons and gamma-

ray lines produced by energetic ions. It covers a broad energy range from 3 keV (soft X-rays) to 17 MeV (gamma-rays), with an energy resolution of 1 keV at the lowest energies and 5 keV at MeV energies. The spatial resolution is down to 2.3 arcsec in the X-ray range. RHESSI provides the first high-resolution hard X-ray imaging spectroscopy, the first high-resolution gamma-ray line spectroscopy, and the first imaging above 100 keV, including the first imaging in narrow gamma-ray lines.

The instrument is a Fourier imager (with a spin period of 4s), made up of 9 rotation-modulated collimators (RMCs) as shown in Figure 1.4. Every RMC has two widely separated grids, one in the front tray and the other in the rear tray. Each grid is a planar array of equally spaced, X-ray-opaque slats separated by transparent slits. The slits of each pair of grids are parallel and with identical pitches, so that the transmission through the grids depends on the incident direction of photons. As the telescope spins, a modulation curve of the intensity of the incoming photon flux (count rate) is generated on each germanium detector that is behind each collimator. The germanium detectors can convert incoming x-rays and gamma-rays to pulses of electric current. The front and rear detectors are separated into two segments by a boundary electric field line where signals are registered separately above and below the boundary line. All photons with energy smaller than 100 keV will be stopped in the front segment, while most photons in the  $\gamma$ -ray regime will pass through and be fully stopped in the rear segments. Saturation from intense soft X-ray fluxes is automatically avoided with extra thin or thick attenuators shuttering the detectors when the count rates exceed predetermined thresholds.

RHESSI hard X-ray observations provide the location, spectral and temporal evolution of the accelerated electrons and protons that contain a large fraction of the total energy released in a flare. Meantime, the RHESSI, through spectral fitting, can determine the location, temperature and emission measures of the hottest plasma closest to the point, both in time and space, where the heating takes place. The combination of these nonthermal and thermal flare components allows solar physicists the study of the initial energy release process, plasma heating, and particle acceleration, as well as particle transportation through the solar atmosphere upward into interplanetary space and downward, into dense atmosphere.

### 1.3 Magnetic Reconnection and Solar Flare Models

The idea of magnetic reconnection was introduced by Dungey (1953) when he was studying the problem of particle acceleration in the Earth's magnetosphere. In the MHD framework, Dungey argued that the current associated with the motion of particles would take the form of a thin sheet in which the diffusion of the magnetic field would necessarily dominate. This diffusion would cause field lines passing through the current sheet to change their connectivity to one another; this process was described as field line disconnection followed by reconnection.

In order to describe the magnetic reconnection process mathematically and for the convenience of future references, we list here the basic resistive MHD equations including the continuity equation (1.11), the momentum equation (1.12) and the energy equation (1.13) together with Maxwell equations including the Faraday Theory (1.14), Ampere's law (1.15) and Ohm's law (1.16), as well as the equation of state (1.17) for fully ionized

plasmas. All the equations are in MKS units.

$$\frac{d\rho}{dt} = \frac{\partial\rho}{\partial t} + \mathbf{u} \cdot \nabla\rho = -\rho\nabla \cdot \mathbf{u} \quad (1.11)$$

$$\rho \frac{d\mathbf{u}}{dt} = -\nabla p + \mathbf{j} \times \mathbf{B} + \mathbf{F} \quad (1.12)$$

$$\frac{dp}{dt} = \frac{\partial p}{\partial t} + \mathbf{u} \cdot \nabla p = -\gamma p \nabla \cdot \mathbf{u} + (\gamma - 1)\eta j^2 + \mathbf{F} \cdot \mathbf{u} + Q \quad (1.13)$$

$$\nabla \times \mathbf{E} = -\frac{\partial \mathbf{B}}{\partial t} \quad (1.14)$$

$$\nabla \times \mathbf{B} = \mu_0 \mathbf{j} \quad (1.15)$$

$$\mathbf{E} = -\mathbf{u} \times \mathbf{B} + \eta \mathbf{j} \quad (1.16)$$

$$p = \rho R_0 T = n_e k_B T_e + n_i k_B T_i \quad (1.17)$$

In the above equations,  $\rho$ ,  $\mathbf{u}$ ,  $p$  and  $T$  are the plasma mass density, flow velocity, pressure and temperature, respectively.  $\mathbf{E}$  is the electric field and  $\mathbf{B}$  is the magnetic field. The quantity  $\gamma$  here, instead of representing the photon spectral index (Section 1.2.3.1), signify the ratio of specific heats, taken as 5/3 for isotropic plasma.  $\mathbf{j}$  is current density and  $Q$  is the radiation and heating function.  $\eta$ , assumed to be a scalar, stands for anomalous resistivity which is negligible in ideal MHD but important for energy diffusion and joule heating in reconnection processes in resistive MHD.  $\mathbf{F}$  represents all the other forces except for the electro-magnetic forces, such as gravity and viscous forces. Current density  $\mathbf{j}$  can be related to magnetic field  $\mathbf{B}$  according to Ampere's law by the constant factor  $\mu_0$ , the permeability of free space, in Equation (1.15).  $R_0$  is the gas constant and  $k_B$  is the Boltzmann constant. Terms such as electron pressure gradient and Hall currents are neglected here.

The equation that governs the temporal evolution of the magnetic field can be obtained from the equations of Ampere's law, Faraday's law and Ohm's law. Equation (1.18) is called induction equation of resistive MHD. The first term at its right-hand-side describes the inductive effect of the velocity field and the second term accounts for the diffusion of magnetic fields due to the finite conductivity of the plasma.

$$\frac{\partial \mathbf{B}}{\partial t} = \nabla \times (\mathbf{v} \times \mathbf{B}) - \nabla \times (\eta \nabla \times \mathbf{B}) \quad (1.18)$$

In most of the plasmas in the solar corona, the resistivity  $\eta$  is very low and the diffusion term can be neglected. So the plasma is taken to be ideal MHD and the magnetic field evolution is governed by the motion of the plasma alone, i.e. the magnetic field is frozen into the plasma. This makes it possible to store energy in the magnetic field by moving the plasma fluids or the sources of the magnetic field. However, the energy could then become available when the ideal MHD conditions break down.

In resistive fluid, resistivity  $\eta$  can be effective and the magnetic fields become diffusive. The enhanced resistivity is usually the result of the formation of small scale structures like current sheets or fine scale magnetic turbulence. When ideal MHD conditions are violated and diffusion occurs, magnetic reconnection can release stored magnetic energies as waves, accelerated particles and heated plasmas, often diagnosed as the occurrence of flares and CMEs.

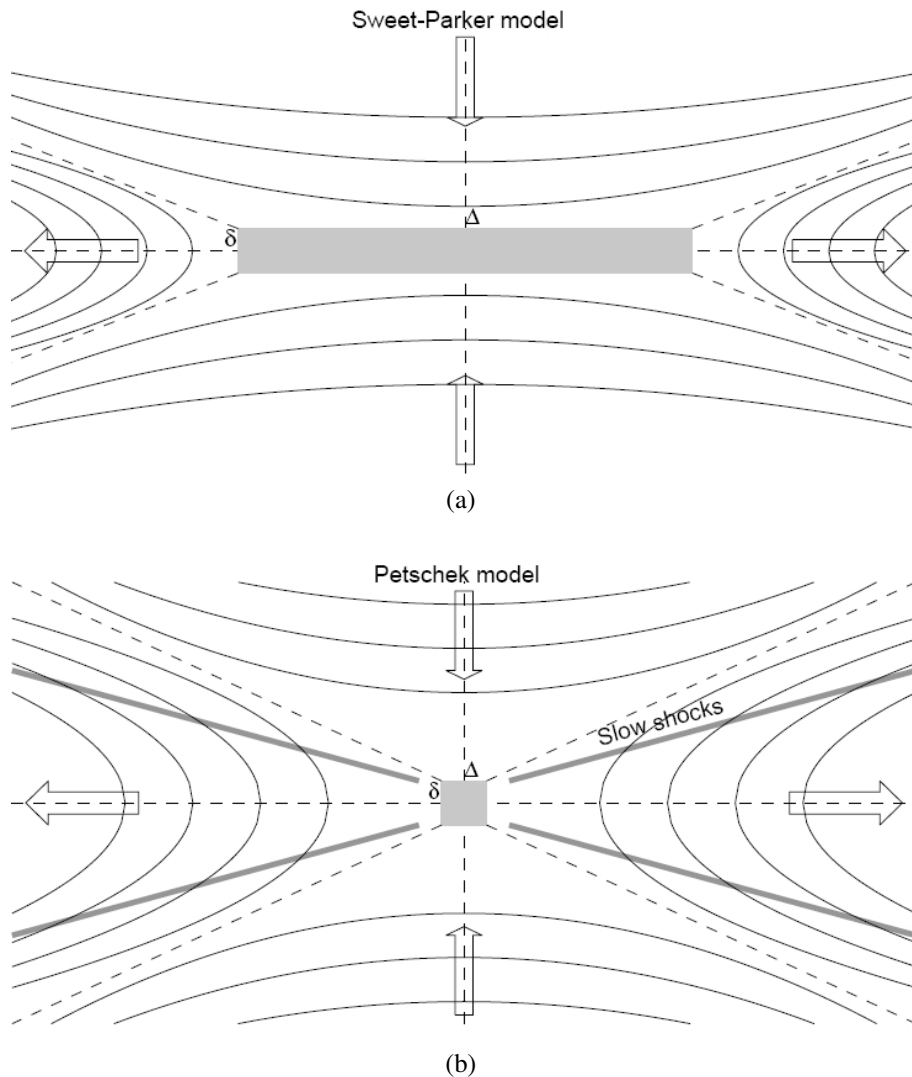


Figure 1.5: (a): Geometry of the Sweet-Parker reconnection model. Lateral inflow plasma and outflow jets are shown as arrows and solid lines represent the magnetic field lines. The gray region in the center is a non-ideal diffusion region while the outside area is in ideal MHD state. (b): Petschek’s field configuration. The length of the current sheet is much shorter than that in the Sweet-Parker model and the magnetic field in the inflow is nonuniform. Two pairs of standing slow shocks extend outward from the central current sheet. Both figures are taken from Aschwanden (2005).

### 1.3.1 Theories of Magnetic Reconnection

#### 1.3.1.1 Sweet-Parker 2-D Reconnection Model

The canonical Sweet-Parker reconnection model was proposed by Sweet (1958) and Parker (1957) as shown in Figure 1.5a. Consider the inflow velocity to be  $u_0$ , outflow velocity to be  $v_A$  and the width and length of the non-ideal region to be  $\delta$  and  $L$  respectively. In incompressible fluids, the inflow and outflow velocity has the relationship as  $\delta v_A = L u_0$  to keep the mass conservation. The inflow velocity can be estimated in units using Am-

per's law and Ohm's law, see Equation (1.15) and Equation (1.16), as  $u_0 = \sqrt{v_A \eta / L}$ . The outflow plasma roughly has the Alfvén speeds representing the changing speed of the magnetic fields:  $v_A = B / \sqrt{\mu_0 \rho}$ . The anti-parallel magnetic fields are assumed to be canceled in the diffusion region with an X-shape magnetic neutral point embedded in the center. The convective electric field, term  $-\mathbf{u} \times \mathbf{B}$  in Ohm's law, is perpendicular to the plane of the figure. Reconnection rate  $M_0$  is defined as the ratio between inflow speed and outflow speed:  $M_0 = u_0 / v_A = 1 / \sqrt{S}$ , where Lundquist number (or magnetic Reynolds number) is defined by  $S = v_A L / \eta$ .

### 1.3.1.2 Petschek 2-D Reconnection Model

In solar coronal plasmas, the magnetic Reynolds number  $S$  is usually very large (more than  $10^6$ ) making the Sweet-Parker model too slow to account for solar flares. Petschek (1964) proposed another model shown in Figure 1.5b, with a greatly reduced length of the current sheet and therefore an increased rate of reconnection. Further, he introduced two pairs of standing slow-mode shocks radiating outwards from the tip of the current sheet. Most of the energy which accelerates and heats the plasma comes from the shock energy. The maximum magnetic reconnection rate in Petschek's model can be up to  $M_{max} = \pi / (8 \ln S)$ . Because of its logarithmic dependence on  $S$ , the reconnection rate, with its typical value around 0.01-0.1, is many orders of magnitude larger than the Sweet-Parker reconnection rate.

### 1.3.1.3 Turbulent 2-D Reconnection Model

The current sheet in both Sweet-Parker and Petschek models can be too long to be stable. Resistive instabilities such as gravitational, rippling, and tearing mode (Furth et al. 1963) can occur and an impulsive turbulent regime of reconnection ensues (Priest 1986, Kliem 1995, Bárta et al. 2009). In the scenario of an impulsive bursty reconnection, tearing mode first leads to current sheet filamentation followed by the formation of magnetic islands. The rapid coalescence of the magnetic islands creates, between groups of coalescing filaments, elongated and nearly uniform sections of current sheets, which however become unstable with respect to (secondary) tearing. Consequently, the process may repeat in a cyclic manner in sections of long current sheets. This allows for a large number of separate energy release events that occur primarily as successive coalescence of individual current filament pairs. However, continued shearing and tearing may reduce the width of the current sheet until the threshold of kinetic instability is reached. Figure 1.6 shows a recent 2.5 D MHD simulation of highly filamented current sheet due to tearing instabilities. Moreover, other instabilities also play an active role in the reconnection process. Recent full-particle simulations of electron-positron reconnection carried out by Liu et al. (2009) revealed that Weibel instability is important in controlling the dynamics of the current layer and maintaining a fast reconnection.

### 1.3.1.4 3-D Magnetic Reconnection and Magnetic Null Points

There are two types of null points (where  $\mathbf{B} = \mathbf{0}$ ) in 2-D reconnection: X-points and O-points. There is a much richer variety of 3-D reconnection topologies, where 3-D volumes with oppositely directed magnetic fields are divided either by 2-D separatrix

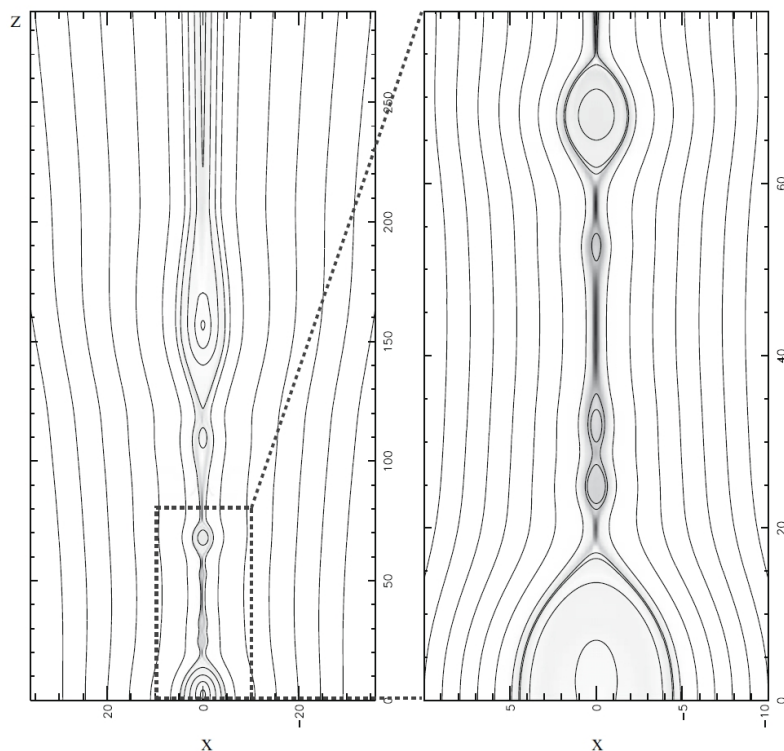


Figure 1.6: A snapshot of simulated turbulent reconnection model ( from Bárta et al. (2009)). The current sheet is intensively filamented due to tearing instability.

surfaces, by intersection lines of two separatrix surfaces, or by the null points as intersections of separator lines. 2-D magnetic reconnection geometries such as a long loop arcade have ignorable coordinate in the third dimension. 3-D reconnection geometries, however, have more complicated topological constraints in the other dimension and loop arcades are replaced by interacting loops. Despite the complex variety of 3-D reconnection mathematical topologies (Priest and Forbes 2000, Parnell et al. 1996), only a few of all the possible mathematical topologies have been identified by observations (Fletcher et al. 2001, Aulanier et al. 2000, Des Jardins et al. 2009). 3-D magnetic reconnection can happen with or without null points. The later is qualitatively the same as the 2-D models with a non-zero guide field  $B_z$  assuming that the X/O-point plane is in the x-y plane. Here we focus on 3-D reconnection with magnetic nulls.

Lau and Finn (1990) and Parnell et al. (1996) studied and classified the basic structure of a null given  $\mathbf{M}$  the Jacobian matrix to describe the local linear structure about a null point. The magnetic field  $\mathbf{B}$  near a neutral point may be expressed to the lowest order as  $\mathbf{B} = \mathbf{M} \cdot \mathbf{r}$ , where  $\mathbf{M}$  is a  $3 \times 3$  matrix with elements  $M_{ij} = \partial B_i / \partial x_j$ . In general, the matrix has three eigenvalues  $\lambda_1$ ,  $\lambda_2$  and  $\lambda_3$  and  $\lambda_1 + \lambda_2 + \lambda_3 = 0$  implied by  $\nabla \cdot \mathbf{B} = 0$ . Depending on the properties of the eigenvalues, the null can fall into three different categories:

- $\lambda_1 = 0$  represents the case that one of eigenvalues vanishes. The 3-D null simply reduces to a 2-D null point. When  $\lambda_2$  and  $\lambda_3$  are real, this is a simple X-point (Figure 1.7(a)). When both of them are imaginary, the null is an O-point (Figure 1.7(b)).
- All the eigenvalues  $\lambda_1$ ,  $\lambda_2$  and  $\lambda_3$  are real. Following  $\lambda_1 + \lambda_2 + \lambda_3 = 0$ , the eigenvalues

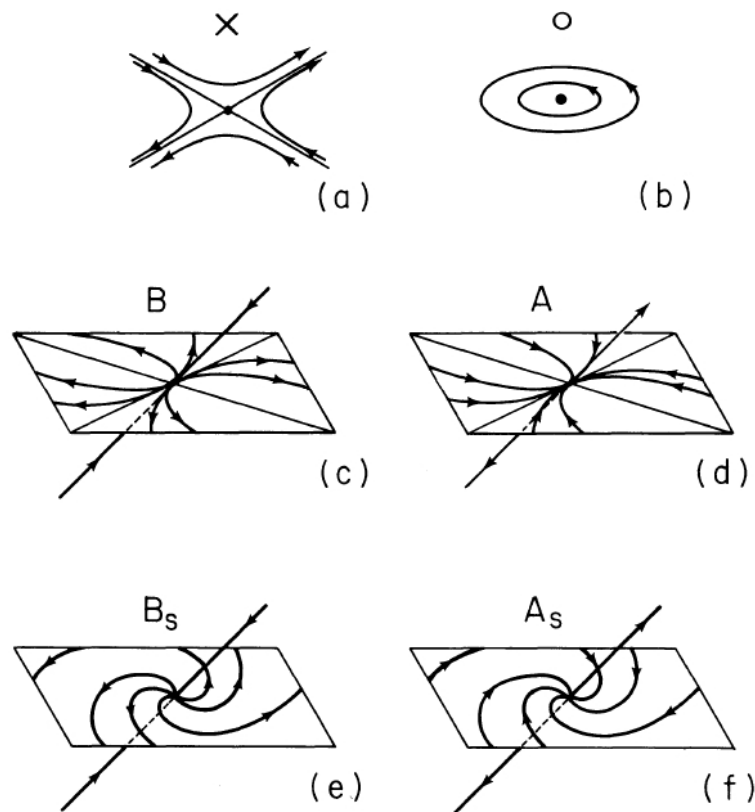


Figure 1.7: Classification of nulls depending on eigenvalues of Jacobian matrix (from Lau and Finn (1990)). 2-D nulls (one vanishing eigenvalue) include (a) X-point or X-line (two real eigenvalues) and (b) O-point (two imaginary eigenvalues). 3-D nulls with three real eigenvalues can be (c) a positive null or (d) a negative null. (e) and (f) are examples of 3-D O-point nulls (one real and two complex eigenvalues).

have the signs to be either  $(+ - -)$  or  $(- + +)$ .  $(+ - -)$  represents a negative null (Figure 1.7(d)) while  $(- + +)$  indicates a positive null (Figure 1.7(c)). When  $\mathbf{M}$  is symmetric, this is a potential null (currents  $\mathbf{j} = \mathbf{0}$ ) and the fan plane (for diverging field lines) is perpendicular to the spine axis (for converging field lines). Figure 1.8 shows the configuration of a potential magnetic null point. When  $\mathbf{M}$  is asymmetric, this is a non-potential null ( $\mathbf{j} \neq \mathbf{0}$ ).

- One of the eigenvalues  $\lambda_1$  is real while the other two are complex and necessarily two complex values conjugates. The null is a 3-D generalization of an O-point (Figure 1.7(e) and (f)).  $\mathbf{M}$  in this case must be asymmetric and there is a current flowing through the null.

### 1.3.2 Observations and Flare Models

The standard large-scale flare reconnection model in two dimensions was developed by H. Carmichael (Carmichael 1964), P. Sturrock (Sturrock 1966), T. Hirayama (Hirayama 1974), R. Kopp, and J. Pneuman (Kopp and Pneuman 1976) and is often called the CSHKP model. It has been further developed by Tsuneta (1997) and Shibata et al. (1995).

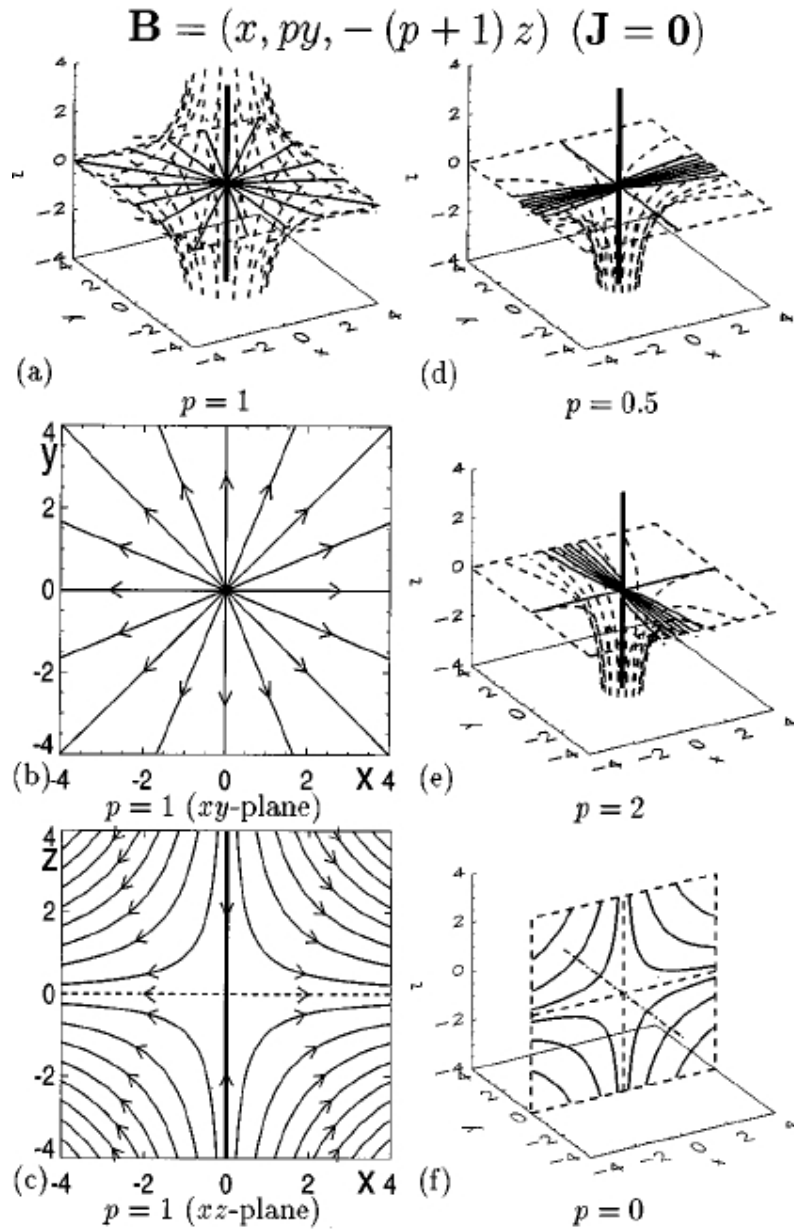


Figure 1.8: The magnetic field configuration of 3-D potential nulls (taken from Parnell et al. (1996)). The 3-D structure of a null with magnetic field  $\mathbf{B} = (x, y, -2z)$  is shown in (a) with its fan  $x$ - $y$  plane in (b) and the spine ( $z$ -axis) in  $x$ - $z$  plane (c). Other 3-D null configurations of magnetic field with  $p=0.5$  and  $p=2$  are shown in (d) and (e) respectively. (f) is the case when the null reduces to a 2-D potential X-point field with the  $y$ -axis a null line.

Here we review briefly the classical image of observational flare reconnection model (see the bottom panel in Figure 1.10 for a standard flare model). Flares occur almost without exception in solar active regions and are associated with strong and complex magnetic fields far from the potential (current free) state. A rising prominence above the neutral line (between oppositely directed open magnetic field lines) carries a current sheet and induces a magnetic collapse on both sides of the current sheet through eruptions accompanied by lateral inflow of plasmas. This magnetic reconnection process dissipates magnetic energy in the corona, heats the plasma in the reconnection region to a temperature of tens of MK and accelerates electrons to super-thermal energies peaking around 20 keV and extending to tens of MeV. Consequently, the energy propagates from the corona into the dense chromosphere along a magnetic loop by thermal conduction or free-streaming of nonthermal particles. Meantime the chromospheric material is heated by these energetic particles and expands into the upper atmosphere, filling up the existing coronal loops. As reconnection continues, the reconnection location rises and new hot loops are powered at a higher altitude while the underlying loops cool down by radiation and conduction and finally plasmas drain back down to the solar surface.

Some small compact flares, however, can be better explained by the emerging flux model (Heyvaerts et al. 1977) which has a different trigger for reconnection. First, a new magnetic flux emerges beneath the flare filament and continuously reconnects and heats the current sheet between the old and new flux; then the heated current sheet loses equilibrium and turbulent electrical resistivity causes the current sheet to expand rapidly, accelerating particles and heating plasmas.

Observationally, hard X-ray (and/or white-light-emission) flare footpoints are usually located at the chromosphere due to bremsstrahlung of injected non-thermal high-energy electrons (Brown 1971), while the flare loop in the corona, appearing to grow upwards and outwards in time, is often a result of chromospheric evaporation due to plasma heating in the chromosphere driven by nonthermal electron fluxes or thermal conduction. The flare loop can also be seen in  $H_\alpha$  (Svestka et al. 1987), microwaves (Li and Gan 2005), UV and EUV (Warren and Warshall 2001, Saba et al. 2006), soft and even HXRs (e.g. Gallagher et al. 2002). For a recent detailed overview of solar flare observations, see e.g., Benz (2008) and Fletcher et al. (2010).

### 1.3.2.1 HXR Footpoints

Footpoints are the direct result of nonthermal processes, often interpreted within the thick-target model, in which electrons lose their energy collisionally in the chromosphere. In general, paired footpoints have opposite polarities because they locate on different sides of the magnetic polarity inversion line (also called PIL or neutral line) in active regions. Sometimes there are more than two HXR footpoints (e.g. Fletcher and Hudson 2002, Lin et al. 2003, Temmer et al. 2007). The sizes of HXR footpoints can be very small, down to sub-arcsecond, and they are difficult to quantify due to the limitation in resolution of the current instruments. RHESSI imaging has revealed HXR footpoint sizes comparable with the instrument resolution capability (2.3 arcseconds FWHM) (e.g. Fletcher et al. 2007, Schmahl et al. 2007, Kontar et al. 2008b), implying that the optical excitation is taking place deeper down, in a converging magnetic field, or that the footpoint sizes have not been resolved yet (Fletcher et al. 2010).

Footpoints has been observed in many flare footpoints to move away from each other with respect to the neutral line (e.g. Fletcher and Hudson 2002, Qiu et al. 2002, Krucker et al. 2003, Veronig et al. 2006, Temmer et al. 2007). The separation motion agrees with the standard model, in which enhanced location of reconnection site and expanding loops drive the footpoints to move apart. However, much more complex HXR footpoint motions, such as moving along the neutral line direction or moving towards each other, have been observed (e.g. Fletcher and Hudson 2002, Krucker et al. 2003, Grigis and Benz 2005, Bogachev et al. 2005, Ji et al. 2006). The complicated footpoint motions indicate that the classic 2-D reconnection model is not sufficient alone to explain the realistic 3-D flare structures and evolutions.

### 1.3.2.2 SXR Loops & Chromospheric Evaporation

In the impulsive phase, precipitating particles lose their energy collisionally in the chromosphere and heat the chromospheric material to coronal and flare temperatures of tens of MK. Driven by the overpressure, chromospheric plasma can expand and fill up the flare magnetic loops in the gradual phase, known as chromospheric evaporation. The loop is therefore often observed as SXR loops with hot and dense plasma. Neupert effect (Neupert 1968) often assumes that time-integrated HXR flux equals the SXR flux and it represents an indirect evidence of chromospheric evaporation. Observations of blueshifted emission of high-temperature plasmas also provide more direct support for chromospheric evaporation (e.g. Milligan 2008).

Theory suggests (Fisher et al. 1985a,b,c, Abnett and Hawley 1999) that depending on the energy deposition rate by accelerated electrons, the evaporation can be either 'gentle' or 'explosive'. Gentle evaporation has energy input rates less than  $10^{10} \text{ergs cm}^{-2} \text{ s}^{-1}$  in the form of thermal conduction from the overlying hot corona or weak non-thermal electron flux. Explosive evaporation often has input nonthermal electron rates larger than  $3 \times 10^{10} \text{ergs cm}^{-2} \text{ s}^{-1}$ . In the explosive case, the overpressure can cause the underlying cooler material to move downward with speed of a few  $\text{km s}^{-1}$ , known as chromospheric condensation.

As an example of explosive evaporation, recent observations by Milligan et al. (2006a) with SOHO/CDS have detected strong blueshifted ( $\sim 250 \text{km s}^{-1}$ ) Fe XIX emission (formation temperature  $\log T_e = 6.9$ ) from flare HXR footpoints where the input nonthermal energy flux is about  $4 \times 10^{10} \text{ergs cm}^{-2} \text{ s}^{-1}$ . For gentle evaporation due to a weak non-thermal electron flux, Milligan et al. (2006b) has found blue shifts of about  $< \sim 100 \text{km s}^{-1}$  at a temperatures range from  $10^4$  to  $10^7$  Kelvin.

### 1.3.2.3 Coronal X-ray Sources & Reconnection Evidences

For some flares, a third hard X-ray source in the corona above/at the loop is the hint for the location where energy is initially released (e.g. Hudson 1978, Masuda et al. 1994). In the famous Masuda flare the location of the coronal hard X-ray source was measured to be about  $10''$  (7250 km) above the soft X-ray loop and at a slightly higher altitude in images taken at higher energy bands, indicating that the reconnection site locates just above the coronal hard X-ray source in the cusp geometry of standard bipolar reconnection models. The height of the reconnection and acceleration region can be estimated also from time-

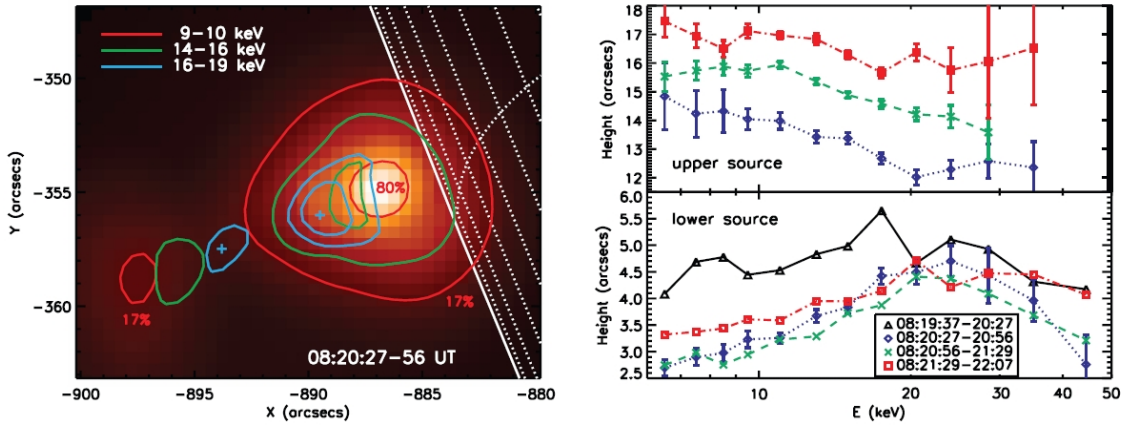


Figure 1.9: *Left*: RHESSI X-ray observations of a double coronal SXR configuration of the flare of 2002 April 20 indicate the presence of a current sheet. The two plus signs mark the centroids (separated by  $4.6'' \pm 0.3''$ ) of the lower and upper 16—19 keV sources inside the 90% and 80% contours, respectively. *Right*: Height above the limb of the centroids for the upper and lower coronal sources in the 2003 April 30 event plotted as a function of energy for four consecutive time intervals. Both figures are taken from Liu et al. (2008).

of-flight measurements. Aschwanden et al. (1996a) calculated the location of acceleration site to be above the soft X-ray loops, consistent with a Masuda flare model.

After the launch of RHESSI in 2002, many more observations and studies of coronal HXR sources have been carried out. A coronal thick target model was originally suggested to explain the HXR emission from the corona (Wheatland and Melrose 1995). Observations by Veronig and Brown (2004) of in-the-loop HXR emissions showed that the loop column density to be as dense as  $> \sim 10^{20} \text{cm}^{-2}$  which allowed electrons up to 50 keV to be fully stopped in the loop. A high coronal loop density can be due to the chromospheric evaporation produced by an earlier flare in the same region (Veronig et al. 2005).

By studying the coronal X-ray emissions, Sui and Holman (2003) showed evidence of reconnection in the corona. Two thermal emission sources were observed: one in the flare loop and the other above the looptop. The dependence of source height on energy reveals a positive temperature gradient in the lower loop source and a negative one in the source above the looptop. This indicates the existence of a current sheet between the higher and the lower coronal sources. Similarly, Liu et al. (2008) also suggested the presence of a reconnection site between the double coronal sources as shown in the left panel of Figure 1.9. The right panel shows the energy-dependent source structure. Up to about 20 keV, the lower source has a positive energy-height gradient and the upper source has a negative one. However, the reversal of the trend at about 25 keV is visible. This may be due to the larger stopping distances of the higher energy electrons leaving from the acceleration site. The distance between the two sources appear to be increasing with time: the height of the upper one shows an obvious increase while that of the lower one decreases first followed by a subsequent subtle increase.

For an overview of observational work and theoretical ideas of coronal X-ray sources, see Fletcher et al. (2010) and Krucker et al. (2008a).

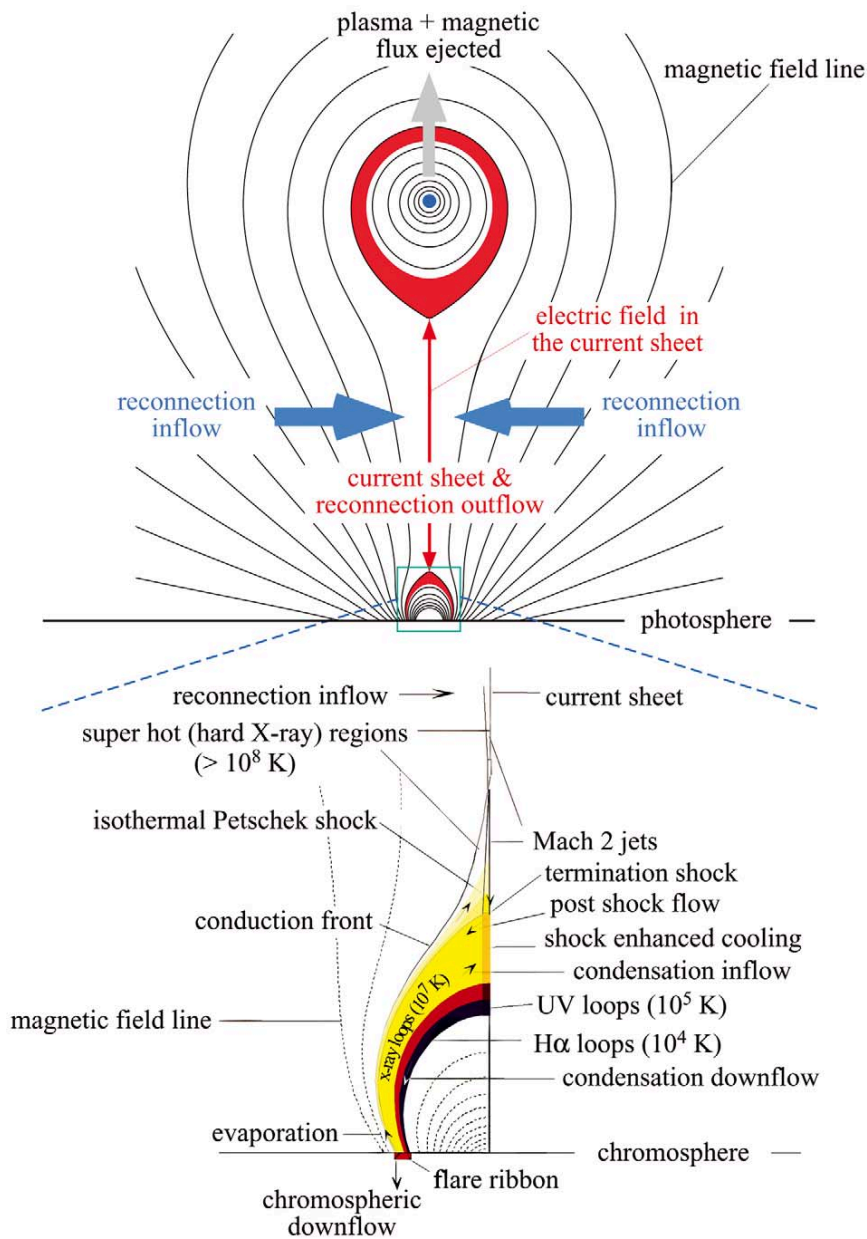


Figure 1.10: Schematic diagram of the standard flare reconnection model incorporated with a CME eruption model (from Lin (2004)).

### 1.3.2.4 Flares & CMEs Relations

Sometimes, however, the flare is just a minor part of a much larger coronal destabilization, when the magnetic confinement of a considerable part of the corona is broken up, expelled by magnetic forces in a Corona Mass Ejection (CME) disruption (see top panel in Figure 1.10). The stored magnetic energy can be released into various other forms that propagate through the solar atmosphere and into interplanetary space. The dominant term of the CME energy appears to be its kinetic energy, while for a flare most of the energy is converted to brightening the solar luminosity.

It is often suggested by reconnection models that the CME kinematics and the energy

release of the associated flare are tightly related (e.g. Forbes and Priest 1995). Figure 1.10 shows that the vertical current sheet is subject to magnetic reconnection which releases magnetic energy to both upward CMEs and downward flares. It has also been shown from observations that there is a close relationship between flares and CMEs (e.g. Hudson et al. 1996, Dere et al. 1997). More recent studies indicate that there is a close synchronization between the CME acceleration and the RHESSI HXR flux (Temmer et al. 2008). It is evident that the CME large-scale acceleration and the flare particle acceleration are intimately connected to a common reconnection region.

## 1.4 Particle Acceleration in Flares

*In future, we hope for a closer link between the macroscopic MHD of the flare and the microscopic plasma of particle acceleration. The global environment for particle acceleration is created by MHD, but there is a feedback, with the MHD affected by the nature of the turbulent transport coefficients.*

*Priest and Forbes (2002)*

The problem of particle acceleration during solar magnetic reconnection process is one of the most challenging and interesting problems in solar physics. Large solar flares are one of the most powerful magnetic reconnection explosions on the Sun, releasing up to  $10^{32} - 10^{33}$  ergs in  $10^2 - 10^3$  s into other forms of energy such as bulk flow energy, thermal and nonthermal energy. The accelerated electrons and ions are estimated to contain 10% to 50% of the total energy released in flares (Lin and Hudson 1976). These particles are assumed to be accelerated by a number of mechanisms occurring at different stages and locations of a flare evolution.

Three major groups of particle acceleration mechanisms essentially govern solar flare-related reconnection processes, e.g. (1) Direct Current (DC) field acceleration in strong electric fields generated in current-carrying loops or in current sheets during magnetic reconnection processes in the corona (Litvinenko 1996); (2) stochastic/turbulent acceleration by MHD turbulent waves where particle energy is gained or lost, e.g. in fast plasma reconnection outflows; (3) shock acceleration by a fast termination shock involved in an inhomogeneous boundary. These are, however, not completely distinct mechanisms, especially in the realistic dynamic flare events. In some models, a large homogeneous static current sheet with a well-defined DC electric field is replaced with more inhomogeneous small-scale time-varying current sheets and coalescing magnetic islands. These highly fragmented dynamic current sheets are approaching the limit of turbulent fields as in stochastic acceleration. For a detailed review of acceleration mechanisms, see e.g. Aschwanden (2002).

Recent observations from space satellites such as SoHO, TRACE, and RHESSI are giving important clues about the nature of particle acceleration process. In the flare model indicated by these observations discussed in Section 1.3.2.1, the hard X-ray and  $\gamma$  ray chromospheric footpoints are caused by bremsstrahlung processes related to high energy

electrons and protons transported downward along the flare loop from the reconnection site high up in the corona. The third coronal hard X-ray source above the soft X-ray loop is an indication of first energy releasing process by accelerated particles encountering the flare loop (see Section 1.3.2.3 for more details). One can normally deduce the electron energy spectrum from the observed HXR spectrum considering either a thick-target model or a thin-target model (Brown 1971). Section 1.2.3.1 gives the basic equations necessary to derive non-thermal electron spectrum (for which Equation 5.11 gives the normalization coefficient) from observational HXR power-law spectrum (shown as Equation 1.6) in the thick-target model. However, the inversion of photon spectra to particle spectra could not answer the question on how particles are accelerated in the corona and then transported downward. It is very difficult to infer from observations how the different acceleration mechanisms work together and how large-scale fields, which accelerate particles, can build up. Hence numerical calculations are necessary to study the microscopic acceleration process in macroscopic configurations. This section will offer an overview of different acceleration mechanisms together with a review of recent simulations exploring particle acceleration processes.

### 1.4.1 Direct Acceleration by Electric Field

Since magnetic fields are ubiquitous in the solar corona, charged particles such as electrons and protons experience a Lorentz force that makes them gyrate around guide magnetic field lines. The basic relativistic equation (1.19) of motion thus includes acceleration/deceleration by an electric field  $\mathbf{E}$  and the Lorentz force exerted by the magnetic field  $\mathbf{B}$ :

$$\frac{dm\gamma\mathbf{v}}{dt} = q(\mathbf{E} + \mathbf{v} \times \mathbf{B}), \quad (1.19)$$

where,  $\gamma = 1/\sqrt{1 - v^2/c^2}$  is the relativistic Lorentz factor (Note that in Section 1.2.3.1  $\gamma$  represents photon spectral index);  $m$  and  $q$  are the rest mass and the charge of the particle;  $\mathbf{x}$  and  $\mathbf{v}$  are the position and velocity vectors of the particle;  $\mathbf{E}$  and  $\mathbf{B}$  are the electric and magnetic fields that the particle experiences on its way. Taking the scalar product of  $\mathbf{v}$  with the equation of motion (1.19), one derives the following equation for the change in kinetic energy

$$\frac{dE_k}{dt} = q\mathbf{v} \cdot \mathbf{E}, \quad (1.20)$$

where  $E_k = mc^2(\gamma - 1)$  is the kinetic energy of a charged particle. According to Equation (1.20), a charged particle can gain or lose kinetic energy in an electromagnetic field only if it has a velocity component in the direction of the electric field, i.e. the drop/increase of electric potential energies transfers into and from the kinetic energies of charged particles. A parallel (to the direction of magnetic fields) electric field, often relying on the existence of current sheets and anomalous resistivity in MHD framework, can therefore accelerate charged particles directly ignoring the gyration in the perpendicular plane. A perpendicular electric field, e.g. convective electric field  $\mathbf{E}_{con} = -\mathbf{u} \times \mathbf{B}$  where  $\mathbf{u}$  is plasma flow velocity and  $\mathbf{B}$  is magnetic field, can hardly accelerate particles in uniform static magnetic fields due to the continuous energy gaining and losing process in terms of regular gyration. However, acceleration can take place in the inhomogeneous vicinity of magnetic X-points and O-points where the guiding center drift of the particles points into

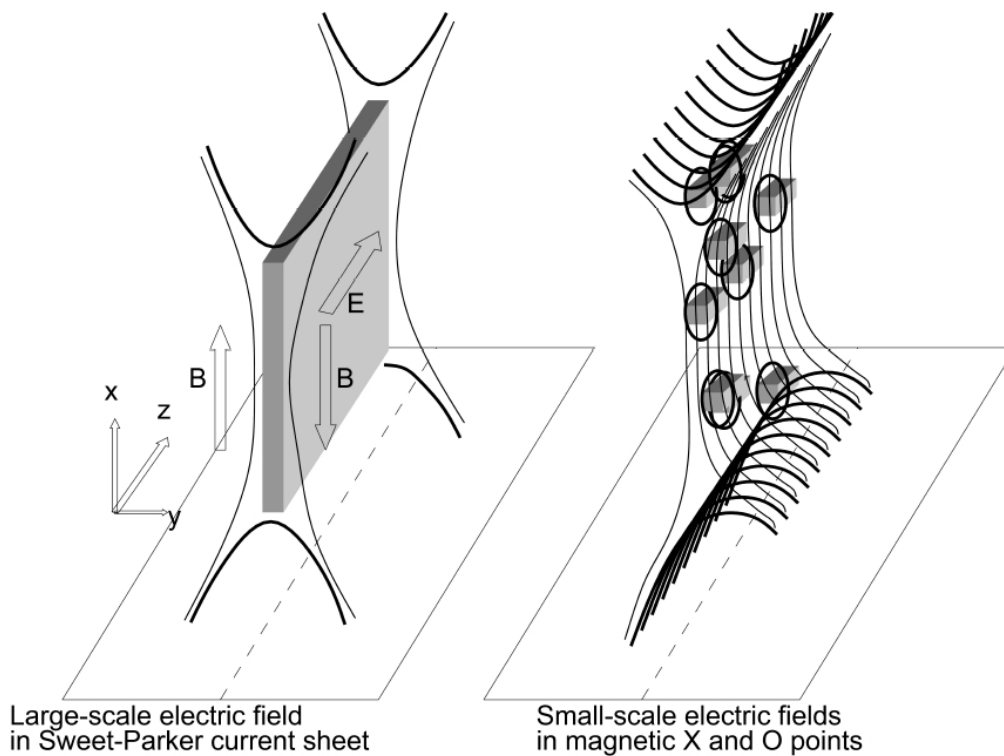


Figure 1.11: *Left*: Large-scale electric fields in the current sheet based on classical Sweet-Parker reconnection model. *Right*: Small-scale electric fields in fragmented magnetic X-points and O-points, considered as an unstable status due to tearing mode instability of the large-scale current sheet (see Section 1.3.1). Both figures are taken from Aschwanden (2002).

the direction of the perpendicular electric field which, therefore, contributes to the particle acceleration (Northrop 1963, Aschwanden 2002). In this section, we will explore mechanisms of particle acceleration by considering electric fields being either parallel or perpendicular to the orientation of magnetic field.

#### 1.4.1.1 Parallel Electric Field Acceleration

The direct way to gain particle energy without any interference of the perpendicular gyromotion is acceleration by a parallel electric field, since magnetized particles can move freely in the direction parallel to the magnetic field. Particle velocities in the perpendicular plane will carry on the gyromotion around magnetic field lines which are actually stabilizing the particle to follow the magnetic and electric field directions (Litvinenko 1996).

Strong electric fields generated in reconnecting current sheets (RCS) are often parallel to the magnetic field and can accelerate particles directly, e.g. along the X-line of 2-D reconnection models (see Figure 1.11) or along separators in 3-D reconnection models. The left panel in Figure 1.11 shows a classical Sweet-Parker reconnection-acceleration model invariant in the third dimension which is the direction of the accelerating field  $E$  in

the RCS. The extent of the RCS is important since it determines the electric potential difference over which a particle can be accelerated. However, an arbitrary extent of the RCS was often assumed in older simplified studies in order to adjust its length to the maximum electric potential difference needed to explain the highest observed energies of nonthermal particles. For an electron to be accelerated to 100 keV in an electric field  $\approx 10^{-3}$  V/m, an unrealistically long RCS of more than  $10^7$  m in length would be needed (Aschwanden et al. 2002). As mentioned in Section 1.3.1, such a large-scale RCS becomes unstable to tearing mode instability (Furth et al. 1963) so that a fragmented topology of magnetic X- and O-points results leading to small-scale RCS in magnetic islands as shown in the right panel in Figure 1.11. Moreover, large-scale electric fields would lead to a charge separation of electrons and ions that sets up a current.

Strictly speaking, the electric field in Figure 1.11 does not count as parallel fields in the absence of a guide magnetic field (in z-direction in Figure 1.11) along the RCS. Nevertheless, assuming that a given particle follows its way sharply along the X-line (where  $B=0$ ), it will be accelerated freely by the electric field, similar to the case in parallel acceleration. A path deviating from the X-line will however carry an electric drift that scatters the particle away from the RCS: given  $\mathbf{B}$  is mainly in the x-direction and  $\mathbf{E} = E_z \hat{\mathbf{z}}$ , the  $\mathbf{E} \times \mathbf{B}$  drift is in y-direction, perpendicular to the RCS. Therefore, despite the efficiency of acceleration along the X-line, the probability for particles to fall into and remain within the thin RCS and get accelerated are minimal.

In this 2-D X-point reconnection model, longitudinal (guide) magnetic field  $B_z$  (which the electric field is parallel to) has often been considered in theories and test particle simulations to explain more efficient accelerations (e.g. Litvinenko and Somov 1993, Litvinenko 1996, Bruhwiler and Zweibel 1992, Mori et al. 1998, Browning and Vekstein 2001, Zharkova and Gordovskyy 2004, Hannah and Fletcher 2006). The conclusion from these calculations is that with larger electric fields and with additional guide magnetic fields in the RCS, particles can be accelerated more efficiently. A guide magnetic field magnetizes the charged particles and reduces their probability of being ejected from the current sheet so that particles can gain more energy from the electric field (Litvinenko 1996). A power-law distribution of accelerated particles is usually obtained and used for comparison with observations. Nevertheless, in these calculations the values of the electric field and the guide magnetic field, as well as the width of current sheet, are prescribed without sufficient considerations of the reconnection process itself, which produces the electromagnetic field. Therefore these results provide a qualitative analysis of the acceleration rather than quantitative results for particle energies and spectrum.

To obtain a self-consistent solution of parallel electric fields, one can employ magnetic electric fields from analytic MHD solutions (e.g. Heerikhuisen et al. 2002, Craig and Litvinenko 2002, Wood and Neukirch 2005, Hamilton et al. 2005) or numerical simulations (e.g. Schopper et al. 1999, Turkmani et al. 2006, Liu et al. 2007, Karlicky and Barta 2006).

According to the Ohm's law in MHD framework, parallel electric fields are balanced in resistive electric fields  $\mathbf{E}_{res} = \eta \mathbf{j}$ . A parallel current density  $j_{\parallel}$  and the existence of a diffusion region with anomalous resistivity  $\eta$  are therefore crucially important for parallel acceleration. Resistive MHD simulations can model the magnetic and electric fields in either 2-D or 3-D framework and test particles are calculated in the evolved reconnection fields containing a parallel electric field component that can effectively accelerate particles

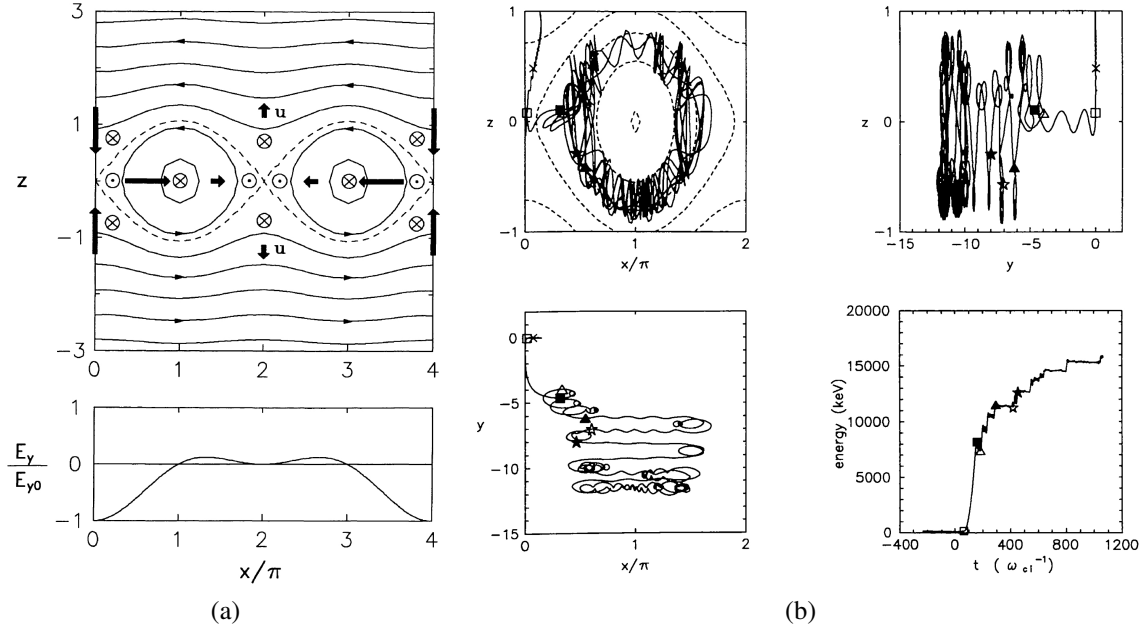


Figure 1.12: (a): Filamentary magnetic islands configuration used for particle acceleration by Kliem (1994). *Top*: Solid lines represent magnetic fields  $\mathbf{B}$  and heavy arrows indicate plasma flow velocity  $\mathbf{u}$ . Arrows out of the plane give the direction of  $\nabla B$  drift for positive charges. *Bottom*: The electric field is in the perpendicular direction. (b): A proton orbit and energy gaining in the magnetic electric fields. The orbit shows meander motion,  $\nabla B$  drift and  $\mathbf{E} \times \mathbf{B}$  drift.

to observational energies (e.g. Schopper et al. 1999, Turkmani et al. 2006, Liu et al. 2007, Karlicky and Barta 2006). Karlicky and Barta (2006) also considered energy losses and pitch-angle scattering of electrons due to Coulomb collisions with Monte-Carlo methods in their test-particle calculations (Bai 1982). Turkmani et al. (2006) investigated net-gain of particle energies through multiple small-scale fragmented current sheets generated by resistive MHD simulations. However, any quantitative results based on prescribed  $\eta$  are somehow arbitrary, since there is no generic way to parameterize the non-ideal property of the collisionless corona plasma in MHD simulation. For example, particle accelerated to energies up to 100 GeV (Turkmani et al. 2006) might be a result of using a numerical "hyper-resistivity", which stabilizes the MHD code. Moreover, the parallel electric fields obtained from kinetic processes are in general confined to regions on the ion inertia scale (Hesse et al. 1999), much smaller than the macroscopic MHD grid scales, which can therefore affect and accelerate only a few particles.

#### 1.4.1.2 Perpendicular Electric Field Acceleration

In static uniform magnetic fields, however, perpendicular electric fields  $\mathbf{E} = -\mathbf{u} \times \mathbf{B}$  cannot lead to the net-gain/loss of particles' kinetic energy; this is because the magnetized particle keeps gyrating in the magnetic fields and is accelerated/decelerated and again decelerated/accelerated within one gyro-period. The perpendicular convective electric

field is therefore often considered as irrelevant for particle acceleration. However, in the inhomogeneous vicinity of magnetic null points, the guiding center drift of the particles can point into the direction of the convective electric field, which, therefore, contributes to the particle acceleration. The drift motion can be due to a magnetic gradient force  $\mathbf{F}_{\nabla B} = (mv_{\perp}^2/2B)\nabla\mathbf{B}$  or a curvature force  $\mathbf{F}_R = (mv_{\parallel}^2/R^2)\mathbf{R}$ . The drift velocity is perpendicular to both the magnetic field  $\mathbf{B}$  and the force direction. The velocity for gradient drift and curvature drift are respectively:  $\mathbf{v}_{grad} = \frac{mv_{\perp}^2}{2qB^3}\mathbf{B} \times \nabla B$  and  $\mathbf{v}_{curv} = \frac{mv_{\parallel}^2}{qB^2R_{curv}^2}\mathbf{R}_{curv} \times \mathbf{B} = \frac{mv_{\parallel}^2}{qB^2}\mathbf{B} \times (\nabla \frac{\mathbf{B}}{|\mathbf{B}|} \cdot \frac{\mathbf{B}}{|\mathbf{B}|})$ .

These drift velocities vary inversely proportional to the magnitude of the magnetic field. Therefore particle drifts are maximum where the magnetic field is minimum and the gradients and curvatures are strong. A null point provides a highly probable location for these effects (e.g. Kliem 1994, Dalla and Browning 2005, 2008, Guo et al. 2010). Moreover, the magnetic field is so weak around the null point that gyroradius can be enlarged to be comparable with the magnetic scale length so that the behavior of a charged particle is in a non-adiabatic regime. The unmagnetized particles can be accelerated directly by the electric fields. It is also suggested by simulations (e.g. Guo et al. 2010) that heavy ions and protons are more easily affected by this mechanism than electrons because they have a larger Larmor radius  $R_i/R_e = \sqrt{m_i/m_e}$  and could be more easily unmagnetized.

The convective electric field can result either from the plasma flow motion or stem from the approaching motion of the coalescing magnetic islands. In the filament current sheet model introduced in Section 1.3.1, Kliem (1994) considered particle orbits, trapping and acceleration processes. Figure 1.12a shows the configuration of two approaching magnetic islands. Since the magnetic gradient drift takes place in the perpendicular plane (shown as out-of-plane arrows in the figure) coincident with the direction of the electric field in 2-D framework, charged particles can therefore be accelerated due to the drift motion. Figure 1.12b shows that the O-type magnetic null point can also trap the particles so that it meanders around while slowly drifting along y-axis so that particles can experience the full energy gain provided by the strength and extent of the electric field near the O-lines. The test protons can be accelerated up to 15 MeV, as shown in the figure. Scaling MHD computational results into solar flare conditions, Karlicky and Barta (2006) investigated electron acceleration process in the cusp structure with the collapsing trap based on two-dimensional MHD model of the magnetic reconnection. They found that this acceleration process essentially modifies the distribution function of electrons pre-accelerated in the reconnection process. The significance of the curvature drift of electrons in the electric field direction for the electron acceleration is confirmed. Nevertheless, 2-D magnetic X- or O-type reconnection models are still far from representing realistic solar coronal magnetic field configurations. It may also give an overestimation of acceleration since the perpendicular electric field is always in the direction of magnetic gradient and curvature drifts (since the magnetic field is only in a plane).

In the 3-D framework, Dalla and Browning (e.g. Dalla and Browning 2005, 2008) used an analytical model of magnetic and electric fields for kinematically prescribed ideal plasma flows around a potential magnetic null. They studied particle acceleration for spine and fan reconnection. For the same configuration of the magnetic field, different plasma flows correspond to different convection electric fields. In the spine reconnection case, plasma flows in and out through the center of the null, resulting in an azimuthal

electric field. An efficient acceleration is obtained assuming that the electric field could be as large as 1 kV/m. In the fan reconnection case, the plasma flow has another azimuthal component and the acceleration is less efficient, because fewer particles can reach the regions of strong electric fields. Note however that the analytic solution of the electric field contains a singularity at the center ( $E \rightarrow \infty$  at  $R = 0$ ), which leads to infinite runaway acceleration. Also, lack of information on the actual scale and magnitude of the reconnecting magnetic field, as well as the strength and configuration of the real plasma flows, may hinder the process of obtaining realistic acceleration energies and spectrum.

In this thesis, we will study the particle acceleration at a three-dimensional magnetic null point in the solar corona, considering self-consistent magnetic fields, plasma flows and the corresponding convective electric fields (Guo et al. 2010). We calculate the electromagnetic fields by 3-D MHD simulations and expose charged particles to these fields within a full-orbit relativistic test-particle approach. In the 3-D MHD simulation part, the initial magnetic field configuration is set to be a potential field obtained by extrapolation from an analytic quadrupolar photospheric magnetic field with a typically observed magnitude. The configuration is chosen so that the resulting coronal magnetic field contains a null. Driven by photospheric plasma motion, the MHD simulation reveals the coronal plasma motion and the self-consistent electric and magnetic fields. In a subsequent test particle experiment the particle energies and orbits, determined by the forces exerted by the convective electric field and the magnetic field around the null, are calculated in time. Through its convective electric field and due to magnetic nonuniform drifts and de-magnetization process, the 3-D null can act as an effective accelerator for protons but not for electrons. Protons are more easily de-magnetized and accelerated than electrons because of their larger Larmor radii. Notice that macroscopic MHD simulations are blind to microscopic magnetic structures where more non-adiabatic processes might be taking place. In the real solar corona, we expect that particles could have a higher probability to experience a de-magnetization process and get accelerated. To trigger a significant acceleration of electrons and even higher energetic protons, however, the existence of a resistive electric field mainly parallel to the magnetic field is required. A physically reasonable resistivity model included in resistive MHD simulations is direly needed for the further investigations of electron acceleration by parallel electric fields.

### 1.4.2 Stochastic Acceleration

The stochastic acceleration model has been developed by Hamilton and Petrosian (1992), Park and Petrosian (1995), Miller et al. (1997), Petrosian and Liu (2004) (For a comprehensive overview, see Aschwanden (2002)). Figure 1.13 shows a stochastic acceleration model in solar flares where turbulent waves generated in the reconnection process can interact and accelerate particles and heat the background plasma stochastically. Second order Fermi acceleration is encountered in form of a stochastic process of wave-particle interaction, if particles move with approximately the phase velocity of the wave or their gyrofrequency is in resonance with the wave frequencies. In solar corona, a large number of different waves can be present, some are expected to have constructive interference with the motion of a particle, and some destructive. In this stochastic process parts of a particle distribution experience a net gain in energy and the accelerated particles are thus either detected via coronal X-ray emission or transported downward to the lower

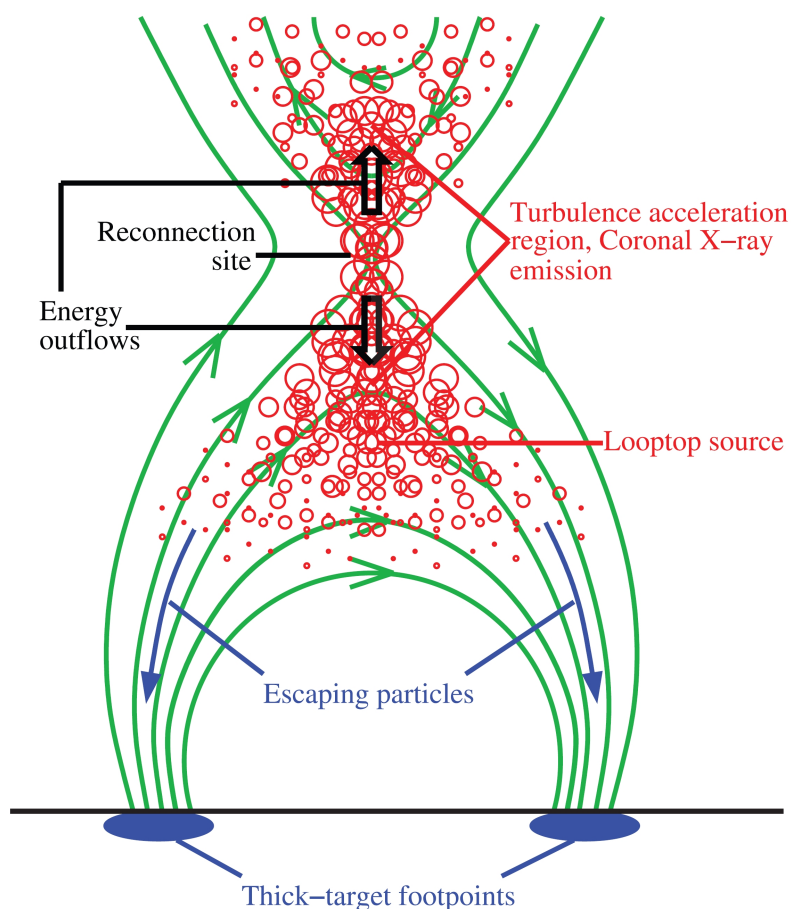


Figure 1.13: Sketch of the stochastic acceleration model for solar flares (from Liu et al. (2008)). The green curves are magnetic field lines; the red circles represent turbulence or plasma waves that are generated during magnetic reconnection.

atmosphere and observed as HXR footpoints (Figure 1.13). Essentially, Alfvén waves, magnetosonic waves, and ion sound waves can accelerate ions, while whistler waves, Langmuir waves, and electromagnetic waves are efficient in the acceleration of electrons. The acceleration volume in turbulent acceleration is much larger than the vicinity of X- and O-point regions in a current sheet, which eases the electron number problem. However, the assumed amount of turbulent wave energy input has not been fully understood in reconnection physics.

Petkaki and MacKinnon (2007) presented test particle calculations designed to illuminate the consequences for particle acceleration of dynamic reconnection waves. A time varying electric field is superimposed on a static X-type neutral point. Different frequencies of the electric fields are used, representing different possible types of waves, to accelerate particles. Resonant acceleration processes can take place when the frequency of the changing fields is resonant with the particle gyrofrequencies or inverse crossing-time (through the non-adiabatic regions near the null). Higher frequency disturbances favour electrons over ions.

### 1.4.3 Shock Acceleration

Shocks are waves with nonlinear amplitudes that propagate faster than the sound speed of the ambient medium. Generally, two types of shock acceleration are distinguished: shock-drift acceleration and diffusive shock acceleration. In the former, each particle has only a single encounter with the shock front while in the latter a particle can be reflected several times by moving fronts of the shock. A review on the history and the various mechanisms of particle acceleration in shocks can be found in Jones and Ellison (1991).

In the scenario of shock-drift acceleration, the normal component of the magnetic field is continuous across the shock front ( $B_{n2} = B_{n1}$ ), while the tangential component varies, being much stronger at downstream than at upstream ( $B_{t2} \gg B_{t1}$ ). The total magnetic field strength increases across the shock front ( $B_2 \gg B_1$ ), and the particle therefore gains perpendicular velocity due to conservation of the magnetic moment ( $\mu = \frac{1}{2}mv_{\perp}^2/B$ ). The energy gain is proportional to the downstream/upstream ratio of the magnetic field strengths ( $B_2/B_1$ ), which is typically a factor of 4. When the shock propagation is nearly perpendicular to the upstream magnetic field, acceleration becomes most efficient. However, this small angle requirement restricts the shock-drift acceleration and only applies to the Earth's bow shock and to radio-type II bursts (Aschwanden 2002). The basic problem of the limited energy gain during a single encounter with the shock front can be overcome in the regime of strong wave turbulence, where particles are scattered many times forth and back across the shock front, so that they experience a cumulative acceleration process.

## 2 3-D MHD Simulation and an X-type Magnetic Null Point

*Technical skill is the mastery of complexity while creativity is the mastery of simplicity.*

*E. Christopher Zeeman*

In order to test particle behaviors and energies in a realistic coronal magnetic null point, we use 3-D MHD simulations with extrapolated magnetic fields as initial conditions to obtain the electromagnetic fields containing a null.

### 2.1 Basic Equations of the 3-D MHD Simulation

A three-dimensional cartesian MHD model was used to describe the evolution of the large-scale magnetic and electric fields from the solar photosphere to the lower corona (e.g. Büchner et al. 2004, Büchner 2007, Guo et al. 2010). This MHD model solves the basic resistive MHD equations as shown in the introduction chapter. The normalized equations (see Appendix A for the normalization processes) are as following, including the continuity equation (2.1), momentum equation (2.2), induction equation (2.4) and energy equation (2.3), together with Ohm's law (2.5), Ampere's law (2.6) and an equation of state (2.7):

$$\frac{\partial \rho}{\partial t} = -\nabla \cdot \rho \mathbf{u} \quad (2.1)$$

$$\frac{\partial \rho \mathbf{u}}{\partial t} = -\nabla \cdot \left[ \rho \mathbf{u} \mathbf{u} + \frac{1}{2}(p + B^2) \mathbf{I} - \mathbf{B} \mathbf{B} \right] - \nu \rho (\mathbf{u} - \mathbf{u}_n) \quad (2.2)$$

$$\frac{\partial p}{\partial t} = -\nabla \cdot p \mathbf{u} - (\gamma - 1) p \nabla \cdot \mathbf{u} + 2(\gamma - 1) \eta \mathbf{j}^2 \quad (2.3)$$

$$\frac{\partial \mathbf{B}}{\partial t} = -\nabla \times \mathbf{E} = \nabla \times (\mathbf{u} \times \mathbf{B} - \eta \mathbf{j}) \quad (2.4)$$

$$\mathbf{E} = -\mathbf{u} \times \mathbf{B} + \eta \mathbf{j} \quad (2.5)$$

$$\nabla \times \mathbf{B} = \mathbf{j} \quad (2.6)$$

$$p = 2nk_B T. \quad (2.7)$$

The momentum equation in this MHD model introduces a viscous term  $\nu\rho(\mathbf{u} - \mathbf{u}_0)$  representing for the transfer of momentum between the neutral gas and the plasma. Both the radiation and heating effects are neglected in the current model. The gravity force is not considered either. The normalization magnetic field, electric field and plasma velocity have the relationship:  $E_0 = B_0 u_0$ . Typical values are  $B_0 = 1$  G,  $u_0 = 50$  km/s and  $E_0 = 5$  V/m, as shown in Table A.1 (for the first run of the MHD simulation) in Appendix A. To simulate the global magnetic field from the bottom of the photosphere up to the corona, the normalization length scale is  $L_0 = 500$  km. For the first run of the MHD simulation, the total box length in the horizontal  $x$  and  $y$  direction is  $93 L_0$  (46.5 Mm), and in the vertical  $z$  direction it is near  $31 L_0$  (15.5 Mm). The height of the transition region is about  $5 L_0 \sim 2.5$  Mm.

## 2.2 Initial and Boundary Conditions of the MHD Simulation

Initial conditions define the starting point for any numerical simulations models. Solving the MHD equations and applying the boundary conditions will drive the system to evolve.

### 2.2.1 Initial Conditions

In order to generate a realistic coronal magnetic null point for a candidate particle accelerator, we build up the initial MHD box with extrapolated magnetic fields and plasma conditions (temperature and density) commonly used in the solar atmospheric models.

For the initial density distributions, we take an one dimensional (varies in  $z$  direction only) pressure equilibrium model, so called VAL model (Vernazza et al. 1981). It mimics the density-height profile observed in the solar atmosphere. The density decreases with increasing height, with abrupt changes at the transition layer. The density in the photosphere is considered to be 100 times larger than that in the solar corona. The density profile used in the simulation is give by

$$\rho(z) = 0.5\rho_f \left( \frac{\tanh(z + z_{tr} - 1) - \tanh(z - z_{tr} + 1)}{\tanh(z_{tr} - 1)} \right) + \rho_c \quad (2.8)$$

where  $\rho_f$  and  $\rho_c$  are the photospheric and coronal densities respectively and  $z_{tr}$  is the location of the transition layer, the boundary between chromosphere and corona. For the normalization scale  $L_0 = 500$  km,  $z_{tr}$  is about 5.

When gravity force is neglected, the hydrostatic equilibrium (gas pressure  $p$  is constant) is satisfied and the temperature increases with height, with abrupt enhance at transition layer. The initial temperature profile is calculated according to Eqs. (2.8) and (2.7).

The initial 3-D magnetic field configuration (Fig. 2.1) was obtained by potential-field extrapolation of a quadrupolar analytic magnetic field (Guo et al. 2010). Appendix B gives the detailed analytic solution of the force-free magnetic extrapolation under line periodic symmetry boundary conditions (Otto et al. 2007).

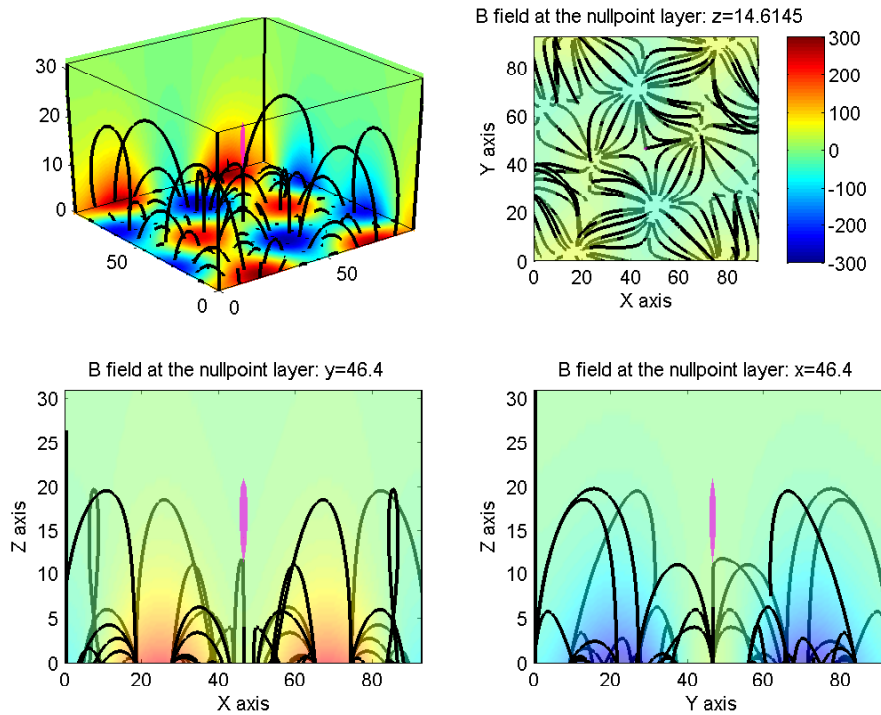


Figure 2.1: Initial potential-extrapolated magnetic field with a null in the center of the box. The upper-left figure shows the 3-D view of the whole simulation box extending from the photosphere to the corona. The upper-right figure is a  $x - y$  face-on view of the null at  $z = 14.6$ . The bottom-left/bottom-right figure is the  $x - z/y - z$  cut through the center of the  $y$ -axis/ $x$ -axis, where the null is located. The black lines are the magnetic field lines.

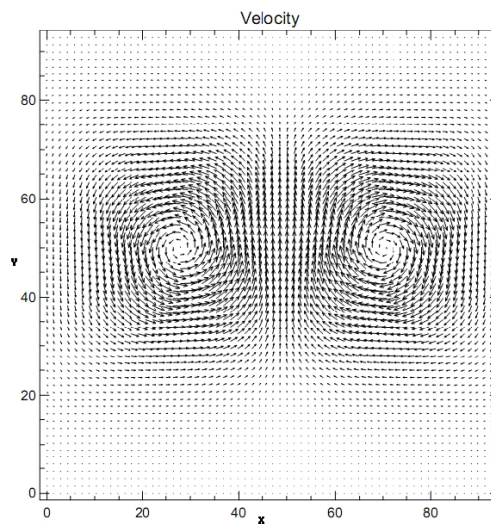


Figure 2.2: Rotating neutral gas velocity imposed at the bottom of the simulation box.

### 2.2.2 Boundary Conditions

The boundary conditions were defined so that the MHD equations remained invariant under transformation of the MHD variables (Otto et al. 2007). The simulation box has 6 boundaries: four lateral boundaries, the bottom boundary and the top boundary.

The top boundary (at  $z = L_z$ ) was an open boundary which means that at the physical boundary the gradients of all quantities in the direction normal to the boundary are equal to the gradients in the same direction immediately at the first layer inside the simulation box. This provides a smooth transition for the forces when they go through the physical boundary.

The four lateral boundary conditions (at  $x = 0, x = L_x, y = 0, y = L_y$ ) were line-mirroring symmetric consistent with the set of MHD equations (Otto et al. 2007). The symmetric conditions of a given variable at each boundaries are expressed as Equation B.3 in Appendix B.

The bottom boundary condition (at  $z = 0$ ) for the magnetic field was obtained by considering that the field should satisfy  $\nabla \cdot \mathbf{B} = 0$  and that there should be no horizontal currents ( $j_x = (\nabla \times \mathbf{B})_x = 0$ , and  $j_y = (\nabla \times \mathbf{B})_y = 0$ ) at  $z = 0$ . For the plasma motion, the momentum flux through the bottom was set to be zero ( $u_z(z = 0) = 0$ ), meaning no emerging flux in the photosphere. Since the horizontal plasma motion in the solar photosphere plays an important role in the build-up of electric currents in solar atmosphere (e.g. Santos and Büchner 2007, Büchner 2006), we applied two vortices of neutral gas motion at the bottom with an average speed of about  $0.0137 u_0$  (see Fig. 2.2). The last term on the right-hand side of the momentum equation (Eq. (2.2)) represents the transfer of momentum from the neutral gas to the plasma through collisions. The neutral gas velocity was set to be a horizontal vortex with  $\mathbf{u}_n = \nabla \times (U \mathbf{e}_z)$ , where  $U$  is a scalar potential so as to keep  $\nabla \cdot \mathbf{u}_n = 0$  to inhibit the piling up of the plasma and magnetic field. The plasma is dragged behind the neutral gas through collisional interaction with the gas. The collision frequency  $\nu$  is height dependent, attaining its maximum at the bottom and decreasing exponentially with height. Therefore the plasma motion is coupled with the neutral gas in the photosphere and chromosphere, while it is decoupled from the neutral gas motion in the corona. Hence the whole evolution of an initially relaxed equilibrium state is due to plasma flows induced by the moving photospheric neutral gas.

The complete set of Eqs. (2.1-2.7) was numerically solved in a 3-D cartesian box with finite-difference discretization methods. The grid was chosen to be equidistant in the  $x$  and  $y$  directions, both with 128 grid points and  $\Delta_x = \Delta_y = 0.73L_0$ . It is non-equidistant in the  $z$  direction (with 64 grid points): the resolution decreases with height. The grid size is  $\Delta_z = 0.3L_0$  at the bottom and stretched to  $\Delta_z = 1.0L_0$  at the top. Eqs. (2.1) to (2.3) were advanced in time with a second-order accurate leapfrog scheme (Potter 1973), because it has a very low numerical dissipation. A Lax scheme was used in the first and last step. Appendix C shows the methods for both leapfrog and Lax Wendroff numerical schemes.

## 2.3 A 3-D Numerical X-type Magnetic Null Point

The magnitude of the magnetic field decreases with height. Its maximum value ( $293 B_0$ ) is located at the bottom of the box. It drops to about  $150 B_0$  at the transition layer and to just tens of  $B_0$  in the corona. In such a configuration, which should not be too rare in the solar

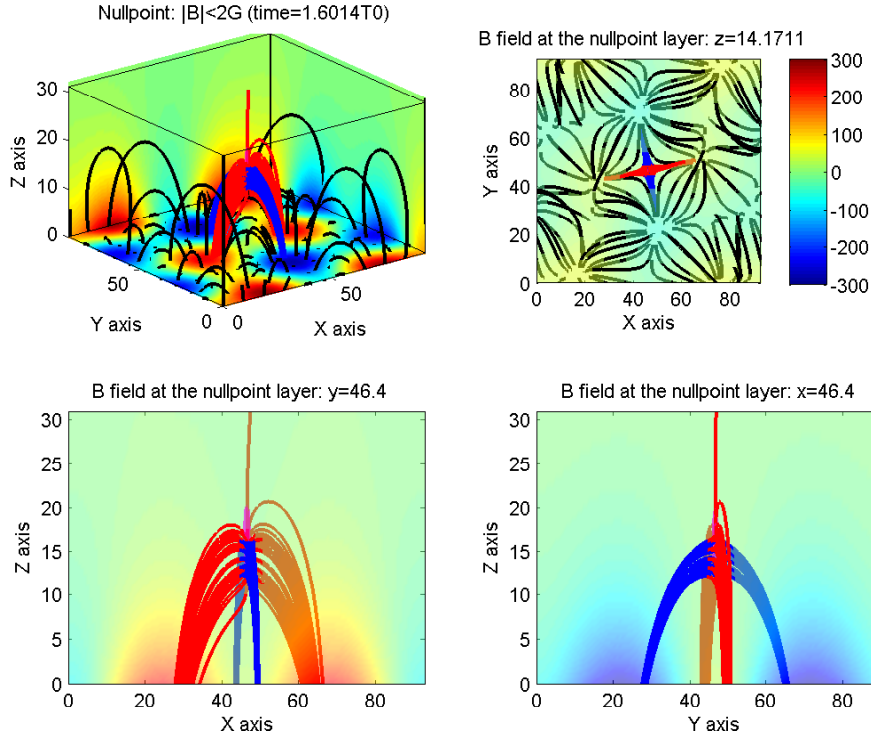


Figure 2.3: Magnetic field configuration with a null in the center of the box. The upper-left figure shows the 3-D view of the whole simulation box extending from the photosphere to the corona. The upper-right figure is a  $x$ - $y$  face-on view of the null at  $z = 14.17$ . The bottom-left/bottom-right figure is the  $x$ - $z$ / $y$ - $z$  cut through the center of the  $y$ -axis/ $x$ -axis, where the null is located. The black lines are the global magnetic field lines. The blue lines are the magnetic field lines leaving from the weak field region ( $B < 2$ ), while the red lines are the magnetic field lines coming into the region.

atmosphere, the magnetic field cancels near the central vertical line of the box. Since the magnetic field vanishes, a null point is located near the box center. Fig. 2.1 shows the initial configuration of magnetic fields (black lines) and the magenta colored region displays where the magnetic field strength is smaller than 2 Gauss. The approximate location of the magnetic null point being 46.4, 46.4, 14.6 is determined by the minimum of the magnetic field magnitude which is 0.08 G on the MHD grids. This reference point is not the location of the actual null point (which requires an interpolation of the magnetic fields between the grid points), but is in its immediate vicinity. For simplification, we call this reference point "the null" throughout the chapter. This field configuration was our starting point for an investigation of particle acceleration near a 3-D null point.

The location of the minimum numerical magnetic field slightly shifts in height from (46.4, 46.4, 14.6) to (46.4, 46.4, 14.2) after the simulation of 1.6 Alfvén times and its value becomes 0.0484 G. The weak field region ( $B < 2$  G) in Fig. 2.3 extends between  $x : 45.0-47.1$ ,  $y : 45.0-47.1$ , and  $z : 12.0-20.5$ . We calculated the Jacobian matrix  $M_{ij} = \partial B_i / \partial x_j$  to evaluate the structure (Lau and Finn 1990) around the null. The eigenvalues of the matrix at the null point are about (2.1, -1.7, -0.3), following the category of a negative null (Section 1.3.1.4). The first positive eigenvalue defines the spine, while the

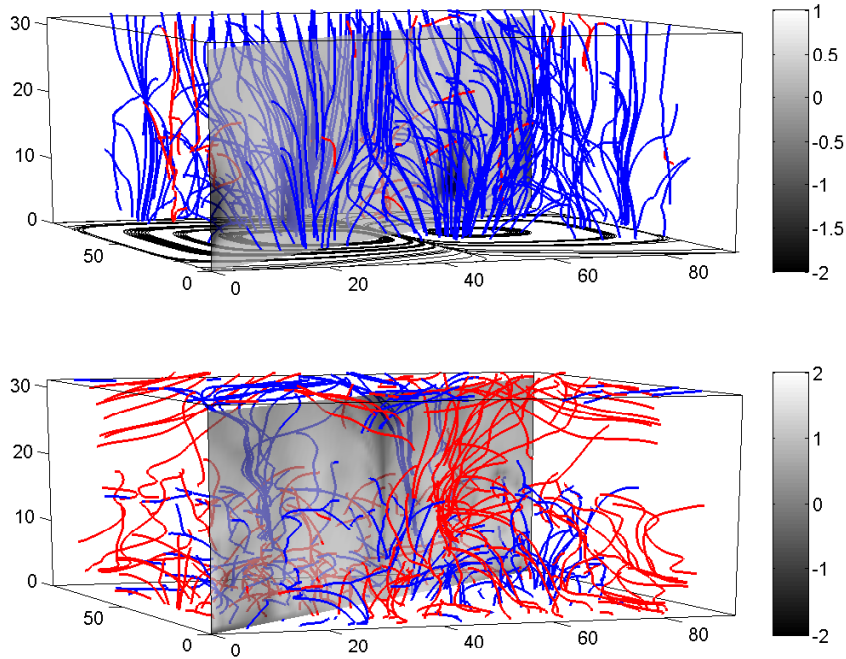


Figure 2.4: Plasma velocity flow lines (top) and corresponding convective electric fields (bottom). The red lines represent velocity flow (electric field) lines with positive (upward directed)  $u_z$  ( $E_z$ ). The blue lines indicate negative (downward directed)  $u_z$  ( $E_z$ ). The diagonal cross-section plane in the top image depicts the grey-coded normalized value of  $u_z$ . The cross-section plane in the bottom image shows the grey-scale  $\lg(E_{con}/E_0)$ .

last negative ones indicate a fan surface. The eigenvector of the matrix gives the direction of a corresponding spine or fan plane: the spine path is in the direction of  $0.18, -0.98, 0.03$  (followed by the blue field lines in Fig. 2.5); the fan surface is a plane defined by two vectors  $(-0.98, -0.18, -0.01)$  and  $(0, 0, 1)$ , i.e. a vertical plane crossing the center of the red field lines in the figure. Since the second eigenvalue ( $-0.3$ ) for the fan plane is much smaller compared to the first ( $-1.7$ ), the field lines tend to follow the direction of  $-0.98, -0.18, -0.01$  (red lines in the horizontal direction) rather than the vertical direction  $0, 0, 1$  (Restante et al. 2009). Actually, if the last eigenvalue vanishes, the 3-D X-type null point simply equals 2-D X-type null point where no field lines extend in the vertical direction. These structures can also be seen in Figs 3.2 and 3.3, where magnetic fields are shown as black lines.

The null point is also globally connected to the bottom of the simulation box by the spine (followed by the blue field lines in Fig. 2.5 and Fig. 2.3) and the fan field lines (red field lines). Applying the photospheric motions at the fan footpoints as shown in Fig. 2.2 would actually cause magnetic field perturbations that propagate to the corona along the field lines at the local Alfvén speed and eventually reach the vicinity of the null (Santos et al. 2011).

Driven by the horizontal photospheric motion, the plasma in the whole simulation box evolves. It reaches a state with an average bulk velocity of  $0.42 u_0$  after the simulation (top image in Fig. 2.4). The global configuration and topology of the magnetic fields do

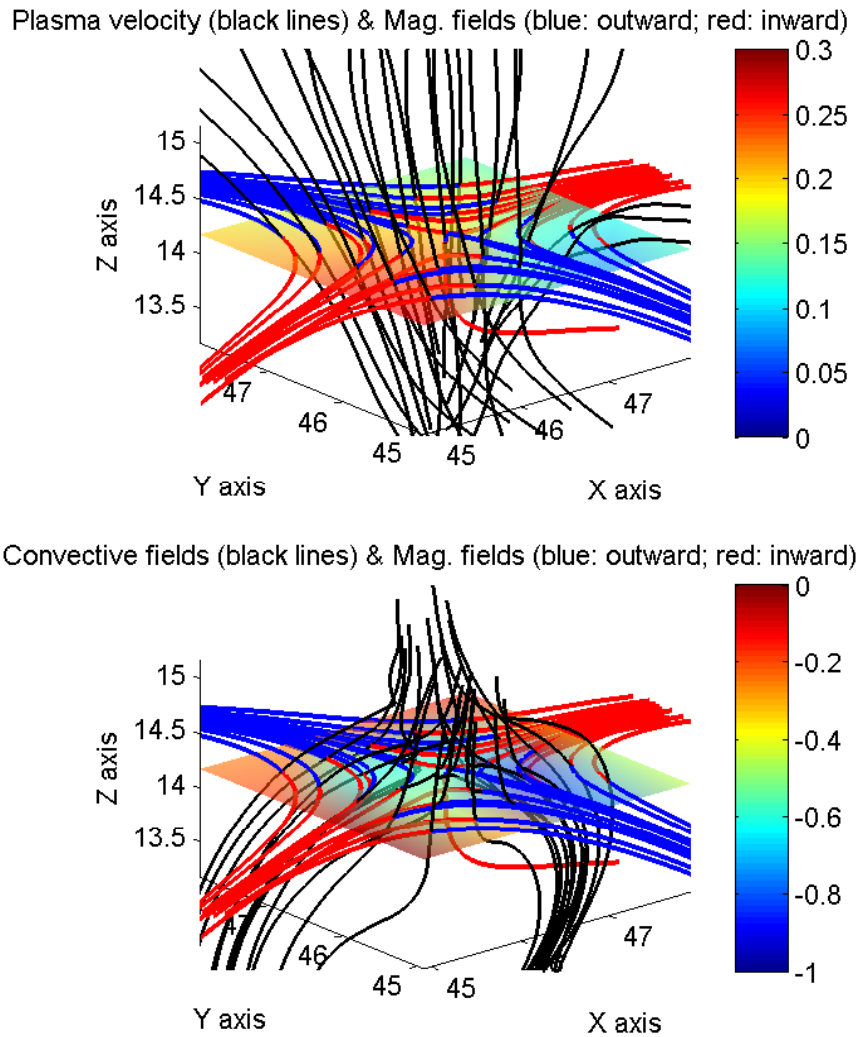


Figure 2.5: Plasma velocity flow lines (top) and the corresponding convective electric fields (bottom) near the null. The red lines represent the magnetic fields coming into the weak field region ( $B < 2$ ), while the blue ones are field lines leaving the region. The black lines indicate the plasma velocity flow lines (top) and convective electric field lines (bottom), with  $u_z < 0$  and  $E_z < 0$ . The horizontal layers cutting through the null show the strength of the normalized plasma velocity  $u$  (top) and the value of  $\lg(E_{con}/E_0)$  (bottom). The color-coding is indicated on the right side.

not show any obvious change. Fig. 2.3 shows the evolved global configuration of the magnetic fields with a magnetic null in the corona. However, convective electric fields arise in the whole box (bottom image in Fig. 2.4) due to the plasma motion across the magnetic field (top image in Fig. 2.4). Since both the magnetic field and plasma flows are stronger in the chromosphere, the convective electric field  $\mathbf{E}_{con} = -\mathbf{u} \times \mathbf{B}$  develops more strongly in the lower part of the box. The convective electric field has an average value of  $4.08 E_0$  in the whole box, and its maximum value is  $3333 E_0$  at  $(50.03, 68.15, 2.10)$  in the chromosphere. Near the null, however, the convective electric field is only  $0.0036 E_0$  (bottom image of Fig. 2.5), because the magnetic field is minimum ( $0.05 B_0$ ) and the plasma bulk velocity is  $0.233 u_0$ . Fig. 2.5 shows the resulting plasma flow lines and the convective electric fields (as black lines) close to the null. It is seen that plasma flows across the null vertically (downwards) and the corresponding convective electric field  $\mathbf{E}_{con}$  is perpendicular to both plasma velocity and magnetic field direction. The value of  $\mathbf{E}_{con}$  is smaller at the center than at the edge of the null due to the vanishing of the magnetic field.

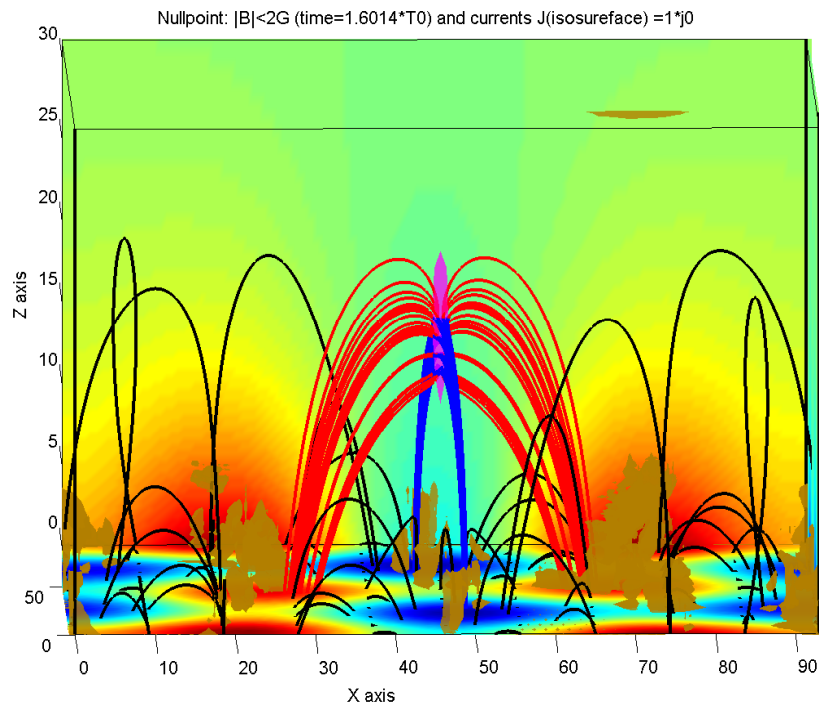
## 2.4 Resistive Electric Fields

The term  $\eta \mathbf{j}$  in Eqs. (2.4) and (2.5) are generally called resistive electric field  $\mathbf{E}_{res}$ . We here diagnose the model of resistivity  $\eta$  and the generated electric currents  $\mathbf{j}$  separately.

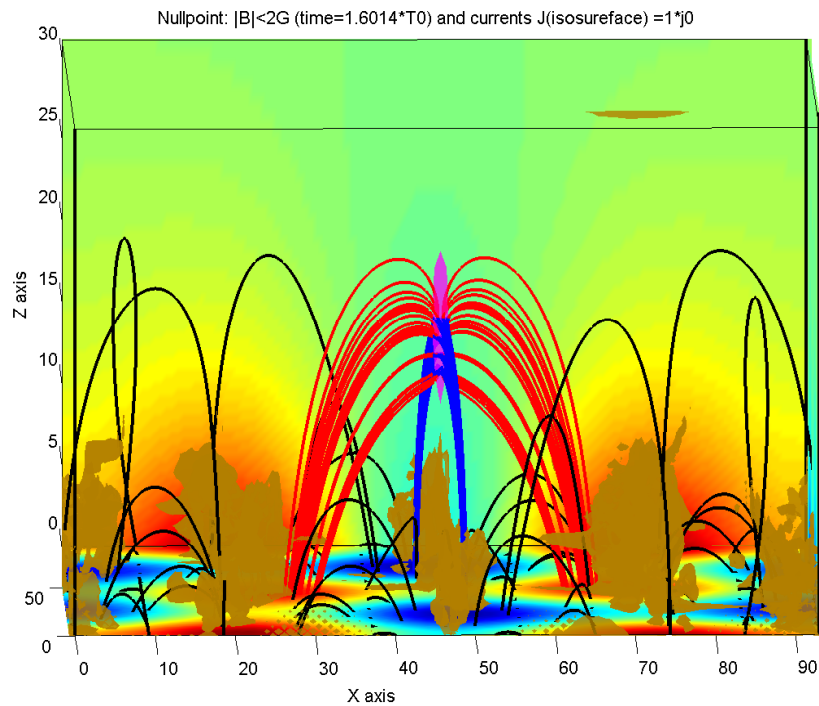
### 2.4.1 Electric currents

The electric currents  $\mathbf{j} = \nabla \times \mathbf{B}$  are expected to develop in regions where the magnetic field strongly changes the connectivity, known as quasi-separatrix layers (Demoulin et al. 1996, Büchner 2006, Santos et al. 2011). The localized places where currents build-up can be induced by photospheric motions often lead to ideal MHD breakdown with strong flows and magnetic energy release. Due to the stronger magnetic field and the stronger coupling between neutral gas (carrying the driving force) and plasma at the lower atmosphere, it is expected that localized electric currents will develop in the chromosphere, transition region and low corona rather than the high corona.

Indeed, the plasma motion driven by the bottom photospheric horizontal vortex give rise to electric currents located mainly below the transition region, over the footpoints of the quadrupolar fields. Fig. 2.6 shows the current densities in both parallel (top) and perpendicular (bottom) (to the direction of magnetic fields) components after 1.6 Alfvén time. The isosurfaces of  $J_{\parallel} = j_0$  and  $J_{\perp} = j_0$  are shown in brown color. Notice that  $j_0 = B_0/\mu_0 L_0$  is about  $1.6 \times 10^{-4} \text{A/m}^2$  in this model. The electric currents perpendicular to the magnetic field is stronger and spatially more extended than the parallel currents. Both of them appear as kernels of current concentrations mainly above the four footpoints. It is also obvious that the currents over the two positive-magnetic footpoints where the neutral gas vortexes were applied (Fig. 2.2) are much stronger than those over the two negative footpoints. However, there are neither parallel nor perpendicular currents generated in the vicinity of the null point area. Santos et al. (2011) also found that the presence of a magnetic null point does not necessarily mean that the strongest currents will form in or around the null.



(a)



(b)

Figure 2.6: (a) Magnetic fields  $\mathbf{B}$  and parallel electric currents  $\mathbf{J}$ . (b) Magnetic fields  $\mathbf{B}$  and perpendicular electric currents  $\mathbf{J}$ . The magenta color shapes where the magnetic field is smaller than 2G and the brown color indicates the isosurface of  $J_{\parallel} = j_0$  in (a) and  $J_{\perp} = j_0$  in (b). The blue lines are the magnetic field lines leaving from the weak field region ( $B < 2$ ), while the red lines are the magnetic field lines coming into the region.

### 2.4.2 Resistivity $\eta$

Notice that throughout the simulation box the resistive electric field  $\eta \mathbf{j}$  is kept very small, because  $\eta$  is chosen so that most of solar corona is considered as ideal plasma. In ideal MHD,  $\eta = 0$  and the resistive term vanishes.

This MHD model, however, introduces anomalous resistivity which is switched on at places where the local current carrier velocity, defined as  $\mathbf{V}_{cc} = \mathbf{j}/ne$ , exceeds the electron thermal speed,  $V_{the}$ , which indicates the onset of a fluid-type electrostatic Buneman instability (Büchner 2007). The switched-on effective resistivity was given by Büchner and Elkina (2006) and reads

$$\eta_{eff} = \frac{0.01 T_e}{\varepsilon_0 \omega_{pe} T_i} \cdot FF \cdot \frac{V_{cc}}{V_{the}}, \quad (2.9)$$

where  $\omega_{pe} = \sqrt{(ne^2/\varepsilon_0 m_e)}$  is the electron plasma frequency,  $\varepsilon_0$  is the vacuum electric permeability, and  $T_i$  and  $T_e$  are the ion and electron temperatures considered to be equal for solar coronal conditions.  $FF$  is a filling factor, which is introduced to bridge the gap between the MHD grid scale ( $\sim 500$  km) and the dissipation scale, which is about the ion skin depth ( $\sim c/\omega_{pi} \sim 7$  m for  $n_p = 10^{15} \text{ m}^{-3}$ ).

The simulated resistive electric field has its maximum value of  $0.08 E_0$  in the transition region at (48.6, 69.6, 4.6). Around the null, no anomalous resistive electric field is switched on by the end of this simulation at  $t = 1.6\tau_A$ . We therefore considered only the perpendicular convective electric field and investigated the acceleration ability of the convective electric field around the 3-D null point in Chapter 3.

## 2.5 Summary of MHD simulations

Electric and Magnetic fields obtained from 3-D MHD simulations with extrapolated magnetic fields as initial conditions can provide us a realistic environment to study particle accelerations in the solar corona.

The initial configuration is set to be a quadrupolar potential field so that the resulting coronal magnetic field contains a null at the center of the simulation box. The plasma conditions (temperature and density) are also chosen to mimic the realistic solar environments: the temperature increases from the photosphere to the corona while the density decreases with height.

The boundary conditions were defined so that the MHD equations remained invariant under transformation of the MHD variables. Two vortices of neutral gas motion are added in the box so that the plasma is dragged behind the neutral gas through collisional interaction. The collision frequency is maximum at the bottom and decreases exponentially with height. Therefore the plasma motion is coupled with the neutral gas in the photosphere and chromosphere, while it is decoupled from the neutral gas motion in the corona.

A magnetic null point is located near the box center. The eigenvalues of the Jacobian matrix at the null are about (2.1, -1.7, -0.3), following the category of a negative null (Section 1.3.1.4). The null point is also globally connected to the bottom of the simulation box by the spine and the fan field lines. The photospheric motions are applied at the fan footpoints and would actually cause magnetic field perturbations that propagate to the corona along the field lines and eventually reach the null.

Driven by photospheric plasma motion, the MHD simulation reveals the coronal plasma motion and the self-consistent electric and magnetic fields. The global configuration and topology of the magnetic fields do not show any obvious change. However, convective electric fields arise due to the plasma motion across the magnetic field. Near the null, however, the convective electric field is only  $0.0036 E_0$  because the magnetic field is minimum ( $0.05 B_0$ ) and the plasma bulk velocity is only  $0.233 u_0$ .

The resistive electric field has its maximum value in the transition region and there is no anomalous resistive electric field switched on around the null by the end of this simulation. Therefore, only convective electric fields are used for the studies of particle acceleration in the following chapter.



# 3 Test Particle Simulations in Convective Electric Fields at an X-Null

*Everything should be made as simple as possible, but not simpler.*

*Albert Einstein*

In this chapter, we study the particle acceleration at the magnetic X-null point in the solar corona as simulated in Chapter 2, considering self-consistent magnetic fields, plasma flows and the corresponding convective electric fields (Guo et al. 2010). We have calculated the electromagnetic fields by 3-D magnetohydrodynamic (MHD) simulations (Chapter 2) and now we expose charged particles to these fields within a full-orbit relativistic test-particle approach. The 3-D magnetic configuration is chosen so that the resulting coronal magnetic field contains a null. Driven by photospheric plasma motion, the MHD simulation reveals the coronal plasma motion and the self-consistent electric and magnetic fields. In a subsequent test particle experiment the particle energies and orbits (determined by the forces exerted by the convective electric field and the magnetic field around the null) are calculated in time.

## 3.1 An Overview of Test Particle Simulations

The basic mechanisms of particle acceleration have been introduced in Section 1.4. In the past decades, a substantial amount of work was carried out to investigate the acceleration of test particles in reconnection electromagnetic fields. Three different approaches were taken to model the magnetic and electric fields:

Early researchers often took an analytical prescription of the 2-D X-type reconnecting magnetic field, imposing a constant and uniform electric field in the third dimension (e.g. Speiser 1965, 1967, Bruhwiler and Zweibel 1992, Mori et al. 1998, Browning and Vekstein 2001, Zharkova and Gordovskyy 2004, Efthymiopoulos et al. 2005, Hannah and Fletcher 2006). The conclusion from these test particle calculations is that with larger electric fields and with additional guiding magnetic fields in the current sheet, particles can be accelerated more efficiently. A longitudinal (guide) magnetic field magnetizes the charged particles and reduces their probability of being ejected from the current sheet so

that particles can gain more energy from the electric field (Litvinenko 1996). A power-law distribution of accelerated particles is usually obtained and used for comparison with observations. Nevertheless, the reconnection process itself, which produces the electric field, is neglected and the magnetic and electric fields are prescribed and independent. Therefore these simulations provide a qualitative analysis of the acceleration rather than quantitative results for particle energies and spectrum.

A further step is to apply analytic reconnection solutions for test particles so as to set up self-consistent electric and magnetic fields. Based on simplified Ohm's law and Ampere's law, the electric fields are calculated from the analytic magnetic fields, plasma velocities and sometimes also from resistivity models (e.g. Sakai 1992, Heerikhuisen et al. 2002, Craig and Litvinenko 2002, Wood and Neukirch 2005, Hamilton et al. 2005, Dalla and Browning 2005, 2008). In these investigations, the reconnection fields are not independent free parameters, but are obtained from MHD solutions. This approach results in a more reliable prediction of the properties of energetic particle populations. For example, Dalla and Browning (e.g. Dalla and Browning 2005, 2008) used an analytical model of magnetic and electric fields for kinematically prescribed ideal plasma flows around a potential 3-D null (Priest and Titov 1996). They studied particle acceleration for spine and fan reconnection. For the same configuration of the magnetic field, different plasma flows correspond to different convection electric fields. In the spine reconnection case, plasma flows in and out through the center of the null, resulting in an azimuthal electric field. An efficient acceleration is obtained assuming that the electric field could be as large as 1 kV/m. In the fan reconnection case, the plasma flow has another azimuthal component and the acceleration is less efficient, because fewer particles can reach the regions of strong electric fields. Note however that the analytic solution of the electric field contains a singularity at the center ( $E \rightarrow \infty$  at  $R = 0$ ), which leads to infinite runaway acceleration. Also, lack of information on the actual scale and magnitude of the reconnecting magnetic field as well as the strength and configuration of the real plasma flows hinders the process of obtaining realistic acceleration energies and spectrum.

A third possible approach is to use the output of self-consistent MHD simulations. Test particles can be traced in the electromagnetic fields obtained e.g. by ideal or resistive MHD numerical simulations (e.g. Schopper et al. 1999, Dmitruk et al. 2003, Turkmani et al. 2006, Liu et al. 2009, Karlicky and Barta 2006). This combination of the test particle method with MHD simulations can provide a semi-realistic and consistent field geometry and strength for the charged particles. Note that because of the coarse resolution of the simulated MHD fields, the magnetic and electric fields have to be interpolated for test particle calculations. Furthermore, a resistivity model has to be carefully used in MHD simulations, as the macroscopic MHD does not consider the microphysical effects that control the resistivity.

As we already discussed in Section 1.4.1.1, the direct way to gain energy without any interference of the perpendicular gyromotion is acceleration by a parallel electric field, because magnetized particles can move freely in the direction parallel to the magnetic field. A simple model as mentioned before is the direct acceleration inside an electric current sheet on which a parallel guiding magnetic field is superposed. Nevertheless, the value of the uniform electric field and the guide magnetic field as well as the width of current sheet are prescribed without sufficient support by observations or simulations. For an electron to be accelerated to 100 keV in a sub-Dreicer electric field, where  $E \approx$

$9 \times 10^{-6}$  V/m, an unrealistically long current sheet of more than  $10^7$  m in length would be needed. To reach the same energy in a super-Dreicer field, the length can be much shorter, i.e.  $10^2$  m, but then the electric field is unrealistically large (up to  $10^3$  V/m) (Aschwanden 2002). A more complicated 3-D model of parallel electric fields can be obtained by resistive MHD simulations. According to Ohm's law, parallel electric fields are balanced as a resistive electric field  $\mathbf{E}_{res} = \eta \mathbf{j}$ . So one would qualitatively expect that a parallel current density  $j_{\parallel}$  and the existence of a diffusion region with a considerable resistivity  $\eta$  would favour direct acceleration. Nevertheless, any quantitative results based on prescribed  $\eta$  are somehow arbitrary, since there is no generic way to parameterize the non-ideal property of the collisionless corona plasma in MHD simulation. For example, test particle acceleration to energies up to 100 GeV (Turkmani et al. 2006) might be a result of using a numerical "hyper-resistivity", which stabilizes the MHD code. Also, the parallel electric fields obtained from kinetic processes are in general confined to regions on the ion inertia scale (Hesse et al. 1999), much smaller than the macroscopic MHD grid scales, which can therefore affect and accelerate only a few particles.

On the other hand it might be possible to accelerate particles in a perpendicular convective electric field (which is much larger than resistive electric fields in big Reynolds-number plasmas) due to drift forces and non-adiabatic motion. The mechanism of this acceleration will be further described in Section 3.2. A null point is supposed to be the most probable location to switch on this convective acceleration. Recent observations (e.g. Aulanier et al. 2000, Fletcher et al. 2001, Des Jardins et al. 2009, Longcope and Parnell 2009) indicate that 3-D null points are likely to be common in solar corona configurations. Unfortunately, there is no direct observation of the magnitude of the magnetic and electric fields around coronal nulls. One can obtain the magnetic field around a 3-D null point in the corona however by extrapolating typical photospheric fields. A parallel electric field is undoubtedly effective for acceleration. Still, its real strength is quite unknown, because in resistive MHD models it is controlled by ad-hoc prescribed or numerical resistivity. In this chapter, we will therefore concentrate on perpendicular electric fields due to convective electric fields (which are determined by convective plasma flows) to explore the acceleration near the 3-D X-null point obtained from Chapter 2.

This chapter is organized as follows. Based on the 3-D null configurations obtained in Chapter 2, we analyze theoretically the process of particle acceleration by convective electric fields due to non-adiabatic and drift motion in the non-uniform magnetic fields near the null (Section 3.2). Thereafter, we calculate the test-particle energy gains and orbits around the null for different electric fields (plasma flows) in Section 3.3.1. We also test different initial distributions of the particles to investigate their acceleration under different initial conditions in Section 3.3.6. We conclude that the convective electric field near the 3-D null point could work as an effective accelerator for protons under realistic assumptions for the field strength and plasma flow velocities. To efficiently accelerate electrons through it appears to be necessary to include parallel electric fields, because electrons are hardly de-magnetized and only shortly drifting in the direction of the convective electric field.

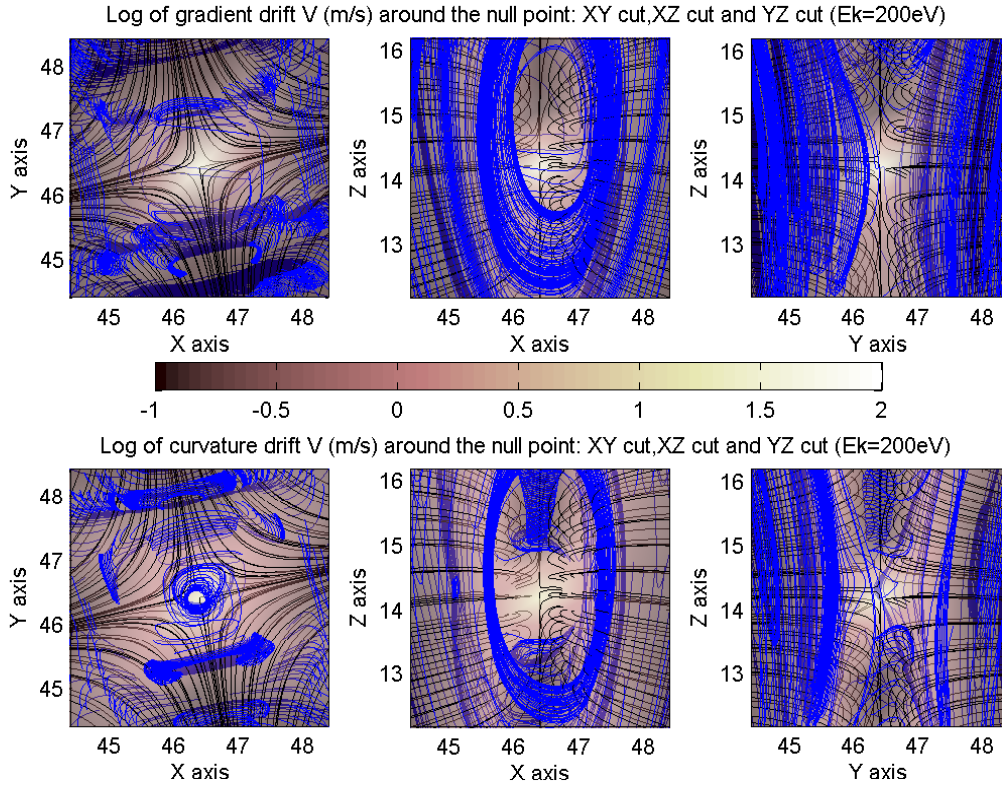


Figure 3.1: Gradient (top) and curvature (bottom) drift lines (blue lines) around the null (magnetic field lines are shown as black lines). The left/middle/right column shows the projection of the flow lines in the  $x - y/x - z/y - z$  2-D plane cutting through the null. The magnitude of the drift velocity in logarithmic-scale is shown in color with a brighter color indicating a higher drift speed.

## 3.2 How can a Perpendicular Convective Electric Field Accelerate Particles?

The basic relativistic equations of motion and energies of an individual charged particle in an electromagnetic field was given as Eqs. (1.19) and (1.20) in Section 1.4.1 in the introduction chapter. Eq. (1.20) indicates that a charged particle can gain or lose kinetic energy in an electromagnetic field only if it has a velocity component in the direction of the electric field. In uniform magnetic fields, however, convective electric fields, which are always perpendicular to magnetic fields, cannot lead to the net-gain of energy. This happens because the magnetized particle keeps gyrating and is accelerated and again decelerated within one gyro-period.

As discussed in Section 1.4.1.2 in the introduction chapter, the possible way to accelerate particles in perpendicular convective electric fields is therefore either to break down their magnetization, or to let them drift in the direction of the electric field due to the gradient and curvature force. De-magnetized particles can be directly accelerated by the electric field. Magnetized particles can only gain energy while undergoing a strong drift motion in the direction of the electric field.

In a non-uniform magnetic field, the magnetic-field gradient force  $\mathbf{F}_{grad} = (mv_{\perp}^2/2B)\nabla\mathbf{B}$

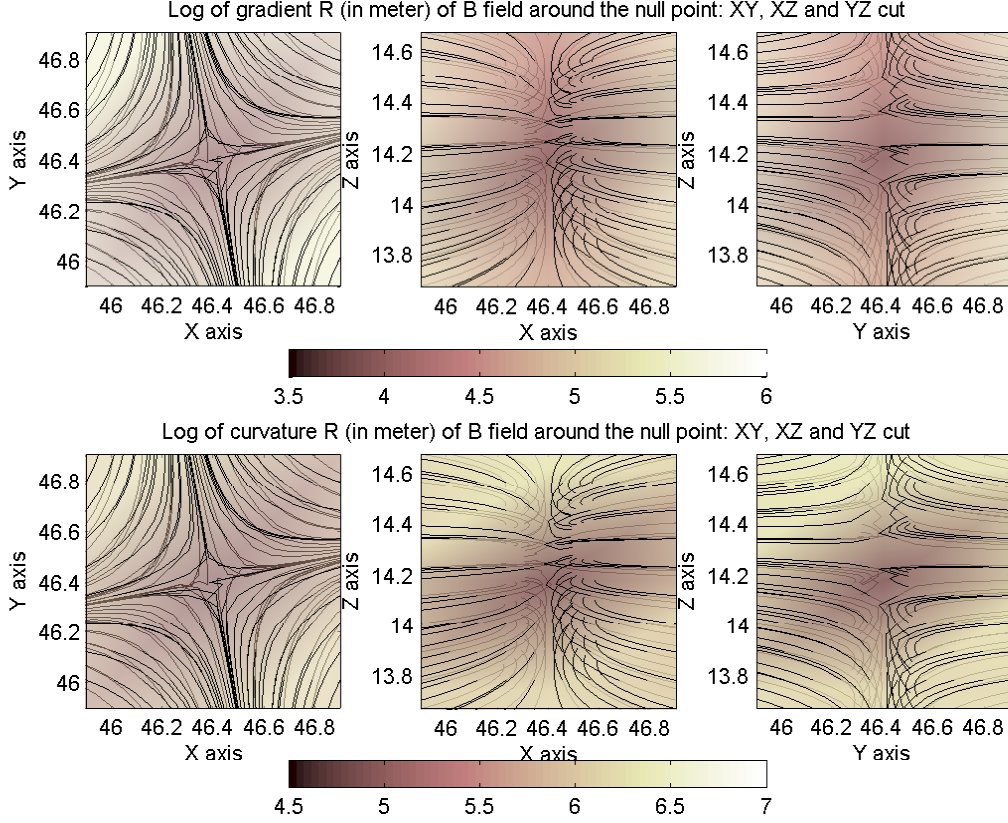


Figure 3.2: Lengths of magnetic gradient scale (top) and curvature scale (bottom) around the null (magnetic fields are shown in black lines). The left / middle / right plot shows the  $x - y/x - z/y - z$  plane cutting through the null. The magnitude of the scale lengths in the logarithmic-scale is color-coded with the darker color indicating a lower value.

and the curvature force  $\mathbf{F}_{curv} = (mv_{\parallel}^2/R^2)\mathbf{R}$  cause a drift motion perpendicular to both the magnetic field and the force direction. If there is a component of the drift velocity in the direction of the electric field, the particles could either gain or lose energy in the electric field according to Eq. (1.20). The gradient drift and the curvature drift velocities are

$$\mathbf{v}_{grad} = \frac{mv_{\perp}^2}{2qB^3}\mathbf{B} \times \nabla B \quad (3.1)$$

$$\mathbf{v}_{curv} = \frac{mv_{\parallel}^2}{qB^2 R_{curv}^2}\mathbf{R}_{curv} \times \mathbf{B} = \frac{mv_{\parallel}^2}{qB^2}\mathbf{B} \times \left(\nabla \frac{\mathbf{B}}{|\mathbf{B}|} \cdot \frac{\mathbf{B}}{|\mathbf{B}|}\right). \quad (3.2)$$

These drift velocities vary inversely proportional to the magnitude of the magnetic field. Therefore particle drifts are maximum where the magnetic field is minimum and the gradients and curvatures are strong. A null point provides a highly probable location for these effects. For  $mv_{\perp}^2/2 = mv_{\parallel}^2/2 = E_k/2$  and  $E_k = 200 \text{ eV} \sim 2.32 \text{ MK}$  we calculated the drift velocities  $\mathbf{v}_{grad}$  and  $\mathbf{v}_{curv}$  for the whole simulation box. We found that their maximum values are attained at the location 46.4, 46.4, 14.2 close to the null, which is 36.9 m/s for  $\mathbf{v}_{grad}$  and 21.6 m/s for  $\mathbf{v}_{curv}$ . The resulting gradient and curvature drift velocities around the null obtained by solving Eqs. (3.1) and (3.2) are shown in Fig. 3.1. These drift velocities are estimated for particles with a thermal energy about 200 eV, which corresponds to

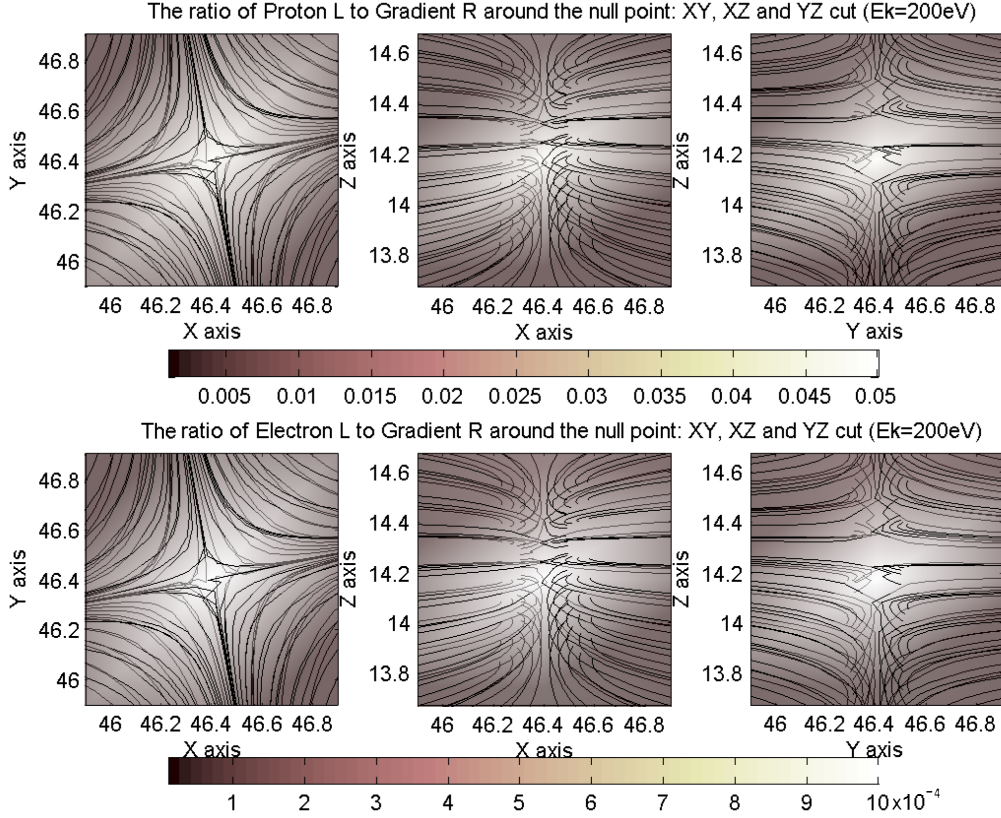


Figure 3.3: Ratios of the Larmor radii to the the magnetic gradient scale lengths for a 200 eV proton (top) and a 200 eV electron (bottom) near the null (magnetic fields are shown in black lines). The left / middle / right column shows  $x - y/x - z/y - z$  2-D cuts through the null. The magnitude of the ratios is shown in gray scale with a brighter color indicating a higher value.

thermal velocities of  $1.95 \times 10^5$  m/s for protons and  $8.37 \times 10^6$  m/s for electrons. Note that the drift velocities are small compared to the particle velocities, as required for the validity of Eqs. (3.1) and (3.2). Thereafter, once particles have been accelerated, their drift velocities will also be heightened, a feedback which favors further acceleration as in a snowball effect.

Moreover, the electric drift  $\mathbf{v}_E = \mathbf{E} \times \mathbf{B}/B^2$  may also cause particle acceleration (e.g, Vekstein and Browning 1997, Northrop 1963). When the particles move away from the null point, the continuous change of the magnetic and electric field will lead to the non-uniformity of the electric drift speed. As a result, particles will not follow the drift stream lines, and the acceleration is associated with the changing electric drift velocity.

In the course of this adiabatic drift-acceleration it may happen that the particle gyration radii ( $L_i = mv/|q|B$ ) become comparable to the scale lengths of the magnetic non-uniformity. In this case particles lose their magnetization and adiabatic state and can be directly accelerated in the perpendicular electric field (e.g. Büchner 1986, Büchner and Zelenyi 1989). A null point should be a prime candidate location for both drift and non-adiabatic acceleration. To verify this hypothesis quantitatively, we calculated the magnetic gradient and curvature scale according to  $R_{grad} = |\mathbf{B}|/|\nabla\mathbf{B}|$  and

$R_{curv} = |\mathbf{B}|^3 / |\mathbf{B} \times (\nabla \mathbf{B} \cdot \mathbf{B})|$ . Figure 3.2 displays the gradient and curvature scale lengths around the null. The average values of  $R_{grad}$  and  $R_{curv}$  around the null (where  $B < 1$ ) are  $0.79 L_0$  and  $5.18 L_0$  respectively. The minimum  $R_{grad}$  and  $R_{curv}$  in the whole MHD-simulation box are located near the null point, which is  $0.0176 L_0$  and  $0.1516 L_0$  i.e.  $8.8 \text{ km}$  and  $76 \text{ km}$ . Notice that the calculation of the gradient and curvature scales is limited by the coarse grid sizes of the MHD box. In coronal fields, one should expect smaller non-uniform scales. On the other hand, the Larmor radius of a gyrating particle ( $\sim v/B$ ) is enlarged near the null by the weak magnetic field. Assuming a typical coronal particle energy of  $200 \text{ eV}$ , one obtains  $L_p$  about  $20 \text{ m}$  and  $L_e$  about  $0.5 \text{ m}$  for  $B = 1 \text{ G}$ . At the location where  $B = 0.0484 \text{ G}$ , the Larmor radii of protons and electrons are  $L_p = 420 \text{ m}$  and  $L_e = 10 \text{ m}$  respectively. The resulting ratios of the Larmor radii to the magnetic gradient scale lengths of both a  $200 \text{ eV}$  proton (top) and a  $200 \text{ eV}$  electron (bottom) are shown in Fig. 3.3. As one can see in the figure, near the null point Larmor radii and magnetic gradient scales are comparable for protons, while for electrons this ratio is much smaller. Therefore we can expect that protons will undergo stronger drifts and are more likely to be non-adiabatically accelerated than electrons. Note that once particle energies are increased, the Larmor radii will also be enlarged and the chance of de-magnetization and consequent direct acceleration will be significantly enhanced. To investigate how particles become accelerated near the null, we used a test-particle approach which we describe in next section.

### 3.3 Simulation of Particle Accelerations near the 3-D X-null

We assumed that the accelerated particles exert negligible feedback forces on the background coronal electromagnetic fields. Hence we could use a full-orbit relativistic test particle approach, in which the protons or electrons individually explore in the prescribed electromagnetic field as described and calculated in Chapter 2. We took a fixed snapshot of the macroscopic fields and froze them during the evaluation of the particle trajectories.

We calculated the particle motion by numerically solving the relativistic momentum equation (1.19). In order to find out whether in ideal MHD the convective electric field as theoretically described in Section 3.2 around the null is able to accelerate particles, we considered only the perpendicular convective electric field and neglected any parallel electric field. Of course, to obtain the field values at the particle position, one has to interpolate between the much more distant grid points of the MHD simulation. We used the eight neighbouring grid points nearest to a particle's position and applied a 3-D linear interpolation scheme to get the magnetic field and plasma velocities, which allowed us to determine the local convective electric field at the actual particle position. With a Runge-Kutta-Fehlberg fourth-fifth-order method with an adaptive time step (Fehlberg 1969), we integrated the positions and velocities of both protons and electrons in time.

We focused on the mechanism and process of particle acceleration by the null point, i.e. the highest energy a proton or electron could most probably gain from the convective electric field. The final acceleration spectrum, which depends on the initial spatial and velocity distributions, is not taken into account. Hence the initial launch point of particles

Table 3.1: Calculation of particle kinetic energies (in keV) under different electric fields

Case	Acc. time	Min $E_k$	Aver $E_k$	Max $E_k$
1: protons	0.27 s	0.2	0.22	0.25
1: electrons	0.007 s	0.2	0.2005	0.201
2: protons	0.23 s	0.17	0.53	0.95
2: electrons	0.007 s	0.2	0.206	0.211
3: protons	0.1 s	7.43	19.21	30.02
3: electrons	0.006 s	0.2	0.26	0.32
4: protons	0.028 s	1779.9	2083.6	2272.0
4: electrons	0.004 s	0.16	1.34	2.73

was taken to be the point with the minimum magnetic field, where the particles are most likely to be accelerated. The initial velocities were shell-distributed: all the particles shared the same speed, but started in random directions. For the initial speed we first took the speed for particles with a kinetic energy of 200 eV (corresponding to the most probable speed at a temperature of 2.32 MK), which yields  $8.37 \times 10^6$  m/s for electrons and  $1.95 \times 10^5$  m/s for protons. In Section 3.3.6, we also investigate the influence of higher initial energies on the acceleration process.

### 3.3.1 Particle Acceleration under Different Plasma Flow Conditions

Since there is no direct observation of the magnitude of coronal convection and corresponding electric fields, we derived these quantities by the MHD simulation. The MHD equations were solved for dimensionless quantities so that we could rescale the dimensional values of the convection plasma flow  $\mathbf{u}_{con} = u_0 \mathbf{u}'$  and the electric field  $\mathbf{E}_{con} = E_0 \mathbf{E}' = u_0 B_0 \mathbf{E}'$  by changing the normalization value  $u_0$ . The rescaling was not applied to  $B_0$  so that the magnetic field strength was unaltered in the vicinity of the magnetic null point. Rescaling the plasma flow velocity corresponds to a change of the magnitude of the driving motions in the photosphere (at the bottom of the simulation box).

Table 3.1 shows the energies acquired by a certain number of particles (1000 particles in each case) with the initial energy  $V_{initial} = 200$  eV and the location  $X_{initial} = (46.4, 46.4, 14.2)$  for different magnitudes of the plasma flow velocities and their corresponding different coronal convective electric fields. "Acc.time" represents the acceleration time which was defined so that the minimum energy (Min  $E_k$ ), average energy (Aver  $E_k$ ) and maximum energy (Max  $E_k$ ) of a group of particles (1000 particles in each case) did not show any obvious changes after this initial acceleration phase. The average plasma flow velocities imposed at the bottom,  $\bar{u}_{z=0}$ , increased from Case 1 to Case 4, being 0.69, 6.9, 69, and 690 km/s respectively. The plasma flow velocities at the reference null,  $u_{null}$ , are 11.64, 116.4, 1164, and 11640 km/s from Case 1 to 4. The corresponding convection electric fields  $E_{null}$  are enhanced from Case 1 to 4: being 0.0181, 0.181, 1.81, and 18.1 V/m respectively.  $\bar{u}_{B<2}$  (being 7.52, 75.2, 752, 7520 km/s from Case 1 to 4) and  $\bar{E}_{B<2}$  (being 1.15, 11.5, 115, 1150 V/m from Case 1 to 4) are the average plasma velocities and convective electric fields around the null area ( $B < 2$  G).

One thousand protons were launched near the null for each case of plasma conditions. In Case 1, the plasma flow (convection) velocity at the reference null point was 11.64 km/s and the average plasma velocity inside the area where  $B < 2$  G was 7.52 km/s. The corresponding convective electric fields were 0.0181 V/m at the point and 1.15 V/m on average. After 0.27 s of motion in the electromagnetic fields, the protons' energies were only slightly enhanced. In Case 2, with stronger driving at the bottom, both the plasma velocity and electric field were ten times higher and more extended than in Case 1. Protons were moderately accelerated within 0.23 s, and the maximum energy nearly reached a value of 1 keV. In Case 3, the bottom driving plasma velocity was on average 70 km/s and the plasma velocity at the reference null point was 1164 km/s, a number that is reasonable for the magnetically active coronal environment. Correspondingly, the convective electric field was 1.81 V/m at the grid. It is shown that protons are efficiently accelerated up to 30 keV within 0.1 s. Case 4 corresponds to the situation of very strong driving (driving velocity being 700 km/s on average), which can be assumed for a powerful flare explosion. The resulting convective electric field was 18.1 V/m at the reference null point and 1150 V/m on average inside the area ( $B < 2$  G). This situation allowed a proton to be accelerated to an energy of more than 2 MeV.

For electrons, however, no acceleration was achieved in Case 1 and Case 2. In Case 3, i.e. in active regions, their kinetic energy was slightly enhanced to 300 eV. Case 4 shows that electrons near coronal nulls of explosive flare conditions may be accelerated to energies close to 3 keV. Electron acceleration by a perpendicular convective electric field is less efficient, because their Larmor radii are much smaller than the non-uniformity scale of the magnetic field (bottom images in Fig. 3.3), and therefore it is very difficult to de-magnetize electrons. Their efficient acceleration may require a parallel electric field, which can accelerate particles adiabatically along the magnetic field lines (Litvinenko 1996). However, the inclusion of parallel electric fields necessitates to consider kinetic processes that enable their formation and determine their spatial scale.

### 3.3.2 Single Proton Orbit Study for Case 3

In order to understand acceleration near the null, we considered the evolution of orbits, kinetic energies, pitch angles and Larmor radii for a single proton in Case 3 (active region).

Figure 3.4 shows a typical proton orbit during the first 0.1 s of acceleration. The spatial distance between two neighboring asterisks, marking 0.02 s time intervals, is increasing. This indicates that the proton is moving faster and faster. The gray scale shows the magnitude of the magnetic field, which increases away from the null. Figure 3.5 shows the evolution of the particle's kinetic energy, the velocity-magnetic field (V-B) pitch angle, the velocity-electric field (V-E) angle, the strength of magnetic and electric fields, and the logarithmic value of curvature scale, gradient scale, Larmor radius and the ratio of Larmor radius to gradient scale. The red high lighted region in the top image indicates the interval of major acceleration, during which the kinetic energy is increasing and the V-E angle for several gyro-periods remains smaller than 90 degrees. This means that the proton is de-magnetized and moves non-adiabatically in the direction of the electric field. The proton is therefore efficiently accelerated during this process. The gray high-lighted region, on the other hand, corresponds to an example of a deceleration moment due to the

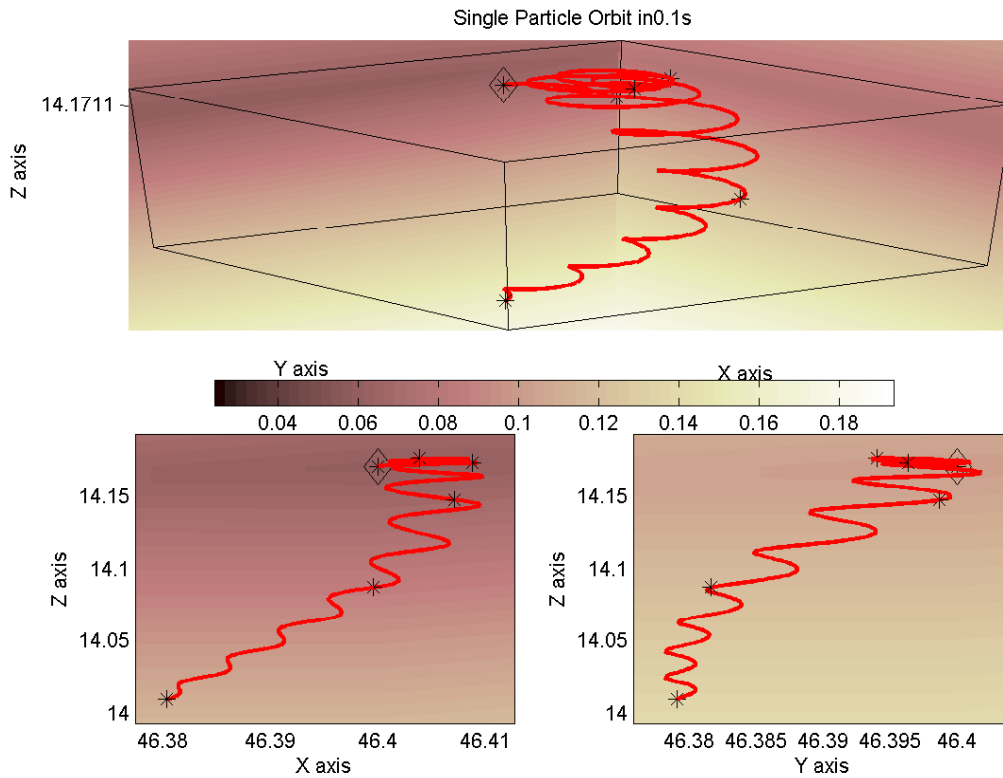


Figure 3.4: Orbit of a single proton during 0.1 s of acceleration (Case 3, active region). Top image: 3-D view of the orbit. Bottom images:  $x - z$  (left) and  $y - z$  (right) projection views. The square-asterisk dotted shows the starting point of the particle, while other asterisks show the locations after each time step of 0.02 s. The gray scale represents the strength of the magnetic field, which increases while the particle moves out of the null.

gyro-motion. The V-E angle stays wider than 90 degrees, meaning that the proton moves against the direction of the electric field.

During the initial 0.07 s, the average Larmor radius (red line in bottom image of Fig. 3.5) was about 2 km, and the proton underwent strong drifts with a transition to non-adiabatic motion (from 0.04 s to 0.06 s) after initial acceleration. As the proton was moving away from the null, the magnetic field increased (middle image in Fig. 3.5) and the particle started to be magnetized with a regular gyration and smaller gyro-radii. The bottom panel of Fig. 3.5 shows that both curvature and gradient scale lengths were increasing, while the Larmor radius decreased because the proton moved towards the stronger magnetic field. When the ratio of Larmor radius to gradient scale dropped below  $10^{-1}$  and the main acceleration phase was finished, the proton became re-magnetized. Notice that magnetic fields from a MHD simulation would significantly smooth small scale non-uniform structures, a process which is very important for demagnetization. This non-adiabatic acceleration process would be more effective if microscopic turbulence of the magnetic field were considered.

Figure 3.6 separately shows the parallel and perpendicular components of both the kinetic energy and velocity of the particle. There are three different phases of acceleration: (a) perpendicular acceleration due to (mostly gradient) drift within the first 0.04 s, (b)

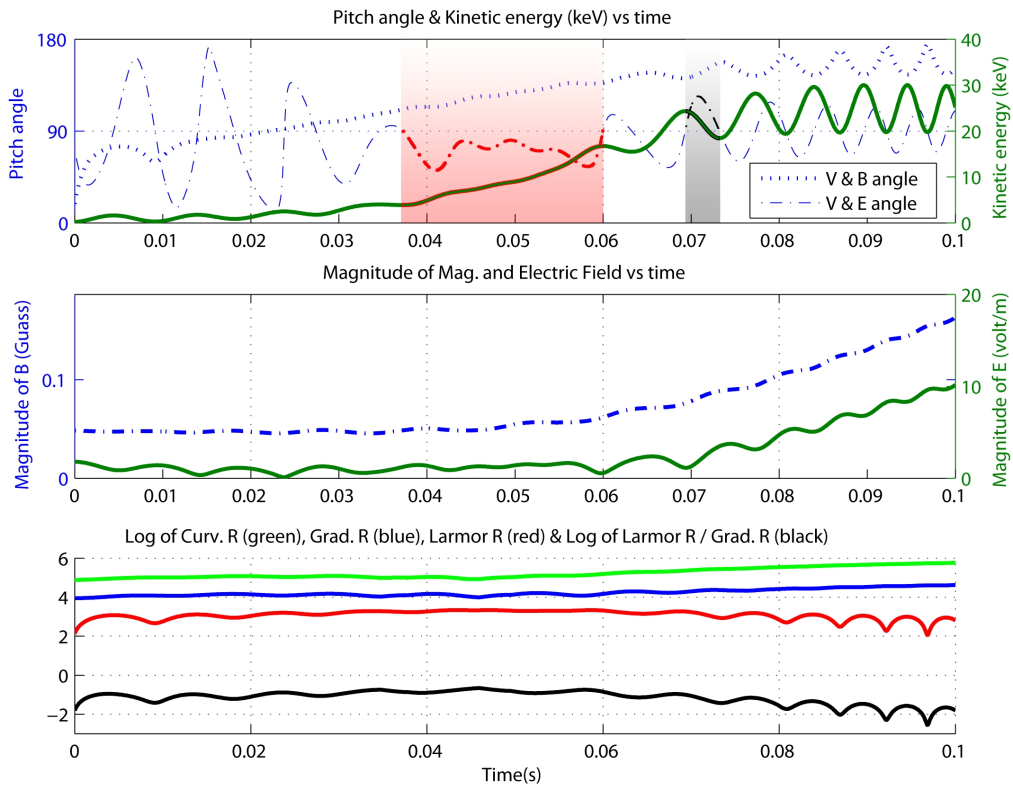


Figure 3.5: Acceleration of a single proton during 0.1 s (Case 3, active region). Top panel: the green solid line shows the energy-gain; the blue dotted and dashdotted lines represent the angle of the proton velocity with respect to the magnetic and electric field. The red/gray high lighted regions give examples of the acceleration/deceleration process, whereby the energy increases/decreases and the angle between velocity and electric field is narrower/wider than 90 degrees. The middle image shows the local magnitude of the magnetic field (G) and electric field (V/m) on the way of the proton orbit. The bottom image shows the logarithmic value of the curvature scale, gradient scale, Larmor radius and the ratio of the Larmor radius to the gradient scale. All length values are in meters.

parallel acceleration due to non-adiabatic motion from 0.04 s to 0.06 s, and (c) parallel acceleration due to (mainly curvature) drift from 0.06 s to 0.08 s. We show in Fig. 3.6 that the parallel kinetic energy stayed relatively small during the initial 0.04 s, and only the perpendicular energy was enhanced from less than 0.2 keV to about 5 keV. This is because the convection electric field is perpendicular to the magnetic field, and thus the perpendicular energy can easily be enhanced. The gradient drift velocity (Eq. 3.1) was hence enlarged and helped the drift acceleration as a feedback. This initial acceleration prepared the particles for the subsequent non-adiabatic acceleration phase.

From 0.04 s to 0.06 s, the proton did not complete full gyrations (de-magnetized) and therefore could be continuously accelerated in the electric field (also shown by the small V-E angle in Fig. 3.5). The perpendicular energy almost stopped growing, while the parallel energy increased a lot (up to 9 keV at 0.06 s). This non-adiabatic process transferred the perpendicular energy immediately into parallel energy. When the proton was re-magnetized at 0.06 s, this high parallel energy enhanced the curvature drift (Eq. 3.2),

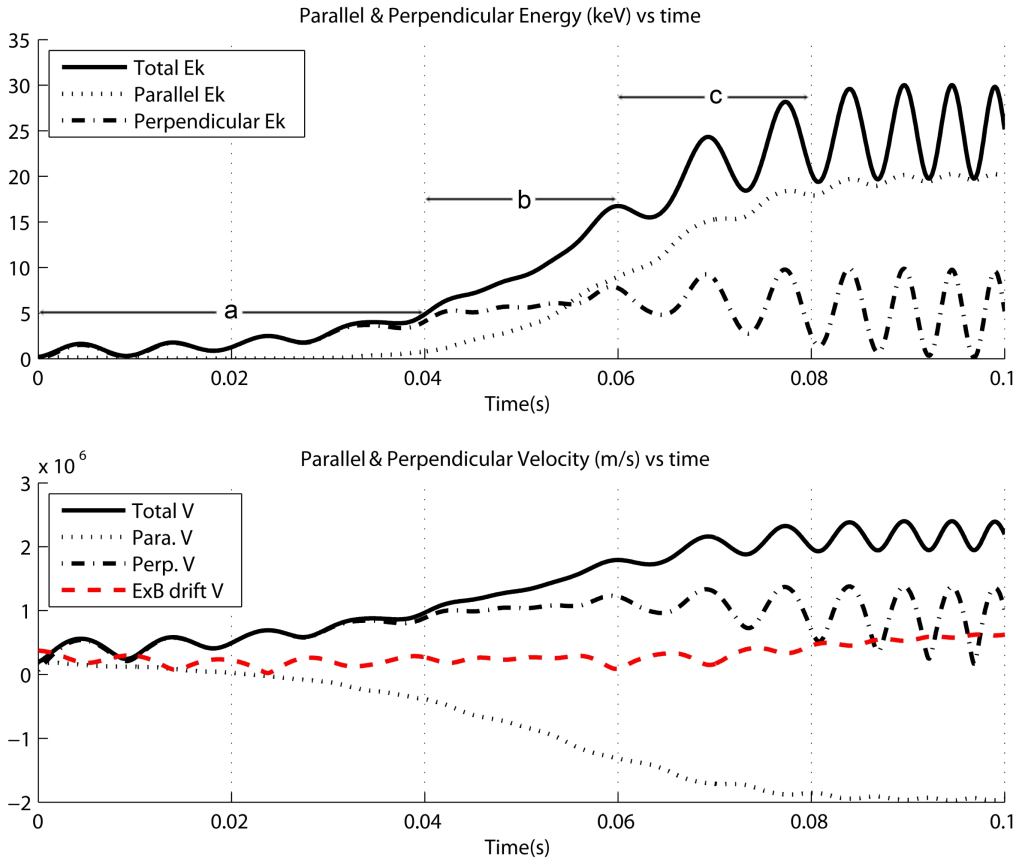


Figure 3.6: Kinetic energy (top) and velocity (bottom) evolutions in both parallel (dotted lines) and perpendicular (dash-dotted lines) directions of a single proton during 0.1 s are shown under Case 3 conditions. Solid lines are showing the total kinetic energy (top) and velocity (bottom). Also the electric drift velocity is shown in dashed line (bottom).

causing further acceleration in the parallel direction (from 9 keV at 0.06 s to 18 keV at 0.08 s), until the proton stopped its perpendicular drift at 0.08 s. The parallel energy stayed around 20 keV, and the perpendicular energy oscillated around 5 keV. Hence the total energy was about 25 keV.

After 0.08 s, the proton pitch (V-B) angle was approaching 180 degrees (see the top panel of Fig. 3.5). This indicates that the proton could escape along (albeit against the direction of) the magnetic field downward to the photosphere. The V-E angle stayed around 90 degrees in the end. Hence the acceleration was finished. The final particle velocity was the sum of three types of motion: parallel velocity, perpendicular drift velocity and perpendicular gyration velocity. The last part was apparent as an oscillation (especially after 0.07 s when the proton is magnetized) of the perpendicular velocity and energy (Fig. 3.6) as well as of the V-B and V-E angle (top panel of Fig. 3.5). After averaging it over the gyration period, the remaining perpendicular velocity is the drift velocity, which is mostly due to the  $\mathbf{E} \times \mathbf{B}$  drift ( $E_{\perp}/B = E/B$ ) in the end. As one can see in the bottom frame of Fig. 3.6, the electric drift velocity (dashed line) approached the average of the perpendicular velocity (dash-dotted line) after 0.08 s and about 600 km/s at 0.1 s. This electric drift velocity is consistent with the perpendicular component of the plasma velocity as

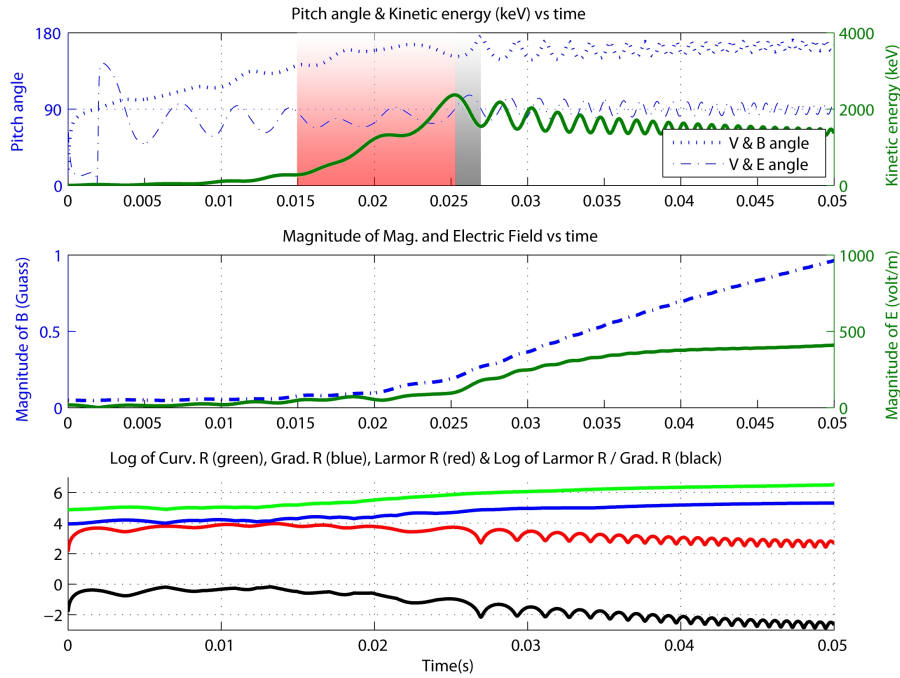


Figure 3.7: Energy evolution of a single proton during 0.05 s under Case 4 conditions. In the top image, the green solid line shows the energy-gaining process. The blue dotted and dash-dotted lines show the V-B angle and V-E angle. The red/gray high-lighted regions give examples of the acceleration/deceleration process, whereby the energy is increasing/decreasing and the V-E angle is narrower/wider than 90 degrees. The middle image shows the local magnitude of the magnetic field (G) and electric field (V/m) on the way of the proton orbit. The bottom image shows the logarithmic value of the curvature scale, gradient scale, Larmor radius and the ratio of the Larmor radius to the gradient scale. All length values are in meters.

obtained from the MHD simulation i.e.  $\mathbf{E}_{con} = -\mathbf{u} \times \mathbf{B}$ .

### 3.3.3 Single Proton Orbit Study for Case 4

In order to understand how protons could be accelerated up to 2 MeV during flares (Case 4 conditions - strong convection which could only happen during big flare explosions), we again study the acceleration process of a typical single proton. Figure 3.7 shows the evolutions of the V-B and V-E angle, local magnetic and electric field strength, gradient and curvature scale and Larmor radius. As in Case 3, the red high-lighted region in the top image indicates the main non-adiabatic acceleration phase, during which the proton is continuously accelerated. The gray high lighted region indicates an example of deceleration phase due to gyro-rotation. Figure 3.8 represents the evolutions of the parallel and perpendicular energies and velocities separately.

It is clear that the acceleration process is much more efficient than that of Case 3, because the electric field is much stronger and the proton is less magnetized. The Larmor radius of the proton during the first 0.02 s (about 6 km) is very close to the gradient scale (about 10 km), as one can see at the bottom panel of Fig. 3.7. As in Case 3, Fig. 3.8

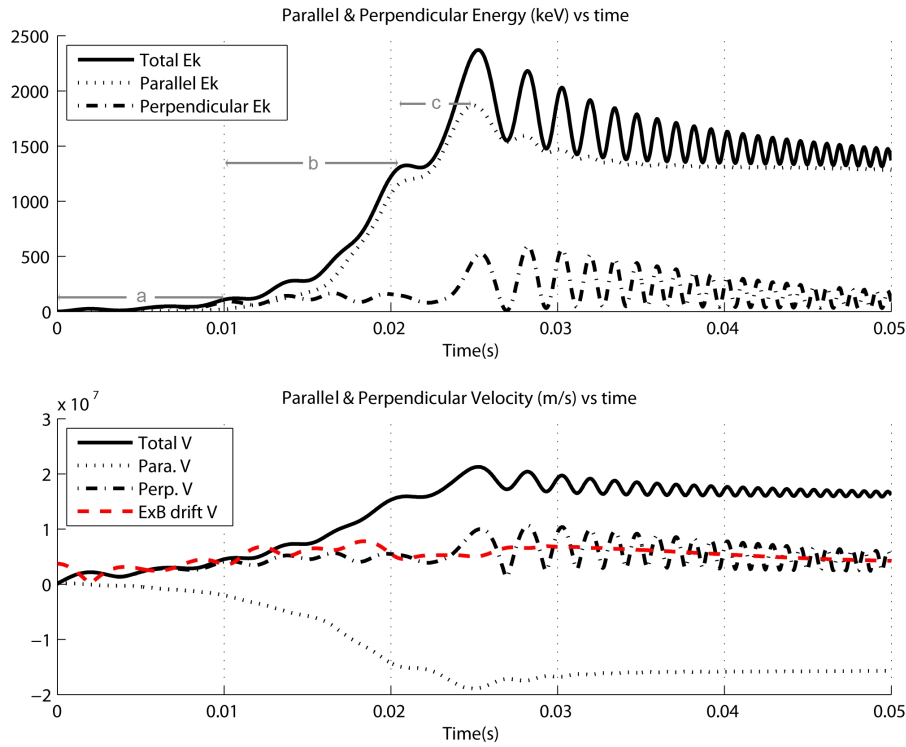


Figure 3.8: Under Case 4 conditions, the evolutions during 0.05 s of the kinetic energy (top) and velocity (bottom) in both parallel (dotted lines) and perpendicular (dash-dotted lines) directions of a single proton are shown. Solid lines represent the total kinetic energy (top) and magnitude of velocity (bottom). Also the electric drift velocity is shown as a dashed line (bottom).

shows that there are also three different phases of acceleration in Case 4: (a) perpendicular acceleration within the first 0.01 s, during which mainly the perpendicular energy is enhanced (from less than 200 eV to nearly 100 keV at 0.01 s), (b) parallel acceleration due to non-adiabatic motion from 0.01 s to 0.021 s, whereby the parallel energy increases dramatically (from about 20 keV at 0.01 s to 1200 keV at 0.021 s), (c) parallel acceleration due to (mainly curvature) drift from 0.021 s to 0.025 s, whereby the parallel energy keeps increasing albeit at a lower speed (to about 1850 keV at 0.025 s) when the proton is re-magnetized. The parallel energy is then slightly decreased after 0.025 s though, because the magnetic field increases while the proton moves out from the null (see middle panel of Fig. 3.7), and the parallel energy is transferred to perpendicular energy by the magnetic-mirror effect. Finally (at 0.05 s), the parallel energy reaches 1.3 MeV (see the dotted line in the top panel of Fig. 3.8). The perpendicular energy, which includes mainly the electric drift (see the red dashed line in the bottom panel of Fig. 3.8) is oscillating (due to the gyration) around 100 keV. The final high parallel velocity (i.e. small pitch angle:  $V_{\parallel}$ - $B$  is close to 180 degrees) lets the proton escape from the null along the field lines.

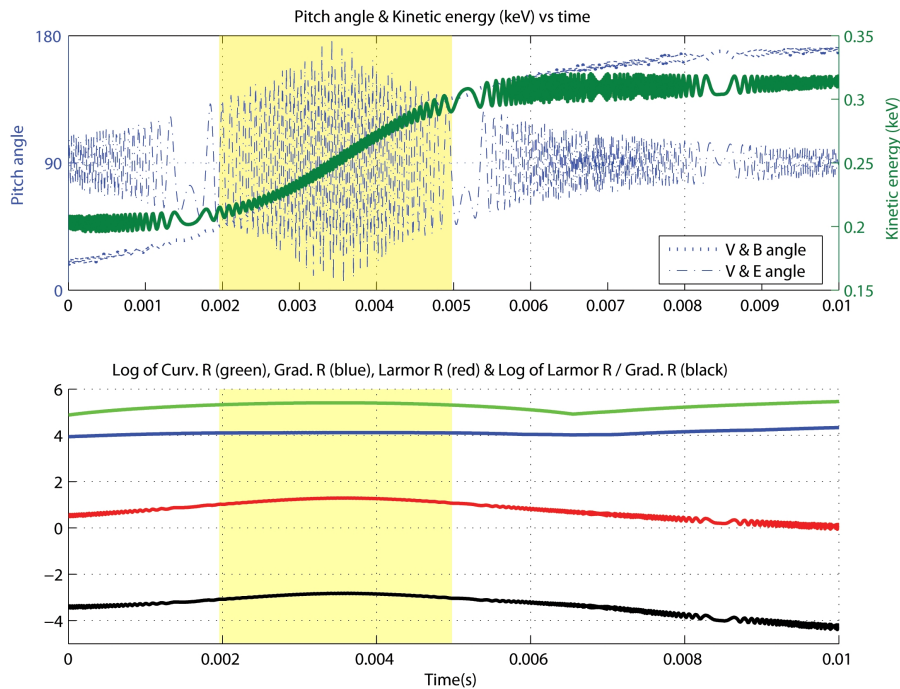


Figure 3.9: Top panel shows the evolution of the kinetic energy and the pitch angles for a typical electron accelerated in active corona (Case 3 condition). The green thick line shows the kinetic energy and the blue dotted and dash-dotted lines represent the V-B and V-E angles respectively. The bottom panel shows the logarithmic value of curvature and gradient scales, electron Larmor radii and the ratio of Larmor radii to gradient scales. All lengths are given in meters.

### 3.3.4 Single Electron Orbit Study for Case 3

Similar to the single proton acceleration, we also investigated a single electron orbit (Fig. 3.9 and Fig. 3.10) for Case 3 (active region) conditions. We found that the electrons were not significantly accelerated. Their kinetic energies were only slightly enhanced due to drifts. Within about 0.006 s, the electron kinetic energy increased from 200 eV to just a little more than 300 eV. During the main acceleration (yellow highlighted region in the figure), the ratio of the Larmor radius to the gradient scale was about  $10^{-3}$  (bottom panel of Fig. 3.9), and the V-E pitch angle indicated a strong parallel (particle velocity parallel to the electric field) component (top panel of Fig. 3.9).

However, the electron did not have a non-adiabatic phase of acceleration due to its much smaller Larmor radius ( $\sim 10$  m) and much shorter gyro-period ( $\sim 10^{-7}$  s). Another reason for the absence of de-magnetization process could be that MHD simulation drops the information of small scale non-uniformity of magnetic fields. The electrons considered here do not have an awareness of the obvious change of the magnetic structure within several gyration periods. In the real solar corona we expect them to have a higher probability to experience non-adiabatic processes and thus to become accelerated.

Note that the electron shown in Fig. 3.10 initially carries mainly parallel energy. During the first 0.0035 s, the perpendicular energy was increasing while the parallel energy decreased. At about 0.0035 s, the parallel velocity changed its sign from parallel to anti-

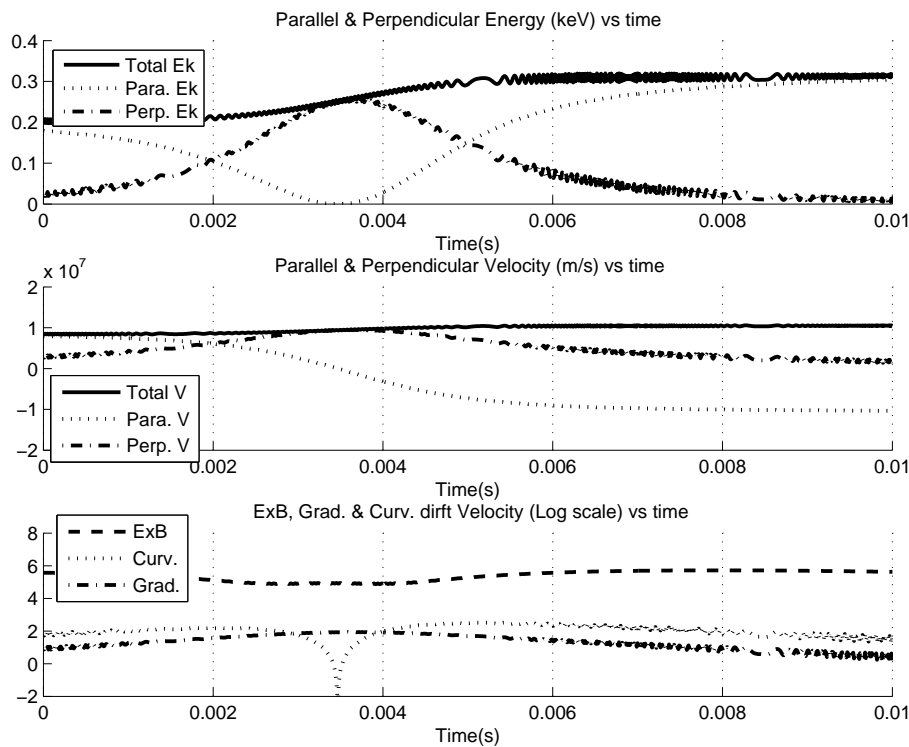


Figure 3.10: In active regions (Case 3), the kinetic energy (top panel) and velocity (middle panel) evolutions in both parallel (dotted lines) and perpendicular (dash-dotted lines) directions of a single electron are shown. Solid lines represent the total kinetic energy (top panel) and velocity (middle panel). In the bottom panel, the electric drift velocity is shown as a dashed line and the gradient and curvature drift velocities are indicated as dotted and dash-dotted lines.

parallel and the curvature drift velocity reached zero according to Eq. 3.2 when  $v_{\parallel} = 0$ . The bottom panel in Fig. 3.10 displays the velocities in logarithmic scale so that the zero value of the curvature drift velocity cannot be shown. Till 0.008 s, the parallel energy grew back while the perpendicular energy decreased. This is similar to a magnetic-mirror effect, which means that when a particle moves into a stronger magnetic field, its parallel energy is transferred to its perpendicular energy until the parallel velocity reaches zero. Then the parallel velocity changes its sign, indicating that the electron is reflected and comes back towards the weaker magnetic field, so that the perpendicular energy starts being transferred to parallel energy. However, the magnetic moment ( $Ek_{\perp}/B$ ) is not conserved during this process, because our 3-D numerical magnetic field is very complex and the electric field is included. A particle experiences not only gradient and curvature drift, but also electric drift. These drift motions change the gyro-center orbit along which the electric field could change the kinetic energy as well as the magnetic moment.

### 3.3.5 Single Electron orbit Study for Case 4

Finally, electron acceleration in flares (Case 4) is shown in Fig. 3.11. There are mainly two phases of acceleration: perpendicular acceleration due to drift until  $2 \times 10^{-3}$ s and

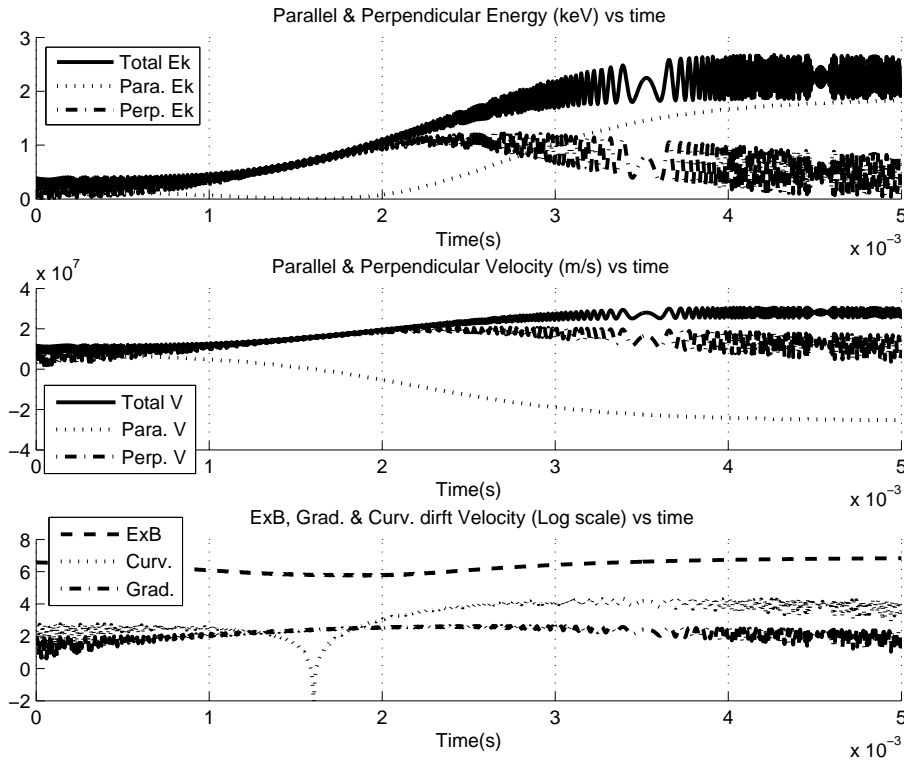


Figure 3.11: In solar flares (Case 4), the kinetic energy (top panel) and velocity (middle panel) evolutions in both parallel (dotted lines) and perpendicular (dash-dotted lines) directions of a typical electron are shown. Solid lines represent the total kinetic energy (top panel) and velocity (middle panel). In the bottom panel, the electric drift velocity is shown as a dashed line and the gradient and curvature drift velocities are indicated as dotted and dash-dotted lines.

parallel acceleration also due to drift till to  $4 \times 10^{-3}$ s. Because of the small electron Larmor radii and the absence of microscopic magnetic structures, there is no phase of non-adiabatic acceleration during which the electron is de-magnetized and continuously accelerated. Nevertheless, a net gain of energy due to the drift motion enhanced the total electron energy from 0.2 keV to more than 2 keV. The final high parallel velocity causes the electron to escape from the null.

### 3.3.6 Influence of the Initial Energy

We also investigated the influence of the initial particle energy on the acceleration process. Higher initial energies with larger  $v_{\perp}$  and  $v_{\parallel}$  reveal higher drift velocities (see Eqs. (3.1) and (3.2)) as well as larger Larmor radii. Hence particles can become more easily de-magnetized (Table 3.2). With the assumption that particles have already been pre-accelerated, we checked the possibility of a secondary acceleration by the null under the plasma flow conditions given in Case 3 (typical for active regions:  $\bar{U}_{z=0} = 69$  km/s,  $U_{null} = 1164$  km/s,  $\bar{U}_{B<2} = 752$  km/s,  $E_{null} = 1.81$  V/m and  $\bar{E}_{B<2} = 115$  V/m.).

Table 3.3 summarizes the changes in kinetic energy for both protons and electrons and for different initial speeds. As one can see, for higher initial energies the final max-

Table 3.2: Gradient and curvature drift velocities (in m/s), gradient and curvature scales (in m) and Larmor radii (in m) of both protons and electrons at the reference null.

At the null	$V_{grad}$	$V_{curv}$	$R_{grad}$	$R_{curv}$	$R_{Larmor}$
200 eV proton	36.9	21.6	8778	75807	422.34
200 eV electron	-	-	-	-	9.85
2 keV proton	369	216	-	-	1335.6
2 keV electron	-	-	-	-	31.2
10 keV proton	1850	1080	-	-	2986.4
10 keV electron	-	-	-	-	69.7

Table 3.3: Calculations of particle kinetic energies (in keV) under different  $V_{initial}$  ( $V_i$ ) conditions.

	Acc. time	Min $E_k$	Aver $E_k$	Max $E_k$
$V_i = 200$ eV				
$10^3$ protons	0.1 s	7.43	19.21	30.02
$10^3$ electrons	0.006 s	0.198	0.258	0.323
$V_i = 2$ keV				
$10^3$ protons	0.056 s	1.26	19.85	44.24
$10^3$ electrons	0.0024 s	1.99	2.17	2.36
$V_i = 10$ keV				
$10^3$ protons	0.032 s	8.49	27.66	63.37
$10^3$ electrons	0.001 s	9.89	10.28	10.68

imum kinetic energy is enhanced due to higher drift velocities and the acceleration time is shorter. However, we notice that protons can even be decelerated (shown as Min  $E_k$ ) for higher initial energies. This is because these protons have an initial velocity direction opposite to the electric field, and the high initial energy pushes them far along this direction so that they may lose kinetic energy according to Eq. (1.20). With higher initial energies, most protons have a chance to be accelerated more strongly, while a few become decelerated.

For electrons, on the other hand, an enhanced initial kinetic energy does neither demagnetize them nor switch on more efficient non-adiabatic acceleration, because the initial electron Larmor radii are only slightly enhanced from  $\sim 10$  m to  $\sim 70$  m (Table 3.2). These larger radii are still too small compared to the magnetic non-uniformity scale, which is obtained by macroscopic MHD simulations. Therefore secondary acceleration of electrons by convection electric fields cannot be expected at least in active regions (Case 3).

## 3.4 Discussions and Conclusions

Using numerical MHD simulations, we investigated the 3-D field structure and plasma flows around a coronal magnetic null point (Chapter 2). Based on the interpolated structure of magnetic fields around the null, we theoretically described how particles can be accelerated by a convective electric field perpendicular to the magnetic field due to the magnetic gradient and curvature drifts in Section 3.2. Finally, test particle calculations in Section 3.3 for both protons and electrons near the null provided a quantitative estimate of the particle acceleration process. Our main results can be summarized as follows.

- With extrapolated magnetic fields as the initial condition, our MHD simulation evolved to a state that plasma flow velocity and convective electric fields were generated through the whole simulation box. In the box center (with the height of solar corona region) the minimum magnetic field being less than 0.05 G indicated the immediate vicinity of a magnetic null point. When rescaled to active region conditions (Case 3), the plasma flow velocity was about 1000 km/s and the corresponding convective electric field was about 2 V/m at the null. Protons could be accelerated up to 30 keV in 0.1 s and electrons gained only small energies, i.e. from 0.2 keV to 0.3 keV.
- With higher plasma flow velocities and stronger convective electric fields ( $\sim 20$  V/m near the null), protons could be accelerated to energies up to 2 MeV in 0.03 s and electrons were accelerated to about 3 keV in 0.005 s.
- The magnetic curvature radii ( $\sim 10^5$  m) near the null exceeded the gradient scale lengths ( $\sim 10^4$  m). Therefore gradient drifts favored the drifting acceleration more than the curvature drifts in the beginning of the acceleration. However, after the particles' parallel energy became much higher than the perpendicular energy, the curvature drift became more important than the gradient drift.
- During the major acceleration process the Larmor radii were about  $10^3$  m to  $10^4$  m for protons and 10 m to 100 m for electrons. The ratio of Larmor radii to gradient scale was about 0.1 to 1 for protons, but merely 0.001 to 0.01 for electrons. Non-adiabatic acceleration stopped when this ratio was smaller than 0.1 for protons. Nevertheless, since the non-uniformity scales obtained from MHD simulations are limited by the coarse grid sizes, one could expect the existence of even more non-uniform structures in realistic solar coronal fields, representing non-adiabatic regions and thus producing more effective acceleration.
- When the V-E angle was less than 90 degrees over several gyro-periods, the proton could be accelerated continuously, which is known as non-adiabatic acceleration. When the particle was magnetized, deceleration could also occur because of the gyration around magnetic field lines.
- For protons, there were mainly three different phases of acceleration: (a) perpendicular acceleration due to (mostly gradient) drift, (b) parallel acceleration due to non-adiabatic motion and (c) parallel acceleration due to (mainly curvature) drift. The non-adiabatic phase yields the most efficient acceleration.

- For electrons, there were only two phases of acceleration: (a) perpendicular acceleration and (b) parallel acceleration, both due to drifts. Due to much smaller electron Larmor radii and also because of the absence of microscopic magnetic structures in macroscopic MHD simulations, the electrons were not aware of any obvious change of the magnetic field within several gyrations, and consequently there was no phase of non-adiabatic acceleration whereby they could be de-magnetized and continuously accelerated.
- The final particle velocity included three parts: parallel velocity, perpendicular drift velocity and perpendicular gyration velocity. The last term appeared as oscillations as particles were re-magnetized. The remaining perpendicular velocity was the drift velocity, which is partly due to gradient and curvature drifts during acceleration, but mainly stems from the  $\mathbf{E} \times \mathbf{B}$  drift ( $E_{\perp}/B = E/B$ ) after re-magnetization of the protons. For electrons the  $\mathbf{E} \times \mathbf{B}$  drift was always much larger than the gradient and curvature drifts. Hence electrons were not accelerated significantly near the null.
- For both protons and electrons, the final parallel velocities were much higher than the perpendicular velocities and the V-B pitch angles were approaching 180 degrees. This means that the particles escaped from the null along the magnetic field lines outward and downward to the photosphere. Particles did not escape to the upper corona because of the non-symmetric configuration of the coronal magnetic field, which is weaker at higher altitudes and has fewer up-going open field lines connecting to the null.
- For higher initial kinetic energies (resulting in enhanced drifts), some protons had the chance to gain more energies in the course of a secondary acceleration process. Nevertheless, a few protons ran the risk to be decelerated (if their initial velocity was opposite to the direction of the electric field). For electrons, a higher initial energy did not lead to efficient acceleration, because they still remained strongly magnetized.
- Electrons could not become de-magnetized, owing to their smaller gyro-radii. Protons could not be accelerated to observational energy bands of about 10 MeV to  $\geq 100$  MeV (Benz 2008) with only convective electric fields. Parallel electric fields appear to be necessary for further higher energy accelerations.

To include a parallel electric field consistently in a MHD model, the existence of a switched on anomalous resistivity is necessary. Therefore a reliable microscopic model is a key factor to generate resistive electric fields and accelerating particles adiabatically to the observed energies. Microphysical kinetic descriptions, which provide the resistivity expressions for the macroscopic MHD coefficients (Büchner and Elkina 2006), are necessarily required for this purpose. This MHD simulation, although tried to include the resistive electric fields, has failed to run long enough for the resistivity to have been switched on in coronal regions where the particles are considered to be initially accelerated. Besides, the parallel electric fields obtained from kinetic processes are in general confined to regions on the ion inertia scale, which is much smaller than the macroscopic MHD grid scales. A multi-scale MHD simulation with a much higher resolution at the dissipation region can somehow decrease this scale gap. More work needs to be done on

for longer MHD simulations with higher resolution to generate parallel resistive electric fields to study adiabatic (direct) acceleration.

Besides, the present work is limited to investigate the mechanisms and processes of acceleration by a null point instead of giving an indication of how many particles could reach the null and get the chance to gain energy. Future work will be focusing on the probability of particles reaching the null point and being accelerated. Moreover, the accelerated spectrum of a large amount of particles with an initial Maxwellian distribution will also be studied and compared with data, in particular from RHESSI.



## 4 Particle Acceleration at a Slow-reconnecting Null Point

*What we observe is not nature itself, but nature exposed to our method of questioning.*

*Werner Heisenberg*

Recent theories and simulations of three dimensional reconnection suggest that reconnection can take place either in configurations containing null points (e.g. Priest and Titov 1996) or at places of non-vanishing magnetic field strength (e.g. Hesse et al. 1999). The latter case is known as finite-B-reconnection which must occur at the vicinity of parallel (to the magnetic field) electric fields. Parallel electric fields often arise from parallel currents and generated resistivity, the so called anomalous resistivity, which is artificial in MHD simulations. The efficiency of particle acceleration by parallel electric fields has been studied both theoretically and numerically (e.g. Litvinenko and Somov 1993, Litvinenko 1996, Bruhwiler and Zweibel 1992, Mori et al. 1998, Browning and Vekstein 2001, Zharkova and Gordovskyy 2004, Hannah and Fletcher 2006, Heerikhuisen et al. 2002, Craig and Litvinenko 2002, Wood and Neukirch 2005, Hamilton et al. 2005, Schopper et al. 1999, Turkmani et al. 2006, Liu et al. 2007, Karlicky and Barta 2006). A signature of reconnection in addition to parallel electric fields is the occurrence of stagnation flows that are often detected numerically (but not observationally) near magnetic null points.

In the previous chapter, we investigated how particles can be accelerated by the convective electric field in the vicinity near an X-type Null point. However, Figure 2.5 shows that the plasma flow does not follow a stagnation pattern after only 1.6 Alfvén times of simulation. A longer simulation of the quadrupolar magnetic field has been studied by Santos et al. (2011) and stagnation flows are generated around the X-type Null point. Based on this new configuration of plasma flows and associated convective electric fields indicating a process of slow reconnection, we study particle (both protons and electrons) acceleration around the X-type null point with the same magnetic field configuration.

### 4.1 3-D MHD Simulation of a Slow-reconnecting Null point

Santos et al. (2011) used the same three-dimensional quadrupolar magnetic field model and solved the same basic resistive MHD equations as Guo et al. (2010), also shown in Chapter 2. The new MHD simulation adopted a higher spacial resolution with equidistant

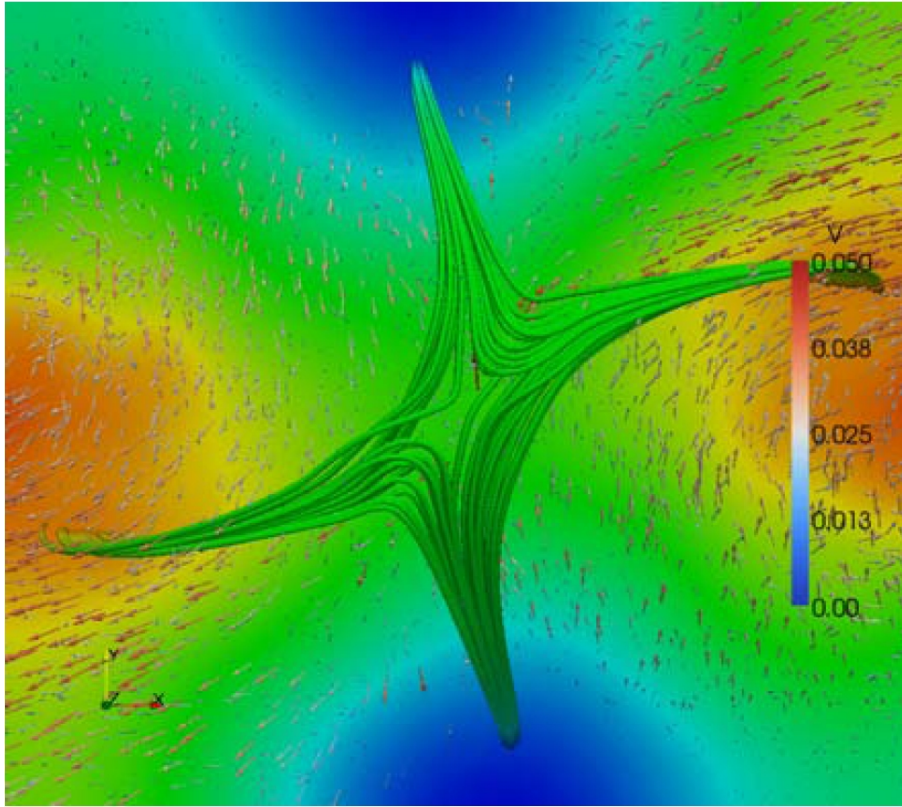


Figure 4.1: Top global view of the plasma flow field showing a stagnation flow pattern, which is characteristic of reconnection (from Santos et al. (2011)). The arrows show the velocity vector direction, the colour code its amplitude, and the size of the arrows the relative strength of the velocity. Also shown are magnetic field lines (green), together with the Z component of the magnetic field at the bottom.

cartesian grid (131x131x131 grid points) and a different setup of normalization parameters (see Table A.1 in Appendix A). The resistivity considered here contains only the background resistivity which is chosen as low as possible to prevent resistive electric fields and fast reconnection.

Note that the initial density profile used in the previous work (Guo et al. 2010) considered the density drop and temperature increase from the bottom photosphere to the upper corona. However, the initial density and temperature used by Santos et al. (2011) is homogeneously distributed throughout the box in order to enhance the efficiency of plasma driving at the bottom. Consequently, the transfer of momentum from the neutral gas to the plasma through collisions (the last term on the right-hand side of the momentum equation, Equation(2.2)) is more efficient in the corona with larger density. Although the photospheric plasma motion follows the same pattern as in the previous work, it causes magnetic field perturbations to propagate more stably and efficiently to the corona along the magnetic field lines at the local Alfvén speed. The magnetic perturbations eventually reach the vicinity of the null and the new MHD simulation develops into a state where current sheets are generated and slow reconnection takes place near the null point.

Driven by the horizontal photospheric motion, the plasma in the whole simulation box evolves. After 50 Alfvén times, the simulation box reaches a state with an average

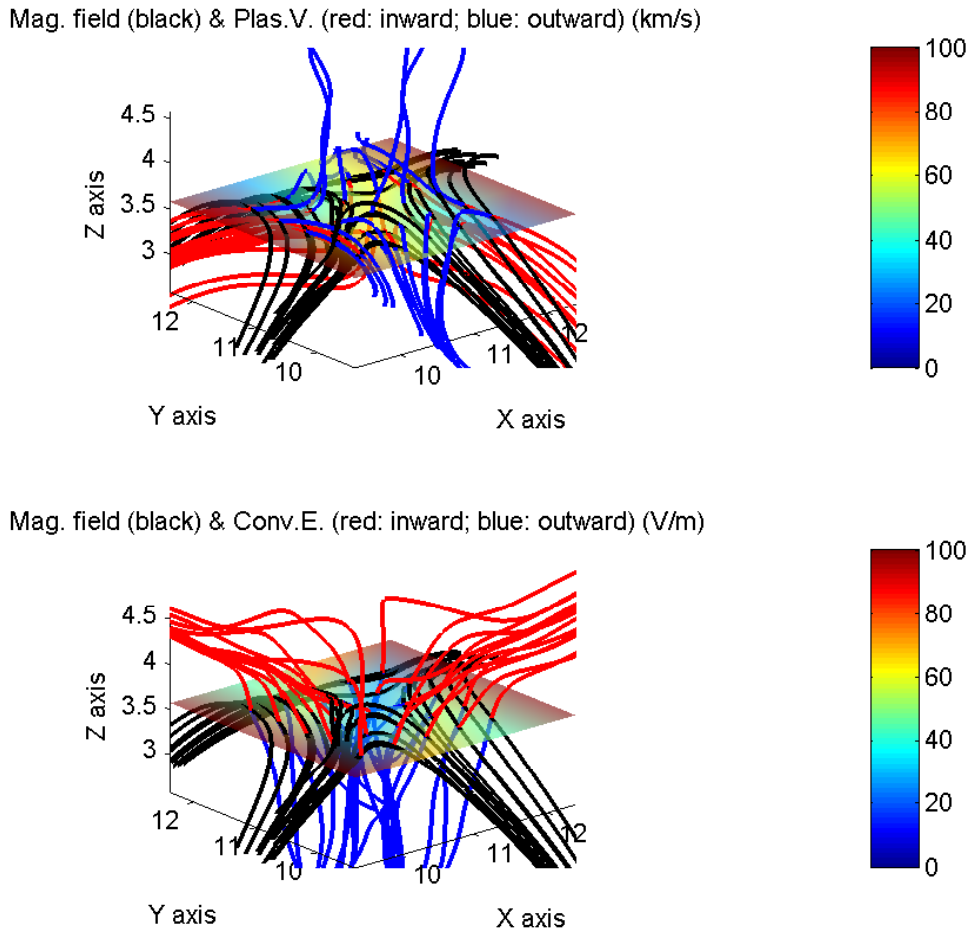


Figure 4.2: Plasma velocity flow lines (top) and the corresponding convective electric fields (bottom) near the null. The black lines represent the magnetic fields. *Top*: The red lines indicated the plasma flow coming into the null area, while the blue ones are plasma flows leaving the region. There is a flow stagnation at the null. *Bottom*: The red lines indicated the electric fields coming into null area, while the blue ones are electric fields leaving the region. At the null, the electric fields are mainly in the vertical direction and they are perpendicular to the magnetic fields that are mostly in the horizontal direction. The horizontal layers cutting through the null show the strength of the plasma velocity (km/s) (top) and the value of convective electric field (V/m) (bottom). The colour-coding is indicated on the right side.

Table 4.1: Comparison of the magnitudes of magnetic fields, plasma flow and electric fields in both simulations

	Simulation 1 (Chap. 2)	Simulation 2 (Chap. 4)
average V in the box	0.42 $u_{01} = 21.0$ km/s	0.0021 $u_{02} = 10.4$ km/s
average E in the box	4.08 $E_{01} = 20.4$ V/m	$9.5 \times 10^{-4}$ $E_{02} = 46.4$ V/m
average B near the null	2.09 G	2.19 G
average V near the null	0.18 $u_{01} = 8.8$ km/s	0.0052 $u_{02} = 26$ km/s
average E near the null	0.32 $E_{01} = 1.6$ V/m	$1.1 \times 10^{-4}$ $E_{02} = 5.4$ V/m
B at the numerical null	0.0484 G	0.0368 G
V at the numerical null	0.2328 $u_{01} = 12$ km/s	0.0055 $u_{02} = 27$ km/s
E at the numerical null	0.0036 $E_{01} = 0.018$ V/m	$4.9 \times 10^{-7}$ $E_{02} = 0.024$ V/m
Grad.R. at the numerical null	8.8 km	11.5 km
Curv.R. at the numerical null	76 km	76 km

bulk velocity of  $\approx 10.4$  km/s. Consequently, convective electric fields arise in the whole box due to the plasma motion across the magnetic field. The convective electric field has an average value of  $\approx 46.4$  V/m within the whole box. Near the null, however, the convective electric field is only  $\approx 0.024$  V/m (bottom image of Figure 4.2), because the magnetic field is minimum ( $\approx 0.04$  G) and the plasma bulk velocity is  $\approx 27$  km/s. Table 4.1 gives the values of average plasma velocity and convective electric fields in the whole simulation box, as well as the magnetic field strength, plasma velocity, and convective electric fields at the "null" (the numerical null). Also shown is the average values of magnetic fields, plasma velocity, and convective electric fields within several numerical grids around the null, offering a glimpse of the immediate 'neighbourhood' of the null. Note that although the normalization parameters  $u_{01}$ ,  $u_{02}$ ,  $E_{01}$ ,  $E_{02}$  are different in two simulations (Table A.1 in Appendix A), the dimensional values share the same order of magnitudes, both giving reasonable estimated strengths of the magnetic fields and plasma velocities in the solar corona. Further, although the average plasma velocity in the whole simulation box was higher in the first simulation, the corresponding average convective electric field was weaker than in the second simulation. This is because the plasma flow in the second simulation is more evolved and it has a larger component across the magnetic field lines.

Figure 4.1 (taken from Santos et al. (2011)) plots the global top view of the plasma flow fields and magnetic fields after 50 Alfvén times of simulation. A stagnation flow pattern is displayed near the center of the box where the null is located. A slow and stable reconnection process should therefore be switched on thereby. Figure 4.2 shows the magnetic fields, plasma flow lines and convective electric fields close to the null. Compared to the null in Chapter 2, this null has similar magnetic field configurations but different plasma flow and convective electric field structures. Plasma flows inward (red lines in the top panel) from the down-side of the X-type null and it leaves (blue lines in the top panel) along both upward and downward directions. A stagnation point of the plasma flow is located near the center of the null. The corresponding convective electric fields (in the bottom panel) cross the null almost vertically. The structure of the magnetic and

electric fields is similar to that of a 2-D X-type null, however, constructed from a more realistic 3-D MHD simulations.

The minimum numerical value of the magnetic field magnitude is about 0.04 G on the MHD grids. This reference point is not the location of the actual null point (which is between the grids) but in its immediate vicinity. For simplification, we call this reference point the "new null" and the previous null (Chapter 2) the "old null". Note that the axis scales in Figure 4.2 are different from those in Figure 2.5 since the normalization lengths are set to be much larger in the new simulation. However, the structures and strengths of the magnetic fields are kept to be almost identical in both simulations. The eigenvalues of the Jacobian matrix at the new null point are about  $(2.0, -1.7, -0.3)$ , which are very close to the results of the old null. The location and direction of the fan plane and spine are therefore very similar to those of the old null. Both the fan and the spine field lines are connected to the bottom of the simulation box where the plasma vortex motion is applied at the fan footpoints (Fig. 2.3).

## 4.2 The Structure of the Magnetic Fields near the Null & Particle Drift Velocities

To diagnose the gradient and curvature drift motions of charged particles at the new null, we calculated the drift velocities around the null by solving Eq. (3.1) for gradient drift and Eq. (3.2) for curvature drift. The obtained drift velocity fields and magnetic fields around the null are shown in Fig. 4.3. These drift velocities are estimated for particles with a thermal energy about 1.5 keV ( $mv_{\perp}^2/2 \approx mv_{\parallel}^2/2 \approx E_k/2$  and  $E_k = 1.5 \text{ keV}$ ), which corresponds to thermal velocities of  $5.36 \times 10^5 \text{ m/s}$  for protons and  $2.30 \times 10^7 \text{ m/s}$  for electrons. At the new null, the gradient and curvature drift velocities are about 28.0 m/s and 34.2 m/s respectively.

The magnetic gradient and curvature scales around the new null are also calculated and shown in Fig. 4.4. The minimum  $R_{grad}$  and  $R_{curv}$  in the whole MHD-simulation box are located at the numerical null, which are about 11.5 km and 76 km respectively (also listed in Table 4.1). The magnetic gradient scale in the new null is slightly larger than that in the old null and the curvature scales in both nulls are almost the same. While the magnetic non-uniform scales are minimum at the null, the Larmor radius of a gyrating particle ( $\sim v/B$ ) is enlarged close to the null by the weak magnetic field. At the location where  $B = 0.0368 \text{ G}$ , the Larmor radii of protons and electrons (both with a kinetic energy of 1.5 keV) are  $L_p = 1.5 \text{ km}$  and  $L_e = 36 \text{ m}$  respectively, which will be enlarged once the particle energies are enhanced. The resulting ratios of the Larmor radii to the magnetic gradient scale lengths are shown in Fig. 4.5. At the new null, this ratio could be as large as 13.2% for protons and merely 0.3% for electrons. As already shown in Chapter 3 (Guo et al. 2010), it is probable for protons to undergo demagnetization when the Larmor-Gradient scale ratio is more than 10%. We expect that the new null would also demagnetize protons and accelerate them non-adiabatically. However, the electrons might still be magnetized at the null since its gyro-scale is much smaller comparing to the magnetic gradient scale. To investigate how particles become accelerated near the new null, we use a test-particle approach in the next section.

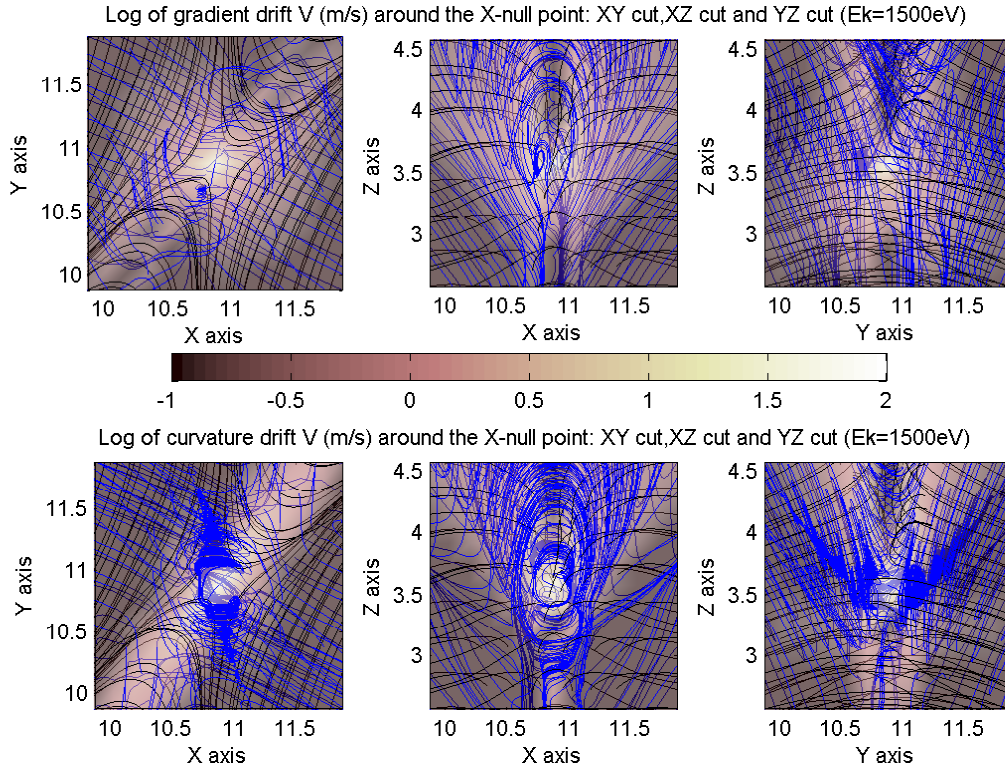


Figure 4.3: Gradient (top) and curvature (bottom) drift lines (blue lines) around the null (magnetic field lines are shown as black lines). The left/middle/right column shows the projection of the flow lines in the  $x - y/x - z/y - z$  2-D plane cutting through the null. The magnitude of the drift velocity in logarithmic-scale is shown in colour with a brighter colour indicating a higher drift speed.

### 4.3 Simulation of Particle Accelerations near the New X-null

We have studied particle acceleration from the old null point in Sect. 3.3. The new null has a magnetic field configuration almost identical to the old null. However, the plasma flow and convective electric fields have a different pattern: the plasma show a stagnation flow near the center of the null indicating a process of slow reconnection. In order to diagnose the acceleration efficiency of this slow-reconnecting null and the differences of the acceleration processes between the new null and the old null, we employ a full-orbit relativistic test particle approach in which the protons or electrons individually explore their orbits in the prescribed electromagnetic field as calculated by Santos et al. (2011) and described in Sect. 4.1.

We calculated the particle motion by numerically solving the relativistic momentum equation (1.19). As in Chapter 3, we considered only the perpendicular convective electric field and neglected any parallel electric field. With a Runge-Kutta-Fehlberg fourth-fifth-order method with an adaptive time step (Fehlberg 1969), we integrated the positions and velocities of both protons and electrons in time.

The final acceleration spectrum, which depends on the initial spatial and velocity dis-

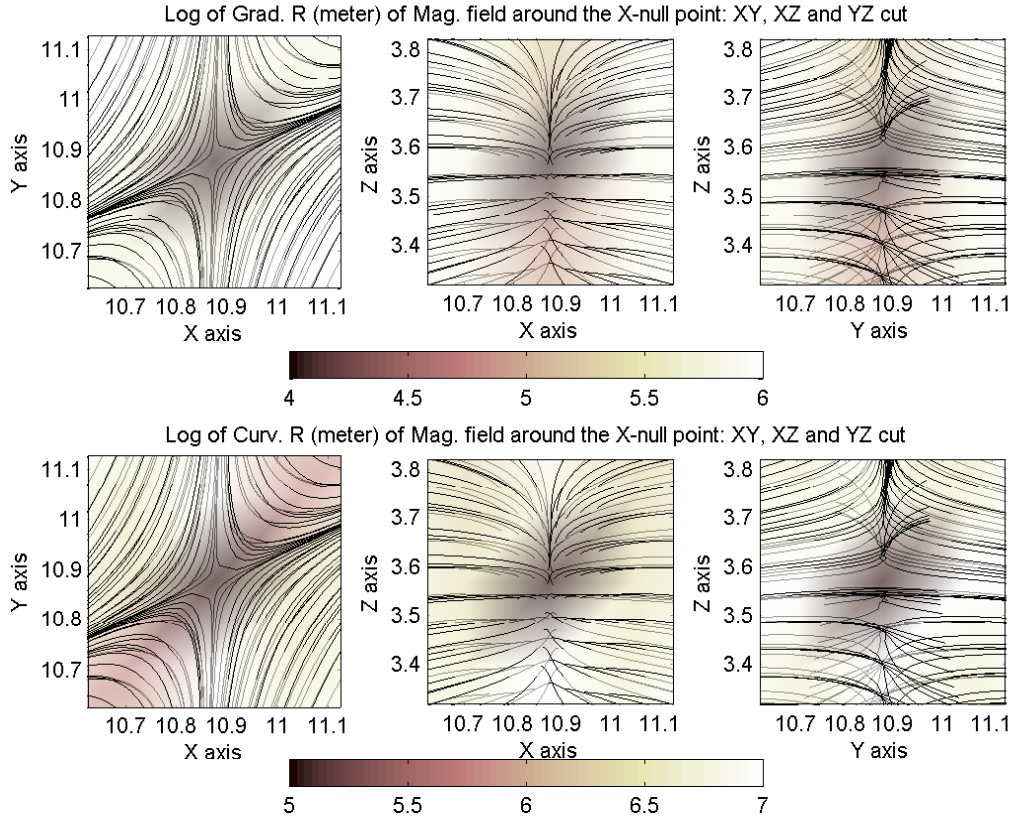


Figure 4.4: Lengths of magnetic gradient scale (top) and curvature scale (bottom) around the null (magnetic fields are shown in black lines). The left / middle / right plot shows the  $x - y/x - z/y - z$  plane cutting through the null. The magnitude of the scale lengths in the logarithmic-scale is colour-coded with the darker colour indicating a lower value.

tributions, is not taken into account at this stage. Hence the initial launch point of particles was taken to be the point with the minimum magnetic field, where the particles are most likely to be accelerated. The initial velocities were shell-distributed: all the particles shared the same speed but started in random directions.

### 4.3.1 Particle Acceleration under Different Plasma Flow Conditions

In this section, we focus on the efficiency of particle acceleration by the new null point under different plasma flow conditions, i.e. different magnitudes of convective electric fields. The MHD equations were solved for dimensionless quantities so that we could rescale the dimensional values of the convection plasma flow and the electric field. The rescaling was not applied to the magnetic field so that its strength was unaltered in the vicinity of the magnetic null point. Rescaling the plasma flow velocity corresponds to a change of the magnitude of the driving motions in the photosphere (at the bottom of the simulation box).

Fig. 4.6 shows the final energies acquired by a given number of protons (1000 in each case) with the initial location at the numerical null under different magnitudes of the plasma flow velocities  $\mathbf{u}_{con}$  and their corresponding convective electric fields  $\mathbf{E}_{con}$ .

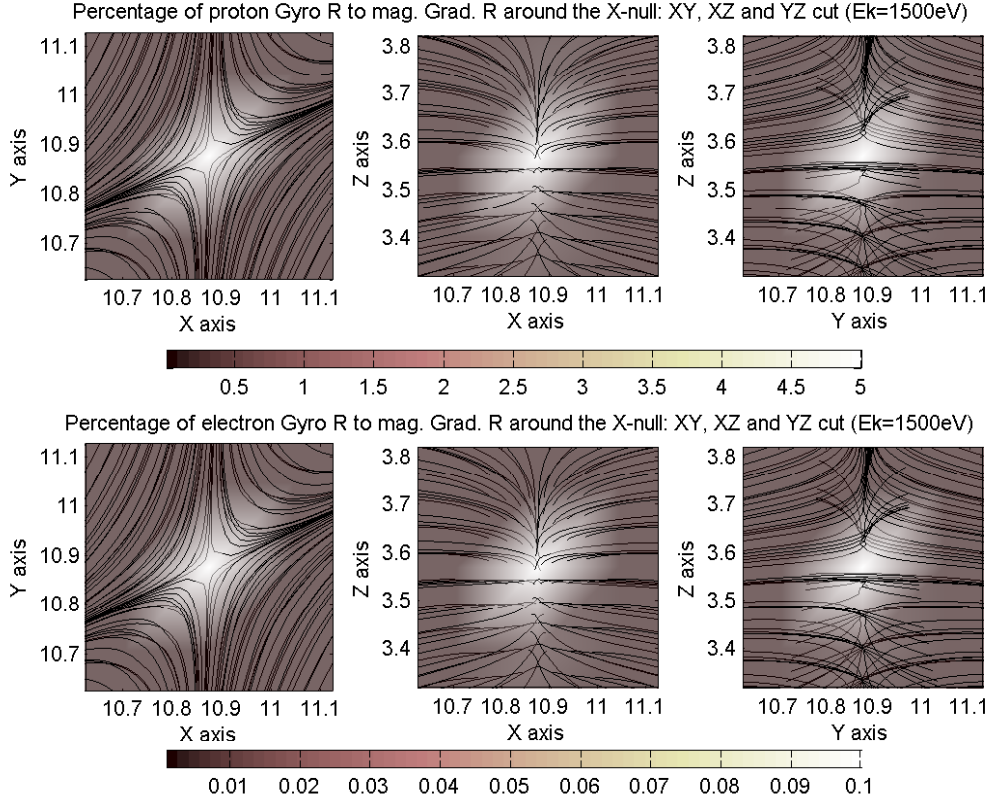


Figure 4.5: Percentage of the Larmor radii to the magnetic gradient scale lengths for a 1.5 keV proton (top) and a 1.5 keV electron (bottom) near the null (magnetic fields are shown in black lines). The left / middle / right column shows  $x - y/x - z/y - z$  2-D cuts through the null. The magnitude of the ratios is shown in grey scale with a brighter colour indicating a higher value.

The rescaled  $\mathbf{u}_{con}$  and  $\mathbf{E}_{con}$  are [1, 5, 10, 20, 30, 40, 50, 60, 70, 80, 90, 100] times of the original magnitudes. Therefore, the plasma flow at the numerical null is rescaled as [27, 135, 270, 540, 810, 1080, 1350, 1620, 1890, 2160, 2430, 2700] km/s in each case. The convective electric field at the numerical null, shown on the x-axis, is rescaled as [0.024, 0.12, 0.24, 0.48, 0.72, 0.96, 1.2, 1.44, 1.68, 1.92, 2.16, 2.4] V/m respectively. The corresponding average plasma flow velocities imposed at the bottom,  $\bar{u}_{z=0}$ , are actually [21, 105, 210, 420, 630, 840, 1050, 1260, 1470, 1680, 1890, 2100] km/s under different cases. Note that even when the plasma flow at the null is as large as thousands of km/s, the convective electric field can only be in the order of V/m. These values from consistent MHD simulation are different from (much smaller than) those used in analytic studies (Dalla and Browning 2005, 2008). We also studied proton accelerations under different initial energies as shown in the figure by different colours: black, green, blue and red dots represent protons with initial energies ( $Ek_{in}$ ) of 0.2 keV, 1 keV, 5 keV and 10 keV respectively. Each dot in the left/middle/right panel plots the maximum/average/minimum energy of 1000 protons accelerated after 0.1 s under different convective electric fields (values on the x-axis) and different initial energies (indicated by different colors). Note that after 0.1 s the average and final energies of all the particles are kept stable.

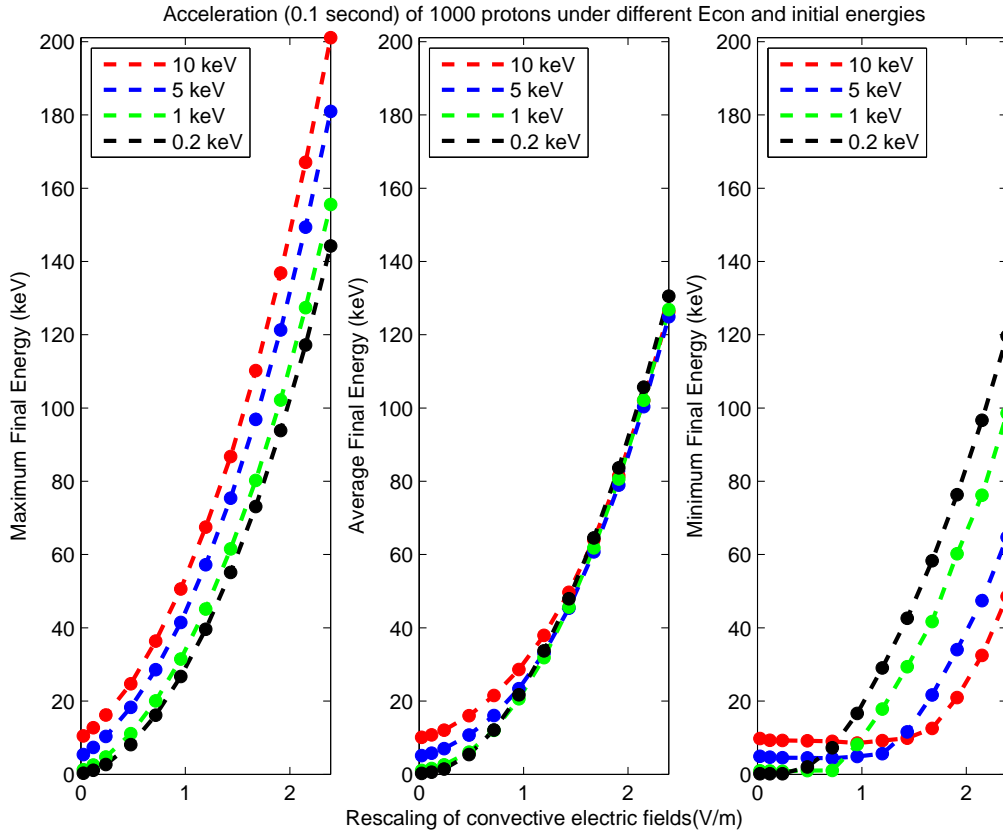


Figure 4.6: Maximum (*left*), average (*middle*) and minimum (*right*) energies of 1000 protons after 0.1 s of acceleration time in each case. There are 48 different cases of acceleration: the convective electric fields are rescaled as [0.024, 0.12, 0.24, 0.48, 0.72, 0.96, 1.2, 1.44, 1.68, 1.92, 2.16, 2.4] V/m respectively (corresponding to [1, 5, 10, 20, 30, 40, 50, 60, 70, 80, 90, 100] times of the original convective electric fields) while the initial shell energies of 1000 protons are set to be: 0.2 keV (black), 1 keV (green), 5 keV (blue) and 10 keV (red) respectively.

It is clearly shown that with stronger  $\mathbf{E}_{con}$ , i.e. stronger convection plasma flow, the final energies of the protons are significantly enlarged. However, the increase of energy versus the change of electric fields is not linear. According to Eq. (D.3), one would expect the change of energy to be linearly proportional to the change of electric field. In fact, in non-uniform electro-magnetic fields, particles do not follow the same path when they are more efficiently accelerated by stronger electric fields and therefore the gained kinetic energy reveals a growth more efficiently than a linear growth.

At a given value of rescaled electric fields, it is apparent that the final maximum energy  $Ek_{max}$  (left panel) of 1000 protons with a higher initial energy is larger than that of protons with a lower initial energy. This is because particles with higher initial energies have larger Gyro-radii and are more easily demagnetized, increasing their chances to be accelerated to a higher final energy. The middle panel shows that when electric fields are smaller than 1.2 V/m (and the rescaling factor is 50), higher initial energies lead to higher final average energies ( $Ek_{avg}$ ) of 1000 protons. However, when the electric fields are larger than 1.2 V/m, higher initial energies do not guarantee higher final average energies.

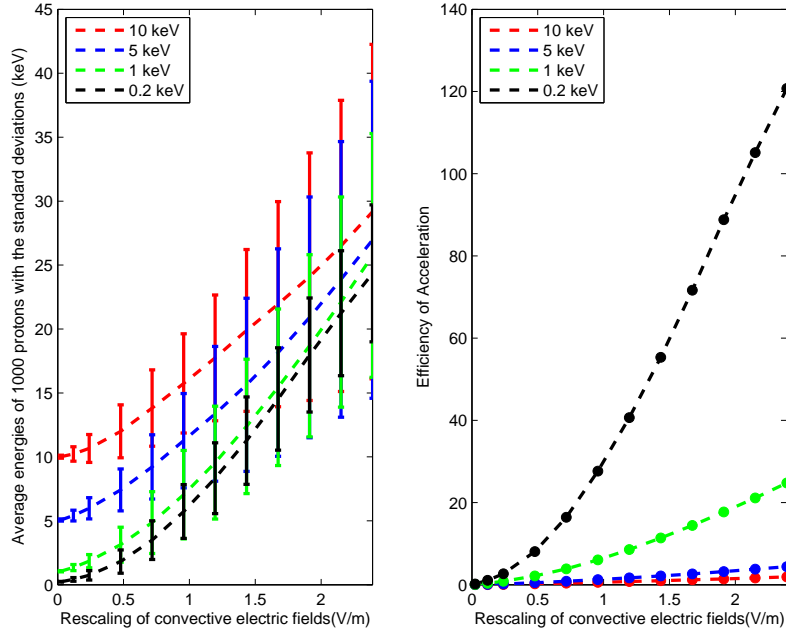


Figure 4.7: *Left*: The final average energies with the standard deviations of 1000 protons accelerated under different convective electric fields (X-axis) and initial kinetic energies (different colours) from the old null point. *Right*: The acceleration efficiencies (Eq. 4.1) under different electric fields and initial energies. There are 48 different cases of acceleration: the convective electric fields are rescaled as [0.024, 0.12, 0.24, 0.48, 0.72, 0.96, 1.2, 1.44, 1.68, 1.92, 2.16, 2.4] V/m respectively while the initial shell energies of 1000 protons are set to be: 0.2 keV (black), 1 keV (green), 5 keV (blue) and 10 keV (red) respectively.

Indeed, with the same magnitude of electric fields, the final minimum energies  $Ek_{min}$  (right panel) decrease as the initial energies are increased. This is to be expected since particles with higher initial energies are more demagnetized and they are more susceptible to be decelerated in the first place when the initial angle is against the direction of the electric fields. In general, particles with higher initial energies tend to show a wider scope of energy range after acceleration. The final average energies do not really depend on the initial energies, especially when the electric fields are stronger than about 1 V/m.

### 4.3.2 Compare the Acceleration Efficiencies of the New and the Old X-null

In order to study and compare the acceleration efficiencies of the new X-null and the old X-null, we re-calculated proton accelerations from the old null (Chapter 2) by rescaling the plasma flow and convective electric field at the numerical old null to make their values comparable with those at the new null. In the following figures we summarize the energy gain aspects of the old null and the new null. For each case with different magnitude of electric fields and different initial kinetic energy, we define the efficiency of energy gain

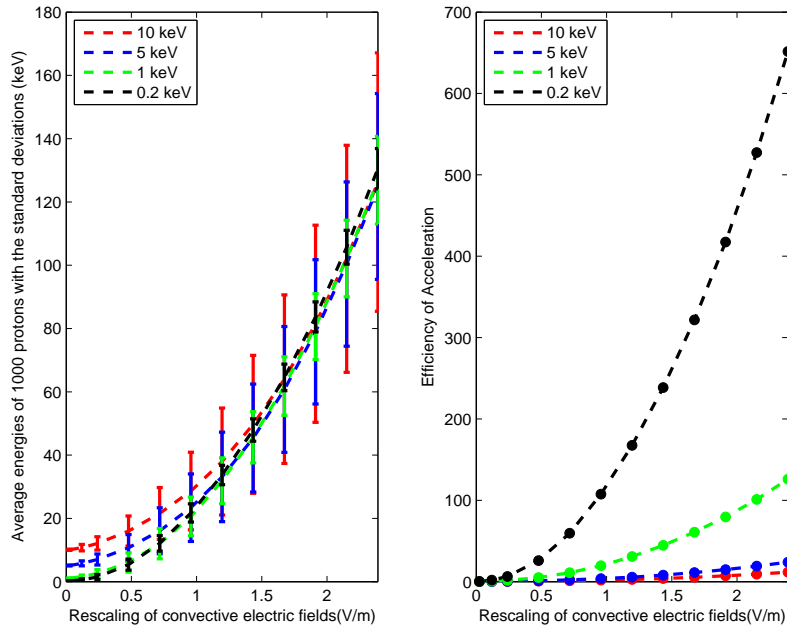


Figure 4.8: The same as Figure 4.7 but for the new null point.

using its initial and final average energy as:

$$\text{Eff} = \frac{Ek_{\text{avg}} - Ek_{\text{in}}}{Ek_{\text{in}}} \quad (4.1)$$

The left panel in Figure 4.7 gives the final average energies with the standard deviations of 1000 protons accelerated (after 0.5 s) under different convective electric fields and initial kinetic energies. The convective electric field at the old null is rescaled to share the same magnitude as that at the new null (see X-axis). The right panel plots the Eff indicating the efficiency of acceleration under different conditions. The figure shows that higher electric fields result in bigger final average energies, more efficient acceleration, and larger deviations of final energies. Also, higher initial energies lead to higher final energies larger deviations. However, with an increasing electric field, the final average energies of particles with lower initial energies are approaching those of particles with higher initial energies. The right panel clearly indicates that particles with lower initial energies have much larger Eff than those with higher initial energies.

Figure 4.8 plots the average accelerated (after 0.1 s) energies with the standard deviations of 1000 protons from the new null for a comparison with the acceleration efficiency of the old null as shown in Figure 4.7. It is seen that both  $Ek_{\text{avg}}$  and Eff obtained from the new null are about 5 times larger than those from the old null. Although the convective electric fields are rescaled to be the same at the old and new null, the configuration of the fields are different due to different patterns of the plasma flows (see Figure 4.2 for the new null and Figure 2.5 for the old null). At the old null, the plasma flows across the null vertically so that the convective electric field lines spread out as they cross the old null downwards. When particles are accelerated in the direction of the electric fields, they tend to escape away from the null. The fields in the new null however stay together close to the neutral line as they cross the null vertically. This helps the particles to be accelerated

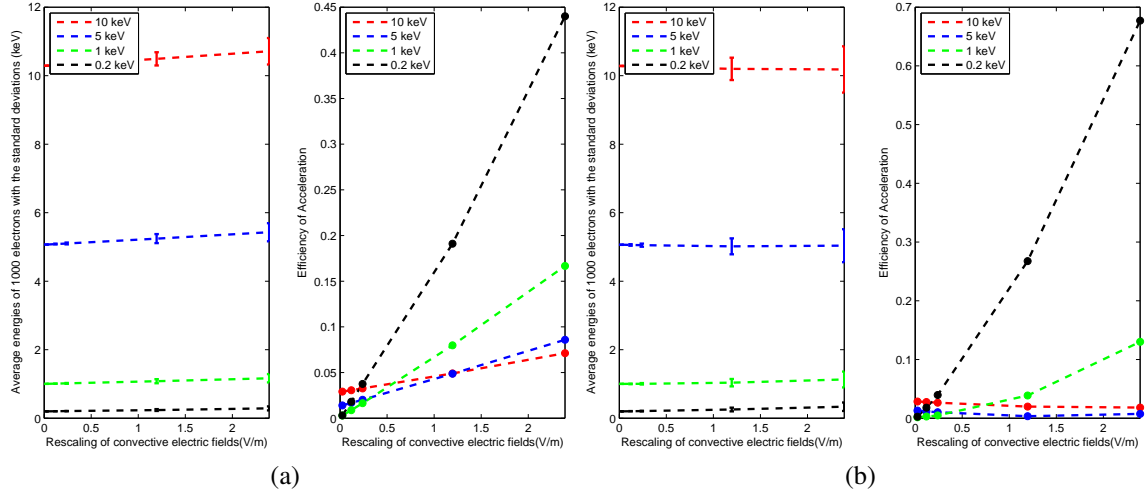


Figure 4.9: (a)*Left*: The final average energies with the standard deviations of 1000 electrons accelerated under different convective electric fields (X-axis) and initial kinetic energies (different colors) from the old null point. *Right*: The acceleration efficiencies (Eq. 4.1) under different electric fields and initial energies. There are 20 different cases of acceleration: the convective electric fields are rescaled as [0.024, 0.12, 0.24, 1.2, 2.4] V/m respectively while the initial shell energies of 1000 electrons are set to be: 0.2 keV (black), 1 keV (green), 5 keV (blue) and 10 keV (red) respectively. (b) The same as (a) but for the new null point.

in the direction of the electric fields along the neutral line where the small magnitude of the magnetic fields is more favourable for demagnetization and acceleration.

### 4.3.3 Energy Gain of Electrons

The acceleration of electrons by convective electric fields from the new X-null is also studied and the results are compared with electron energy gains obtained from the old X-null. By rescaling convective electric fields ( $E_{con} = [0.024, 0.12, 0.24, 1.2, 2.4]$  V/m at the null) and changing initial energies ( $Ek_{in} = [0.2, 1, 5, 10]$  keV), we calculated the energy evolutions of 1000 electrons in 20 cases. The acceleration time is 0.01 s in each case and the average energies are kept stable from then on.

Although the final average energies of electrons are higher than their initial energies in each case, as shown in Figure 4.9, the efficiency of acceleration is very low compared to that of protons. The deviations of final energies are larger under stronger electric fields and bigger initial energies. The acceleration efficiency can be as high as  $\sim 45\%$  for the old null and  $\sim 70\%$  for the new null. In general, larger electric fields lead to more energy gains. However, the acceleration is not more efficient for particles with higher initial energies especially when the electric fields are larger than 0.24 V/m.

Neither of the old X-null nor the new X-null can accelerate electrons effectively according to our test particle simulations. In the absence of parallel electric fields (embedded in resistive electric fields), particles can be accelerated most probably by non-

adiabatic motions caused by small-scale changes of magnetic fields. When the spacial variation scales of magnetic fields are comparable with particle gyroradii, particles can break down regular gyromotions and undergo a demagnetization phase during which perpendicular electric fields can effect directly. For electrons, the small scale of gyromotion is far from comparable with magnetic field scales. Therefore, they keep being magnetized even near the null point and the moderate acceleration is only due to some adiabatic drift (both curvature and gradient drift) motions.

## 4.4 Summaries and Discussions

Based on a new configuration of plasma flows (so as the convective electric fields) indicating a process of slow reconnection, we studied particle (both protons and electrons) acceleration around the three-dimensional X-type null point with the similar magnetic field configuration as that in Chapter 2. A stagnation point of the plasma flow is located near the null. The corresponding convective electric fields cross the null almost vertically.

The minimum  $R_{grad}$  and  $R_{curv}$  in the whole MHD-simulation box are located at the numerical null where  $B = 0.04G$ , being about  $11.5 km$  and  $76 km$  respectively. The ratio of Larmor radii to magnetic gradient scale lengths could be as large as 13.2% for protons and merely 0.3% for electrons.

We studied proton accelerations under different initial energies and different magnitudes of convective electric fields. It is clearly shown that with stronger  $\mathbf{E}_{con}$ , i.e. stronger convection plasma flow, the final energies of the protons are significantly enlarged. At a given value of electric fields, the final maximum energy  $Ek_{max}$  of 1000 protons with a higher initial energy is larger than that of protons with a lower initial energy because particles with higher initial energies are more demagnetized. The final minimum energies  $Ek_{min}$  decrease when the initial energies are increased also due to the stronger demagnetization of more energized particles. The values of final average energies  $Ek_{avg}$  do not depend on the initial proton energies when the convective electric fields are larger than  $\sim 1.2 V/m$ . For both the old X-null and the new X-null, higher electric fields result in higher final average energies, more efficient acceleration, and larger deviations of final energies. The new null is a more effective accelerator compared to the old null due to the different pattern of plasma flow.

Both the old and the new X-nulls can only accelerate electrons moderately due to the strong magnetization of electrons in the magnetic field.

In order to investigate more efficient acceleration for both protons and electrons, one needs to introduce (a)the existence of a parallel electric field, (b)smaller (microscopic) scales of magnetic fields which enlarge the probability of demagnetization processes, and (c)temporally varying fields representing electro-magnetic waves which can cause resonant acceleration.



## 5 Relationship between Hard and Soft X-ray Emission Components

*Scientific knowledge is a body of statements of varying degrees of certainty — some most unsure, some nearly sure, but none absolutely certain.*

*Richard Feynman*

X-ray observations of solar flares routinely reveal an impulsive high-energy and a gradual low-energy emission component, whose relationship is one of the key issues of solar flare study. The gradual and impulsive emission components are believed to be associated with, respectively, the thermal and nonthermal components identified in spectral fitting. In this chapter, a prominent  $\sim 50$  second hard X-ray (HXR) pulse of a simple GOES class C7.5 flare on 20 February 2002 is used to study the association between high energy, non-thermal and impulsive evolution, and low energy, thermal and gradual evolution (Guo et al. 2011). We use regularized methods to obtain time derivatives of photon fluxes to quantify the time evolution as a function of photon energy, obtaining a break energy between impulsive and gradual behavior. These break energies are consistent with a constant value of  $\sim 11$  keV in agreement with those found spectroscopically between thermal and non-thermal components, but the relative errors of the former are greater than 15% and much greater than the a few percent errors found from the spectral fitting. These errors only weakly depend on assuming an underlying spectral model for the photons, pointing to the current data being inadequate to reduce the uncertainties rather than there being a problem associated with an assumed model. The time derivative method is used to test for the presence of a ‘pivot energy’ in this flare. Although these pivot energies are marginally consistent with a constant value of  $\sim 9$  keV, its values in the HXR rise phase appear to be lower than those in the decay phase. Assuming that electrons producing the high-energy component have a power law distribution and are accelerated from relatively hot regions of a background plasma responsible for the observed thermal component, a low limit is obtained for the low-energy cutoff. This limit is always lower than the break and pivot energies and locates in the tail of the Maxwellian distribution of the thermal component.

## 5.1 Introduction

High-energy observations of solar flares with the Reuven Ramaty High-Energy Solar Spectroscopic Imager (RHESSI) (Lin et al. 2002) allows high resolution studies over a broad energy range from 3 keV soft X-rays to  $\gamma$ -rays up to 17 MeV. The photon flux in the energy range of  $\sim 20 - 100$  keV can be reasonably well fitted with a power-law function, and its time-variability increases with the photon energy (Aschwanden 2005, McAteer et al. 2007). It is commonly assumed that this emission is produced by an electron population distinct from electrons forming a thermal background plasma, which is presumed to produce the low-energy X-ray emission (e.g. Aschwanden 2002). The impulsive high-energy emission originates predominantly from the chromospheric footpoints, while — at least later in the flare — the more slowly-varying low-energy emission is dominated by a hot coronal source, observed in many cases to be located near EUV flare loops (e.g. Gallagher et al. 2002). These observations are usually interpreted in the framework of the standard flare model where the hard X-ray (HXR) emission at the chromospheric footpoints of magnetic loops is bremsstrahlung of non-thermal high-energy electrons moving downward along flare loops from acceleration sites higher up in the corona (Brown 1971), with the resulting footpoint heating and evaporation leading to the hot (usually dense) coronal thermal component (Neupert 1968, Petrosian 1973, Fisher 1989). Note, we do not automatically adopt this assumed relationship between accelerated and heated particles. In fact, in Section 5.4, we interpret the observations in a framework where the non-thermal electrons are accelerated out of a heated thermal background. The ‘non-thermal’ electron distribution is usually assumed to have a low-energy cutoff, the presence of which ensures that the total electron number and power are finite. However, it is not clear that there is a theoretical mechanism for particle acceleration which can naturally lead to the low-energy cutoff distinguishing non-thermal from thermal particles (Benz 1977, Miller et al. 1997, Petrosian and Liu 2004). Indeed, it has been argued by Emslie (2003) that the low energy cutoff may be a redundant concept. Hannah et al. (2009) suggested that a sharp cutoff in the injected electron spectrum disappears with the inclusion of wave-particle interactions. A dip in the electron distribution obtained through the inversion of the observed photon spectrum of some flares may be associated with the low-energy cutoff. Kontar et al. (2008a), however, showed that such a feature vanishes when isotropic albedo correction is applied.

The time correlation between the impulsive HXR and/or radio emission and the derivative of the gradual emissions at certain energies, the so-called ‘Neupert effect’, (Neupert 1968, Dennis and Zarro 1993) carries with it the implication that most gradual emissions are a “by-product”, resulting from energy deposition by non-thermal electrons. This is also suggested by the high non-thermal electron energy content resulting from application of the standard collisional thick-target model (e.g. Emslie et al. 2004, 2005), which points to high-energy electrons forming a dominant channel in the energy conversion process. However, more quantitative examination of relevant observations show that the picture is somewhat less clear. Some flares involve heating of thermal coronal plasma in the absence of a power-law emission component (Battaglia et al. 2009), many show footpoints with impulsive phase emission within the energy range usually considered as thermal (Mrozek and Tomczak 2004), and the ‘Neupert effect’, which never represents a perfect correlation, does not hold in all flares or at all (thermal) energies (McTiernan

et al. 1999, Veronig et al. 2002, Veronig et al. 2005). So the possibility of heating of the solar plasma as a direct part of the energy release before and/or during the acceleration is still an open issue for investigation (Petrosian and Liu 2004, Liu and Fletcher 2009). By deriving abundances of elements with low first ionization potentials, such as calcium and iron, Feldman et al. (2004) found that at least the hot plasmas of some flares result from direct in situ heating of corona plasma, possibly due to a compression process. This approach may also lead to a measurement of the partition of hot flare plasmas originated from the corona and chromosphere.

The general question of how the pre-flare magnetic energy is converted into radiation, plasma bulk motion, thermal and non-thermal particle energy may not have a simple answer (Emslie et al. 2005). Although flares share the same kind of energy source, different flares can have quite different appearances, and possibly involve different physical processes. Nevertheless, some well-observed characteristics can still set constraints on the overall energy dissipation process. The soft-hard-soft spectral evolution of some HXR pulses is one of the most important characteristics of high-energy emissions (Kane and Anderson 1970, Grigis and Benz 2004) and may point to a turbulent particle acceleration mechanism (Grigis and Benz 2005). Early analyses (Gan 1998) suggested that there is a value of photon energy at which the non-thermal flux does not change, so that the power-law pivots about this location, a possible further model constraint. Grigis and Benz (2004) showed that there is no single ‘pivot energy’, rather there is a small range. Battaglia and Benz (2006) determined that in the rise phase this energy may be lower than that in the decay phase. In the context of stochastic particle acceleration from the thermal background plasma, the pivot energy should evolve with the background plasma properties (Petrosian and Liu 2004, Liu et al. 2010). However, distinguishing between different models on the basis of observations remains a challenging task (Grigis and Benz 2005).

Other constraints based on the evolution of HXR light curves include the observation that sub-second HXR pulses peak earlier in high than in low energies, consistent with a time-of-flight dispersion if the electrons producing these pulses are accelerated at some distance from the location where the bremsstrahlung radiation is produced (Aschwanden et al. 1996a). However, this does not mean that all the energetic electrons have to be associated with these sub-second pulses. The reverse delay in the longer timescale (seconds) HXR pulses could indicate collisional escape from a coronal trap (Aschwanden et al. 1996b, Aschwanden 1998, Krucker et al. 2008a), but could also be a result of a more gradual acceleration process (e.g. Bai and Ramaty 1979).

In this chapter we investigate the characteristics of flare emission across a range of photon energies, and examine the association between temporal, spatial and spectral characteristics, with particular interest in the region between thermal and non-thermal parts of the spectrum. The chapter is organised as follows. We first review theoretical considerations and present a simple model for the flare with an isothermal and a power-law X-ray emission component (Section 5.2). A simple RHESSI flare on 20th February 2002, with distinct gradual low-energy and impulsive high-energy emissions is analysed in detail (Section 5.3). An overview of the flare is presented in Section 5.3.1. The semi-calibrated photon flux is then used to derive the rate of change of photon fluxes at different energies during a prominent HXR pulse, and two temporal components are identified (Section 5.3.2). This is repeated in Section 5.3.3 but using a full spectral fit. The evolution of model parameters and the corresponding photon fluxes are used to check self-consistency

of the model, and in Section 5.3.4 we look at the pivot energy derived from the rate of change of the photon fluxes. In Section 5.4, we discuss the implications of these results, and conclusions are drawn in Section 5.5.

## 5.2 Thermal and Non-thermal X-ray Emission Components of Solar Flares

The impulsive phase of most flares is characterised by a monotonically increasing flux of low-energy emission and a rapidly varying flux of high-energy emission. RHESSI photon spectra are usually fitted with an isothermal component at low energies and a power-law component at high energies. For the sake of simplicity, we will ignore details of the radiative processes and assume that the observed photon flux consists of an isothermal component plus a power-law component. The photon spectrum therefore is given by

$$I(\epsilon, t) = I_{th}(\epsilon, t) + I_{nth}(t) (\epsilon/\text{keV})^{-\gamma(t)} \quad (5.1)$$

where  $\epsilon$  is the photon energy,  $I_{th}(\epsilon, t)$  and  $I_{nth}(t)(\epsilon/\text{keV})^{-\gamma(t)}$  correspond to the thermal and nonthermal component, respectively. In the presence of a pivot energy  $\epsilon_0$ ,  $I_{nth}(\epsilon_0) = I_{nth}(\epsilon_0/\text{keV})^{-\gamma}$  is independent of time  $t$  and the variation of the nonthermal component is purely due to changes in the photon spectral index  $\gamma$ :  $I_{nth}(t) (\epsilon/\text{keV})^{-\gamma(t)} = I_{nth}(\epsilon_0)(\epsilon/\epsilon_0)^{-\gamma(t)}$ . From the spectral fitting with  $I_{th}(\epsilon)$  determined from the full line-plus-continuum spectrum derived from CHIANTI (5.2) as a function of temperature  $T$  and emission measure  $EM$ , one obtains  $I(\epsilon, t_0)$  at a given time indicated by  $t_0$ . The transition energy  $\epsilon_t$  between thermal and non-thermal emissions, where the photon fluxes produced by the corresponding electron populations are equal, is determined by  $I_{th}(\epsilon_t, t_0) = I_{nth}(t_0)(\epsilon_t/\text{keV})^{-\gamma(t_0)}$ , where  $I_{nth}$  and  $\gamma$  are fitting parameters.

The normalized time rate of change of the photon flux at a given energy  $\epsilon$  is given by

$$R(\epsilon, t) \equiv \frac{dI(\epsilon, t)}{I(\epsilon, t) \cdot dt} = \frac{\dot{I}_{th}(\epsilon, t) + \dot{I}_{nth}(t)(\epsilon/\text{keV})^{-\gamma} - I_{nth}(t)\dot{\gamma}(t) \ln(\epsilon/\text{keV})(\epsilon/\text{keV})^{-\gamma}}{I_{th}(\epsilon, t) + I_{nth}(t) (\epsilon/\text{keV})^{-\gamma(t)}} \quad (5.2)$$

$$\approx \begin{cases} R_{th} \equiv \dot{I}_{th}(\epsilon, t)/I_{th}(\epsilon, t) & \text{for } \epsilon \leq \epsilon_t \\ R_{nth} \equiv \dot{I}_{nth}(t)/I_{nth}(t) - \dot{\gamma}(t) \ln(\epsilon/\text{keV}) & \text{for } \epsilon > \epsilon_t \end{cases} \quad (5.3)$$

where the dot above the relevant quantities indicates the derivative with respect to time and we have used the fact that the thermal and nonthermal components dominate the low- and high-energy photon spectra, respectively, to derive the approximate expression. The rate of change of photon flux of the thermal and power-law component are indicated by  $R_{th}$  and  $R_{nth}$ , respectively. In the RHESSI energy range we consider, the thermal continuum spectrum always dominates at low energies and the free-free thermal bremsstrahlung emission is proportional to  $EM(t)/\{\epsilon T(t)^{1/2} \exp[\epsilon/k_B T(t)]\}$ , where  $EM(t) = n_{th}^2 V$  and  $V$  and  $n_{th}$  indicate the source volume and density of the thermal electrons respectively.  $k_B$  is the Boltzmann constant.

$$R_{th} = \frac{\dot{I}_{th}(\epsilon, t)}{I_{th}(\epsilon, t)} = \frac{\dot{EM}(t)}{EM(t)} + \frac{\epsilon \dot{T}}{k_B T^2} - \frac{\dot{T}}{2T}. \quad (5.4)$$

Inclusion of emission lines and free-bound emission will introduce correction terms to this equation.

In principle, one can obtain the right-hand side of Equation (5.2) from the spectral fits. The left-hand side can be obtained from light curves of different energy bands directly. If the photon spectral model given by Equation (5.1) is sufficient, Equation (5.2) should be satisfied. If the change in the temperature of the thermal component is small, then the rate of change of the photon flux is independent of the photon energy  $\epsilon$  in the thermally-dominated energy range (Eq. 5.4). One can therefore obtain  $R_{th}$  by fitting the rate of change of photon flux in the thermal regime with a function independent of  $\epsilon$ . There will be an energy  $\epsilon'_t$ , where the time derivatives of thermal and non-thermal components are equal, i.e.  $R_{th} = R_{nth}(\epsilon'_t)$  and if the simple equivalence between non-thermal/thermal emission and impulsive/gradual emission holds then  $\epsilon'_t$  should be comparable to  $\epsilon_t$  obtained from spectral fits. Equation (5.2) also provides a means to investigate the presence of a constant ‘pivot’ energy  $\epsilon_0$  for the power-law component, which will occur where  $R_{nth}$  goes to zero - the invariant point in the photon spectrum of the power-law component.

## 5.3 Observations

RHESSI observed a flare on 20th February 2002 in the NOAA active region 9825, located near the northwest limb of the Sun at N16W80 (919 arcsec W, 285 arcsec N) a few days after its successful launch on 5 February 2002. It is the focus of several earlier studies dealing with the characteristics during the HXR peak (Sui et al. 2002, Aschwanden et al. 2002). The imaging and spectroscopic software has been improved significantly since then and the instrumental response is better understood and incorporated in the RHESSI software packages. We choose this event because of the very simple shape of its light curves, and present an investigation here emphasizing the relationship between the low-energy and high-energy emission components.

### 5.3.1 Light curves, Images, and Spectra

This GOES 1-8 Å C7.5 flare exhibits a prominent HXR pulse lasting for about 50 seconds with count rates above 12 keV peaking near 11:06:20 UT. The first three panels of Figure 5.1 show a summary of GOES and RHESSI observations of this flare. The 3-6 keV light curve shows some impulsive behavior, while the 6-12 keV counts are relatively smooth. The RHESSI attenuator state during this flare was A1. Counts in the 3-6 keV channel when the attenuators are in place are almost all from higher energy photons above 11 keV, because of the effect of K-escape (Smith et al. 2002). We therefore only analyze counts above 6 keV in this work. The attenuator also reduces the count rate at low energies significantly leading to a livetime better than 93% for all the detectors. Pulse pileup can then be ignored in the spectral study (Smith et al. 2002). The rise of the RHESSI count rates below 25 keV becomes evident after 11:04 UT marking the onset of the flare. The slowly rising count rates before 11:04 UT are likely caused by particle events as is evident from the gradual varying count rates in higher energy channels where the statistical errors are significant. The background profile can be subtracted with sufficient accuracy by modeling this gradual varying component in different energy channels separately.

The fourth and fifth panels of Figure 5.1 show the GOES temperature and emission measure, respectively. The background fluxes in the two energy channels are chosen as

## 5 Relationship between Hard and Soft X-ray Emission Components

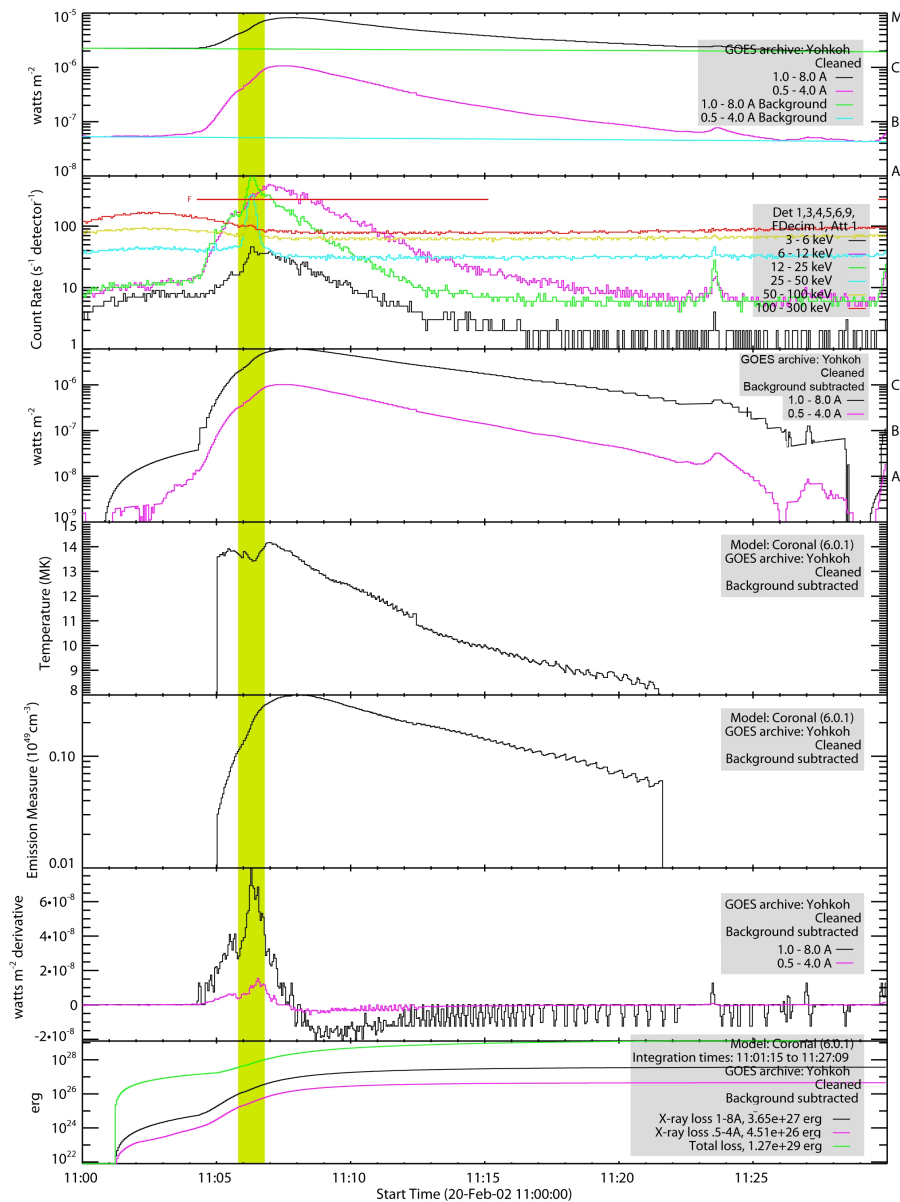


Figure 5.1: Summary of RHESSI and GOES observations. The high-lightened range shows the time interval (11:05:50 —11:06:50) used for images and spectra in Figures 5.2 and 5.3. The top panel shows the soft X-ray (SXR) lightcurves and chosen backgrounds (as linear interpolation of fluxes of two intervals before and after the flare) for both energy bands observed by GOES. The second panel shows the RHESSI count rate in several energy bands. The third panel shows GOES lightcurves with the background subtracted. The fourth and fifth panels show, respectively, the temperature and emission measure derived from the GOES fluxes, in agreement with results obtained by Sui et al. (2002). The sixth panel shows the time-derivatives of the GOES lightcurves, which is qualitatively correlated with the HXR count rates in the top panel. The bottom panel shows the energies radiated by the hot plasma observed with GOES obtained using CHIANTI 6.0.1 with coronal abundances.

a linear interpolation between average fluxes during two intervals before and after the flare and are shown in the first panel. The temperature and emission measure can not be obtained before 11:05 UT, presumably due to the relatively low background subtracted fluxes shown in the third panel. The values obtained for the impulsive phase are rather insensitive to the background selection. These results are in agreement with those obtained by Sui et al. (2002) for the prominent HXR pulse. We note that the temperature does not change significantly throughout the rise phase of the 6-12 keV count rate from 11:05 to 11:07 UT. The emission measure appears to grow exponentially at the beginning with a growth time of  $\sim 40$  seconds, and the growth rate decreases significantly after the HXR pulse. The sixth panel shows the time derivatives of the GOES fluxes. Although these derivatives peak near the peak of the HXR pulse, and a secondary peak before the major peak appears to be correlated with RHESSI light curves below 25 keV in rough agreement with the Neupert effect, a broader correlation is not very obvious. Since the first peak does not contain high energy ( $> 25$  keV) emissions which normally have a longer decay time than lower energies, we assume that the two peaks are independent and the first peak does not significantly affect the spectral properties determined for the major one. The bottom panel shows the radiative energy produced by the isothermal source, obtained by fitting the GOES fluxes using CHIANTI 6.0.1 and assuming coronal abundances (Dere et al. 2009). The total radiated energy from the hot plasma is about  $10^{29}$  ergs for this flare.

The right panel in Figure 5.2 shows the source structure at several energies during the prominent HXR peak from 11:06:10 to 11:06:30 UT obtained using the Pixon algorithm

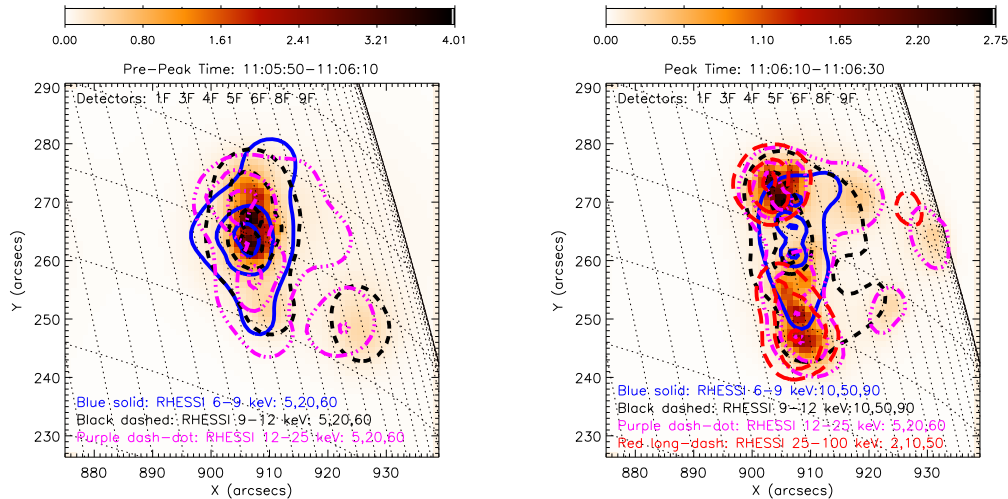


Figure 5.2: Images of the flare for a 20 second interval before (Left) and a 20 second interval during (right) the HXR peak. The map color is in the unit of photons  $\text{cm}^{-2} \text{s}^{-1} \text{arcsec}^{-2}$ . *Left*: The image and dashed contours (5, 20, and 60 % of the peak brightness) are for 9-12 keV energy band. The solid (5, 20, and 60 %) and dash-dot (5, 20, and 60 %) contours are for the 6-9 keV and 12-25 keV energy band, respectively. *Right*: The image and dot-dash contours (5, 20, and 60 %) are for the 12-25 keV energy band. The solid (10, 50, and 90 %), dashed (10, 50, and 90%) and long-dash (2, 10, 50%) contours are for the 6-9 keV, 9-12 keV and 25-100 keV energy band, respectively.

## 5 Relationship between Hard and Soft X-ray Emission Components

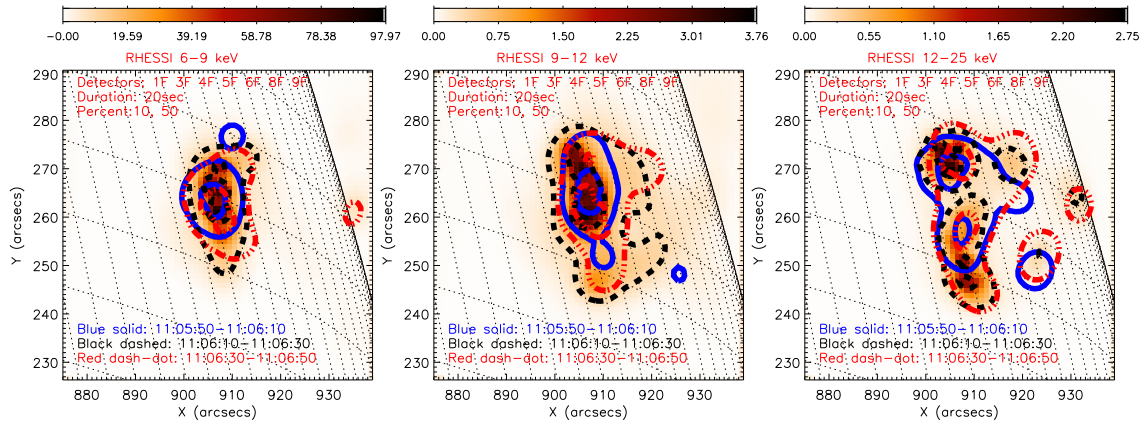


Figure 5.3: Evolution of the X-ray images at 6-9 keV (left), 9-12 keV (middle), and 12-25 keV (right). The map color is in the unit of photons  $\text{cm}^{-2} \text{s}^{-1} \text{arcsec}^{-2}$ . The image and dashed contours (10, 50%) are for the interval of the HXR peak. The solid contours and dash-dot contours are for the interval before and after the HXR peak, respectively.

(Pina and Puetter 1993). The weak HXR coronal source near the solar limb has been interpreted as the site of particle acceleration by Sui et al. (2002). Aschwanden et al. (2002), on the other hand, inferred a much smaller loop. Our results suggest that both large and small loops are present at energies up to 25 keV. There are also clear footpoints at  $> 25$  keV which appear to be at the end of the lower energy loops. This imaging does not support the suggestion by Sui et al. (2002) that there is an independent low-energy thermal source between the two HXR footpoints, rather it indicates that the small loop connects to the HXR footpoints. The structure just before the flare peak is shown in the left panel of Figure 5.2.

The time evolution of X-ray sources at 6-9 keV, 9-12 keV, and 12-25 keV are shown in Figure 5.3. The 6-9 keV source structure (in the left panel) is relatively simple, loop-like and compact before the HXR pulse. It becomes more extended in the following two time intervals and develops three sub-sources (though there is a possibility that this is over-resolution by the Pixon algorithm). The 9-12 keV emission is primarily loop-like but more extended than its 6-9 keV counterparts. Features associated with the footpoints start to emerge. The distinction between footpoint sources and loop source(s) becomes very ambiguous at 12-25 keV (in the right panel of Figure 5.3). The brightest locations are associated with the footpoints at the HXR peak, but the 12-25 keV structure is elongated (as is the 9-12 keV source in the middle panel) and may include a loop component. The X-ray images therefore reveal a complicated pattern of low and high energy sources, with no clear distinction between footpoints and loop at energies from  $\sim 10$  to 25 keV.

Figure 5.4 shows the photon spectra fitted with an isothermal plus a power-law component for the three 20-second intervals of Figure 5.3. For this preliminary study, the RHESSI background is chosen as a linear interpolation, made between the average counts during the intervals 11:01:58 - 11:02:38 and 11:20:38 - 11:21:18. More detailed modeling of the background is carried out in Section 5.3.3, where the spectra for 4-second intervals are analyzed. (Although we choose a broken power-law model in the fitting, the break energy is fixed at 5 keV which is below the energy range of the data.) The soft-hard-soft spectral evolution is evident with the photon spectral index varying from 4.1 to 3.4 and

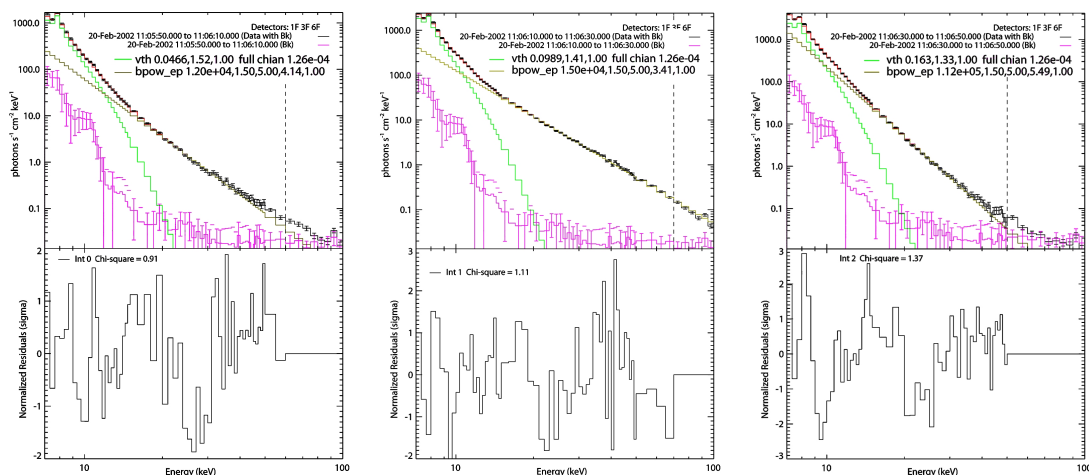


Figure 5.4: Photon spectra of the three 20-second intervals in Figure 5.3 fitted with an isothermal plus a power-law model. Time starts from 11:05:50 and increases from left to right. Model parameters are indicated in the figure.

to 5.5. The emission measure and temperature are  $EM = 4.7 \times 10^{47} \text{ cm}^{-3}$ ,  $kT = 1.5 \text{ keV}$ ;  $EM = 9.9 \times 10^{47} \text{ cm}^{-3}$ ,  $kT = 1.4 \text{ keV}$ , and  $EM = 1.6 \times 10^{48} \text{ cm}^{-3}$ ,  $kT = 1.3 \text{ keV}$ , respectively. The emission measure is slightly lower and the temperature is slightly higher than those from the GOES spectral fit, which may be attributed to the different energy ranges covered by these two instruments. Comparison of these spectra shows that the 12-25 keV emission is more and more dominated by the power-law component as the flare evolves. The spectral fit of the last interval has also the highest values of reduced  $\chi^2$  (1.37) and residuals, leading to a probability of 8% to get a larger  $\chi^2$  assuming a correct model. Indeed, for the last interval a thermal plus a broken power-law model gives much improved spectral fit. We also study the spectral evolution after the impulsive phase. The simple thermal plus a single power-law model can be ruled out by the relatively softer high-energy spectra, which imply dominance of very low-energy emission by the power-law component. A thermal plus a broken power law or multi-thermal model can give acceptable fit. However, one should note that the high-energy photon fluxes change dramatically during the two intervals before and after the HXR peak and the large systematic residuals around the iron-line complex at 6.7 keV indicate that this feature has not been modeled properly. Currently, the only way to improve the modeling of emission lines is to fit spectra from individual detectors and take into account small gain changes and pulse pile up, which is beyond the scope of the current investigation.

### 5.3.2 Semi-calibrated light curves and their rate of change

We here study the photon flux change rate  $R(\epsilon, t)$  given by Equation (5.3) to quantify the rate of change of photon flux — how impulsive or gradual the event is — as a function of both energy and time. We do this first in a model-independent way using the semi-calibrated photon flux. Semi-calibrated photon fluxes can be obtained from the observed count rates by using the diagonal elements of the spectral response matrix. Although the photon flux obtained this way does not take into account the full spectral response matrix

of RHESSI, it can be readily obtained and gives an approximate description of the photon flux from the source, and one which does not depend on assuming a particular form of the photon spectrum (note, we investigate full spectral fitting in Section 5.3.3). Following the arguments of Section 5.2, with the photon spectrogram obtained this way, one can test whether the two components identified from spectral fits are compatible with the two temporal components.

Figure 5.5 shows some of the detailed semi-calibrated photon fluxes  $f(\epsilon, t)$  in forty energy bands between 6 and 50 keV. Each energy bin is set to be no smaller than 1 keV which is the energy resolution of RHESSI (Smith et al. 2002). The vertical axis indicates the photon flux averaged over a 4 second interval in the corresponding energy band. The background fluxes of high energy bands decrease gradually with time. We model these background fluxes for different energy bands with a first order polynomial fitting of background values obtained before and after the HXR pulse.

We use the regularized method developed by Kontar and MacKinnon (2005) to obtain the time derivatives of these light curves. This method gives smoother derivatives while avoiding large errors, typical of finite differences of discrete numerical data. We assume statistical error for the photon flux  $\sigma f(\epsilon, t) = M^{-1}(\epsilon) C(\epsilon, t)^{1/2}$  where  $M$  is the diagonal components of the instrument response matrix and  $C$  is the count rate. The top panel in Figure 5.6 gives the photon flux  $f(\epsilon, t)$  and its  $1\sigma$  statistical error  $\sigma f(\epsilon, t)$  in different energy bands during the HXR pulse. The bottom panel shows the rate of change of photon flux  $R(\epsilon, t) = df(\epsilon, t)/dt/f(\epsilon, t)$  and its  $1\sigma$  error  $\sigma R(\epsilon, t)$ , which is the standard deviation of  $R(\epsilon, t)$  modeled with a Gaussian by sampling 5000 points in  $df(\epsilon, t)/dt$  and  $f(\epsilon, t)$  within their respective  $1\sigma$  range of a Gaussian distribution. Here only the  $1\sigma$  range of a Gaussian distribution is sampled for the following reason. The relatively low flux  $f$  and its relatively large  $1\sigma$  error mean that a sampling over the full distribution will have points with  $f(\epsilon, t)$  close to zero. This will lead to very high values of  $R(\epsilon, t)$ , whose distribution is poorly fitted with a Gaussian. The  $1\sigma$  error obtained this way should be considered as a lower limit. The photon fluxes at lower energies have a more gradual temporal evolution and lower rate of change, in contrast to the high-energy band photon fluxes, which have rapid rise and decay phases and highly variable rate of change. The absolute value of the rate of change often increases with the photon energy. However, the  $1\sigma$  error of the rate of change of photon flux also increases with energy, and the variation in the rates of change at high energies may not be significantly different from those at low energies. At the time bin for the peak from 11:06:20 to 11:06:24, however, the rates for all energies are around zero.

Figure 5.7 shows the energy dependence of the rate of change of photon flux at different 4 second time intervals of the HXR pulse. It is clear that the higher energy fluxes have higher values of the derivative in the rise phase (before 11:06:20) and lower values of the derivative in the decay phase (after 11:06:24). This confirms that higher energy fluxes are more variable than those at low energies. There appears to be two temporal components. At low energies, the rate of change is nearly independent of the photon energy. At high energies, the energy dependence of the rate of change appears to increase linearly with the logarithm of the photon energy. To quantify these results, we adopt the following model for the rate of change  $R$

$$R = \begin{cases} C1 & \text{for } \epsilon \leq \epsilon'_t \\ C1 + C2 \log_{10}(\epsilon/\epsilon'_t) & \text{for } \epsilon > \epsilon'_t. \end{cases} \quad (5.5)$$

There are therefore three model parameters: C1, C2, and  $\epsilon'_t$ . The solid lines in Figure 5.7 indicate the best-fit model (using the curvefit function in IDL). Note that the 5th and 7th time intervals are not fitted with the model due to significant uncertainty in  $\epsilon'_t$  because of low values of the rate of change of photon flux at all energies near the HXR peak.

A comparison of equations (5.3) and (5.5) shows that

$$C1 = R_{th} = \dot{EM}(t)/EM(t), \quad (5.6)$$

$$C2 = -\ln 10 \cdot \dot{\gamma}, \quad (5.7)$$

where we have assumed that the temperature of the thermal component does not change during the HXR pulse (demonstrated using spectral fitting in the next Section).  $\epsilon'_t$  is the transition energy, where the rate of change of the high and low energy components are equal:  $R_{th} = R_{nth}(\epsilon'_t)$ . If the isothermal and power-law model of equation (5.1) indeed gives sufficient description of the observations,  $\epsilon'_t$  should be comparable to the transition energy identified from the spectral fit  $\epsilon_t$ .

### 5.3.3 Spectral fit and the rate of change of photon flux and model parameters

The semi-calibrated photon flux, which is simple and fast to obtain, may give a sufficient approximation of the photon flux from the source at high photon energies, but the non-diagonal elements of the response matrix become important at low energies. By carrying out a full spectral fit, which is much more time-consuming, and determining the model parameters from this, we can check for consistency with the results based on the semi-calibrated flux. With the spectral fitting package OSPEX, the spectrum of counts from 6 to 60 keV are fitted with an isothermal plus a single power-law model for time bins of 4 seconds from 11:05:56 to 11:06:44 UT. Note that the model of CHIANTI (5.2) rather than CHIANTI (6.0.1) used in GOES data is applied here due to the lack of implementation of the newer model in OSPEX. Due to the change of background fluxes in both time and energy, the background is separately selected for five different energy bands (3 to 6 keV, 6 to 12 keV, 12 to 25 keV, 25 to 50 keV and 50 to 100 keV) both before and after the flare and fitted with the first order polynomial.<sup>1</sup> Since we are mostly interested in a relatively low energy range, where the transition between the high and low energy component occurs, an upper energy bound of 60 keV is chosen to avoid potential spectral steepening at even higher energies (Sui et al. 2002) and to ensure adequate counts above background throughout the period of interest. Aschwanden et al. (2002) also fitted the spectra of this flare with a single power-law from 15 to 50 keV.

We first fit with the temperature, emission measure, power-law index and normalization of the power-law component as free parameters. The results are indicated by the black lines in Figure 5.8. Both the emission measure and power-law index show significant variation during the HXR pulse. The variation of the temperature, however, is

<sup>1</sup>The time intervals chosen for fitting the background fluxes are 11:01:52 - 11:02:56 and 11:21:00 - 11:21:56 for 3 - 6 keV, 11:02:00 - 11:02:56 and 11:19:56 - 11:21:00 for 6 - 12 keV, 11:01:56 - 11:02:32 and 11:18:04 - 11:19:00 for 12 - 25 keV, 11:04:08 - 11:04:24 and 11:11:12 - 11:13:16 for 25 - 50 keV, and 11:04:20 - 11:04:48 and 11:08:04 - 11:09:04 for 50 - 100 keV. We also modeled the background fluxes for eleven energy bins from 3 to 100 keV using a third order polynomial fit with six intervals chosen around the peak time and obtained very similar spectral results.

relatively small, between 1.3 and 1.7 keV. To facilitate comparison with the theoretical model, we then fix the temperature at a typical value of 1.5 keV and do the spectral fit again. The results are indicated by the red lines in Figure 5.8. From the  $\chi^2$  of the bottom right panel, we conclude that this model gives a fit to the observations which is as good as that in the model having the temperature as a free parameter. The smaller number of free parameters also gives smaller uncertainties for other model parameters, and the emission measure (top-left panel) has a smoother evolution when the temperature is fixed. The power-law spectral indices (bottom-left panel) from both fits are almost identical and both have a soft-hard-soft evolution. The goodness of the spectral fitting is evaluated by the reduced  $\chi^2$  which is shown in the bottom-right panel. The  $\chi^2$  for both fits are very similar except during one rise time bin (11:06:04 to 11:06:08) and one decay time bin (11:06:32 to 11:06:36).

For the sake of simplicity, in the following we only use results obtained with the model temperature fixed at 1.5 keV. Figure 5.9 shows the photon spectral fit with the thermal plus power-law model for the peak time bin (11:06:20 to 11:06:24). The emission measure is  $7.69 \pm 0.18 \times 10^{47} \text{cm}^{-3}$ . The normalization of the power-law component at 50 keV is  $0.66 \pm 0.01 \text{ photons s}^{-1} \text{cm}^{-2} \text{keV}^{-1}$ . The power-law spectral index is  $3.3 \pm 0.02$ . The normalized residuals are shown below the spectrum. The residuals are between -3 and 3 with slightly larger values at 6-7 keV where the iron emission lines locate. To model this feature correctly, one needs to fit spectra from individual detectors and take into account small gain changes and pulse pile up. We focus on the transition between thermal and nonthermal components here and leave this caveat for a future investigation.

With the forward-fitted photon fluxes  $f$  obtained above, we calculated the normalized rate of change  $R(\epsilon, t) = (df(\epsilon, t)/dt)/f(\epsilon, t)$  with the same regularized method as was used on the semi-calibrated photon fluxes. Figure 5.10 shows the energy dependence of the rate of change with different colors representing different time bins. The errors are large for high energies because the photon fluxes at high energies are low and their relative errors are big. The solid lines are the model fit shown in Eq. (5.5). Notice that the 5th and 7th lines are again not fitted with the model.

According to Eqs. 5.6 and 5.7, the rate of change of the  $EM(t)$  and  $\gamma(t)$  can be obtained directly from the semi-calibrated photon flux, and from the spectral fits with the regularized method for derivatives (Kontar and MacKinnon 2005). Figure 5.11 compares the rate of change of the emission measure and the power-law spectral index with the above three methods: first with the semi-calibrated data (see Figure 5.7), second with the photon flux derived from spectral fit (see Figure 5.10), and third directly from the evolution of these parameters determined in the spectral fit (see Figure 5.8). One can see that these rates obtained with different methods are consistent. The rate of change of the emission measure is positive in most of the time bins. This indicates that the thermal emission is increasing nearly monotonically during the HXR pulse. The time evolution of  $\dot{\gamma}$  is also consistent with the soft-hard-soft evolution. The regularized method provides a powerful means to quantify this behavior.

### 5.3.4 Transition and Pivot energy

With the results obtained above, one can check the consistency of the model given by Equation (5.1) and test whether there is one pivot energy  $\epsilon_0$  for the duration of the whole

HXR pulse. The transition energy between the two temporal components  $\epsilon'_t$  and between the two spectral components  $\epsilon_t$  should be comparable if the two spectral components have distinct energy and time dependences, as expected. For results obtained with the spectral fitting in Section 5.3.3, good spectral fits will guarantee that  $\epsilon'_t$  be comparable to  $\epsilon_t$ . However, with the semi-calibrated data, these two transition energies characterized the spectral evolution in two distinct dimensions. There is no guarantee that the two spectral components will match the two temporal components self-consistently. The top panel of Figure 5.12 shows  $\epsilon_t$  and  $\epsilon'_t$  obtained from the analyses above.  $\epsilon_t$  has a relative error of a few percent and varies between 10 and 12 keV, which is consistent with a constant value of  $\sim 11$  keV. Although  $\epsilon'_t$  varies in a larger energy range of 8 to 20 keV, the relative errors are greater than 15% and its values are also consistent with a constant of  $\sim 11$  keV. The agreement of these quantities implies consistency of the model. The big error bars of  $\epsilon'_t$  are due to the uncertainty of determining the cross point of the two lines in the fitting shown in Figures 5.7 and 5.10. This may reveal a complicated physical process where the transition between the slow-varying gradual component and the impulsive component is rather an energy range than a single point.

The usual method of determining  $\epsilon_0$  by spectroscopic fitting depends on the assumed spectral model. We instead use the above rate of change study to derive  $\epsilon_0$  and its errors for each interval. From equation (5.5), one can show that the rate of change of the photon flux of the power-law component is zero at

$$\epsilon_0 = \epsilon'_t \cdot 10^{-C1/C2}. \quad (5.8)$$

This is the pivot energy at a given time interval. With parameters  $C1$ ,  $C2$ , and  $\epsilon'_t$  obtained above, we calculated the pivot energy  $\epsilon_0$  as shown in the bottom panel of Figure 5.12. The error of  $\epsilon_0$  is taken as the standard deviation of simulated  $\epsilon_0$  with 5000 sampling points of  $\epsilon'_t$ ,  $C1$ , and  $C2$  distributed within their respective  $1\sigma$  range of a Gaussian distribution. The results are consistent with a constant value of  $\sim 9$  keV except for the fourth and tenth intervals where deviations of  $\epsilon_0$  from 9 keV are greater than  $3\sigma$ . These values of the pivot energy are also less than those obtained by Battaglia and Benz (2006) for the loop top source of a few other flares, but are in agreement with these of the footpoint sources especially for values in the HXR decay phase. Since  $C1$  is mostly positive and  $C2$  evolves from positive to negative values from the HXR rise to decay phase,  $10^{-C1/C2}$  evolves from less than 1 to greater than 1, implying that  $\epsilon_0$  increases from  $\lesssim \epsilon'_t$  to  $\gtrsim \epsilon'_t$ . It should be noticed that when  $C2$  approaches zero, the amplitude of  $C1/C2$  approaches infinity and  $10^{-C1/C2}$  approaches either 0 or infinity, both of which are not physical. It also leads to huge error bars for time bins near and after the HXR peak. Indeed, a sampling of  $C2$  over a full Gaussian distribution after the peak (when  $C2 < 0$  and  $C1 > 0$ ) will lead to infinite values of  $\epsilon_0$ , whose distribution is poorly fitted with a Gaussian. Theoretically, for HXR pulses with soft-hard-soft spectral evolution, if the transition energy and temperature do not change significantly and the emission measure has a gradual and monotonic increase, the pivot energy in the decay phase should be higher than that in the rise phase, as indicated in Figure 5.12. This result is in agreement with previous studies (Grigis and Benz 2005, Battaglia and Benz 2006) and may be attributed to an effect of chromospheric evaporation (Liu et al. 2010). The pivot energy  $\epsilon_0$  is also comparable to the transition energies  $\epsilon_t$  and  $\epsilon'_t$ , in agreement with the scenario where energetic electrons are accelerated from a low-energy thermal background plasma (Benz 1977, Petrosian and Liu 2004, Grigis and

Benz 2006).

## 5.4 Discussion

We started with the hypothesis that there are two distinct emission components with low energy photons evolving gradually and high energy photons having a rapid evolution. One consequence of this is that, as long as the temperature of the thermal component varies slowly (much slower than the emission measure), which simplifies the model significantly [see eq. (5.4)], the break energy between non-thermal and thermal emission in the photon spectrum should be comparable to the transition energy between slowly- and rapidly-varying photon fluxes found by evaluating time derivatives. Within the uncertainties of this method, we have demonstrated that this is the case (top panel of Figure 5.12), and that the transition energies are always around 11 keV. However, it is clear that there are substantial error bars on the values of the transition energy  $\epsilon'_t$ , which are relatively independent of whether the spectral fitting approach (model-dependent) or the semi-calibrated approach (model independent) is used. In fact it is not possible to pin down the gradual/rapid boundary within about  $\pm 5$  keV throughout most of the flare, especially near the HXR peak. This is due to the difficulty of determining the folding point of the broken line. Better data with much higher count rates and lower statistical errors are required — for example, a more intense but equally simple flare — to examine whether or not such a boundary can be more clearly identified.

To understand further the relationship between the high and low energy emission components produced presumably by two distinct electron populations through the bremsstrahlung process, we investigate the electron numbers in each population. In one version of the standard model, it is postulated that electrons are accelerated at a reconnection current sheet and the acceleration process is decoupled from the electron transport and magnetic field evolution after the reconnection (Aschwanden 1998), which would imply an ideal Neupert effect not wholly supported by observations (Veronig et al. 2005). This scenario also encounters the well-known number problem (Fletcher and Hudson 2008). Given the high energy release during some large flares (Emslie et al. 2004, 2005), energy flows likely play more important roles than nonthermal electron fluxes in our exploration of the physics in the impulsive phase. It is possible that a significant fraction of the magnetic energy is converted into particle energies after the reconnection during the relaxation of magnetic field lines. The reconnection only permits the changes of magnetic field topology and may not correspond to the dominant energy dissipation and particle acceleration process, which can proceed after the reconnection (Fletcher and Hudson 2008). In the context of stochastic particle acceleration, it is usual to assume that electrons arriving at the chromosphere are accelerated out of a population in the loop (Petrosian and Liu 2004), therefore — assuming for simplicity no magnetic convergence — the number density of non-thermal electrons should be no larger than the loop number density. Sui et al. (2002) suggested that high-energy electrons might be accelerated from a cool background plasma not observed in X-rays. There is no observational evidence for such a cold background. Theoretically, it is also difficult to understand why the acceleration should proceed in relatively cool regions given the microphysics of particle energization by electric fields is the same for both thermal and nonthermal populations. Moreover, as we will show be-

low, the observed thermal plasma is dense enough to provide electrons responsible for the high energy emission. The assumption of a cooler background source for the high energy electrons appears to be unnecessary. In the following, we will assume that electrons producing the high energy component are accelerated from the observed thermal component. The number density of a nonthermal electron beam can be estimated as

$$n_{nth} = \frac{P_c}{\bar{E}\bar{v}_e A_{HXR}}, \quad (5.9)$$

where  $P_c$  is the power in electrons of energy greater than  $E_c$ ,  $A_{HXR}$  is the area of HXR footpoints where electrons enter the chromosphere and can be estimated from flare images,  $\bar{E}$  is the average electron energy and  $\bar{v}_e$  is the corresponding electron velocity.  $P_c$  is given by

$$P_c = \frac{A_E}{\delta - 2} (E_c/\text{keV})^{-(\delta-2)} [\text{keVs}^{-1}], \quad (5.10)$$

where  $\delta$  is the spectral index of the underlying non-thermal electron flux spectrum ( $\delta = \gamma + 1$  in the collisional thick target model),  $A_E$  is a normalization parameter and is numerically related to the photon spectrum (Brown 1971, Saint-Hilaire and Benz 2005, Fletcher et al. 2007):

$$A_E = 6.44 \times 10^{33} \frac{\gamma(\gamma - 1)}{B(\gamma - 1, 1/2)} A_\epsilon, \quad (5.11)$$

where  $B$  is the beta function, and  $A_\epsilon$  is the normalization of the power-law fit to the photon spectrum  $f(\epsilon) = A_\epsilon(\epsilon/\text{keV})^{-\gamma}$  (in photons  $\text{s}^{-1}\text{cm}^{-2}\text{keV}^{-1}$ ). It can be shown that  $\bar{E} \equiv \int_{E_c}^{\infty} F(E)E dE / \int_{E_c}^{\infty} F(E) dE = (\delta - 1)E_c / (\delta - 2)$  where  $F(E) = A_E(E/\text{keV})^{-\delta}$  is the electron flux injected into the footpoints (Brown 1971).  $\bar{v}_e \equiv \int_{E_c}^{\infty} F(E) dE / \int_{E_c}^{\infty} F(E)/v_e(E) dE = (\delta - 1/2)v_e(E_c) / (\delta - 1)$ , where we have assumed the nonthermal electron distribution is given by  $F(E)/(v_e(E)A_{HXR})$ .

The thermal electron number density is estimated as  $n_{th} = (EM/V_{SXR})^{1/2}$ , where  $EM$  is the emission measure of the thermal component and  $V_{SXR}$  is the volume of the SXR thermal coronal loop. For the sake of simplicity,  $V_{SXR}$  is evaluated as  $A_{SXR}^{3/2}$  where  $A_{SXR}$  is the projected area of the observed thermal coronal source. The areas within the 30% contours of the maximum value of 25-100 keV (for HXR source) and 6-9 keV (for SXR source) images can be obtained from the Pixion images directly. From the peak-time 20-second integrated image shown in Figure 5.2, we estimate  $A_{HXR}$  to be 20 square arcsec,  $A_{SXR}$  to be 100 square arcsec, and  $V_{SXR}$  is then about 1000 cubic arcsec. The corresponding  $n_{th}$  is greater than  $\sim 10^{11} \text{ cm}^{-3}$ .

The fraction of the thermal electrons accelerated into a non-thermal distribution  $\alpha$  should be less than 1. We then have  $n_{nth} \leq n_{th}$  and

$$\left(\frac{E_c}{\text{keV}}\right)^{-\delta+1/2} = \alpha \left(\frac{2EM}{m_e}\right)^{1/2} \frac{\delta - 1/2}{A_E} \frac{A_{HXR}}{V_{SXR}^{1/2}}. \quad (5.12)$$

Setting  $\alpha = 1$ , which would correspond to the minimum possible value of  $E_c$ , and with the parameters  $EM$ ,  $\gamma$ ,  $A_\epsilon$  from Section 5.3.3, we calculate the low limit of  $E_c$  in each 4 second time bin of the spectral fitting, and the dependence of  $E_c$  on  $EM$  and  $\gamma$  is shown in Figure 5.13. It can be seen that larger spectral index results in an increase of the minimum  $E_c$ . According to Equation 5.12, the increase of  $EM$  will lead to the decrease

of the minimum  $E_c$ . However, this effect is not as obvious as that from the changes of  $\gamma$  as shown in Figure 5.13. A comparison of low limit of  $E_c$  and the transition energies derived from variability of the semi-calibrated data ( $\epsilon'_{11}$ ), the modelled spectral data ( $\epsilon'_{12}$ ) and from the isothermal plus power-law spectral fit ( $\epsilon_t$ ) is presented in Figure 5.12. At the peak of the flare, the minimum possible  $E_c$  is around 5.2 keV, and throughout the event it is always smaller than the transition energy  $\epsilon_t$ , which is around 10 keV. This is fully consistent with the stochastic acceleration model where non-thermal electrons are accelerated from a thermal background (Benz 1977, Petrosian and Liu 2004, Grigis and Benz 2006). We note that  $\delta$  is always greater than 4 for this flare, the  $E_c$  obtained with equation (5.12) is rather insensitive to the poorly-determined source size  $A_{HXR}$  and  $A_{SXR}$ .

To accommodate reasonable uncertainties in the sizes of the HXR footpoints and SXR loop sources obtained from RHESSI imaging, we evaluate the values of  $A_{HXR}$  and  $A_{SXR}$  within reasonable limits. We show  $E_c$  versus different values of  $A_{HXR}$  (changing from 10 to 40 arcsec<sup>2</sup>) and  $A_{SXR}$  (changing from 10 to 200 arcsec<sup>2</sup>) in Figure 5.14.  $E_c$  shown in the left panel is calculated from  $\gamma$  and  $EM$  obtained from spectral fitting of the peak of flare from 11:06:20 to 11:06:24 shown in Figure 5.9.  $E_c$  of the right panel employs parameters from the spectral fitting of the time bin of 11:06:40 to 11:06:44. It is clear that with larger SXR loop and smaller footpoint size the low limit of  $E_c$  is increased. However it is not sensitive to X-ray source sizes  $A_{SXR}$  and  $A_{HXR}$ , which are not well determined from observations.

Rearranging Equation (5.12), and keeping other factors constant,  $\alpha$  and  $E_c$  vary as  $\alpha \propto E_c^{-(\delta-1/2)}$ . If we set the low-energy cutoff  $E_c \sim \epsilon_t \sim 10$  keV, with the low limit of  $E_c = 5$  keV at  $\alpha = 1$  for the flare peak where  $\delta = \gamma + 1 = 4.3$ , this gives  $\alpha = 0.07$ . In other words, accelerating 7% of the hot thermal distribution in the loop would satisfy the footpoint requirements. One may further assume that these accelerated electrons come from the high energy tail of the thermal distribution. In the tail of a Maxwellian, the fraction  $\alpha_\chi$  of electrons with energy above  $E = \chi kT$  is  $\alpha_\chi = \sqrt{4\chi/\pi} \exp(-\chi)$ , so  $\alpha = 0.07$  corresponds to  $\chi = 3.4$ . Since  $kT = 1.5$  keV, the non-thermal population would correspond to the accelerated tail of electrons with initial energy above 5.1 keV. This in turn sets a requirement that the acceleration timescale would have to be less than the electron-electron Coulomb collision timescale  $\tau_{ee}$  for an electron of energy 5.1 keV in a Maxwellian plasma of temperature 1.5 keV and density  $4.5 \times 10^{10} \text{ cm}^{-3}$  (using  $EM$ ,  $V_{SXR}$  determined above). The value of  $\tau_{ee}$  for an electron in the core of such a distribution is 0.02 s, and that for an electron of energy  $\chi kT$  is approximately  $\chi^{3/2} \tau_{ee}$  or 0.13 s in this case. Note that this threshold energy should not be compared with the transition energies in the overall photon spectra directly. The electron transport and X-ray emission processes will make the transition energy in the electron population different from that of the emitted photons. In the context of stochastic acceleration in the flare loop, a higher break energy in the overall photon spectrum than in the electron distribution in the corona acceleration site implies that the electron escape timescale from the acceleration site to the footpoints is relatively long compared to the Coulomb collision timescale at these break energies so that the HXR fluxes from the footpoints are suppressed (Petrosian and Liu 2004).

It should here be remarked that the low values obtained for  $E_c$  call into question the application of the cold collisional thick target. Emslie (2003) shows that the cold collisional thick target loss rates are overestimated for electrons of energy less than  $5 kT$ . Though we have put bounds on  $E_c$ , it remains a fit parameter, and one can instead con-

sider the energetics of an injected non-thermal electron distribution extending from  $kT$ , which merges into the ambient thermal distribution. For this event at its peak ( $\gamma = 3.3$ ) the collisional thick target power requirement above  $5kT$  is  $7.3 \times 10^{28} \text{ erg s}^{-1}$ , which is already too high compared with the total radiation energy of  $\sim 10^{29}$  ergs obtained from the GOES observation. Following the calculation of Emslie (2003) gives about 35 times as much as this in total injected power above  $kT$ , which further demonstrates the necessity of going beyond the classical cold thick target model.

The discussion above assumes a beam of electrons with a power-law distribution. Considering the pitch-angle scattering, the average electron velocity will be lower giving rise to a higher local non-thermal electron density and hence a larger  $E_c$ . Indeed, X-ray images reveal more complex structure near the transition energy between thermal and non-thermal components. The separation of the emission into two distinct components is rather ambiguous near the transition energy. It is possible that this separation is an artifact of a simplified model of X-ray spectrum and the energy dependence of the rate of change of the photon fluxes. Two distinct electron populations can be due to different physical processes, which dominate at different energies, with the electron behavior varying considerably from low to high energies and the apparent distinction between the low and high energy emission components being just a consequence of these processes.

## 5.5 Conclusions

We have developed a new method to study in detail the temporal evolution of thermal and non-thermal photon fluxes in solar flares. The application of this method to a flare on February 20 2002 demonstrates that as expected, the low energy part of the spectrum evolves slowly, and the high energy part evolves rapidly, with an intermediate range between a few keV and 20 keV where the behavior is in transition. The data support the scenario in which the non-thermal component of the flare spectrum is impulsive, and the thermal component is gradual, in that the transition energies between these two behaviors are the same within errors whether examined in time or in energy.

However, although in the spectral fitting exercise it is possible to make a clean separation between a non-thermal, impulsive component, and a thermal, gradual component, time evolution gives a more ambiguous picture, due to the large error bars. Imaging is also ambiguous, with no clear distinction between footpoints and loops in the energy range around 9-25 keV. Therefore we must leave open the possibility that the electrons form a continuous distribution over this range. Further studies with larger flares should help to improve the precision with which we can identify the transition between gradual and impulsive behavior.

Finally, the presence of a single pivot point throughout the flare is not supported by our analysis, though a pivot ‘range’ is. There is some evidence of a slightly higher value for this pivot range in the decay phase than in the rise phase.

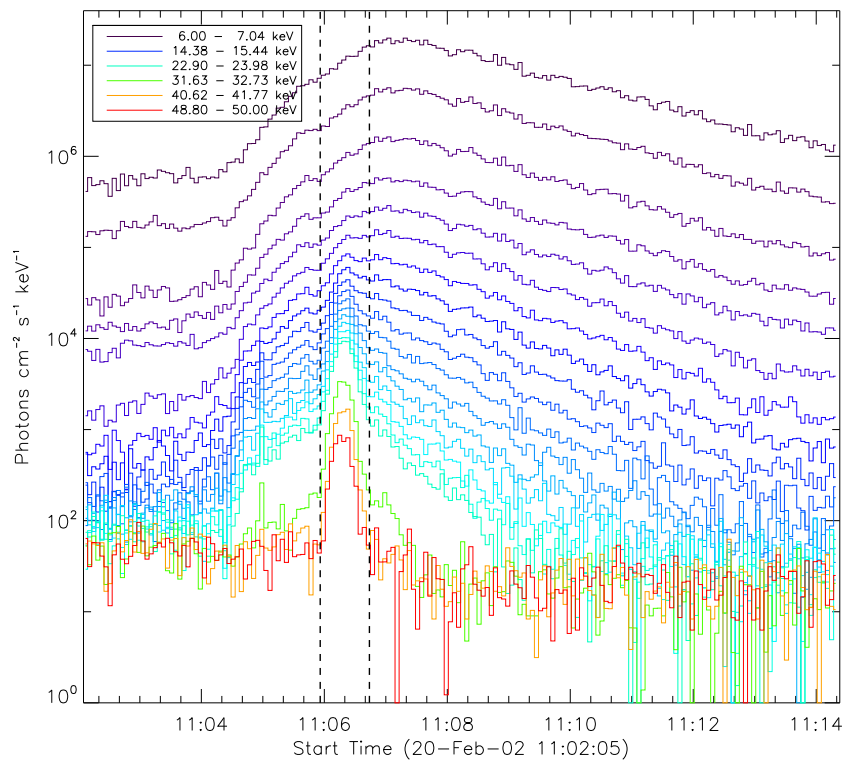


Figure 5.5: Semi-calibrated photon flux  $f(\epsilon, t)$  of the flare averaged over 4 s intervals. The curves with different colors represent photon counts in 40 different energy bands from 6 to 50 keV. The vertical dash lines represent the start (11:05:56) and end time (11:06:44) of the HXR pulse. Notice that not all of the 40 energy bands are shown.

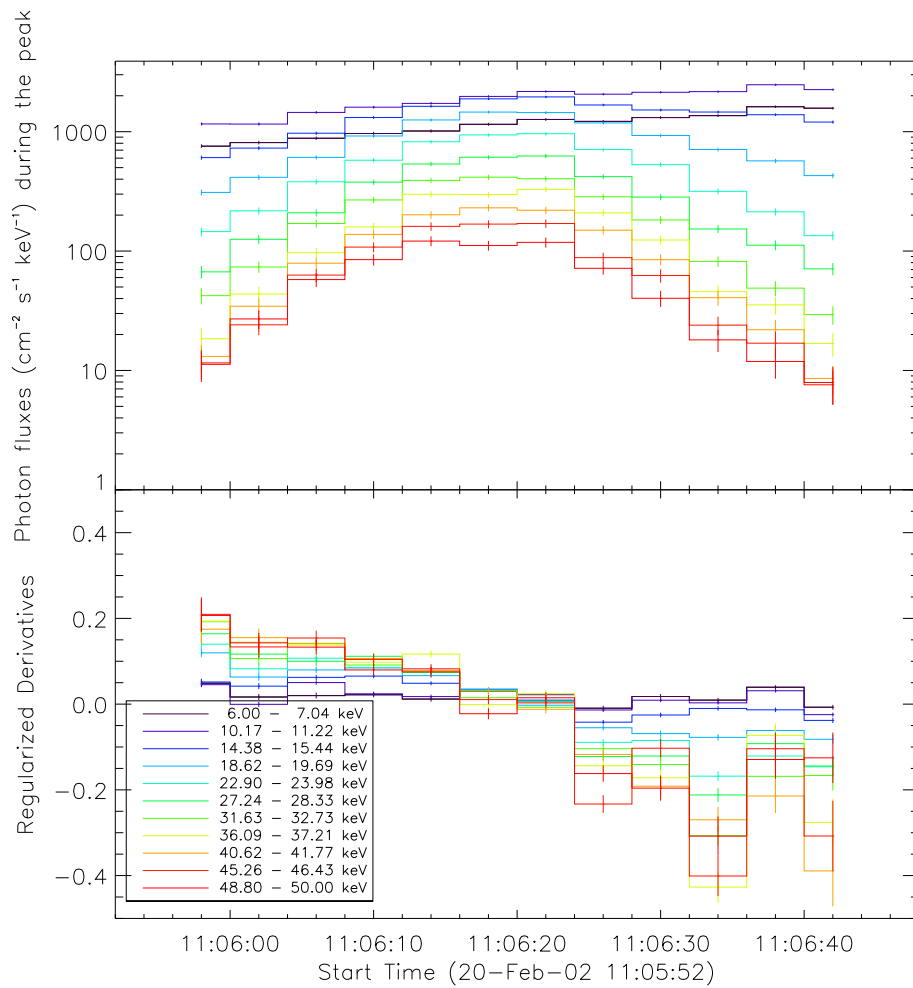


Figure 5.6: *Top*: Semi-calibrated photon flux  $f(\epsilon, t)$  and its  $\pm 1\sigma$  statistical errors during the HXR pulse (11:05:56—11:06:44). *Bottom*: The rate of change of the photon flux  $R(\epsilon, t) = df(\epsilon, t)/dt/f(\epsilon, t)$  ( $s^{-1}$ ) and its corresponding  $\pm 1\sigma$  errors calculated with the regularized method. Notice that we have shown only 11 out of the 40 energy bands.

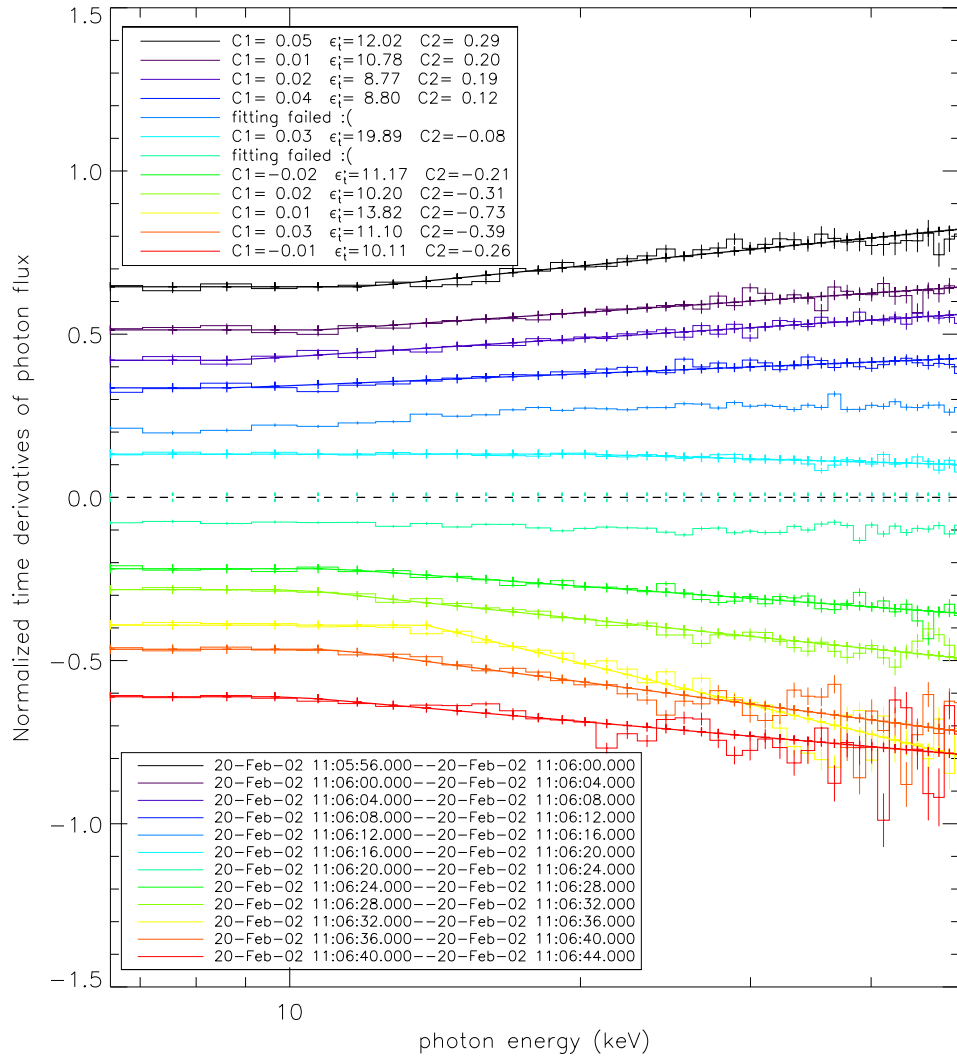


Figure 5.7: Rate of change of semi-calibrated photon flux  $R(\epsilon, t) = df(\epsilon, t)/dt/f(\epsilon, t)$  ( $s^{-1}$ ) versus the photon energy for 12 4-second time bins. The error bars give  $\pm 1\sigma$  uncertainties. The data are fitted with the model described by Equation (5.5) and the best fit models are shown as solid lines. For illustrative purpose, the lines are shifted vertically by the values of [0.6, 0.5, 0.4, 0.3, 0.2, 0.1, -0.1, -0.2, -0.3, -0.4, -0.5, -0.6] in time sequence. The fit does not converge for the fifth and seventh time intervals. The model parameters  $C1$ ,  $\epsilon_i$  and  $C2$  of the fit are indicated in the legend.

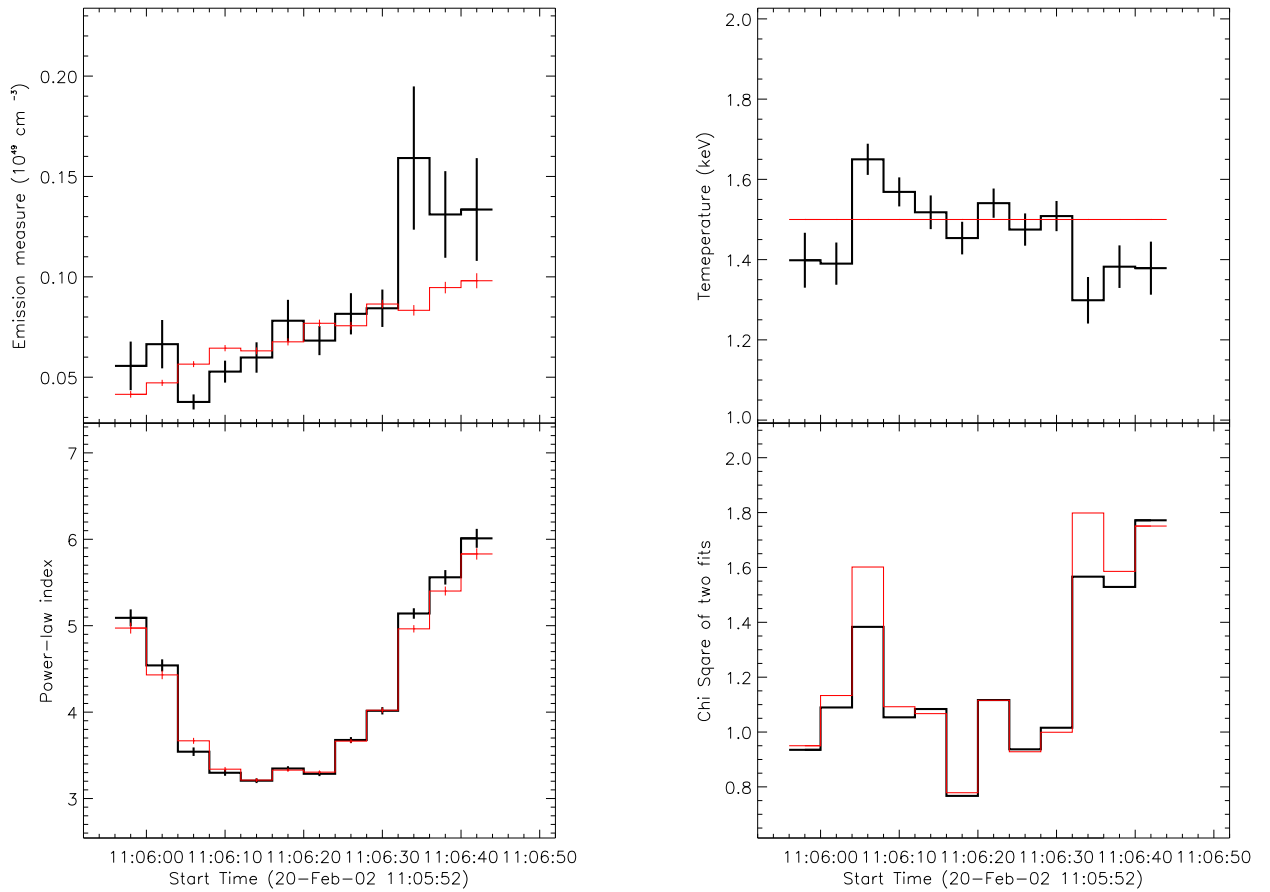


Figure 5.8: Parameters of an isothermal plus a single power-law spectral fits with temperature adjustable (thick black lines) and temperature fixed at 1.5 keV (thin red lines). The top-left, top-right, bottom-left, bottom-right panels show the emission measures, temperatures, the power-law spectral indexes, and the  $\chi^2$  of both fits, respectively.

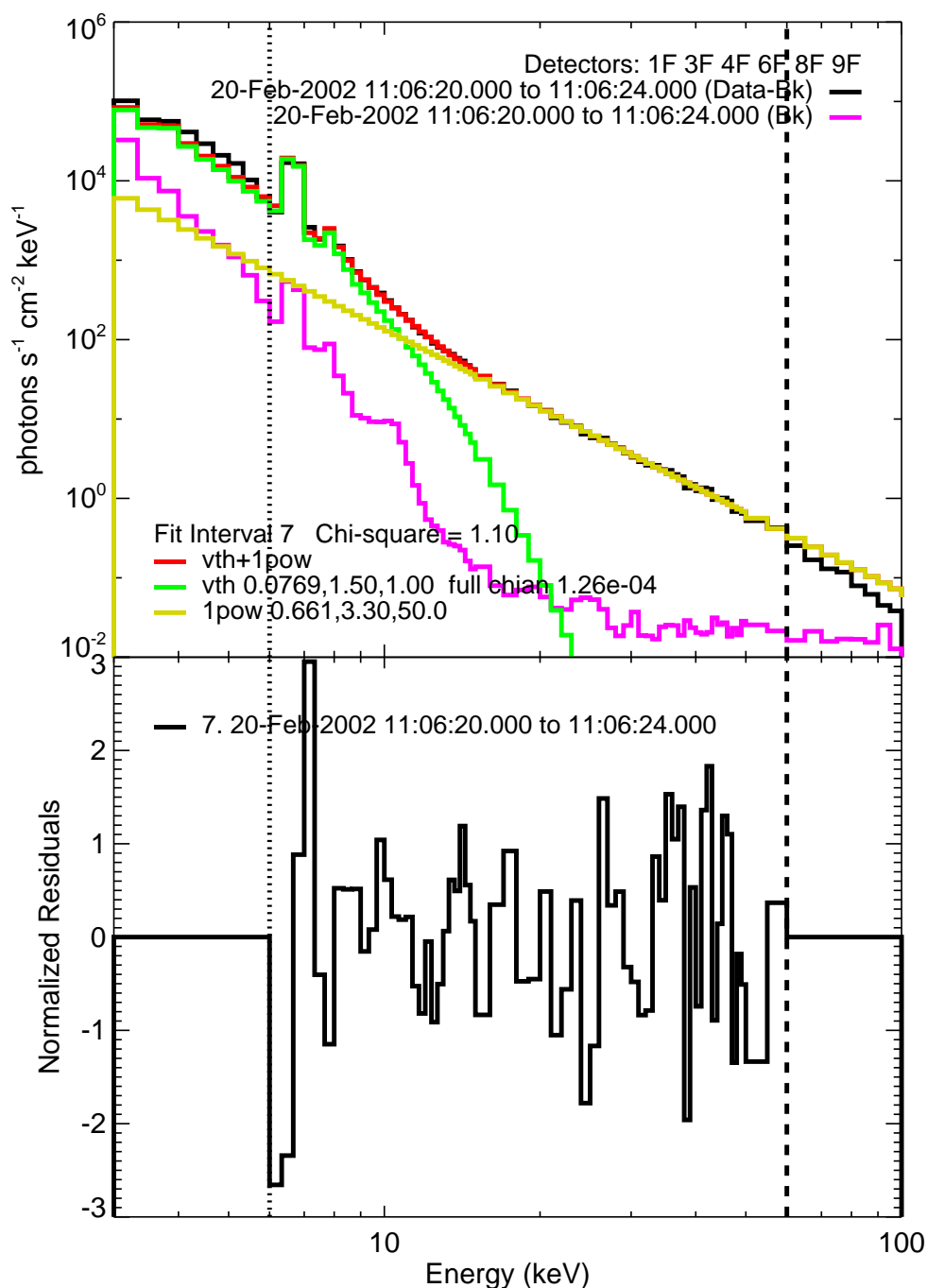


Figure 5.9: Top panel: photon flux spectrum for the peak time interval: 11:06:20 to 11:06:24. The magenta line shows the background and the black line is the photon data with background subtracted. The spectrum of data from 6 to 60 keV is fitted with an isothermal plus a single power-law model. The green line represents the thermal model and the yellow line is for the power-law model. The red line is for the total thermal plus power-law spectrum. Bottom panel: normalized residuals of the spectral fit.

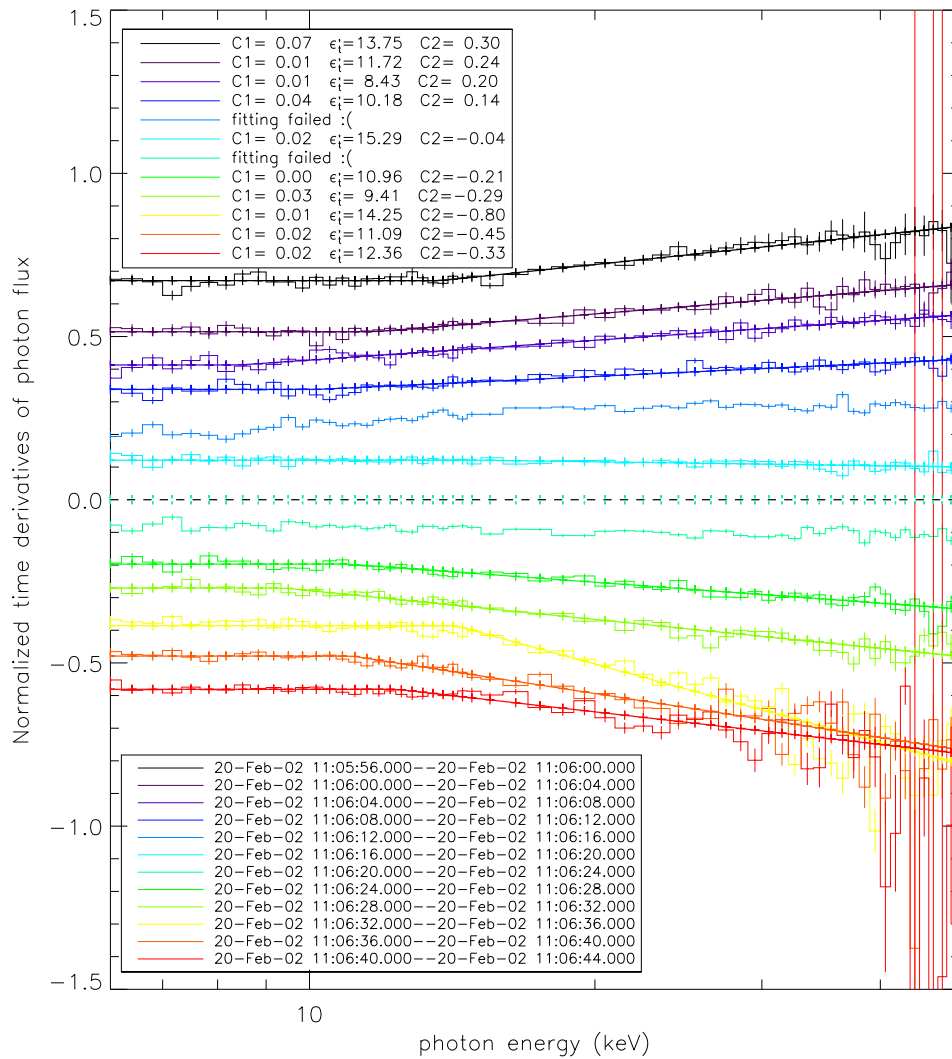


Figure 5.10: Same as Figure 5.7 ( $R(\epsilon, t)$  in  $\text{s}^{-1}$ ) but for the photon flux derived from spectral modelling.

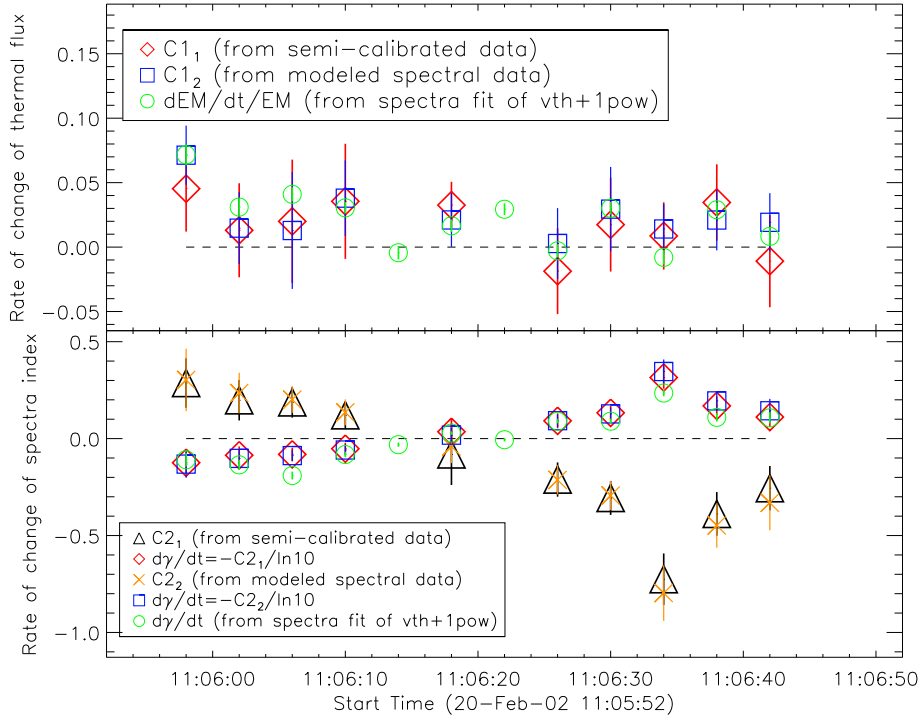


Figure 5.11: *Top panel*: comparison of the rate of change of low-energy photon flux  $C1_1$  (red diamonds) derived with the semi-calibrated data,  $C1_2$  (blue squares) with the modelled spectral data, and the rate of change of the emission measure  $\dot{EM}/EM$  (green circles). *Bottom panel*: comparison of parameters  $C2_1$  (black triangles) and  $C2_2$  (orange crosses) derived with the semi-calibrated data and modelled spectral data respectively. The rate of change of the spectral index  $\dot{\gamma}$  can be obtained from  $C2_1$  and  $C2_2$  as shown in the legend. Red diamonds, blue squares and green circles represent  $\dot{\gamma}$  from semi-calibrated photon fluxes, from modelled spectral photon fluxes, and from the time derivatives of the power-law index respectively. Error bars of  $\dot{EM}/EM$  and  $d\gamma/dt$  (both in green circles) are obtained with the regularized method. Error bars of all the other parameters indicate the  $1\sigma$  uncertainties of curve fit in Figures 5.7 and 5.10 and described by Eq. (5.5).

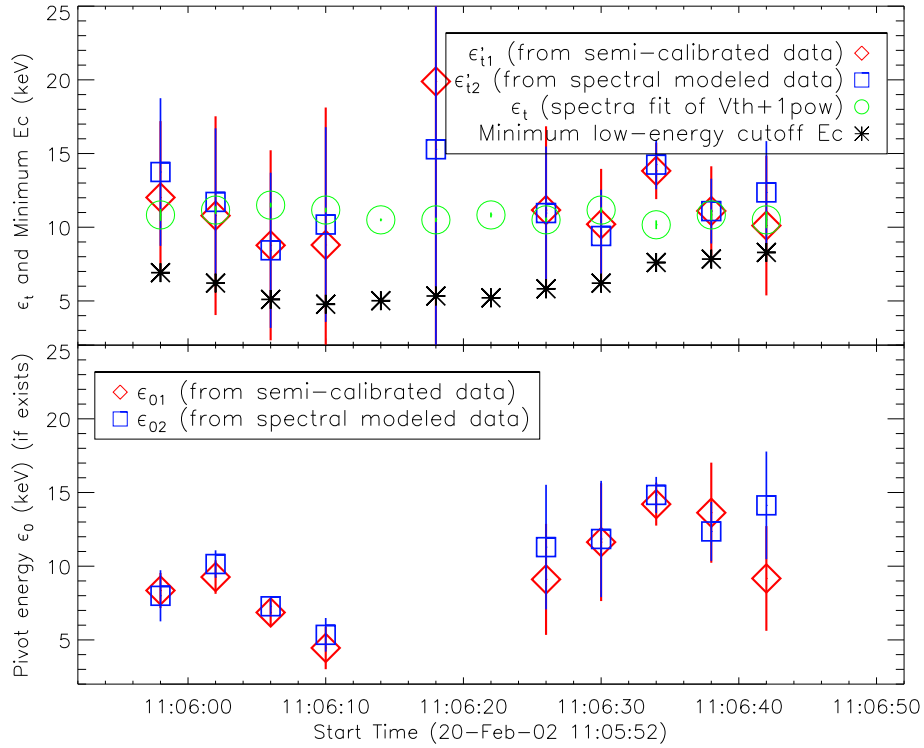


Figure 5.12: *Top panel:* evolution of the transition energy between the low and high energy component derived from variability of the semi-calibrated data (red diamonds), the modelled spectral data (blue squares) and from the isothermal plus power-law spectral fit (green circles). The error bars of  $\epsilon'_{t1}$  and  $\epsilon'_{t2}$  show, respectively, the uncertainties of curve fit in Figures 5.7 and 5.10 as described by Eq. (5.5). The error of  $\epsilon_t$  is the standard deviation of 5000 simulated intersections between thermal and nonthermal components taking into account uncertainties of all the spectral fitting parameters. Also shown is the possible minimum electron low-energy cutoff  $E_c$  (Section 5.4). *Bottom panel:* pivot energy  $\epsilon_0$  with  $1\sigma$  errors (see Section 5.3.4 for more details) derived from the variability of the semi-calibrated data (red diamonds) and modelled spectral photon fluxes (blue squares).

## 5 Relationship between Hard and Soft X-ray Emission Components

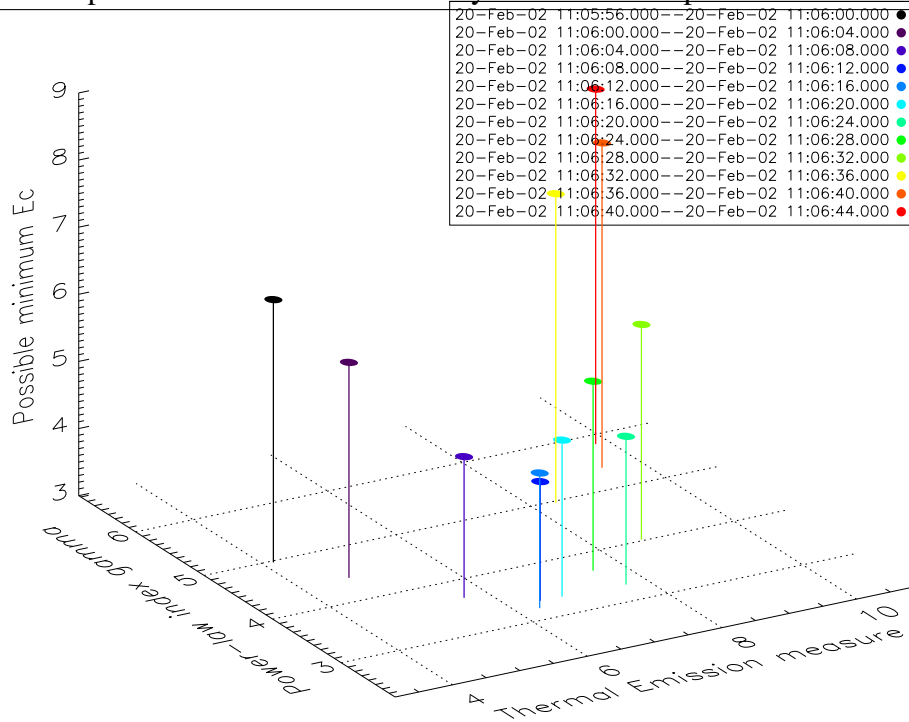


Figure 5.13: The minimum low-energy cutoff to the electron spectrum  $E_c$  (keV) in Eq. (5.12) as a function of thermal emission measure  $EM$  ( $10^{47}\text{cm}^{-3}$ ) and photon spectral index  $\gamma$ , both obtained from photon spectral fitting in Section 5.3.3. The time sequence can be traced by noting that the EM is increasing nearly monotonically during the flare peak as shown in Figure 5.8.

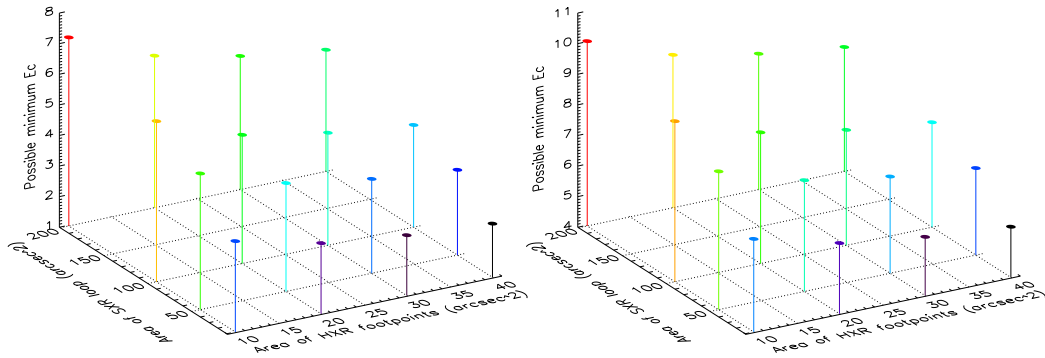


Figure 5.14: The minimum low-energy cutoff  $E_c$  (keV) as a function of the size of SXR source  $A_{SXR}$  ( $\text{arcsec}^2$ ) and size of HXR footprints  $A_{HXR}$  ( $\text{arcsec}^2$ ).  $A_{SXR}$  and  $A_{HXR}$  change between 10 to 200 and 10 to 40  $\text{arcsec}^2$  respectively. *Left panel:*  $\gamma = 3.3$  and  $EM = 7.7 \times 10^{47}\text{cm}^{-3}$  as parameters for the calculation. *Right panel:*  $\gamma = 5.8$  and  $EM = 9.8 \times 10^{47}\text{cm}^{-3}$ .

## 6 Summary and Outlook

*There are no such things as applied sciences, only applications of science.*

*Louis Pasteur*

This dissertation focuses on the investigation of particle acceleration mechanisms and processes in the solar corona via numerical simulations along with the study of energy releases of energized electrons during solar flares with observational data. The next and final chapter will present a summary of our work and results, including an outline of potential future research and aims.

### **Summary of Test Particle Simulations in Convective Electric Fields at X-type Magnetic Nulls**

Particle acceleration mechanisms at a three-dimensional magnetic null point in the solar corona have been investigated for the first time considering self-consistent magnetic fields, plasma flows and the corresponding convective electric fields obtained from MHD simulations (Chapter 2 and 3). A full-orbit relativistic test-particle approach has been employed to study the orbits and energies of charged particles (both protons and electrons) around the numerical magnetic null point. In the 3-D MHD simulation part, the initial magnetic field configuration is set to be a potential field obtained by extrapolation from an analytic quadrupolar photospheric magnetic field with a typically observed magnitude. The configuration is chosen in such a way that the resulting coronal magnetic field contains a null. Driven by the photospheric plasma motion, the MHD simulation reveals the coronal plasma motion and the self-consistent electric and magnetic fields. In a subsequent test particle experiment the particle energies and orbits, determined by the forces exerted by the convective electric field and the magnetic field around the null, are calculated in time. Test particle calculations in the MHD fields show that protons can be accelerated up to 30 keV near the magnetic null if the local plasma flow velocity is of the order of 1000 km/s (in solar active regions). Since the final parallel velocity is much larger than the perpendicular velocity, the accelerated particles can escape from the null along the magnetic field lines. Stronger convection electric field can accelerate protons up to 2 MeV and electrons to 3 keV. To summarize, the 3-D null can act as an effective accelerator for protons but not for electrons through its convective electric field, as the result of magnetic nonuniform drifts and de-magnetization processes. Protons are more easily de-magnetized and accelerated than electrons given their larger Larmor radii.

Chapter 4 describes the study of a slow-reconnecting magnetic null point for comparing the acceleration efficiencies of magnetic null points with similar magnetic field structure but different plasma flow patterns. With a similar MHD model as used in Chapter 2, a longer simulation of the quadrupolar magnetic field has been studied by Santos et al. (2011) and stagnation flows are generated around the X-type Null point which is a sign of slow-reconnecting process. We studied proton accelerations under different initial energies and different magnitudes of convective electric fields around the null. It is clearly shown that with stronger  $\mathbf{E}_{con}$ , i.e. stronger convection plasma flow, the final energies of the protons are significantly enlarged. At a given value of electric fields, the final maximum energy  $Ek_{max}$  of 1000 protons with a higher initial energy is larger than that of protons with a lower initial energy because particles with higher initial energies are more demagnetized. The final minimum energies  $Ek_{min}$  decrease when the initial energies are increased also due to the stronger demagnetization of more energized particles. The values of final average energies  $Ek_{avg}$  do not depend on the initial proton energies when the convective electric fields are larger than  $\sim 1.2$  V/m. For both the old X-null and the new X-null, higher electric fields result in higher final average energies, more efficient acceleration, and larger deviations of final energies. The new null is a more effective accelerator compared to the old null due to its different pattern of plasma flow. However, both the old and the new X-nulls can only accelerate electrons moderately due to the strong magnetization of electrons in the magnetic field.

## Discussions and Future Work

An X-type null point with convective electric fields (in ideal MHD) can work as a possible pre-accelerator for charged particles. This may mitigate the number problem in flare observations since the existence of magnetic null points is suggested to be common in the solar atmosphere (Longcope and Parnell 2009). However, an electric current sheet with a finite dissipation region can only energize a small amount of particles in a limited volume.

For electrons accelerated up to tens of keV and protons having energies as high as hundreds of MeV, one needs to consider other acceleration mechanisms for interpreting the observations: (a)the existence of a parallel electric field, (b)smaller (microscopic) scales of magnetic fields which enlarge the probability of demagnetization processes, and (c)temporally varying fields representing electro-magnetic waves which can cause resonant acceleration.

(a)A parallel electric field can accelerate magnetized particles directly along the magnetic fields without any interference of gyrations in the perpendicular plane. Therefore, for triggering significant acceleration of electrons and even higher energetic protons as observed in solar flares, the existence of a resistive electric field that is mainly parallel to the magnetic field is required. A physically plausible resistivity model included in resistive MHD simulations is needed for further investigation of electron acceleration by parallel electric fields.

Including (b)small (microscopic) scales of magnetic fields has always been a challenge in MHD simulations since macroscopic MHD scales are blind to microscopic magnetic structures where more non-adiabatic acceleration process might be taking place. In real solar corona, we expect a more complicated magnetic field with microscopic

non-uniform structures where particles could have more probability to experience demagnetization process and get accelerated. However, to study this process either theoretically or numerically, one needs to employ several approaches, such as turbulent acceleration theories, particle in cell simulations, and full kinetic simulations.

(c) Temporally varying fields representing electro-magnetic waves should be another effective process for energizing particles (Petkaki and MacKinnon 2007). If the frequency of the changing fields is resonant with the particle gyrofrequencies or inverse crossing-time (through the non-adiabatic regions near the null), particles are likely to be accelerated most efficiently. Note that higher frequency disturbances favour electrons over ions.

### Summary of the Relationship between Hard and Soft X-ray Emission Components

A prominent  $\sim 50$  second hard X-ray (HXR) pulse of a simple GOES class C7.5 flare on 20 February 2002 is used to study the association between high energy, non-thermal and impulsive evolution, and low energy, thermal and gradual evolution. We use regularized methods to obtain time derivatives of photon fluxes to quantify the time evolution as a function of photon energy, obtaining a break energy between impulsive and gradual behaviour. These break energies are consistent with a constant value of  $\sim 11$  keV in agreement with those found spectroscopically between thermal and non-thermal components, but the relative errors of the former are greater than 15% and much greater than a few percent errors found from the spectral fitting. These errors only weakly depend on assuming an underlying spectral model for the photons, pointing to the current data being inadequate to reduce the uncertainties rather than the result of a problem associated with an assumed model. The time derivative method is used to test for the presence of a ‘pivot energy’ in this flare. Although these pivot energies are marginally consistent with a constant value of  $\sim 9$  keV, its values in the HXR rise phase appear to be lower than those in the decay phase. Assuming that electrons producing the high-energy component have a power law distribution and are accelerated from relatively hot regions of a background plasma responsible for the observed thermal component, a low limit is obtained for the low-energy cutoff. This limit is always lower than the break and pivot energies and locates in the tail of the Maxwellian distribution of the thermal component.

### Discussions and Outlook

We started with the hypothesis that there are two distinct emission components with low energy photons evolving gradually and high energy photons having a rapid evolution. One consequence of this is that, as long as the temperature of the thermal component varies slowly (much slower than the emission measure), which simplifies the model significantly, the break energy between non-thermal and thermal emission in the photon spectrum should be comparable to the transition energy between slowly- and rapidly-varying photon fluxes found by evaluating time derivatives. Within the uncertainties of this method, we have demonstrated that the transition energies are always around 11 keV. However, it is clear that there are substantial error bars on the values of the transition energy  $\epsilon'_t$ , which are relatively independent of whether the spectral fitting approach (model-dependent) or the semi-calibrated approach (model independent) is used. In fact, it is not possible to pin down the gradual/rapid boundary within about  $\pm 5$  keV throughout most

of the flare, especially near the HXR peak. This is due to the difficulty of determining the folding point of the broken line. Better data with much higher count rates and lower statistical errors are required — for example, a more intense but equally simple flare — to examine whether or not such a boundary can be more clearly identified.

Although in the spectral fitting exercise it is possible to make a clean separation between a non-thermal, impulsive component, and a thermal, gradual component, time evolution gives a more ambiguous picture due to the large error bars. Imaging is also ambiguous, with no clear distinction between footpoints and loops in the energy range around 9-25 keV. Hence, we must leave open the possibility that the electrons form a continuous distribution over this range. Further studies with larger flares should help improving the precision with which we can identify the transition between gradual and impulsive behaviour.

# A Normalization of the MHD Equations

The basic dimensional resistive MHD equations includes the continuity equation (1.11), the momentum equation (1.12) and the energy equation (1.13) together with Maxwell equations including the Faraday Theory (1.14), Ampere's law (1.15) and Ohm's law (1.16), as well as the equation of state (1.17) for fully ionized plasmas. The normalization parameters of the MHD equations are shown in Table A.1. There are three free normalization parameters:  $B_0$ ,  $L_0$  and  $n_0$ . All the other normalization parameters are related and therefore determined by these three parameters as show in the table.

The radiation heating function  $Q$  in the energy equation (1.13) is neglected in this MHD model. The momentum equation in the current model introduces a viscous term  $\nu\rho(\mathbf{u} - \mathbf{u}_0)$  representing for the transfer of momentum between the neutral gas and the plasma. The neutral gas velocity  $\mathbf{u}_0$  is set to be a horizontal vortex  $\mathbf{u}_n = \nabla \times (U\mathbf{e}_z)$  where  $U$  is a scalar potential in order to keep  $\nabla \cdot \mathbf{u}_n = \mathbf{0}$  to inhibit a pilling up of plasma and magnetic field. The collision between the neutral gas and the plasma is the driver of the MHD evolution: The plasma interacts with the neutral gas with collision frequency  $\nu$  and is therefore dragged behind. The collision frequency  $\nu$  is height dependent, larger at the lower box and smaller at the higher box. So the plasmas in the lower box (normally representing for hotosphere and chromosphere) are coupled with neutral gas motion and

Table A.1: Normalization Parameters of the MHD Equations

Dimensional Values	Normalization	Model 1	Model 2	
magnetic field $\mathbf{B}$	$= B_0\mathbf{B}'$	$B_0$ (T)	$10^{-4}$	$10^{-2}$
length $L$	$= L_0L'$	$L_0$ (m)	$5 \times 10^5$	$10^6$
mass density $\rho$	$= \rho_0\rho' = m_p n_0\rho'$	$n_0$ ( $\text{m}^{-3}$ )	$2 \times 10^{15}$	$2 \times 10^{15}$
flow velocity $\mathbf{u}$	$= v_0\mathbf{u}' = \frac{B_0}{\sqrt{\mu_0\rho_0}}\mathbf{u}'$	$v_0$ (m/s)	$5 \times 10^4$	$5 \times 10^6$
time $t$	$= t_0t' = \frac{L_0}{v_0}t'$	$t_0$ (s)	10	0.2
pressure $p$	$= p_0p' = \frac{B_0^2}{2\mu_0}p'$	$p_0$ (Pa)	0.004	4
temperature $T$	$= T_0T' = \frac{p_0}{2n_0k_B}T'$	$T_0$ (K)	$7.2 \times 10^4$	$7.2 \times 10^7$
electric field $\mathbf{E}$	$= E_0\mathbf{E}' = v_0B_0\mathbf{E}'$	$E_0$ (V/m)	5	$5 \times 10^4$
current density $\mathbf{j}$	$= j_0\mathbf{j}' = \frac{B_0}{\mu_0L_0}\mathbf{j}'$	$j_0$ ( $\text{A}/\text{m}^2$ )	$1.6 \times 10^{-4}$	$8 \times 10^{-3}$
resistivity $\eta$	$= \eta_0\eta' = \mu_0L_0v_0\eta'$	$\eta_0$ (ohm-m)	$3.1 \times 10^4$	$6 \times 10^6$
collision frequency $\nu$	$= \nu_0\nu' = \frac{1}{t_0}\nu'$	$\nu_0$ ( $\text{s}^{-1}$ )	0.1	5

plasmas in the higher box (generally considered to be corona region) are decoupled with neutral gas velocities. The whole evolution of an initial equilibrium magnetic field is driven by this plasma velocity pattern.

The normalization processes are as following.

*Continuity equation:*

$$\begin{aligned}
\frac{\partial \rho}{\partial t} &= -\nabla \cdot \rho \mathbf{u} \Rightarrow \\
\frac{\rho_0}{t_0} \frac{\partial \rho'}{\partial t'} &= -\frac{\rho_0 v_0}{L_0} \nabla \cdot \rho' \mathbf{u}' \Rightarrow \\
\frac{\partial \rho'}{\partial t'} &= -\nabla \cdot \rho' \mathbf{u}' \tag{A.1}
\end{aligned}$$

*Momentum equation:*

$$\begin{aligned}
\frac{\partial \rho \mathbf{u}}{\partial t} &= -\nabla \cdot \rho \mathbf{u} \mathbf{u} - \nabla p + \mathbf{j} \times \mathbf{B} - \nu \rho (\mathbf{u} - \mathbf{u}_0) \Rightarrow \\
\frac{\partial \rho \mathbf{u}}{\partial t} &= -\nabla \cdot \rho \mathbf{u} \mathbf{u} - \nabla p + \frac{1}{\mu_0} \nabla \times \mathbf{B} \times \mathbf{B} - \nu \rho (\mathbf{u} - \mathbf{u}_0) \Rightarrow \\
\frac{\partial \rho \mathbf{u}}{\partial t} &= -\nabla \cdot \left[ \rho \mathbf{u} \mathbf{u} + \left( p + \frac{B^2}{2\mu_0} \right) \mathbf{I} - \frac{\mathbf{B} \mathbf{B}}{\mu_0} \right] - \nu \rho (\mathbf{u} - \mathbf{u}_0) \Rightarrow \text{(normalization)} \\
\frac{\rho_0 v_0}{t_0} \frac{\partial \rho' \mathbf{u}'}{\partial t'} &= -\frac{1}{L_0} \nabla \cdot \left[ \rho_0 v_0^2 \rho' \mathbf{u}' \mathbf{u}' + \left( p_0 p' + \frac{B_0^2 B'^2}{2\mu_0} \right) \mathbf{I} - B_0^2 \frac{\mathbf{B}' \mathbf{B}'}{\mu_0} \right] - \frac{\rho_0 v_0}{t_0} \nu' \rho' (\mathbf{u}' - \mathbf{u}_0') \Rightarrow \\
\frac{\partial \rho' \mathbf{u}'}{\partial t'} &= -\frac{t_0}{\rho_0 v_0} \frac{1}{\nu_0 t_0} \nabla \cdot \left[ \rho_0 v_0^2 \rho' \mathbf{u}' \mathbf{u}' + \frac{B_0^2}{2\mu_0} (p' + B'^2) \mathbf{I} - B_0^2 \frac{\mathbf{B}' \mathbf{B}'}{\mu_0} \right] - \nu' \rho' (\mathbf{u}' - \mathbf{u}_0') \Rightarrow \\
\frac{\partial \rho' \mathbf{u}'}{\partial t'} &= -\nabla \cdot \left[ \rho' \mathbf{u}' \mathbf{u}' + \frac{1}{2\nu_0^2 \rho_0 \mu_0} B_0^2 (p' + B'^2) \mathbf{I} - \frac{B_0^2}{\nu_0^2 \rho_0 \mu_0} \mathbf{B}' \mathbf{B}' \right] - \nu' \rho' (\mathbf{u}' - \mathbf{u}_0') \Rightarrow \\
\frac{\partial \rho' \mathbf{u}'}{\partial t'} &= -\nabla \cdot \left[ \rho' \mathbf{u}' \mathbf{u}' + \frac{1}{2} (p' + B'^2) \mathbf{I} - \mathbf{B}' \mathbf{B}' \right] - \nu' \rho' (\mathbf{u}' - \mathbf{u}_0') \tag{A.2}
\end{aligned}$$

*Induction equation:*

$$\begin{aligned}
\frac{\partial \mathbf{B}}{\partial t} &= \nabla \times (\mathbf{u} \times \mathbf{B} - \eta \mathbf{j}) \Rightarrow \\
\frac{B_0}{t_0} \frac{\partial \mathbf{B}}{\partial t'} &= \frac{1}{L_0} \nabla \times (\nu_0 B_0 \mathbf{u}' \times \mathbf{B}' - \eta_0 j_0 \eta' \mathbf{j}') \Rightarrow \\
\frac{\partial \mathbf{B}'}{\partial t'} &= \frac{t_0}{B_0 L_0} \nabla \times (\nu_0 B_0 \mathbf{u}' \times \mathbf{B}' - \mu_0 L_0 \nu_0 \frac{B_0}{\mu_0 L_0} \eta' \mathbf{j}') \Rightarrow \\
\frac{\partial \mathbf{B}'}{\partial t'} &= \nabla \times (\mathbf{u}' \times \mathbf{B}' - \eta' \mathbf{j}') \tag{A.3}
\end{aligned}$$

*Energy equation:*

$$\begin{aligned}
 \frac{\partial p}{\partial t} &= -\nabla \cdot p\mathbf{u} - (\gamma - 1)p\nabla \cdot \mathbf{u} + (\gamma - 1)\eta\mathbf{j}^2 \Rightarrow \\
 \frac{p_0}{t_0} \frac{\partial p'}{\partial t'} &= -\frac{p_0 v_0}{L_0} \nabla \cdot p'\mathbf{u}' - \frac{p_0 v_0}{L_0} (\gamma - 1)p'\nabla \cdot \mathbf{u}' + \frac{\mu_0 L_0 v_0 B_0^2}{(\mu_0 L_0)^2} (\gamma - 1)\eta'\mathbf{j}'^2 \Rightarrow \\
 \frac{\partial p'}{\partial t'} &= -\nabla \cdot p'\mathbf{u}' - (\gamma - 1)p'\nabla \cdot \mathbf{u}' + \frac{t_0 v_0 B_0^2}{p_0 \mu_0 L_0} (\gamma - 1)\eta'\mathbf{j}'^2 \Rightarrow \\
 \frac{\partial p'}{\partial t'} &= -\nabla \cdot p'\mathbf{u}' - (\gamma - 1)p'\nabla \cdot \mathbf{u}' + \frac{2\mu_0 B_0^2}{B_0^2 \mu_0} (\gamma - 1)\eta'\mathbf{j}'^2 \Rightarrow \\
 \frac{\partial p'}{\partial t'} &= -\nabla \cdot p'\mathbf{u}' - (\gamma - 1)p'\nabla \cdot \mathbf{u}' + 2(\gamma - 1)\eta'\mathbf{j}'^2 \tag{A.4}
 \end{aligned}$$

Replace pressure with  $h = \left(\frac{p'}{2}\right)^{\frac{1}{\gamma}}$  to obtain:

$$\begin{aligned}
 \frac{\partial p'}{\partial t'} &= -\nabla \cdot p'\mathbf{u}' - (\gamma - 1)p'\nabla \cdot \mathbf{u}' + 2(\gamma - 1)\eta'\mathbf{j}'^2 \Rightarrow \\
 2\frac{\partial h^\gamma}{\partial t'} &= -2\nabla \cdot h^\gamma\mathbf{u}' - 2(\gamma - 1)h^\gamma\nabla \cdot \mathbf{u}' + 2(\gamma - 1)\eta'\mathbf{j}'^2 \Rightarrow \\
 \gamma h^{\gamma-1} \frac{\partial h}{\partial t'} &= -h^\gamma\nabla \cdot \mathbf{u}' - \mathbf{u}' \cdot \nabla h^\gamma - (\gamma - 1)h^\gamma\nabla \cdot \mathbf{u}' + (\gamma - 1)\eta'\mathbf{j}'^2 \Rightarrow \\
 \gamma h^{\gamma-1} \frac{\partial h}{\partial t'} &= -\mathbf{u}' \cdot \nabla h^\gamma - \gamma h^\gamma\nabla \cdot \mathbf{u}' + (\gamma - 1)\eta'\mathbf{j}'^2 \Rightarrow \\
 \gamma h^{\gamma-1} \frac{\partial h}{\partial t'} &= -\gamma h^{\gamma-1}\mathbf{u}' \cdot \nabla h - \gamma h^\gamma\nabla \cdot \mathbf{u}' + (\gamma - 1)\eta'\mathbf{j}'^2 \Rightarrow \\
 \frac{\partial h}{\partial t'} &= -\mathbf{u}' \cdot \nabla h - h\nabla \cdot \mathbf{u}' + \frac{(\gamma - 1)}{\gamma h^{\gamma-1}}\eta'\mathbf{j}'^2 \Rightarrow \\
 \frac{\partial h}{\partial t'} &= -\nabla \cdot h\mathbf{u}' + \frac{(\gamma - 1)}{\gamma} h^{1-\gamma}\eta'\mathbf{j}'^2 \tag{A.5}
 \end{aligned}$$

*Ohm's law:*

$$\begin{aligned}
 \mathbf{E} &= -\mathbf{u} \times \mathbf{B} + \eta\mathbf{j} \Rightarrow \\
 E_0\mathbf{E}' &= -v_0 B_0 \mathbf{u}' \times \mathbf{B}' + \mu_0 L_0 v_0 \frac{B_0}{\mu_0 L_0} \eta'\mathbf{j}' \Rightarrow \\
 \mathbf{E}' &= -\mathbf{u}' \times \mathbf{B}' + \eta'\mathbf{j}' \tag{A.6}
 \end{aligned}$$

*Ampere's law:*

$$\begin{aligned}
 \nabla \times \mathbf{B} &= \mu_0\mathbf{j} \Rightarrow \\
 \frac{B_0}{L_0} \nabla \times \mathbf{B}' &= \mu_0 \frac{B_0}{\mu_0 L_0} \mathbf{j}' \Rightarrow \\
 \nabla \times \mathbf{B}' &= \mathbf{j}' \tag{A.7}
 \end{aligned}$$

*State equation:*

$$\begin{aligned} p &= n_i k_B T + n_e k_B T \approx 2n k_B T \Rightarrow \\ p_0 p' &= n_0 T_0 2n' k_B T' \Rightarrow \\ 2n_0 k_B T_0 p' &= n_0 T_0 2n' k_B T' \Rightarrow \\ p' &= n' T' \end{aligned} \tag{A.8}$$

## B Magnetic Field Extrapolation

We used a four mode Fourier expansion for the potential extrapolation of the quadrupolar magnetic field (Guo et al. 2010). We considered a square geometry ( $L_x = L_y = L$ ) and line symmetry condition at four side boundaries (Otto et al. 2007).

### Force-free Condition

To obtain the final quadrupolar potential magnetic fields, we start from the force-free condition ( $\mathbf{j} \times \mathbf{B} = \mathbf{0}$ ) of the magnetic field:

$$\nabla \times \mathbf{B} = \kappa \mathbf{B}, \quad (\text{B.1})$$

assuming an expansion in the form

$$\begin{aligned} B_x &= \exp(-\lambda z) (c_{1x} \sin \alpha x \cos \beta y + c_{2x} \cos \alpha x \sin \beta y) \\ B_y &= \exp(-\lambda z) (c_{1y} \sin \alpha x \cos \beta y + c_{2y} \cos \alpha x \sin \beta y) \\ B_z &= c_z \exp(-\lambda z) \sin \alpha x \sin \beta y. \end{aligned}$$

Computing  $\nabla \times \mathbf{B}$  and considering Equation B.1, one obtains the relations of the param-

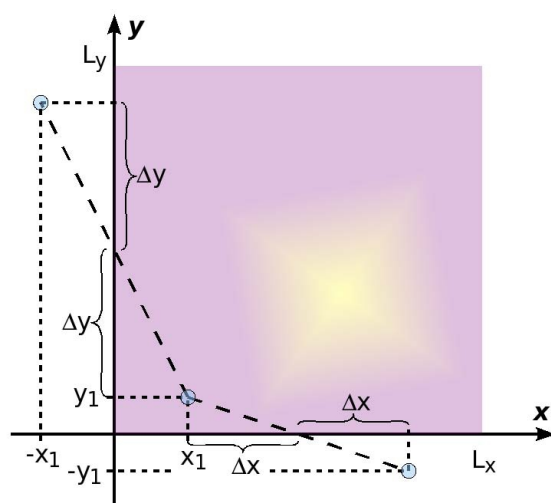


Figure B.1: Line periodic symmetry boundary conditions in the domain  $0 < x < L_x$  and  $0 < y < L_y$ , adapted from Otto et al. (2007)

eters:

$$\begin{aligned}
 c_{1x} &= \frac{\beta\kappa}{\kappa^2 + \lambda^2} c_z \\
 c_{2x} &= -\frac{\alpha\lambda}{\kappa^2 + \lambda^2} c_z \\
 c_{1y} &= -\frac{\beta\lambda}{\kappa^2 + \lambda^2} c_z \\
 c_{2y} &= -\frac{\alpha\kappa}{\kappa^2 + \lambda^2} c_z \\
 \kappa^2 + \lambda^2 &= \alpha^2 + \beta^2
 \end{aligned} \tag{B.2}$$

**Line Symmetry in the Domain  $0 < x < L_x$  and  $0 < y < L_y$**

We assume Fourier expansion:

$$\begin{aligned}
 \Psi_{mn} &= c_1 \sin \frac{\pi m}{L_x} x \sin \frac{\pi n}{L_y} y + c_2 \sin \frac{\pi m}{L_x} x \cos \frac{\pi n}{L_y} y \\
 &+ c_3 \cos \frac{\pi m}{L_x} x \sin \frac{\pi n}{L_y} y + c_4 \cos \frac{\pi m}{L_x} x \cos \frac{\pi n}{L_y} y
 \end{aligned}$$

in a domain  $0 < x < L_x$  and  $0 < y < L_y$ . Considering line symmetry condition (Figure B.1) at four boundaries:

$$\begin{aligned}
 y = 0 & : \Psi_{mn}(L_x - x, -y) = \Psi_{mn}(x, y) \\
 y = L_y & : \Psi_{mn}(L_x - x, 2L_y - y) = \Psi_{mn}(x, y) \\
 x = 0 & : \Psi_{mn}(-x, L_y - y) = \Psi_{mn}(x, y) \\
 x = L_x & : \Psi_{mn}(2L_x - x, L_y - y) = \Psi_{mn}(x, y),
 \end{aligned} \tag{B.3}$$

one obtains that the parameters  $c_1 = c_4 = 0$  when  $m$  is odd and that  $c_2 = c_3 = 0$  when  $m$  is even. The expansion of  $\Psi$  is then:

$$\begin{aligned}
 \Psi &= \sum_{m,n \text{ odd}} \left[ c_{mn}^{(2)} \sin \frac{\pi m}{L_x} x \cos \frac{\pi n}{L_y} y + c_{mn}^{(3)} \cos \frac{\pi m}{L_x} x \sin \frac{\pi n}{L_y} y \right] \\
 &+ \sum_{m,n \text{ even}} \left[ c_{mn}^{(1)} \sin \frac{\pi m}{L_x} x \sin \frac{\pi n}{L_y} y + c_{mn}^{(4)} \cos \frac{\pi m}{L_x} x \cos \frac{\pi n}{L_y} y \right]
 \end{aligned}$$

### Complete Solution of Force-free Magnetic Fields

With the solutions of the sin sin and cos cos terms derived in Equation B.2, we have

the complete solution as following with  $\alpha_m = \pi m/L_x$ ,  $\beta_n = \pi n/L_y$ , and  $\lambda_{mn}^2 = \alpha_m^2 + \beta_n^2 - \kappa^2$ :

$$\begin{aligned}
 B_x &= \sum_{m,n \text{ even}, m+n>0} \frac{\exp(-\lambda_{mn}z)}{\kappa^2 + \lambda_{mn}^2} \left[ c_{mn}^{(1)} (\beta_n \kappa \sin \alpha_m x \cos \beta_n y - \alpha_m \lambda_{mn} \cos \alpha_m x \sin \beta_n y) \right. \\
 &\quad \left. + c_{mn}^{(4)} (\alpha_m \lambda_{mn} \sin \alpha_m x \cos \beta_n y - \beta_n \kappa \cos \alpha_m x \sin \beta_n y) \right] \\
 &\quad + \sum_{m,n \text{ odd}} \frac{\exp(-\lambda_{mn}z)}{\kappa^2 + \lambda_{mn}^2} \left[ c_{mn}^{(2)} (-\beta_n \kappa \sin \alpha_m x \sin \beta_n y - \alpha_m \lambda_{mn} \cos \alpha_m x \cos \beta_n y) \right. \\
 &\quad \left. + c_{mn}^{(3)} (\alpha_m \lambda_{mn} \sin \alpha_m x \sin \beta_n y + \beta_n \kappa \cos \alpha_m x \cos \beta_n y) \right] \\
 B_y &= \sum_{m,n \text{ even}, m+n>0} \frac{\exp(-\lambda_{mn}z)}{\kappa^2 + \lambda_{mn}^2} \left[ c_{mn}^{(1)} (-\beta_n \lambda_{mn} \sin \alpha_m x \cos \beta_n y - \alpha_m \kappa \cos \alpha_m x \sin \beta_n y) \right. \\
 &\quad \left. + c_{mn}^{(4)} (\alpha_m \kappa \sin \alpha_m x \cos \beta_n y + \beta_n \lambda_{mn} \cos \alpha_m x \sin \beta_n y) \right] \\
 &\quad + \sum_{m,n \text{ odd}} \frac{\exp(-\lambda_{mn}z)}{\kappa^2 + \lambda_{mn}^2} \left[ c_{mn}^{(2)} (\beta_n \lambda_{mn} \sin \alpha_m x \sin \beta_n y - \alpha_m \kappa \cos \alpha_m x \cos \beta_n y) \right. \\
 &\quad \left. + c_{mn}^{(3)} (\alpha_m \kappa \sin \alpha_m x \sin \beta_n y - \beta_n \lambda_{mn} \cos \alpha_m x \cos \beta_n y) \right] \\
 B_z &= \sum_{m,n \text{ even}, m+n>0} \exp(-\lambda_{mn}z) \left[ c_{mn}^{(1)} \sin \alpha_m x \sin \beta_n y + c_{mn}^{(4)} \cos \alpha_m x \cos \beta_n y \right] \\
 &\quad + \sum_{m,n \text{ odd}} \exp(-\lambda_{mn}z) \left[ c_{mn}^{(2)} \sin \alpha_m x \cos \beta_n y + c_{mn}^{(3)} \cos \alpha_m x \sin \beta_n y \right] \quad (\text{B.4})
 \end{aligned}$$

#### 4 Mode Potential Field

Our initial condition of the MHD simulation chooses the 4 mode (expansion up to  $m + n = 4$ ) potential field in a square geometry ( $L_x = L_y = L$ ). The corresponding coefficients are:  $\alpha_m = \pi m/L$ ,  $\beta_n = \pi n/L$ , and  $\lambda_{mn}^2 = (m^2 + n^2) \frac{\pi^2}{L^2} - \kappa^2$ , i.e,  $\lambda_2 \equiv \lambda_{02} = \lambda_{20} = \sqrt{4\pi^2/L^2 - \kappa^2}$ ,  $\lambda_{11} = \sqrt{2\pi^2/L^2 - \kappa^2}$ ,  $\lambda_4 \equiv \lambda_{04} = \lambda_{40} = \sqrt{16\pi^2/L^2 - \kappa^2}$ ,  $\lambda_{22} = \sqrt{8\pi^2/L^2 - \kappa^2}$ ,  $\lambda_{13} = \lambda_{31} = \sqrt{10\pi^2/L^2 - \kappa^2}$ . The solution of the 4 mode potential fields

are:

$$\begin{aligned}
 B_x = & \exp(-\lambda_2 z) \left[ c_{20}^{(4)} \sin \frac{2\pi}{L} x \right] + \exp(-\lambda_4 z) \left[ c_{40}^{(4)} \sin \frac{4\pi}{L} x \right] \\
 & + \frac{\exp(-\lambda_{11} z)}{\sqrt{2}} \left[ -c_{11}^{(2)} \cos \frac{\pi}{L} x \cos \frac{\pi}{L} y + c_{11}^{(3)} \sin \frac{\pi}{L} x \sin \frac{\pi}{L} y \right] \\
 & + \frac{\exp(-\lambda_{22} z)}{\sqrt{2}} \left[ -c_{22}^{(1)} \cos \frac{2\pi}{L} x \sin \frac{2\pi}{L} y + c_{22}^{(4)} \sin \frac{2\pi}{L} x \cos \frac{2\pi}{L} y \right] \\
 & + \frac{\exp(-\lambda_{13} z)}{\sqrt{10}} \left[ -c_{13}^{(2)} \cos \frac{\pi}{L} x \cos \frac{3\pi}{L} y + c_{13}^{(3)} \sin \frac{\pi}{L} x \sin \frac{3\pi}{L} y \right. \\
 & \quad \left. - 3c_{31}^{(2)} \cos \frac{3\pi}{L} x \cos \frac{\pi}{L} y + 3c_{31}^{(3)} \sin \frac{3\pi}{L} x \sin \frac{\pi}{L} y \right]
 \end{aligned}$$

$$\begin{aligned}
 B_y = & \exp(-\lambda_2 z) \left[ c_{02}^{(4)} \sin \frac{2\pi}{L} y \right] + \exp(-\lambda_4 z) \left[ c_{04}^{(4)} \sin \frac{4\pi}{L} y \right] \\
 & + \frac{\exp(-\lambda_{11} z)}{\sqrt{2}} \left[ c_{11}^{(2)} \sin \frac{\pi}{L} x \sin \frac{\pi}{L} y - c_{11}^{(3)} \cos \frac{\pi}{L} x \cos \frac{\pi}{L} y \right] \\
 & + \frac{\exp(-\lambda_{22} z)}{\sqrt{2}} \left[ -c_{22}^{(1)} \sin \frac{2\pi}{L} x \cos \frac{2\pi}{L} y + c_{22}^{(4)} \cos \frac{2\pi}{L} x \sin \frac{2\pi}{L} y \right] \\
 & + \frac{\exp(-\lambda_{13} z)}{\sqrt{10}} \left[ 3c_{13}^{(2)} \sin \frac{\pi}{L} x \sin \frac{3\pi}{L} y - 3c_{13}^{(3)} \cos \frac{\pi}{L} x \cos \frac{3\pi}{L} y \right. \\
 & \quad \left. + c_{31}^{(2)} \sin \frac{3\pi}{L} x \sin \frac{\pi}{L} y - c_{31}^{(3)} \cos \frac{3\pi}{L} x \cos \frac{\pi}{L} y \right]
 \end{aligned}$$

$$\begin{aligned}
 B_z = & \exp(-\lambda_2 z) \left[ c_{02}^{(4)} \cos \frac{2\pi}{L} y + c_{20}^{(4)} \cos \frac{2\pi}{L} x \right] \\
 & + \exp(-\lambda_4 z) \left[ c_{04}^{(4)} \cos \frac{4\pi}{L} y + c_{40}^{(4)} \cos \frac{4\pi}{L} x \right] \\
 & + \exp(-\lambda_{11} z) \left[ c_{11}^{(2)} \sin \frac{\pi}{L} x \cos \frac{\pi}{L} y + c_{11}^{(3)} \cos \frac{\pi}{L} x \sin \frac{\pi}{L} y \right] \\
 & + \exp(-\lambda_{22} z) \left[ c_{22}^{(1)} \sin \frac{2\pi}{L} x \sin \frac{2\pi}{L} y + c_{22}^{(4)} \cos \frac{2\pi}{L} x \cos \frac{2\pi}{L} y \right] \\
 & + \exp(-\lambda_{13} z) \left[ c_{13}^{(2)} \sin \frac{\pi}{L} x \cos \frac{3\pi}{L} y + c_{13}^{(3)} \cos \frac{\pi}{L} x \sin \frac{3\pi}{L} y \right. \\
 & \quad \left. + c_{31}^{(2)} \sin \frac{3\pi}{L} x \cos \frac{\pi}{L} y + c_{31}^{(3)} \cos \frac{3\pi}{L} x \sin \frac{\pi}{L} y \right]
 \end{aligned}$$

#### 4 mode Potential Quadrupolar Field

To construct a 3D quadrupolar magnetic field, we use the coefficients as following:  $c_{02}^{(4)} = c_{20}^{(4)} = 25$ ,  $c_{04}^{(4)} = -c_{40}^{(4)} = 125$ ,  $c_{22}^{(1)} = c_{22}^{(4)} = 75$ , and  $c_{11}^{(2)} = c_{11}^{(3)} = c_{13}^{(2)} = c_{13}^{(3)} = c_{31}^{(2)} = c_{31}^{(3)} = 0$ . The resulting 3D quadrupolar magnetic field as an initial condition of the MHD

simulation has the following analytical solutions

$$\begin{aligned}
 B_x = & \exp(-\lambda_2 z) \left[ 25 \sin \frac{2\pi}{L} x \right] + \exp(-\lambda_4 z) \left[ -125 \sin \frac{4\pi}{L} x \right] \\
 & + \frac{\exp(-\lambda_{22} z)}{\sqrt{2}} \left[ -75 \cos \frac{2\pi}{L} x \sin \frac{2\pi}{L} y + 75 \sin \frac{2\pi}{L} x \cos \frac{2\pi}{L} y \right] \quad (\text{B.5})
 \end{aligned}$$

$$\begin{aligned}
 B_y = & \exp(-\lambda_2 z) \left[ 25 \sin \frac{2\pi}{L} y \right] + \exp(-\lambda_4 z) \left[ 125 \sin \frac{4\pi}{L} y \right] \\
 & + \frac{\exp(-\lambda_{22} z)}{\sqrt{2}} \left[ -75 \sin \frac{2\pi}{L} x \cos \frac{2\pi}{L} y + 75 \cos \frac{2\pi}{L} x \sin \frac{2\pi}{L} y \right] \quad (\text{B.6})
 \end{aligned}$$

$$\begin{aligned}
 B_z = & \exp(-\lambda_2 z) \left[ 25 \cos \frac{2\pi}{L} y + 25 \cos \frac{2\pi}{L} x \right] \\
 & + \exp(-\lambda_4 z) \left[ 125 \cos \frac{4\pi}{L} y - 125 \cos \frac{4\pi}{L} x \right] \\
 & + \exp(-\lambda_{22} z) \left[ 75 \sin \frac{2\pi}{L} x \sin \frac{2\pi}{L} y + 75 \cos \frac{2\pi}{L} x \cos \frac{2\pi}{L} y \right]. \quad (\text{B.7})
 \end{aligned}$$



## C Leapfrog and Lax Wendroff Schemes

A rather simple and second order accurate scheme is the so-called leapfrog scheme and it is used as the main numerical scheme to solve all the MHD equations (Appendix A). Consider the very simple one-dimensional linear convection equation

$$\frac{\partial f}{\partial t} + u \frac{\partial f}{\partial x} = 0 \quad (\text{C.1})$$

where for simplicity  $u$  is assumed to be known and constant. The Leapfrog scheme is given by the following equation:

$$\frac{f_i^{n+1} - f_i^{n-1}}{2\Delta t} + \frac{u}{2\Delta x}(f_{i+1}^n - f_{i-1}^n) = 0 \quad (\text{C.2})$$

which leads to the solution of the next time step as:

$$f_i^{n+1} = f_i^{n-1} - u \frac{\Delta t}{\Delta x}(f_{i+1}^n - f_{i-1}^n) = 0 \quad (\text{C.3})$$

Note that the error is of order  $O(\Delta t^2, \Delta x^2)$  such that the scheme is second order accurate. The Leapfrog is, however, not without problems. Thus the differencing decouples odd and even grid points at any given time step such that a solution can develop independently on the interlaced odd/even grid and thus may lead to strong oscillations on the grid scales.

A scheme closely related to the leapfrog is the Lax Wendroff method. It was used in the first and last step to solve the MHD equations since leapfrog is a two level scheme in both time and space. Lax Wendroff scheme uses the forward time discretization with a correction that eliminates the lowest order error of the forward time differencing

$$\begin{aligned} \frac{\partial f}{\partial t} &\approx \frac{f_i^{n+1} - f_i^n}{\Delta t} - \frac{1}{2}\Delta t \frac{\partial^2 f}{\partial t^2} \\ &= \frac{f_i^{n+1} - f_i^n}{\Delta t} - \frac{1}{2}\Delta t u^2 \frac{\partial^2 f}{\partial x^2} \end{aligned} \quad (\text{C.4})$$

which yields

$$f_i^{n+1} = f_i^n - \frac{1}{2}u \frac{\Delta t}{\Delta x}(f_{i+1}^n - f_{i-1}^n) + \frac{1}{2}u^2 \frac{(\Delta t)^2}{(\Delta x)^2}(f_{i+1}^n - 2f_i^n + f_{i-1}^n) \quad (\text{C.5})$$

The resulting error is  $O(\Delta t^2, \Delta x^2)$ . Note that the above formulation has problems in two dimensions or in general in cases where  $u$  or  $\Delta x$  is not constant. Therefore the Lax

Wendroff scheme is typically implemented as a two step method with the steps

$$\begin{aligned}f_{i+1/2}^* &= \frac{1}{2}(f_{i+1}^n + f_i^n) + \frac{1}{2}u \frac{\Delta t}{\Delta x}(f_{i+1}^n - f_i^n) \\f_i^{n+1} &= f_i^n + \frac{1}{2}u \frac{\Delta t}{\Delta x}(f_{i+1/2}^* - f_{i-1/2}^*)\end{aligned}\tag{C.6}$$

This two step Lax Wendroff has the same accuracy as the one step scheme and stability requires  $u\Delta t \leq \Delta x$ .

# D Test Particle Calculations

## Basic Equations

We calculated the particle trajectories and energies by numerically solving the relativistic equations of a charged particle in electromagnetic fields (also see Section 1.4.1):

$$\frac{dm\gamma\mathbf{v}}{dt} = q(\mathbf{E} + \mathbf{v} \times \mathbf{B}) \quad (\text{D.1})$$

$$\frac{d\mathbf{x}}{dt} = \mathbf{v} \quad (\text{D.2})$$

$$\frac{dE_k}{dt} = q\mathbf{v} \cdot \mathbf{E} \quad (\text{D.3})$$

Here,  $\mathbf{E}$  and  $\mathbf{B}$  are the local electric and the magnetic fields a charged particle experiences on its way.  $\gamma = 1/\sqrt{1 - v^2/c^2}$  is the relativistic Lorentz factor;  $m$  and  $q$  are the rest mass and the charge of the particle;  $\mathbf{x}$  and  $\mathbf{v}$  are the position and velocity vectors of the particle;  $E_k = mc^2(\gamma - 1)$  is the kinetic energy of a charged particle. Notice that Equation (D.3) is not independent. It can be obtained from Equation (D.1) as following.

$$\begin{aligned} \frac{dm\gamma\mathbf{v}}{dt} &= q(\mathbf{E} + \mathbf{v} \times \mathbf{B}) \Rightarrow \\ \mathbf{v} \cdot \frac{dm\gamma\mathbf{v}}{dt} &= q\mathbf{v} \cdot (\mathbf{E} + \mathbf{v} \times \mathbf{B}) \Rightarrow \\ m\mathbf{v} \cdot \left( \mathbf{v} \frac{d\gamma}{dt} + \gamma \frac{d\mathbf{v}}{dt} \right) &= q\mathbf{v} \cdot \mathbf{E} \Rightarrow \\ m\mathbf{v}^2 \frac{d\gamma}{dt} + \frac{1}{2}m\gamma \frac{d\mathbf{v}^2}{dt} &= q\mathbf{v} \cdot \mathbf{E} \Rightarrow \\ mc^2 \left( 1 - \frac{1}{\gamma^2} \right) \frac{d\gamma}{dt} + \frac{1}{2}m\gamma c^2 \frac{d\left(1 - \frac{1}{\gamma^2}\right)}{dt} &= q\mathbf{v} \cdot \mathbf{E} \Rightarrow \\ mc^2 \frac{d\gamma}{dt} - m \frac{c^2}{\gamma^2} \frac{d\gamma}{dt} - \frac{1}{2}mc^2 \gamma \frac{d\gamma^{-2}}{dt} &= q\mathbf{v} \cdot \mathbf{E} \Rightarrow \\ mc^2 \frac{d\gamma}{dt} &= q\mathbf{v} \cdot \mathbf{E} \end{aligned} \quad (\text{D.4})$$

## Normalization of the Equations

To simplify the calculation of the integration, we use dimensionless equations by normalizing all the dimensional variables:  $m = m_0 m'$ ,  $q = q_0 q'$ ,  $L = L_0 L'$ ,  $t = \tau_0 t'$ ,  $\mathbf{v} = v_0 \mathbf{v}'$ ,

$\mathbf{B} = B_0 \mathbf{B}'$ , and  $\mathbf{E} = v_0 B_0 \mathbf{E}'$ . The normalization parameters  $m_0$  and  $q_0$  are chosen to be the mass and charge of a proton:  $m_0 = 1.67 \times 10^{-27}$  kg and  $q_0 = 1.6 \times 10^{-19}$  C.  $L_0, v_0, B_0$  and  $E_0$  are set to be the same as those for normalizing MHD equations as shown in Table A.1. However, normalization time  $\tau_0$  here is much smaller ( $10^{-4}$  s) than that in the MHD simulation since the acceleration time scale is much shorter.

The normalization of Equation (D.1) is as following.

$$\begin{aligned}
\frac{d\gamma \mathbf{v}}{dt} &= q(\mathbf{E} + \mathbf{v} \times \mathbf{B}) \Rightarrow \\
\frac{m_0}{\tau_0} m' \frac{d\gamma \mathbf{v}'}{dt'} &= q_0 q' B_0 (\mathbf{E}' + \mathbf{v}' \times \mathbf{B}') \Rightarrow \\
\frac{d\gamma \mathbf{v}'}{dt'} &= (\tau_0 B_0 \frac{q_0}{m_0}) \frac{q'}{m'} (\mathbf{E}' + \mathbf{v}' \times \mathbf{B}') \Rightarrow \\
\frac{d\gamma \mathbf{v}'}{dt'} &= A_1 \frac{q'}{m'} (\mathbf{E}' + \mathbf{v}' \times \mathbf{B}'), \tag{D.5}
\end{aligned}$$

where  $A_1 \equiv \tau_0 B_0 \frac{q_0}{m_0}$ .

The normalization of Equation (D.2) is as following.

$$\begin{aligned}
\frac{d\mathbf{x}}{dt} &= \mathbf{v} \Rightarrow \\
\frac{L_0}{\tau_0} \frac{d\mathbf{x}'}{dt'} &= v_0 \mathbf{v}' \Rightarrow \\
\frac{d\mathbf{x}'}{dt'} &= \frac{v_0 \tau_0}{L_0} \mathbf{v}' \Rightarrow \\
\frac{d\mathbf{x}'}{dt'} &= A_2 \mathbf{v}', \tag{D.6}
\end{aligned}$$

where  $A_2 \equiv \frac{v_0 \tau_0}{L_0}$ .

The normalization of Equation (D.3) is as following.

$$\begin{aligned}
mc^2 \frac{d\gamma}{dt} &= q\mathbf{v} \cdot \mathbf{E} \Rightarrow \\
\frac{m_0}{\tau_0} m' c^2 \frac{d\gamma}{dt'} &= q_0 q' v_0 E_0 \mathbf{v}' \cdot \mathbf{E}' \Rightarrow \\
\frac{d\gamma}{dt'} &= \frac{\tau_0 q_0 v_0^2 B_0}{m_0 c^2} \frac{q'}{m'} \mathbf{v}' \cdot \mathbf{E}' \Rightarrow \\
\frac{d\gamma}{dt'} &= A_3 \frac{q'}{m'} \mathbf{v}' \cdot \mathbf{E}' \Rightarrow \tag{D.7}
\end{aligned}$$

where  $A_3 \equiv \frac{\tau_0 q_0 v_0^2 B_0}{m_0 c^2}$ .

Since  $\mathbf{x}$  and  $\mathbf{v}$  are three-dimensional vectors, there are in total 7 equations to be integrated using Runge-Kutta-Fehlberg fourth-fifth-order method (Fehlberg 1969).

## E Regularized Time Derivatives of Photon Fluxes

We use the regularized method developed by Kontar and MacKinnon (2005) to obtain the time derivatives of these photon fluxes. This method gives smoother derivatives while avoiding large errors, typical of finite differences of discrete numerical data.

One has a finite sample  $y_i$  of measured values over the interval  $x_0 \leq x \leq x_n$  (the grids are  $x_0 < x_1 < \dots < x_i < \dots < x_n$  with mesh size  $\Delta x$ ). The noisy data set has an error of  $\delta y$  which is an uncertainty of measurement. Assume the existence of a function  $f(x)$ , which is a close approximation to the data set:

$$\frac{1}{n-1} \sum_{i=1}^{n-1} (y_i - f(x_i))^2 \leq (\delta y)^2. \quad (\text{E.1})$$

Here, we have taken the boundary conditions:  $f(x_0) = y_0$  and  $f(x_n) = y_n$ . One also requires the function  $f(x)$  has a smooth derivative, in the sense that the its second derivative has the smallest norm:

$$\|f''\| = \min, \quad (\text{E.2})$$

where  $\|f''\|$  is the norm of  $f''$ :  $\|f''\| \equiv \left( \int_{x_0}^{x_n} f''(x)^2 dx \right)^{1/2}$ . Roughly speaking, if one represents  $f(x)$  locally by the first two terms of its Taylor expansion,  $f''$  gives an estimate of the error on  $f'(x)$  and minimising  $\|f''\|$  minimises the error in the resulting estimate for  $f'$ . Collecting the two requirements (E.1) and (E.2) into a single equation, one needs to minimise the following function:

$$\Phi(f) \equiv \frac{1}{n-1} \sum_{i=1}^{n-1} (y_i - \int_{x_0}^{x_i} f'(\xi) d\xi - y_0)^2 + \lambda \|f''(x)\|^2 \quad (\text{E.3})$$

where  $\lambda$  is so that

$$\frac{1}{n-1} \sum_{i=1}^{n-1} (y_i - f_\lambda(x_i))^2 = (\delta y)^2 \quad (\text{E.4})$$

Therefore,  $f_\lambda(x_i)$  is a regularized solution of minimum problem (E.3). The derivative of the regularized data  $f_\lambda(x_i)$  gives a much smoother solution than that calculated just by simple differencing of the data points.



# Bibliography

- Abbett, W. P., Hawley, S. L., 1999, Dynamic Models of Optical Emission in Impulsive Solar Flares, *ApJ*, 521, 906–919
- Aschwanden, M., 1998, Deconvolution of directly precipitating and trap-precipitating electrons in solar flare hard X-rays. I. Method and tests, *ApJ*, 502, 455
- Aschwanden, M., 2002, Particle acceleration and kinematics in solar flares—A Synthesis of Recent Observations and Theoretical Concepts (Invited Review), *Space Sci. Rev.*, 101, 1–227
- Aschwanden, M., Benz, A., Dennis, B., Schwartz, R., 1995, Solar electron beams detected in hard X-rays and radio waves, *ApJ*, 455, 347
- Aschwanden, M., Kosugi, T., Hudson, H., Wills, M., Schwartz, R., 1996a, The scaling law between electron time-of-flight distances and loop lengths in solar flares, *ApJ*, 470, 1198
- Aschwanden, M., Wills, M., Hudson, H., Kosugi, T., Schwartz, R., 1996b, Electron time-of-flight distances and flare loop geometries compared from CGRO and Yohkoh observations, *ApJ*, 468, 398
- Aschwanden, M. J., 2005, *Physics of the Solar Corona. An Introduction with Problems and Solutions* (2nd edition)
- Aschwanden, M. J., Brown, J. C., Kontar, E. P., 2002, Chromospheric Height and Density Measurements in a Solar Flare Observed with RHESSI II. Data Analysis, *Sol. Phys.*, 210, 383–405
- Aulanier, G., DeLuca, E., Antiochos, S., McMullen, R., Golub, L., 2000, The topology and evolution of the bastille day flare, *ApJ*, 540, 1126–1142
- Bai, T., 1982, Transport of energetic electrons in a fully ionized hydrogen plasma, *ApJ*, 259, 341–349
- Bai, T., Ramaty, R., 1979, Hard X-ray time profiles and acceleration processes in large solar flares, *ApJ*, 227, 1072–1081
- Bárta, M., Karlický, M., Büchner, J., 2009, Multi-scale MHD Modelling of the Current Sheet Fragmentation in Turbulent Solar Flare Reconnection, *Central European Astrophysical Bulletin*, 33, 299–308

- Battaglia, M., Benz, A., 2006, Relations between concurrent hard x-ray sources in solar flares, *A&A*, 456, 751–760
- Battaglia, M., Benz, A. O., 2007, Exploring the connection between coronal and footpoint sources in a thin-thick target solar flare model, *A&A*, 466, 713–716
- Battaglia, M., Fletcher, L., Benz, A., 2009, Observations of conduction driven evaporation in the early rise phase of solar flares, *A&A*, 498, 891–900
- Benka, S., Holman, G., 1994, A thermal/nonthermal model for solar hard X-ray bursts, *ApJ*, 435, 469–481
- Benz, A., 2008, Flare Observations, *Living Rev. Sol. Phys.*, 5
- Benz, A. O., 1977, Spectral features in solar hard X-ray and radio events and particle acceleration, *ApJ*, 211, 270–280
- Bogachev, S. A., Somov, B. V., Kosugi, T., Sakao, T., 2005, The Motions of the Hard X-Ray Sources in Solar Flares: Images and Statistics, *ApJ*, 630, 561–572
- Brown, J., 1971, The deduction of energy spectra of non-thermal electrons in flares from the observed dynamic spectra of hard X-ray bursts, *Sol. Phys.*, 18, 489–502
- Brown, J., 1974, On the thermal interpretation of hard X-ray bursts from solar flares, in *Coronal disturbances: symposium held at Surfers Paradise, Queensland, Australia, 7-11 September, 1973*, p. 395, Springer
- Browning, P., Vekstein, G., 2001, Particle acceleration at an X-type reconnection site with a parallel magnetic field, *J. Geophys. Res.*, 106
- Bruhwyler, D., Zweibel, E., 1992, Energy spectrum of particles accelerated near a magnetic x line, *J. Geophys. Res.*, 97, 10 825–10 830
- Büchner, J., 1986, About the third integral of charged particle motion in strongly curved magnetic fields, *Astron. Nachr.*, 307, 191–199
- Büchner, J., 2006, Locating Current Sheets in the Solar Corona, *Space Sci. Rev.*, 122, 149–160
- Büchner, J., 2007, Investigation of Reconnection in the Solar Corona by Numerical Simulation Based on Solar-B Observations, in *New Solar Physics with Solar-B Mission*, (Eds.) K. Shibata, S. Nagata, T. Sakurai, vol. 369, pp. 407–420, Astronomical Society of the Pacific
- Büchner, J., Elkina, N., 2006, Vlasov code simulation of anomalous resistivity, *Space Sci. Rev.*, 121, 237–252
- Büchner, J., Zelenyi, L. M., 1989, Regular and chaotic charged particle motion in magnetotail-like field reversals, 1. Basic theory, *J. Geophys. Res.*, 93, 11.821–11.842

- Büchner, J., Nikutowski, B., Otto, A., 2004, Coronal Heating by Transition Region Reconnection, in Proceedings of the SOHO 15 Workshop-Coronal Heating. 6-9 September 2004, St. Andrews, Scotland, UK (ESA SP-575). Editors: RW Walsh, J. Ireland, D. Danesy, B. Fleck. Paris: European Space Agency, 2004., p. 23
- Carmichael, H., 1964, A Process for Flares, NASA Special Publication, 50, 451–+
- Craig, I., Litvinenko, Y., 2002, Particle Acceleration Scalings Based on Exact Analytic Models for Magnetic Reconnection, *ApJ*, 570, 387–394
- Dalla, S., Browning, P., 2005, Particle acceleration at a three-dimensional reconnection site in the solar corona, *A&A*, 436, 1103–1111
- Dalla, S., Browning, P., 2008, Particle trajectories and acceleration during 3D fan reconnection, *A&A*, 491, 289–295
- de Jager, C., de Jonge, G., 1978, Properties of elementary flare bursts, *Sol. Phys.*, 58, 127–137
- Demoulin, P., Henoux, J. C., Priest, E. R., Mandrini, C. H., 1996, Quasi-Separatrix layers in solar flares. I. Method., *A&A*, 308, 643–655
- Dennis, B., 1985, Solar hard X-ray bursts, *Sol. Phys.*, 100, 465–490
- Dennis, B. R., Zarro, D. M., 1993, The Neupert effect - What can it tell us about the impulsive and gradual phases of solar flares?, *Sol. Phys.*, 146, 177–190
- Dere, K. P., Brueckner, G. E., Howard, R. A., Koomen, M. J., Korendyke, C. M., Kreplin, R. W., Michels, D. J., Moses, J. D., Moulton, N. E., Socker, D. G., St. Cyr, O. C., Delaboudinière, J. P., Artzner, G. E., Brunaud, J., Gabriel, A. H., Hochedez, J. F., Millier, F., Song, X. Y., Chauvineau, J. P., Marioge, J. P., Defise, J. M., Jamar, C., Rochus, P., Catura, R. C., Lemen, J. R., Gurman, J. B., Neupert, W., Clette, F., Cugnon, P., van Dessel, E. L., Lamy, P. L., Llebaria, A., Schwenn, R., Simnett, G. M., 1997, EIT and LASCO Observations of the Initiation of a Coronal Mass Ejection, *Sol. Phys.*, 175, 601–612
- Dere, K. P., Landi, E., Young, P. R., Del Zanna, G., Landini, M., Mason, H. E., 2009, CHIANTI - an atomic database for emission lines. IX. Ionization rates, recombination rates, ionization equilibria for the elements hydrogen through zinc and updated atomic data, *A&A*, 498, 915–929
- Des Jardins, A., Canfield, R., Longcope, D., Fordyce, C., Waitukaitis, S., 2009, Reconnection in Three Dimensions: The Role of Spines in Three Eruptive Flares, *ApJ*, 693, 1628–1636
- Dmitruk, P., Matthaeus, W., Seenu, N., Brown, M., 2003, Test Particle Acceleration In Three-Dimensional Magnetohydrodynamic Turbulence, *ApJ*, 597, 81–84
- Dulk, G., 1985, Radio Emission from the Sun and Stars, *Annual Rev. in A&A*, 23, 169–224

- Dungey, J., 1953, Conditions for the occurrence of electrical discharges in astrophysical systems, *Phil. Mag*, 44, 725–738
- Efthymiopoulos, C., Gontikakis, C., Anastasiadis, A., 2005, Particle dynamics in 3-D reconnecting current sheets in the solar atmosphere, *A&A*, 443, 663–678
- Emslie, A. G., 2003, The Determination of the Total Injected Power in Solar Flare Electrons, *ApJL*, 595, L119–L121
- Emslie, A. G., Kucharek, H., Dennis, B. R., Gopalswamy, N., Holman, G. D., Share, G. H., Vourlidas, A., Forbes, T. G., Gallagher, P. T., Mason, G. M., Metcalf, T. R., Mewaldt, R. A., Murphy, R. J., Schwartz, R. A., Zurbuchen, T. H., 2004, Energy partition in two solar flare/CME events, *J. Geophys. Res. (Space Physics)*, 109, 10 104–+
- Emslie, A. G., Dennis, B. R., Holman, G. D., Hudson, H. S., 2005, Refinements to flare energy estimates: A followup to “Energy partition in two solar flare/CME events” by A. G. Emslie et al., *J. Geophys. Res. (Space Physics)*, 110, 11 103–+
- Fehlberg, E., 1969, Low-order classical Runge-Kutta formulas with stepsize control and their application to some heat transfer problems, National Aeronautics and Space Administration
- Feldman, U., Dammasch, I., Landi, E., Doschek, G. A., 2004, Observations Indicating That 10 million K Solar Flare Plasmas May Be Produced in Situ from 1 million K Coronal Plasma, *ApJ*, 609, 439–451
- Fisher, G. H., 1989, Dynamics of flare-driven chromospheric condensations, *ApJ*, 346, 1019–1029
- Fisher, G. H., Canfield, R. C., McClymont, A. N., 1985a, Flare loop radiative hydrodynamics. V - Response to thick-target heating. VI - Chromospheric evaporation due to heating by nonthermal electrons. VII - Dynamics of the thick-target heated chromosphere, *ApJ*, 289, 414–441
- Fisher, G. H., Canfield, R. C., McClymont, A. N., 1985b, Flare Loop Radiative Hydrodynamics - Part Six - Chromospheric Evaporation due to Heating by Nonthermal Electrons, *ApJ*, 289, 425–+
- Fisher, G. H., Canfield, R. C., McClymont, A. N., 1985c, Flare Loop Radiative Hydrodynamics - Part Seven - Dynamics of the Thick Target Heated Chromosphere, *ApJ*, 289, 434–+
- Fletcher, L., Hudson, H., 2002, Spectral and spatial variations of flare hard X-ray footpoints, *Sol. Phys.*, 210, 307–321
- Fletcher, L., Hudson, H., 2008, Impulsive phase flare energy transport by large-scale Alfvén waves and the electron acceleration problem, *ApJ*, 675, 1645
- Fletcher, L., Metcalf, T., Alexander, D., Brown, D., Ryder, L., 2001, Evidence for the flare trigger site and three-dimensional reconnection in multiwavelength observations of a solar flare, *ApJ*, 554, 451–463

- Fletcher, L., Hannah, I., Hudson, H., Metcalf, T., 2007, A TRACE white light and RHESSI hard X-ray study of flare energetics, *ApJ*, 656, 1187
- Fletcher, L., Dennis, B. R., Hudson, H. S., Krucker, S., Phillips, K., A., V., et al., 2010, An Observational Overview of Solar Flares, *Space Sci. Rev.*
- Forbes, T., Priest, E., 1995, Photospheric Magnetic Field Evolution and Eruptive Flares, *ApJ*, 446, 377
- Foullon, C., Verwichte, E., Nakariakov, V., Fletcher, L., 2005, X-ray quasi-periodic pulsations in solar flares as magnetohydrodynamic oscillations, *A&A*, 440, L59–L62
- Frost, K., Dennis, B., 1971, Evidence from Hard X-Rays for Two-Stage Particle Acceleration in a Solar Flare, *ApJ*, 165, 655
- Furth, H. P., Killeen, J., Rosenbluth, M. N., 1963, Finite-Resistivity Instabilities of a Sheet Pinch, *Physics of Fluids*, 6, 459–484
- Gallagher, P. T., Dennis, B. R., Krucker, S., Schwartz, R. A., Tolbert, A. K., 2002, RHESSI and TRACE Observations of the 21 April 2002 x1.5 Flare, *Sol. Phys.*, 210, 341–356
- Gan, W., 1998, An invariable point in the energy spectra of non-thermal electrons of solar flares, *Astrophysics and Space Science*, 260, 515–519
- Gan, W., Li, Y., Chang, J., Tiernan, J., 2002, An improved method to derive the lower energy cutoff of non-thermal electrons from hard X-rays of solar flares, *Sol. Phys.*, 207, 137–147
- Grigis, P. C., Benz, A. O., 2004, The spectral evolution of impulsive solar X-ray flares, *A&A*, 426, 1093–1101
- Grigis, P. C., Benz, A. O., 2005, The spectral evolution of impulsive solar X-ray flares. II. Comparison of observations with models, *A&A*, 434, 1173–1181
- Grigis, P. C., Benz, A. O., 2006, Electron acceleration in solar flares: theory of spectral evolution, *A&A*, 458, 641–651
- Guo, J., Büchner, J., Otto, A., Santos, J., Marsch, E., Gan, W., 2010, Is the 3-D magnetic null point with a convective electric field an efficient particle accelerator?, *A&A*, 513, A73+
- Guo, J., Liu, S., Fletcher, L., Kontar, E. P., 2011, Relationship Between Hard and Soft X-ray Emission Components of a Solar Flare, *ApJ*, 728, 4–+, 1012.4346
- Hamilton, B., Fletcher, L., McClements, K., Thyagaraja, A., 2005, Electron Acceleration at Reconnecting X-Points in Solar Flares, *ApJ*, 625, 496–505
- Hamilton, R. J., Petrosian, V., 1992, Stochastic acceleration of electrons. I - Effects of collisions in solar flares, *ApJ*, 398, 350–358

- Hannah, I., Fletcher, L., 2006, Comparison of the Energy Spectra and Number Fluxes From a simple Flare Model to Observations, *Sol. Phys.*, 236, 59–74
- Hannah, I. G., Particle heating and acceleration in solar flares: energization at a reconnecting X-point and RHESSI microflare observations
- Hannah, I. G., Kontar, E. P., Sirenko, O. K., 2009, The Effect of Wave-Particle Interactions on Low-Energy Cutoffs in Solar Flare Electron Spectra, *ApJL*, 707, L45–L50
- Heerikhuisen, J., Litvinenko, Y., Craig, I., 2002, Proton Acceleration in Analytic Reconnecting Current Sheets, *ApJ*, 566, 512–520
- Hesse, M., Schindler, K., Birn, J., Kuznetsova, M., 1999, The diffusion region in collisionless magnetic reconnection, *Physics of Plasmas*, 6, 1781
- Heyvaerts, J., Priest, E., Rust, D., 1977, An emerging flux model for the solar flare phenomenon, *ApJ*, 216, 123–137
- Hirayama, T., 1974, Theoretical Model of Flares and Prominences. I: Evaporating Flare Model, *Sol. Phys.*, 34, 323–338
- Hodgson, R., 1859, On a curious appearance seen in the Sun, *Monthly Notices of the Royal Astronomical Society*, 20, 15–16
- Holman, G., 2003, The Effects of Low-and High-Energy Cutoffs on Solar Flare Microwave and Hard X-Ray Spectra, *ApJ*, 586, 606–616
- Hudson, H., 1978, A purely coronal hard X-ray event, *ApJ*, 224
- Hudson, H. S., Acton, L. W., Freeland, S. L., 1996, A Long-Duration Solar Flare with Mass Ejection and Global Consequences, *ApJ*, 470, 629–+
- Hurford, G., Schwartz, R., Krucker, S., Lin, R., Smith, D., Vilmer, N., 2003, First Gamma-Ray Images of A Solar Flare, *ApJ*, 595, 77–80
- Hurford, G. J., Krucker, S., Lin, R. P., Schwartz, R. A., Share, G. H., Smith, D. M., 2006, Gamma-Ray Imaging of the 2003 October/November Solar Flares, *ApJL*, 644, L93–L96
- Inglis, A., Nakariakov, V., 2009, A multi-periodic oscillatory event in a solar flare, *A&A*, 493, 259–266
- Ji, H., Huang, G., Wang, H., Zhou, T., Li, Y., Zhang, Y., Song, M., 2006, Converging Motion of  $H\alpha$  Conjugate Kernels: The Signature of Fast Relaxation of a Sheared Magnetic Field, *ApJL*, 636, L173–L174
- Jones, F. C., Ellison, D. C., 1991, The plasma physics of shock acceleration, *Space Science Reviews*, 58, 259–346
- Kane, S. R., Anderson, K. A., 1970, Spectral Characteristics of Impulsive Solar-Flare X-Rays larger than 10 KeV, *ApJ*, 162, 1003–+

- Karlicky, M., Barta, M., 2006, X-Ray Loop-Top Source Generated by Processes in a Flare Collapsing Trap, *ApJ*, 647, 1472–1479
- Kliem, B., 1994, Particle orbits, trapping, and acceleration in a filamentary current sheet model, *ApJ Supplement Series*, 90, 719–728
- Kliem, B., 1995, Coupled Magnetohydrodynamic and Kinetic Development of Current Sheets in the Solar Corona, in *Coronal Magnetic Energy Releases*
- Kontar, E., MacKinnon, A., 2005, Regularized energy-dependent solar flare hard x-ray spectral index, *Sol. Phys.*, 227, 299–310
- Kontar, E. P., Dickson, E., Kašparová, J., 2008a, Low-Energy Cutoffs in Electron Spectra of Solar Flares: Statistical Survey, *Sol. Phys.*, 252, 139–147
- Kontar, E. P., Hannah, I. G., MacKinnon, A. L., 2008b, Chromospheric magnetic field and density structure measurements using hard X-rays in a flaring coronal loop, *A&A*, 489, L57–L60
- Kopp, R. A., Pneuman, G. W., 1976, Magnetic reconnection in the corona and the loop prominence phenomenon, *Sol. Phys.*, 50, 85–98
- Krucker, S., Christe, S., Lin, R., Hurford, G., Schwartz, R., 2002, Hard X-ray microflares down to 3 keV, *Sol. Phys.*, 210, 445–456
- Krucker, S., Hurford, G. J., Lin, R. P., 2003, Hard X-Ray Source Motions in the 2002 July 23 Gamma-Ray Flare, *ApJL*, 595, L103–L106
- Krucker, S., Battaglia, M., Cargill, P., Fletcher, L., Hudson, H., MacKinnon, A., Masuda, S., Sui, L., Tomczak, M., Veronig, A., et al., 2008a, Hard X-ray emission from the solar corona, *A&A Review*, 16, 155–208
- Krucker, S., Hurford, G., MacKinnon, A., Shih, A., Lin, R., 2008b, Coronal  $\gamma$ -ray bremsstrahlung from solar flare-accelerated electrons, *ApJL*, 678, L63
- Lau, Y., Finn, J., 1990, Three-dimensional kinematic reconnection in the presence of field nulls and closed field lines, *ApJ*, 350
- Li, Y., Gan, W., 2008, Observational Studies of the X-Ray Quasi-Periodic Oscillations of a Solar Flare, *Sol. Phys.*, 247, 77–85
- Li, Y. P., Gan, W. Q., 2005, The Shrinkage of Flare Radio Loops, *ApJL*, 629, L137–L139
- Lin, J., 2004, CME-Flare Association Deduced from Catastrophic Model of CMEs, *Sol. Phys.*, 219, 169–196
- Lin, R., Hudson, H., 1976, Non-thermal processes in large solar flares, *Sol. Phys.*, 50, 153–178
- Lin, R., Dennis, B., Hurford, G., Smith, D., Zehnder, A., Harvey, P., Curtis, D., Pankow, D., Turin, P., Bester, M., et al., 2002, The Reuven Ramaty High-Energy Solar Spectroscopic Imager (RHESSI), *Sol. Phys.*, 210, 3–32

## Bibliography

---

- Lin, R., Krucker, S., Hurford, G., Smith, D., Hudson, H., Holman, G., Schwartz, R., Dennis, B., Share, G., Murphy, R., et al., 2003, RHESSI observations of particle acceleration and energy release in an intense solar gamma-ray line flare, *ApJL*, 595, L69
- Litvinenko, Y., 1996, Particle Acceleration in Reconnecting Current Sheets with a Nonzero Magnetic Field, *ApJ*, 462
- Litvinenko, Y. E., Somov, B. V., 1993, Particle acceleration in reconnecting current sheets, *Sol. Phys.*, 146, 127–133
- Liu, S., Fletcher, L., 2009, Elementary Energy Release Events in Solar Flares, *ApJL*, 701, L34–L38
- Liu, S., Han, F., Fletcher, L., 2010, Elementary Energy Release Events in Flaring Loops: Effects of Chromospheric Evaporation on X-Rays, *ApJL*, 709, 58–66
- Liu, W., Chen, P., Fang, C., Ding, M., 2007, Evolution of electron energy spectrum during solar flares, *Advances in Space Research*, 39, 1394–1397
- Liu, W., Petrosian, V., Dennis, B. R., Jiang, Y. W., 2008, Double Coronal Hard and Soft X-Ray Source Observed by RHESSI: Evidence for Magnetic Reconnection and Particle Acceleration in Solar Flares, *ApJ*, 676, 704–716
- Liu, W., Chen, P., Ding, M., Fang, C., 2009, Energy spectrum of the electrons accelerated by reconnection electric field: exponential or power-law?, *ApJ*, 690, 1633–1638
- Liu, Y., Swisdak, M., Drake, J. F., 2009, The Weibel instability inside the electron-positron Harris sheet, *Physics of Plasmas*, 16, 042 101–+
- Longcope, D. W., Parnell, C. E., 2009, The Number of Magnetic Null Points in the Quiet Sun Corona, *Sol. Phys.*, 254, 51–75, 0811.0097
- Masuda, S., Kosugi, T., Hara, H., Tsuneta, S., Ogawara, Y., 1994, A loop-top hard X-ray source in a compact solar flare as evidence for magnetic reconnection, *Nature*, 371, 495–497
- McAteer, R., Young, C., Ireland, J., Gallagher, P., 2007, Bursty X-Ray Flare Emission, *ApJ*, 662, 691–700
- McTiernan, J. M., Fisher, G. H., Li, P., 1999, The Solar Flare Soft X-Ray Differential Emission Measure and the Neupert Effect at Different Temperatures, *ApJ*, 514, 472–483
- Metcalf, T., Fisher, G., 1996, A Test of a New Flare Loop Scaling Law Using YOHKOH SXT and GOES Observations, *ApJ*, 462, 977
- Miller, J. A., Cargill, P. J., Emslie, A. G., Holman, G. D., Dennis, B. R., LaRosa, T. N., Winglee, R. M., Benka, S. G., Tsuneta, S., 1997, Critical issues for understanding particle acceleration in impulsive solar flares, *J. Geophys. Res.*, 102, 14 631–14 660

- Milligan, R. O., 2008, A Hot Microflare Observed with RHESSI and Hinode, *ApJL*, 680, L157–L160
- Milligan, R. O., Gallagher, P. T., Mathioudakis, M., Bloomfield, D. S., Keenan, F. P., Schwartz, R. A., 2006a, RHESSI and SOHO CDS Observations of Explosive Chromospheric Evaporation, *ApJL*, 638, L117–L120
- Milligan, R. O., Gallagher, P. T., Mathioudakis, M., Keenan, F. P., 2006b, Observational Evidence of Gentle Chromospheric Evaporation during the Impulsive Phase of a Solar Flare, *ApJL*, 642, L169–L171
- Mori, K., Sakai, J., Zhao, J., 1998, Proton Acceleration near an X-Type Magnetic Reconnection Region, *ApJ*, 494, 430–437
- Mrozek, T., Tomczak, M., 2004, Solar impulsive soft X-ray brightenings and their connection with footpoint hard X-ray emission sources, *A&A*, 415, 377–389
- Neupert, W. M., 1968, Comparison of Solar X-Ray Line Emission with Microwave Emission during Flares, *ApJL*, 153, L59+
- Northrop, T., 1963, Adiabatic charged-particle motion, *Rev. Geophys*, 1, 283
- Ofman, L., Sui, L., 2006, Oscillations of Hard X-Ray Flare Emission Observed by RHESSI: Effects of Super-Alfvénic Beams?, *ApJL*, 644, L149
- Otto, A., Büchner, J., Nikutowski, B., 2007, Force-free magnetic field extrapolation for MHD boundary conditions in simulations of the solar atmosphere, *A&A*, 468, 313–321
- Pallavicini, R., Serio, S., Vaiana, G., 1977, A survey of soft X-ray limb flare images-The relation between their structure in the corona and other physical parameters, *ApJ*, 216, 108–122
- Park, B. T., Petrosian, V., 1995, Fokker-Planck Equations of Stochastic Acceleration: Green's Functions and Boundary Conditions, *ApJ*, 446, 699–+
- Parker, E., 1957, Sweet's Mechanism for Merging Magnetic Fields in Conducting Fluids, *J. Geophys. Res.*, 62
- Parker, E., 1993, A solar dynamo surface wave at the interface between convection and nonuniform rotation, *ApJ*, 408, 707–719
- Parks, G., Winckler, J., 1969, Sixteen-Second Periodic Pulsations Observed in the Correlated Microwave and Energetic X-Ray Emission from a Solar Flare, *ApJ*, 155
- Parnell, C., Smith, J., Neukirch, T., Priest, E., 1996, The structure of three-dimensional magnetic neutral points, *Physics of Plasmas*, 3, 759–770
- Petkaki, P., MacKinnon, A. L., 2007, Particle acceleration by fluctuating electric fields at a magnetic field null point, *A&A*, 472, 623–632, 0707.1254

- Petrosian, V., 1973, Impulsive Solar X-Ray Bursts: Bremsstrahlung Radiation from a Beam of Electrons in the Solar Chromosphere and the Total Energy of Solar Flares, *ApJ*, 186, 291–304
- Petrosian, V., Liu, S., 2004, Stochastic Acceleration of Electrons and Protons. I. Acceleration by Parallel-Propagating Waves, *ApJ*, 610, 550–571
- Petschek, H., 1964, Magnetic Field Annihilation, *The Physics of Solar Flares*
- Pina, R. K., Puetter, R. C., 1993, Bayesian image reconstruction - The pixon and optimal image modeling, *PASP*, 105, 630–637
- Potter, D., 1973, *Computational Physics*, John Wiley & Sons
- Priest, E., Forbes, T., 2000, *Magnetic Reconnection*
- Priest, E., Titov, V., 1996, Magnetic reconnection at three-dimensional null points, *Phil. Trans. R. Soc. Lond. A*, 354, 2951–2992
- Priest, E. R., 1986, Magnetic Reconnection on the Sun, *Mitteilungen der Astronomischen Gesellschaft Hamburg*, 65, 41–+
- Priest, E. R., Forbes, T. G., 2002, The magnetic nature of solar flares, *A&A Rev.*, 10, 313–377
- Qiu, J., Lee, J., Gary, D. E., Wang, H., 2002, Motion of Flare Footpoint Emission and Inferred Electric Field in Reconnecting Current Sheets, *ApJ*, 565, 1335–1347
- Restante, A., Aulanier, G., Parnell, C., 2009, How skeletons turn into quasi-separatrix layers in source models, *A&A*, 508, 433–443
- Saba, J. L. R., Gaeng, T., Tarbell, T. D., 2006, Analysis of Solar Flare Ribbon Evolution: A Semiautomated Approach, *ApJ*, 641, 1197–1209
- Saint-Hilaire, P., Benz, A. O., 2005, Thermal and non-thermal energies of solar flares, *A&A*, 435, 743–752
- Sakai, J., 1992, Prompt particle acceleration around moving X-point magnetic field during impulsive phase of solar flares, *Sol. Phys.*, 140, 99–119
- Santos, J., Büchner, J., 2007, MHD simulation of electric currents in the solar atmosphere caused by photospheric plasma motion, *Astrophys. Space Sci. Trans.*, 3, 29–33
- Santos, J. C., Büchner, J., Otto, A., 2011, Development of electric currents in a magnetic field configuration containing a magnetic null point, *A&A*, 525, A3+
- Schmahl, E. J., Pernak, R. L., Hurford, G. J., Lee, J., Bong, S., 2007, Analysis of RHESSI Flares Using aRadio Astronomical Technique, *Sol. Phys.*, 240, 241–252
- Schopper, R., Birk, G., Lesch, H., 1999, Particle acceleration in three-dimensional reconnection regions: A new test particle approach, *Physics of Plasmas*, 6, 4318

- Shibata, K., Masuda, S., Shimojo, M., Hara, H., Yokoyama, T., Tsuneta, S., Kosugi, T., Ogawara, Y., 1995, Hot-Plasma Ejections Associated with Compact-Loop Solar Flares, *ApJL*, 451, L83+
- Smith, D., Lin, R., Turin, P., Curtis, D., Primbsch, J., Campbell, R., Abiad, R., Schroeder, P., Cork, C., Hull, E., et al., 2002, The RHESSI spectrometer, *Sol. Phys.*, 210, 33–60
- Speiser, T., 1965, Particle Trajectories in Model Current Sheets, 1. Analytical Solutions, *J. Geophys. Res.*, 70, 4219–4226
- Speiser, T., 1967, Particle trajectories in model current sheets. II(Particle trajectories for two model configurations of electric and magnetic fields in geomagnetic tail, noting application to auroral acceleration), *J. Geophys. Res.*, 72, 3919–3932
- Sturrock, P. A., 1966, Model of the High-Energy Phase of Solar Flares, *Nature*, 211, 695–697
- Sui, L., Holman, G. D., 2003, Evidence for the Formation of a Large-Scale Current Sheet in a Solar Flare, *ApJL*, 596, L251–L254
- Sui, L., Holman, G. D., Dennis, B. R., Krucker, S., Schwartz, R. A., Tolbert, K., 2002, Modeling Images and Spectra of a Solar Flare Observed by RHESSI on 20 February 2002, *Sol. Phys.*, 210, 245–259
- Svestka, Z. F., Fontenla, J. M., Machado, M. E., Martin, S. F., Neidig, D. F., 1987, Multi-thermal observations of newly formed loops in a dynamic flare, *Sol. Phys.*, 108, 237–250
- Sweet, P., 1958, The Neutral Point Theory of Solar Flares, in *Electromagnetic Phenomena in Cosmical Physics*, Proceedings from IAU Symposium, 6
- Tandberg-Hanssen, E., Emslie, A., 1988, The physics of solar flares
- Temmer, M., Veronig, A. M., Vršnak, B., Miklenic, C., 2007, Energy Release Rates along  $H\alpha$  Flare Ribbons and the Location of Hard X-Ray Sources, *ApJ*, 654, 665–674
- Temmer, M., Veronig, A. M., Vršnak, B., Rybák, J., Gömöry, P., Stoiser, S., Maričić, D., 2008, Acceleration in Fast Halo CMEs and Synchronized Flare HXR Bursts, *ApJL*, 673, L95–L98
- Tsuneta, S., 1997, Moving Plasmoid and Formation of the Neutral Sheet in a Solar Flare, *ApJ*, 483, 507–514
- Turkmani, R., Cargill, P., Galsgaard, K., Vlahos, L., Isliker, H., 2006, Particle acceleration in stochastic current sheets in stressed coronal active regions, *A&A*, 449, 749–757
- Van Beek, H., De Feiter, L., De Jager, C., 1974, Time profiles and photon spectra of solar hard X-rays, in *Correlated interplanetary and magnetospheric observations*, vol. 42, pp. 533–543

- Vekstein, G., Browning, P., 1997, Electric-drift generated trajectories and particle acceleration in collisionless magnetic reconnection, *Physics of Plasmas*, 4, 2261
- Vernazza, J., Avrett, E., Loeser, R., 1981, Structure of the solar chromosphere. III- Models of the EUV brightness components of the quiet-sun, *ApJ Supplement Series*, 45, 635–725
- Veronig, A., Brown, J., 2004, A coronal thick-target interpretation of two hard X-ray loop events, *ApJL*, 603, L117
- Veronig, A., Vršnak, B., Dennis, B. R., Temmer, M., Hanslmeier, A., Magdalenic, J., 2002, Investigation of the Neupert effect in solar flares. I. Statistical properties and the evaporation model, *A&A*, 392, 699–712
- Veronig, A., Brown, J., Dennis, B., Schwartz, R., Sui, L., Tolbert, A., 2005, Physics of the Neupert effect: estimates of the effects of source energy, mass transport, and geometry using RHESSI and GOES data, *ApJ*, 621, 482
- Veronig, A. M., Karlický, M., Vršnak, B., Temmer, M., Magdalenic, J., Dennis, B. R., Otruba, W., Pötzi, W., 2006, X-ray sources and magnetic reconnection in the X3.9 flare of 2003 November 3, *A&A*, 446, 675–690
- Warren, H. P., Warshall, A. D., 2001, Ultraviolet Flare Ribbon Brightenings and the Onset of Hard X-Ray Emission, *ApJL*, 560, L87–L90
- Wheatland, M. S., Melrose, D. B., 1995, Interpreting YOHKOH hard and soft X-ray flare observations, *Sol. Phys.*, 158, 283–299
- Wood, P., Neukirch, T., 2005, Electron Acceleration in Reconnecting Current Sheets, *Sol. Phys.*, 226, 73–95
- Zharkova, V., Gordovskyy, M., 2004, Particle Acceleration Asymmetry in a Reconnecting Nonneutral Current Sheet, *ApJ*, 604, 884–891
- Zirin, H., 1988, *Astrophysics of the Sun*

# Publications

## *First-author Refereed Articles:*

- Jingnan Guo, Siming Liu, Lyndsay Fletcher and Eduard Kontar. *Relationship between Hard and Soft X-ray Emission Components of A Solar Flare*, 2011, ApJ, 728, 4
- Guo, J.-N., Buechner, J., Otto, A., Santos, J., Marsch, E. and Gan, W.-Q. *Is the 3-D magnetic null point with a convective electric fields an efficient particle accelerator?*, 2010, A&A, 513, 13.

## *Abstracts, Posters and Talks:*

- Jingnan Guo, Lyndsay Fletcher, Siming Liu and Eduard Kontar. *Solar flare electrons — testing the two-component model*, 2010, Sep, UKSP nugget
- Guo, J., Buechner, J., Santos, J. C. and Otto, A. *Particle Acceleration in 3D MHD Reconnection Fields*, 2008, 12th European Solar Physics Meeting, p.3.44, Abstract
- Jingnan Guo, 10th RHESSI workshop, Annapolis, U.S., Aug 2010, Talk
- UK MHD Meeting, Leeds, U.K., May 2010, Talk
- The 2010 Royal Astronomical Society National Astronomy Meeting (RAS NAM), Glasgow, U.K., Apr 2010, Poster
- The 3rd SOLAIRE Network Meeting and Flux Emergence Workshop, Tenerife, Spain, Nov 2009, Talk
- The 9th International School for Space Simulations, Paris, France, Jul 2009, Poster
- The 2nd Solaire Network Meeting, Catania, Italy, Jan 2009, Talk
- The 12th European Solar Physics Meeting, Freiburg, Germany, Sep 2008, Poster
- The 5th International "Cambridge" Workshop on Magnetic Reconnection, Bad-Honnef, Germany, Aug 2008, Poster
- Third Workshop for Young Researchers on CME and Related Phenomena, Observatoire de Paris-Meudon, France, May 2008, Talk
- First Solaire network-wide meeting, Leuven, Belgium, Dec 2007, Poster



# Acknowledgements

I am heartily thankful to all my supervisors, Dr. Lyndsay Fletcher, Prof. Jörg Büchner, Prof. Gan Weiqun, and Prof. Eckart Marsch. Their encouragement, guidance and support from the initial to the final level of my post-graduate study enabled me to develop a deep understanding of the subject and to fulfill my wish to finish a good PhD thesis.

It is an honor for me to thank Prof. Fang Cheng, Prof. Chen Pengfei, and Prof. Ding Mingde, Prof. Wu Dejin, Dr. Thomas Wiegmann, and Prof. Sami Solanki. Their courses on the subjects of solar physics, plasma physics and computational skills have helped me to grow my strong interest and to build up a solid background in this field. I would also like to thank Prof. Chang Jin, Prof. Li Hui, Prof. Ji Haisheng, Prof. Li Youping, Prof. Huang Guangli, Dr. Su Yang, Dr. Feng li, Dr. Huang Yu, Chen Wei, Du Qiusheng, Han Feiran and Bai Weidong who work together with me in Purple Mountain Observatory (PMO).

I am indebted to the European project Solaire Research Training Network and its coordinator Fernando Moreno-Insertis for giving me the opportunity to work in such a wonderful topic and believing in my capacity to do this work. Without the opportunity to study in both Max-Planck-Institut für Sonnensystemforschung (MPS) in Germany and University of Glasgow (GLAS) in U.K., it would not have been possible for me to learn so much in solar physics or to collaborate with so many good scientists.

I am grateful to Prof. Antonius Otto and Dr. Jean Santos for the helpful discussions about the MHD model and for their patience to answer my questions and their help to solve the problems. It is a pleasure to thank all my friends who have spent the unforgotten time with me in the small village Lindau. Without your company, it would have been too difficult for me to 'survive' for two years in the cornfield. I remember all our laughs sweetening the bitter espresso in the tiny little coffee room. I remember all the amazing dinners and parties we had in the movie-club.

I would like to show my gratitude to the whole astro-group in GLAS where Dr. Eduard Kontar, Dr. Liu Siming, Dr. Marina Battaglia, Dr. Iain Hannah, Dr. Hugh Hudson and Prof. John Brown have helped me so much from detailed RHESSI tips to theoretical discussions, where Dr. Declan Diver has given me a surprising chance to extend my contract for another three months, where my colleges and friends have accompanied me with coffee, biscuits, and jokes every weekday through the last year of my PhD.

I would also acknowledge Prof. Michele Piana and Rosita Timossi. Michele has brought me a fantastic chance to continue my research after my PhD in the University of Genoa in Italy. Rosita has been very important in helping me to prepare the paperwork for the job to start.

At last, but not the least, I would love to say that I own my deepest gratitude to my parents and my boyfriend for their unwavering support.



# Curriculum Vitae

## Education

- **Ph.D., Purple Mountain Observatory (PMO), Chinese Academy of Sciences, Nanjing, China, (expected graduating date: Jun 2011)**
  - Thesis Topic: *Particle Acceleration in Solar Flares: Simulation and Observation*
  - Advisers:
    - Prof. Weiqun Gan, PMO, China
    - Prof. Jörg Büchner and Prof. Eckart Marsch, Max-Planck-Institut für Sonnensystemforschung (MPS), Germany
    - Dr. Lyndsay Fletcher, University of Glasgow (GLAS), U.K.
- **B.S., Nanjing University (NJU), Nanjing, China, June 2006**
  - Subject: Astronomy and Physics
  - Thesis Topic: *RHESSI Observation of a Loop-like Flare on 3 November 2004*

## Scholarships and Awards

- Early Stage Researcher - **SOLAIRE** Research Training Network, 2007-2010
  - University of Glasgow, United Kingdom, Oct 2009 - Sep 2010
  - Max-Planck-Institut für Sonnensystemforschung, Germany, Sep 2007 - Sep 2009
- Nanjing University, China
  - Spirit of Ethics Awards (for students dedicated to teamwork), Dec 2005
  - People Scholarship (for students with outstanding academic progress), Nov 2003 and Dec 2004

## Skills

- Fluent in **Chinese** (Mandarin) and **English**. Good knowledge of **Italian, German, and Russian**
- Proficient in **Matlab** (> 6000 lines written), **IDL** (> 5000 lines written) and **Fortran**(~ 2000 lines written). Familiar with **C, C++, Paraview** and **Mathematica**. Capable of learning a new programming language within a short time period.
- Skilled in **LaTeX**, **Microsoft Office**, and other common productivity packages for both Windows and Linux platforms
- Experienced in **oral** and **poster presentations**, as well as **scientific writings**